NORTHWESTERN UNIVERSITY

Atomic-Scale Surface Studies of Alkaline-Earth Metals on Si(001)

A DISSERTATION

SUBMITTED TO THE GRADUATE SCHOOL
IN PARTIAL FULLFILLMENT OF THE REQUIREMENTS

for the degree

DOCTOR OF PHILOSOPHY

Field of Materials Science and Engineering

By

Duane Martin Goodner

EVANSTON, ILLINOIS

December 2005

ABSTRACT

Atomic-Scale Surface Studies of Alkaline-Earth Metals on Si(001)

Duane Martin Goodner

Surface phases consisting of sub-monolayer amounts of the alkaline-earth metal (AEM) atoms Sr and Ba on Si(001) have been studied using X-ray standing waves (XSW), low-energy electron diffraction (LEED), Auger electron spectroscopy (AES) and X-ray photoemission spectroscopy (XPS). XSW triangulation indicates that the same position relative to the bulk unit cell is occupied by Sr atoms in 1/2 ML (2x1) and 1/6 ML (2x3) phases. The same position appears to be occupied in a (3x1) phase as well. The XSW results, in conjunction with nearest-neighbor bond length considerations, are consistent with Sr atoms occupying valley-bridge sites in both the (2x3) and (2x1) phases. XSW results and surface symmetry suggest that the in-plane confinement of the thermal vibration amplitude of Sr is greater in the (2x3) phase than it is in the (2x1) phase. LEED, AES and X-ray fluorescence (XRF) measurements indicate that Sr/Si(001) surfaces with Sr coverage between 1/6 ML and 1/3 ML consist of a mixture of (2x3) and c(2x6) phases.

XSW measurements of a 1/2 ML(2x1) Ba/Si(001) phase indicate that the in-plane position of Ba atoms on this surface is the same as that of Sr in the (2x1) and (2x3) Sr/Si(001) phases. Ordered Ba/Si(001) and Sr/Si(001) surfaces have been observed to degrade due to the presence of residual gases in the ultra-high vacuum (UHV) environment. Ba/Si(001) appears to be the more sensitive of the two systems. This degradation influences both the coherent positions and the coherent fractions measured by XSW.

XSW evidence indicates that oxygen contamination on Sr/Si(001) can have two different effects on the atomic-scale structure of the surface. The particular effect that dominates depends on whether the contamination is introduced before or after the formation of a long-range ordered phase. XPS measurements of Sr/Si(001) surfaces intentionally exposed to O_2 have been used to monitor accumulation of oxygen in two different bonding environments. The rate constant for the accumulation of oxygen bonded to Sr is several orders of magnitude higher than that of oxygen bonded to Si. The formation of Si-O bonding occurs more rapidly on the (2x3) Sr/Si(001) surface than it does on (2x1) Sr/Si(001).

Approved:

Professor Michael J. Bedzyk
Department of Materials Science and Engineering
Northwestern University
Evanston, IL

ACKNOWLEDGEMENTS

First, I would like to give huge thanks my advisor, Professor Michael Bedzyk, for guiding and supporting me throughout my graduate studies.

I am also grateful to the members of my qualifier and thesis committees: Professor Mark Asta, Dr. Orlando Auciello, Professor Mark Hersam and Professor Thomas Mason.

I would also like to acknowledge the funding support from the National Science Foundation (through the Northwestern University Materials Research Science Engineering Center). Use of the Advanced Photon Source was supported by the U. S. Department of Energy, Office of Science, Office of Basic Energy Sciences, under Contract No. W-31-109-Eng-38.

I am grateful to many past and present members of the Bedzyk research group. I thank Alexander Kazimirov, Osami Sakata and William Rodrigues for helping get started with my research. I am also grateful to Brad Tinkham, Kai Zhang, John Okasinski, Joe Libera, Lixin Cao, Yongseong Choi, Don Walko, Jeff Klug, Brent Fiedler and Steve Christensen for providing various forms of help along the way. I thank Zhan Zhang for selflessly providing extremely vital assistance with software and detectors during beamtimes. I am indebted to Chang-Yong Kim for spending an untold number of hours answering my questions and helping with UHV equipment. I especially thank David Marasco and Anthony Escuadro for all of their help. They played integral roles in so many of my experiments, and working with them was always enjoyable.

I am grateful to beamline staff members at BESSRC-CAT: Mark Beno, Jennifer Linton, Guy Jennings, and Soenke Seifert; at DND-CAT: Denis Keane and John Quintana; and at X15A:

Zhong Zhong. I also owe a big thanks to Jerry Carsello for managing the Northwestern X-ray Lab and providing lots of help and advice.

I am also very grateful to other research collaborators: Pete Baldo and Loren Funk for providing implanted standards used for Sr and Ba coverage calibration; Rodney McKee and Fred Walker for providing valuable wisdom and samples; Jimmy Yu for providing additional samples; Darrel Schlom for selfless advice; and Venu Vaithyanathan for providing samples and even traveling to Chicago to take part in experiments.

I also thank the many friends who have enriched the past six years of my life in so many ways. I will refrain from listing you here. I apologize for not giving you the recognition you deserve. But please, know that I am extremely grateful.

Finally, I want to give an enormous thanks to my family – my mom, dad and sister. Their love and support is invaluable.

TABLE OF CONTENTS

LIST OF TABLES

LIST OF FIGURES

CHAPTER 1

Introduction

Interest in the atomic-scale structure and properties of the alkaline-earth metals (AEMs) Ba, and especially Sr on Si(001) has coincided with efforts to grow high quality films of $SrTiO_3$ on Si(001). In bulk, room-temperature form, $SrTiO_3$ has a simple cubic perovskite structure with a lattice constant $a = 3.905$ Å. The mismatch between the $SrTiO_3$(100) and Si(110) interplanar d-spacings is 1.7%. Under certain growth conditions, this relatively small mismatch facilitates the epitaxial growth of $SrTiO_3$ films with the relationship $SrTiO_3$(001) || Si(001) : $SrTiO_3$[100] || Si[110]. Ball and stick models of the bulk $SrTiO_3$ perovskite and Si diamond cubic unit cells are shown in Fig. 2.1.

Films of $SrTiO_3$ on Si(001) began receiving attention in the early 1990s, largely due to their utility as buffer layers for growing films of the high transition temperature (T_C) superconducting oxides Y-Ba-Cu-O [1; 2] and Bi-Sr-Ca-Cu-O [3] on Si, although the $SrTiO_3$ films used in these studies were not epitaxial in the strictest sense since they always contained at least two crystallographic orientations. The growth of $SrTiO_3$ films exhibiting a single crystallographic orientation on Si(001) was first reported in 1991 by Mori *et al.* [4] who deposited ~100 Å Sr onto the native SiO_2 oxide before growing $SrTiO_3$ by electron beam evaporation of a bulk $SrTiO_3$ target. Although the films

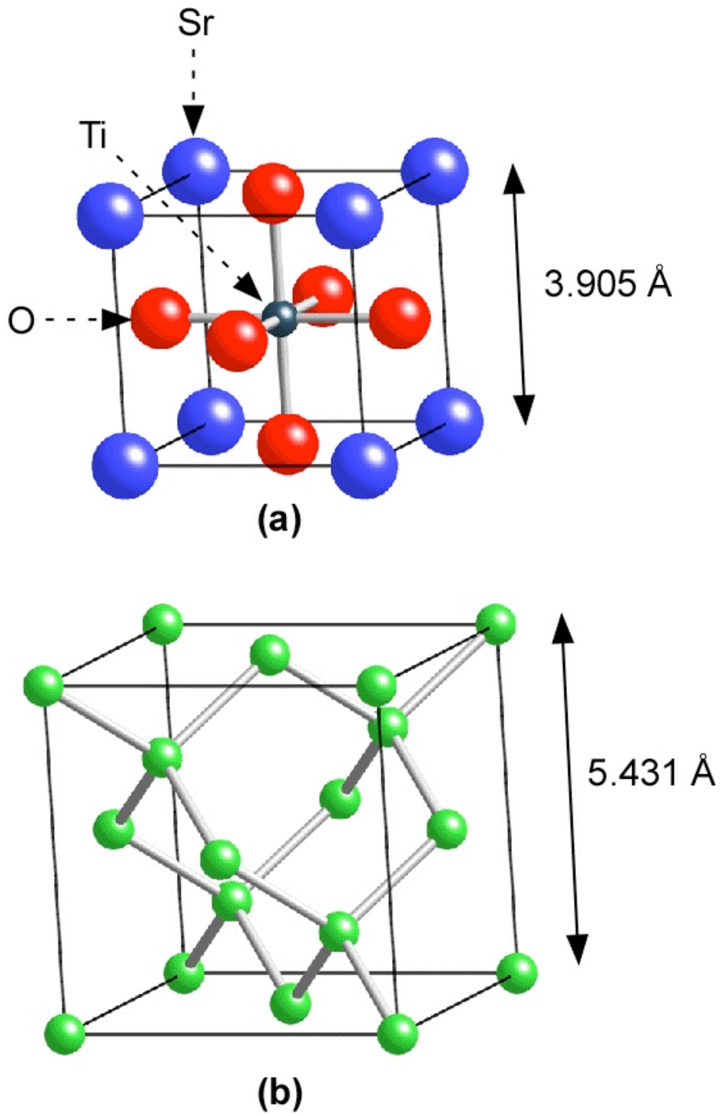

Fig. 2.1: Bulk unit cells of (a) $SrTiO_3$ with a simple cubic perovskites structure and (b) Si with a face-centered diamond cubic structure.

reported in this work were epitaxial, their rough surface morphology was less than ideal for most applications.

As techniques for growing epitaxial $SrTiO_3$/Si(001) have matured, initiating film growth with the deposition of Sr and/or SrO has remained an essential part of the film growth process. In 1998, Tambo *et al.* [5] reported on a molecular beam epitaxy (MBE) process in which 100 – 500 Å SrO was deposited prior to $SrTiO_3$ growth. Later that same year, McKee *et al.* [6] reported an MBE growth method involving the formation of an ordered sub-monolayer phase of Sr on a clean Si(001) surface followed by the growth of a few (one, two or three) atomic layers of SrO before depositing the $SrTiO_3$ film as alternating atomic layers of TiO_2 and SrO. Transmission electron microscopy (TEM) images showed that an oxide-Si interface resulting from this growth recipe was free of amorphous secondary phases (e.g. SiO_2). The stability of the Si(001) – Sr – SrO – $TiO_2\cdots$ stacking sequence against the formation of unwanted phases is sometimes explained in terms of the bulk Sr-Si-O phase diagram [see Fig. 2.2(a)] in which stable tie lines exist between Sr-Si compounds and SrO but are absent between Sr-Si compounds and SiO_2. By contrast, in the Ti-Si-O phase diagram shown in Fig.2.2(b), there are no stable tie lines between TiO_2 and any of the Ti-Si compounds, but there are stable tie lines between the Ti-Si compounds and SiO_2.

The finding that $SrTiO_3$ films with a particular atomic layering sequence and in-plane plane order at the interface could result in an atomically sharp boundary had at least

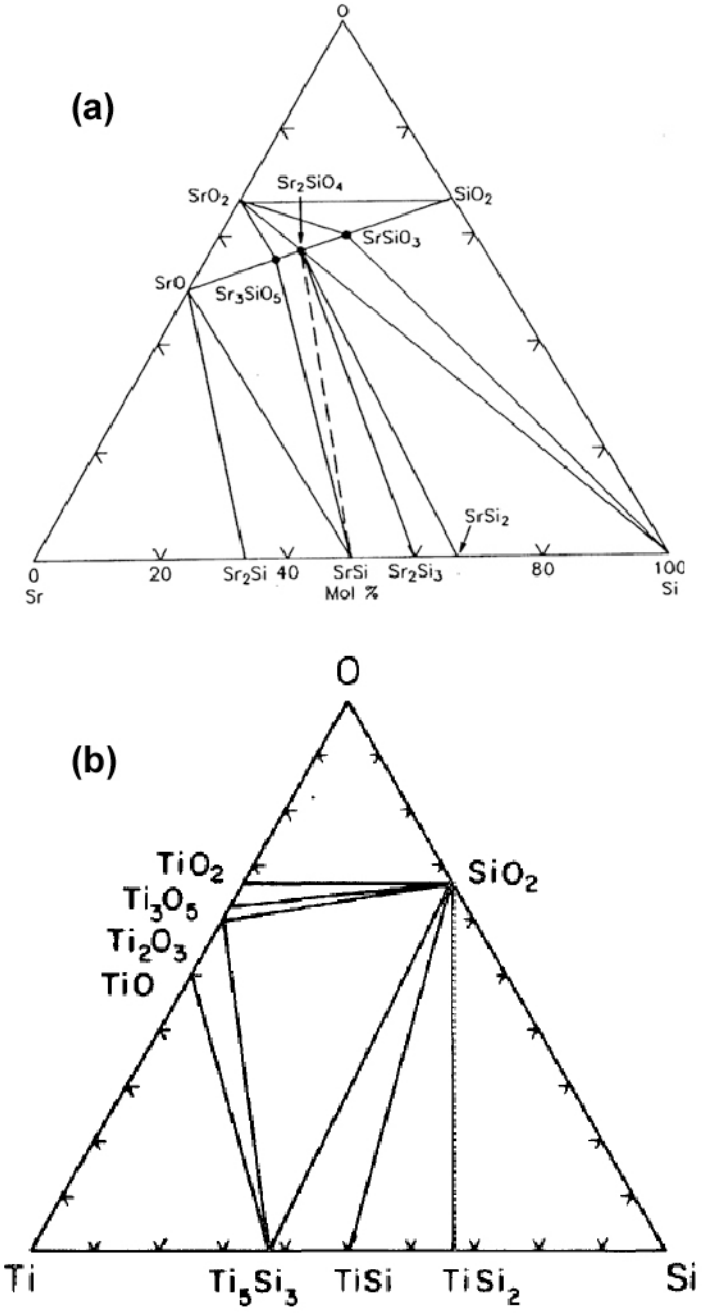

Fig. 2.2: Calculated bulk ternary phase diagrams for (a) Sr-Si-O at 25°C and (b) Ti-Si-O at 700 – 1000°C. Figures taken from Refs. [7] and [8].

two major effects on the direction of research on this material system. From an applications point of view, it produced significant interest in the possibility of using $SrTiO_3$ as a gate dielectric in field effect transistors (FETs). From a research point of view, it generated curiosity in the surface phases of Sr and SrO and other alkaline-earth metals (AEMs) and oxides (such as Ba and BaO) on Si(001).

The focus of this thesis work has been to use surface sensitive characterization techniques, primarily X-ray standing waves (XSW), to elucidate details related to the atomic-scale structure of Sr/Si(001) and Ba/Si(001) surfaces.

Chapter 2 begins with a review of some important aspects of the clean Si(001) surface that is used as a starting point for the formation of AEM/Si(001) surface phases. Previous studies of Sr/Si(001) and Ba/Si(001) surfaces are then discussed. These works contain a variety of proposed atomic-scale structural models. The status of research and technological applications of $SrTiO_3$/Si(001) is also covered in Chapter 2. The theory and application of XSW analysis of adsorbates on single crystal substrates is reviewed in Chapter 3. Details specific to the triangulation of adatoms on the Si(001) surface are included there. Chapter 4 describes the X-ray optics and ultra-high vacuum (UHV) systems used to conduct experiments.

Chapter 5 includes the results of XSW measurements made on three different Sr/Si(001) surface phases. Considering these results in conjunction with expected Sr-Si nearest-neighbor distances points to the valley-bridge site as the most likely in-plane position of Sr atoms in (2x3) and (2x1) surface phases. Models specifying both the in-plane and out-of-plane positions of Sr in 1/6 ML (2x3) and 1/2 ML (2x1) phases are presented. The XSW results also suggest that there may be a significant difference between the thermal vibration behavior of Sr atoms in the (2x3) and (2x1) phases. Chapter 5 also contains results from additional low-energy electron diffraction (LEED) and Auger electron spectroscopy (AES) measurements. These LEED results include diffraction patterns of a mixed (2x3) + c(2x6) Sr/Si(001) surface. While these types of diffraction patterns have been commonly observed for Ba/Si(001), the only previous evidence of any c(2x6) periodicity on Sr/Si(001) surfaces has been in the form of "streaky" diffraction features indicative of small surface domains. The relative ease with which Ba and Sr would be able to overcome an energy barrier to c(2x6) nucleation is discussed in terms of the difference between their respective electronegativities.

Measurements performed on Ba/Si(001) surfaces are presented in Chapter 6. XSW results for a 1/2 ML (2x1) phase are consistent with Ba atoms occupying the same in-plane position that was determined to be the most probable Sr adsorption site in the (2x1) and (2x3) Sr/Si(001) phases (but at a slightly higher vertical position). Ba/Si(001) samples were found to deteriorate quite rapidly – over the course of a few hours. Based on AES and residual gas analyzer (RGA) measurements, it is proposed that the observed deterioration is due to residual H_2O in the UHV chamber. The fact that such deterioration could occur with in a UHV chamber at $1.5\text{x}10^{-10}$ Torr is a testament to the extreme reactivity of AEMs. The magnitude of the error that this deterioration could cause in the Ba position determined by XSW is discussed in some detail.

Sr/Si(001) surfaces studied by XSW were also observed to deteriorate, but these surfaces did not change as quickly as Ba/Si(001) surfaces did. Chapter 7 describes two different types of changes (observed by XSW) that apparently occurred on Sr/Si(001) surface, most likely due to O and/or –OH contamination. The first type of change is essentially the same as that observed on Ba/Si(001) samples – albeit at a slower rate. The second type of change is caused by the presence of O on the surface during high-temperature anneals used to form long-range ordered phases. Chapter 7 also contains results of XPS measurements of Sr/Si(001) surfaces that were intentionally exposed to O_2 in the $1x10^{-9}$ – $1x10^{-8}$ Torr range. These measurements were able to track the changes in the amounts of O in two different bonding environments – one attributed to O–Sr bonding and the other to O–Si.

The overall results of the thesis work and an outlook on future research into AEM/Si(001) surfaces are discussed in Chapter 8.

CHAPTER 2

Background

2.1 Clean Si(001) surfaces

Before reviewing investigations of AEM, overlayers on Si, it is worth noting some key features of the clean Si(001) surface. Since surface atoms of any crystalline material have surroundings that differ from those of their bulk counterparts, they can often reduce their energy by occupying non-bulk lattice positions. For the (001) surfaces of group IV semiconductors, surface reconstructions are driven by the high energy state of the two non-bonding, unpaired electrons that would be present on each surface atom if these atoms and their surrounding orbitals were to retain their bulk lattice positions.

Soon after being detected by low-energy electron diffraction (LEED) [9], a (2x1) Si(001) surface reconstruction was proposed to be due to the dimerization of Si surface atoms in neighboring rows along the bulk Si <110> directions. Two types of domains can from on a (2x1) Si(001) surface. The dimer rows can be oriented along either [110] or $[\bar{1}10]$ directions. Domains on adjacent terraces separated by a monoatomic step are rotated by 90° with respect to one another giving rise to the "two-domain" (2x1) diffraction pattern typically observed by LEED. Fig. 2.3 shows the [001] projection of a two-domain dimerized (2x1) Si(001) surface. The domain consisting of dimer rows oriented parallel to the atomic step separating the two domains is referred to as an “A” domain, and the domain with dimer rows oriented perpendicular to the atomic step is referred to as a “B” domain. Outlines of the (2x1) reconstructed surface unit cell as well as the (1x1) unit cell that would describe a bulk-terminated surface are drawn on both terraces. The edges of both types of surface cells are rotated by 45° with respect to the [100] and [010] bulk diamond cubic axes. The Si(001)-(2x1) surface contains four different two-fold symmetry sites – the cave, bridge, valley-bridge and pedestal sites (labeled C, B, V and P respectively in Fig. 2.3).

It is now generally accepted [10; 11] that at room temperature, the dimers on a clean Si(001)-(2x1) surface are asymmetric (i.e. “tilted” so that one atom of the dimer is slightly higher than the other). The dimer asymmetry is due to a rehybridization that can be thought of as leaving the “down” atom with an unoccupied p-type orbital and the “up” atom with a fully occupied s-type orbital [12]. A slightly different interpretation considers the two orbitals to be hybridized into π (bonding) and π^* (anti-bonding) orbitals with the filled π orbital originating primarily from the “up” atom and the unfilled π^* orbital (also referred to as a “dangling bond”) originating from the “down” atom [13]. At room temperature, the dimer tilt direction switches back and forth at very high frequency (~200 fs according to a molecular dynamics simulation [14]) causing the dimers to appear symmetric in a time-averaged sense. The oscillation frequency decreases as the temperature is lowered, and LEED [15] and STM [16; 17] studies have indicated that at ~200 K, an ordering of neighboring dimers into opposite tilt states “locks” the Si(001)

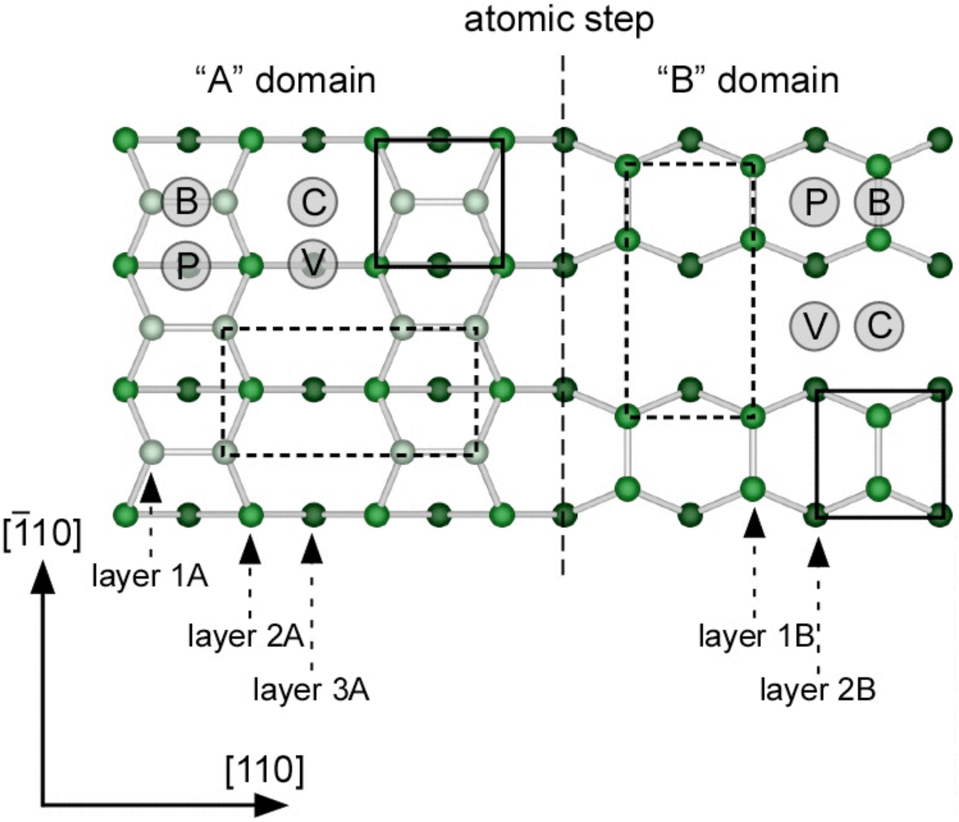

Fig 2.3: [001] projection of a two-domain Si(001)-(2x1) surface. The "B" domain is one atomic step lower than the "A" domain. High symmetry bridge (B), cave (C), pedestal (P) and valley-bridge (V) sites are indicated on both types of terraces. (2x1) and (1x2) unit cells of the reconstructed surface are drawn as dashed rectangles. The (1x1) unit cells that would describe a bulk-terminated surface are drawn as solid squares. Si(001)-(2x1) surface with high symmetry adsorption sites indicated. The orientations of dimer rows on adjacent terraces (separated by single atomic step) differ by 90°. A (2x1) surface unit cell is marked by the dashed line. Dimer asymmetry is not shown in this figure.

surface into a c(4x2) reconstruction. Fig. 2.4 shows a ball and stick model of an [001] projection of a c(4x2) Si(001) surface.

Formation of a clean (2x1) Si(001) surface is typically accomplished by heating the crystal in ultra-high vacuum (UHV) to thermally remove SiO_2 from the surface. If the surface is properly treated to remove contaminants such as C prior to introduction into UHV, a clean, two-domain Si(001)-(2x1) surface can typically be formed by UHV annealing at 800 – 900°C. Single domain Si(001)-(2x1) surfaces have been formed using substrates with relatively large miscut (~4°) along the [110] direction to promote the formation of biatomic rather than monoatomic steps [18; 19].

2.2 Sr/Si(001)

Based on fundamental chemistry principles, a group II element like Sr on a dimerized Si(001) surface would be expected to donate its two valence electrons to the empty anti-bonding orbital of a Si dimer. The effects of this charge transfer have been detected by XPS measurements [20; 21] of Sr/Si(001) surfaces in the form of shifts of the Sr-3d and Si-2p states toward higher and lower respective binding energies. XPS studies have also suggested that the donation of electrons from Sr into a Si dimer's anti-bonding orbital, localized around the "down" atom of an asymmetric Si dimer, causes the dimer to become symmetric [21]. It has been suggested that the Sr-Si interaction possesses a significant covalent character since Sr adatoms showed up brightly in filled state STM

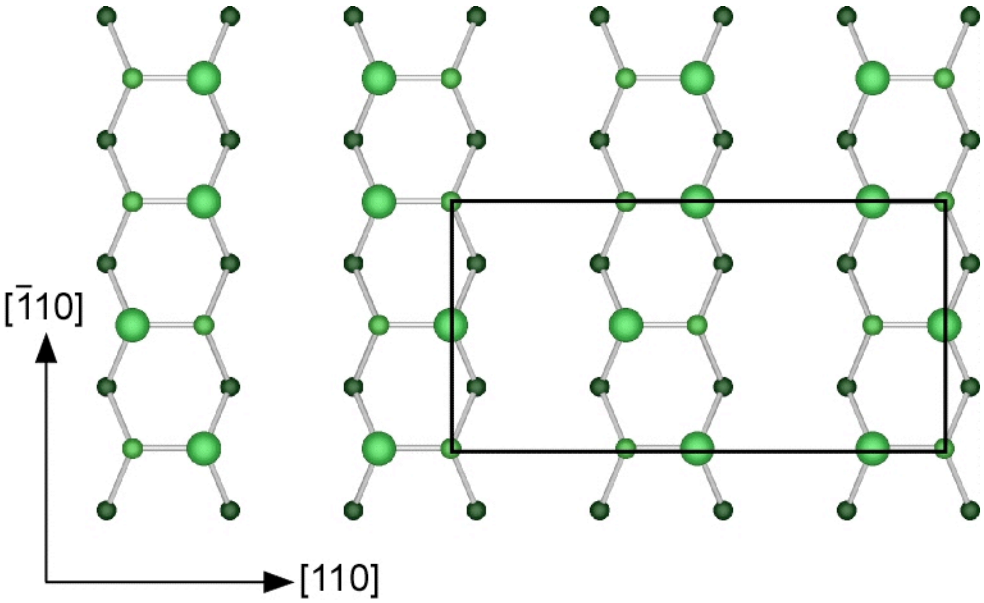

Fig. 2.4: Ball and stick model of a Si(001) surface with dimers “locked” into alternating tilt directions resulting in a c(4x2) unit cell as indicated by the solid rectangle.

Images [22; 23], indicating that the Sr adatoms are not fully ionized. Short-range ordered Sr/Si(001) structures studied by STM include isolated Sr atoms on dimerized Si(001) and chain structures (at Sr coverages between 0.1 and 0.3 ML) that zigzagged across the Si dimer rows, although the specific adsorption site(s) of the Sr atoms in the STM images was unclear. Density functional theory (DFT) calculations [24] have indicated that the valley-bridge site is the minimum energy adsorption site for Sr on dimerized Si(001) and that Sr occupying this site is the fundamental structural motif for all stable Sr/Si(001) structures with Sr coverage between 0 and 1/2 ML. The relative energies, calculated by DFT, for individual Sr atoms adsorbed on each of the two-fold symmetry sites on a dimerized Si(001) surface are listed in Table 2.1.

Site	**E (ev)**
Valley-bridge	0
Pedestal	0.29
Cave	0.55
Bridge	0.75

Table 2.1. Relative energies, as calculated by DFT [24], of individual Sr atoms adsorbed on high-symmetry sites on a dimerized Si(001) surface. Here, net energy of the system *increases* with increasing adsorption energy.

DFT calculations [24] also predicted that Sr atoms in valley-bridge sites would form chains oriented along $<2\ 1>_{1x1}$ directions. Both “straight chains” (aligned along a single $<2\ 1>_{1x1}$ directions) and “zigzag chains” (alternating back and forth between two different $<2\ 1>_{1x1}$ directions) were expected. These chains were predicted to condense into long-range ordered phases at 1/6 ML and 1/4 ML Sr coverage. At each of these coverages, the Sr chains were expected to result in two types of unit cells – one due to "straight" chains aligned along a single direction and another due "zigzag" chains alternating back and forth between two different <2 1>$_{1x1}$ directions. In terms of the [1 0] and [0 1] basis vectors of a (1x1) bulk-terminated unit cell reciprocal lattice, the reciprocal-space lattice vectors of these ordered phases would be $\left(\frac{1}{2},0\right)$ and $\pm\left(\frac{1}{2n},\frac{1}{n}\right)$ for the straight chain phases and $\left(\frac{1}{4},0\right)$ and $\left(0,\frac{1}{n}\right)$ for the zigzag chain phases, with $n = 3$ at 1/6 ML and $n = 4$ at 1/4 ML. To date, long-range ordered Sr/Si(001) surfaces with these periodicities have not been observed by any diffraction technique, although individual zigzag chains similar to those predicted by Ashman *et al.* [24] have been observed in STM images of Sr/Si(001) [22; 23]. There is also experimental evidence of Ba/Si(001) surfaces exhibiting the zigzag periodicity Ashman *et al.* predicted for Sr at 1/4 ML (see section 2.2.3).

A number of long-range ordered Sr/Si(001) surface phases have been revealed by LEED [21; 25-28], reflection high-energy electron diffraction (RHEED) [29-33] and STM [22; 23; 28; 33-35]. These phases (in order of increasing Sr coverage) include (2x3), (2x1), (5x1) and (3x1) surface reconstructions. Several variant processing schemes, all requiring an UHV environment, have been used to prepare Sr/Si(001) surfaces. The formation of long-range ordered phases typically involves annealing the surface during (or after) at least part of the deposition process. Some groups [22; 23; 25-27] have deposited up to 1.4 ML Sr [1 ML = 6.78 atoms·nm^{-2}, the areal density of top-layer Si atoms on a bulk-terminated Si(001) surface] onto a clean, room-temperature

Si(001)-(2x1) surface and then induced long-range ordering of Sr atoms by annealing at temperatures ≥ 600°C, while others [6; 21; 29-33] have deposited Sr onto Si(001)-(2x1) surfaces held at 500 – 800°C during the deposition process. A third method involves the deposition of Sr onto a heated (720 - 800°C) Si substrate that still contains a SiO_2 film on its surface. In this latter method, Sr catalyzes the thermal desorption of SiO_2, and depending on the exact anneal temperature, either a (2x3) or (2x1) Sr/Si(001) surface is left behind [28; 33; 35].

Several different graphical representations of the relationships between phase formation temperature, Sr coverage, and surface periodicity that have been reported in the literature for Sr/Si(001) are shown in Fig. 2.5. It is evident from these "phase maps" that there is considerable disagreement regarding the Sr coverage and temperatures required to form the various long-range ordered Sr/Si(001) surface phases. In addition to general experimental error, there are possible systematic causes for these discrepancies. For example, it is likely that the coverage values in Fig. 2.5(a) are artificially high because Fan *et al.* [25] measured the Sr coverage deposited onto the room temperature substrates, but did not measure the amount of Sr that remained after the high temperature anneals (which most likely caused a significant amount of Sr to desorb). Also, since kinetic parameters such as the anneal time and deposition rate employed by different researchers has varied widely, it is not clear which (if any) phases were observed under true equilibrium conditions.

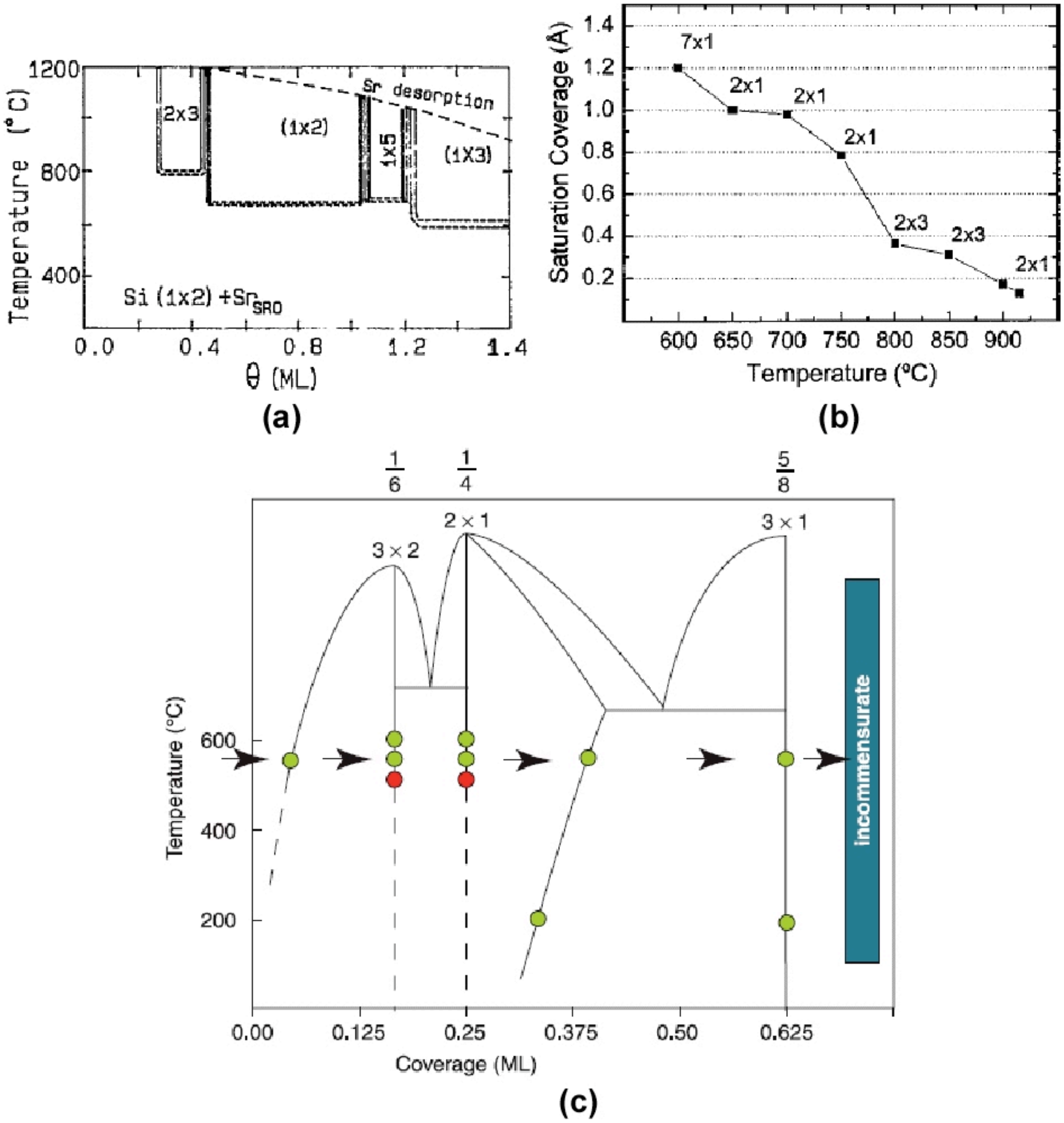

(a) (b)

(c)

Fig. 2.5: Graphical representations of the reported relationships between substrate temperature, Sr coverage and surface periodicity for Sr/Si(001). Figures taken from Refs. [25], [21] and [31].

STM images [22; 23] of a (2x3) phase formed by depositing 0.1 – 0.3 ML Sr onto a room-temperature Si(001)-(2x1) surface and then annealing at 800°C were interpreted as evidence that the Si dimers remained intact and that Sr atoms in the (2x3) phase formed straight chains aligned exactly perpendicular to the Si dimer rows (i.e. along $<1\ 0>_{1x1}$ directions). Based on these STM images, one of which is shown in Fig. 2.6(a), Bakhtizin *et al.* [22; 23] proposed a model for a 1/3 ML (2x3) phase consisting of Sr atoms occupying 2/3 of the cave sites on a dimerized Si(001) surface as drawn in Fig. 2.6(b). However, Hu *et al.* [26] used LEED, AES and STM observations to argue that a Sr/Si(001) surface with (2x3) periodicity only forms at a Sr coverage of 1/6 ML with one Sr atom per surface unit cell, although no particular atomic-scale structural model was proposed in this work. Variations in the intensities of RHEED spots monitored during Sr deposition onto heated (~700°C) Si(001) also suggest that the (2x3) phase saturates at 1/6 ML [30; 31].

DFT calculations cited by Droopad *et al.* [36] predicted that stable (2x3) Sr/Si(001) surface phases would form at both 1/6 and 1/3 ML. Sr atoms in these surface phases were arranged in chains along the $<1\ 0>_{1x1}$ directions as STM images had suggested, but were located in valley-bridges sites (rather than cave sites as Bakhtizin *et al.* [22; 23] had proposed). Interestingly, the DFT calculations of Ashman *et al.* [24] did not find a stable (2x3) Sr/Si(001) surface phase at any coverage. Instead, the straight and zigzag chain structures (described earlier) along the $<2\ 1>_{1x1}$ directions were predicted.

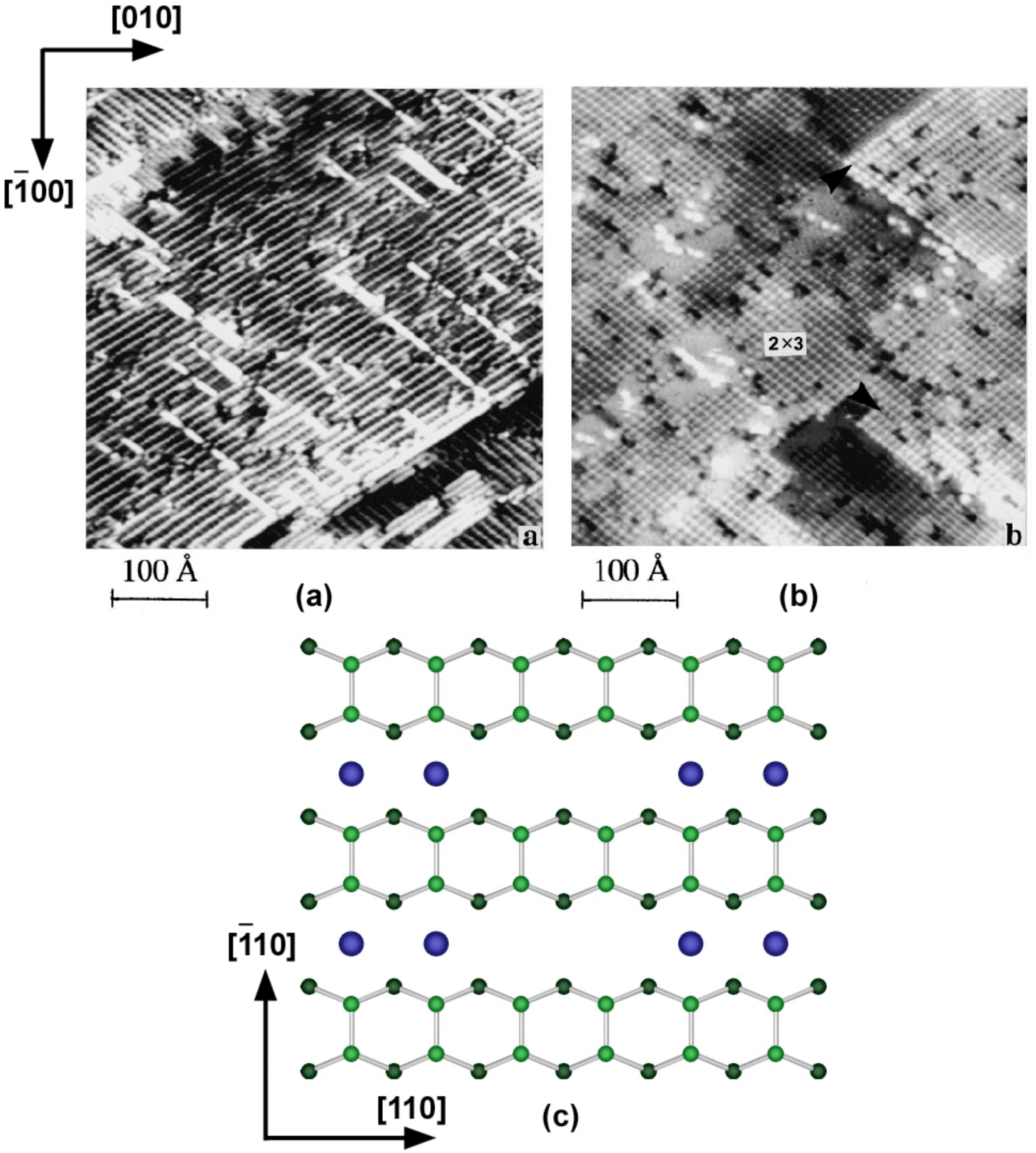

Fig. 2.6. (a) Filled and (b) empty state STM images of a (2x3) Sr/Si(001) surface and (c) 2/3 ML that was proposed based on the images in (a) and (b). STM images taken from Ref. [23].

The Sr/Si(001) surface phase that has been most widely cited as the key precursor to $SrTiO_3$ growth on Si(001) exhibits (2x1) periodicity. [27; 30; 35] Most experimental and theoretical work indicates that this phase saturates at 1/2 ML Sr coverage, although McKee *et al.* [6; 31] claimed that it saturates at 1/4 ML. In light of this disagreement, it is worth noting that since every (2x1) unit cell of an AEM/Si(001) surface phase must contain at least one AEM atom, and the areal number density of surface unit cells on any (2x1) reconstructed Si(001) surface is 1/2 ML, the AEM saturation coverage of a (2x1) AEM/Si (001) surface phase must be *at least* 1/2 ML. STM images [33] showed Sr atoms in the (2x1) phase, like those in the (2x3) phase, aligned in chains along the $<1\ 0>_{1x1}$ directions, but the inter-chain distance in the (2x1) phase was smaller than that of the lower coverage (2x3) phase. DFT calculations [24; 33; 36] have predicted a stable 1/2 ML (2x1) Sr/Si(001) phase consisting of Sr atoms occupying all of the valley-bridge sites on dimerized Si(001). Ashman *et al.* [24] calculated the band structure for a number of Sr/Si(001) surfaces ranging from 0 ML to 4/3 ML Sr coverage and found that only the 1/2 ML (2x1) phase was devoid of states in the Si band gap. It was noted that this band structure would be expected to make the (2x1) phase less reactive than other Sr/Si(001) surfaces. A XPS study [27] has in fact indicated that the stability of (2x1) phase against SiO_2 formation is greater than that of any other Sr/Si(001) surface.

Early studies of Sr/Si(001) showed XPS and Auger electron spectroscopy (AES) results [20; 37] indicating that (at least under some conditions) SiO_2 forms more readily on Sr/Si(001) surfaces than it does on clean Si(001)-(2x1). The Sr coverage used in these studies ranged from 0 to 1.8 ML, and surfaces were exposed to ~100 – 2x10^5 Langmuir O_2 (1 Langmuir = 10^{-6} Torr·s). These O_2 exposure levels were considerably higher than the 30 – 60 Langmuir O_2 used by Liang *et al.* [27]. The authors of the earlier studies noted that SiO_2 formation on the Sr/Si(001) surfaces was accompanied by degradation in the LEED pattern(s), but they did not state what the actual periodicity was prior to O_2 exposure.

Just as some disagreement remains over the coverage of the (2x3) and (2x1) Sr/Si(001) surfaces, a variety of coverages have also been reported for the (3x1) phase(s). McKee *et al.* [31] reported that the (3x1) phase saturates at 5/8 ML; Lettieri *et al.* observed (3x1) periodicity at coverages between 7/8 and 1 ML; Bakhtizin *et al.* [22] claimed that it saturates at exactly 1 ML; and Fan *et al.* reported that it formed at coverages above 1.2 ML. DFT calculations [24] have actually predicted three different stable (3x1) phases, with coverages of 2/3 ML, 1 ML and 4/3 ML.

2.3 Ba/Si(001)

Part of the interest in sub-monolayer phases of another alkaline-earth metal (AEM) atom, Ba, on Si(001) is due to the chemical and structural similarities between the Ba/Si(001) and Sr/Si(001) surfaces. Also, Ba/Si(001) surfaces have been used as templates for growing epitaxial $Ba_xSr_{1-x}TiO_3$ films [36] on Si(001). Ba/Si(001) surfaces are also important for "interface engineering" strategies that have been proposed to effectively increase the conduction band offset at the interface between $SrTiO_3$ and Si

[31; 38-40]. Relevance to the integration of the high-T_C oxide Y-Ba-Cu-O onto Si (through means other than the use of a $SrTiO_3$ template) has also been cited as a motivation for studying Ba/Si(001) [41; 42].

The behavior of Ba on Si(001) is in many ways similar to that of Sr. DFT calculations of Ba atoms adsorbed on dimerized Si(001) indicate that the valley-bridge site adsorption should be favored and that the pedestal site provides the second most likely adsorption site [36; 43; 44]. The difference between the Ba adsorption energies calculated for these two sites was 0.88 eV [43]. Ion-scattering [45] and STM measurements [46; 47] of Ba adsorbed onto room-temperature Si(001) support both of these predictions. STM images of Ba adsorbed onto room temperature Si(001) have also shown that the four Si surface atoms nearest an occupied valley-bridge site were found to be locked in the "up" position. This constraint determined the tilt direction of surrounding dimers (which would otherwise be oscillating) and forced local dimer rows to order into the buckled c(4x2) pattern is observed in the area labeled "C" in the STM image of Fig. 2.7(a) and is drawn schematically in the surface model in Fig. 2.7(b). DFT calculations [43; 46] for a single Ba atom in a valley-bridge site have indicated that a redistribution of the Ba 6s valence electrons results in the formation of directional Ba-Si bonds with significant covalent character. Several XPS [42; 48-50] and ultraviolet photoelectron spectroscopy (UPS) [50; 51] studies have suggested that electrons from the Ba 6s valence orbitals end up occupying the Si dangling bond orbitals and that the adsorption of more than 1/2 ML Ba causes the Si dimers to lose their asymmetry. In

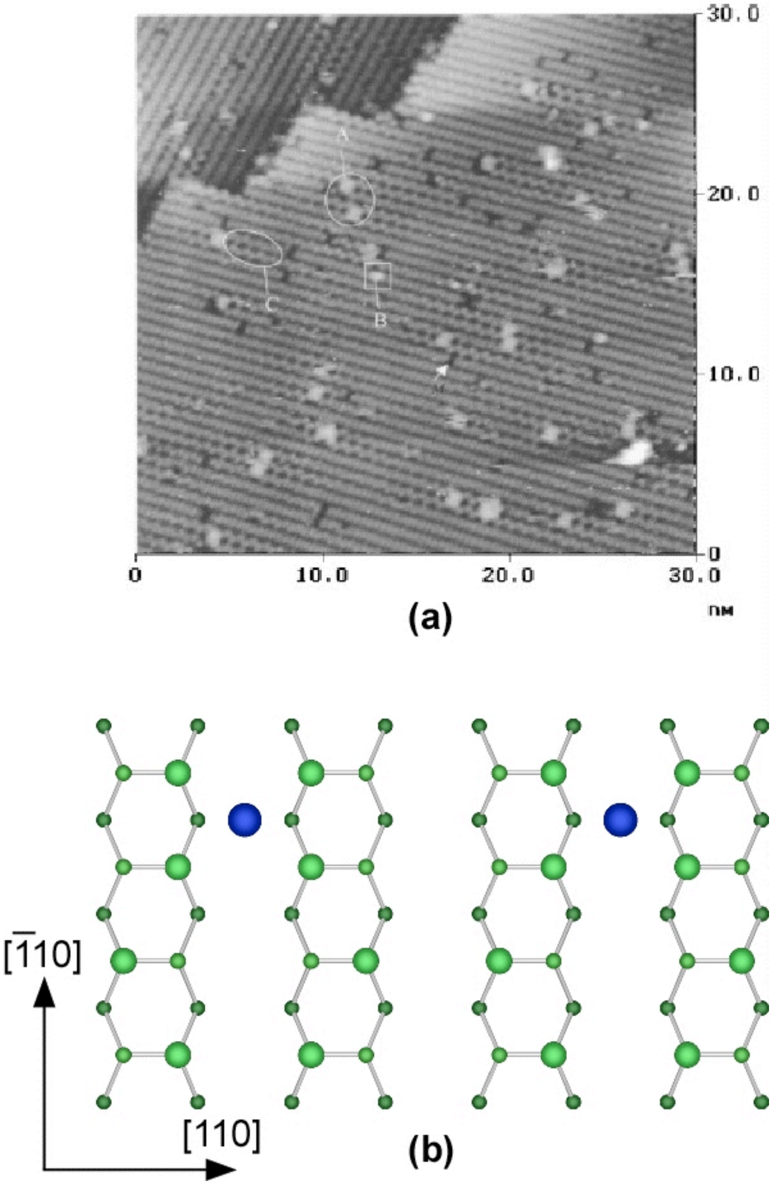

Fig. 2.7. (a) Filled state STM image of initial stages of Ba adsorption onto room-temperature Si(001)-(2x1). The circle marked "A" contains two Ba atoms occupying valley-bridge sites. The square labeled "B" contains a Ba atom adsorbed onto a Si dimer vacancy. The ellipse denoted by "C" contains Si dimers buckled into the c(4x2) pattern due to a Ba atom occupying a nearby valley-bridge site. (b) Ball-stick model showing an [001] projection of c(4x2) dimer buckling induced by Ba atoms occupying valley-bridge sites on dimerized Si(001). STM image taken from Ref. [47].

some cases this charge transfer has been interpreted primarily as an ionization of surface atoms, but Cheng *et al.* [49] argued the Ba-Si interaction remains largely covalent up to Ba coverages of at least 1 ML.

A surface potential energy map of Ba on Si(001) calculated by Wang *et al.* [43] showed that Ba diffusion should be fastest along the direction parallel to the Si dimer row. Based on the energy barrier associated with adatoms hopping between adjacent valley-bridge sites, 637°C was predicted to be the minimum temperature required long-range ordering of Ba atoms on Si(001). Experimentally, values between 550°C and 775°C have been reported as the lowest temperature necessary for the formation of long-range ordering of Ba/Si(001) surface phases [41; 52-54].

Long-range ordered, sub-monolayer Ba/Si(001) surfaces exhibiting (2x3), c(2x6), (2x1) and (2x4) periodicity have been observed by LEED [41; 46; 50; 52-55]. Two different phase maps showing the Ba coverages, formation temperatures and periodicities of long-range ordered Ba/Si(001) surfaces are shown in Fig. 2.8. Most authors have reported that Ba/Si(001), like the Sr/Si(001) system, forms a (2x3) phase at Ba coverages below ~1/3 ML and a (2x1) phase between ~0.4 ML and ~0.6 ML. There are also some important differences between the Ba/Si(001) phase maps shown in Fig. 2.9 and the Sr/Si(001) phase maps shown in Figs. 2.5 and 2.6. While (5x1) and (3x1) phases have been observed at Sr coverages above ~0.6 ML, Ba/Si(001) surfaces in this coverage range instead exhibit (2x4) periodicity. Also, there have been several reports of a c(2x6) Ba/Si(001) phase coexisting with the (2x3) phase [50; 55-57].

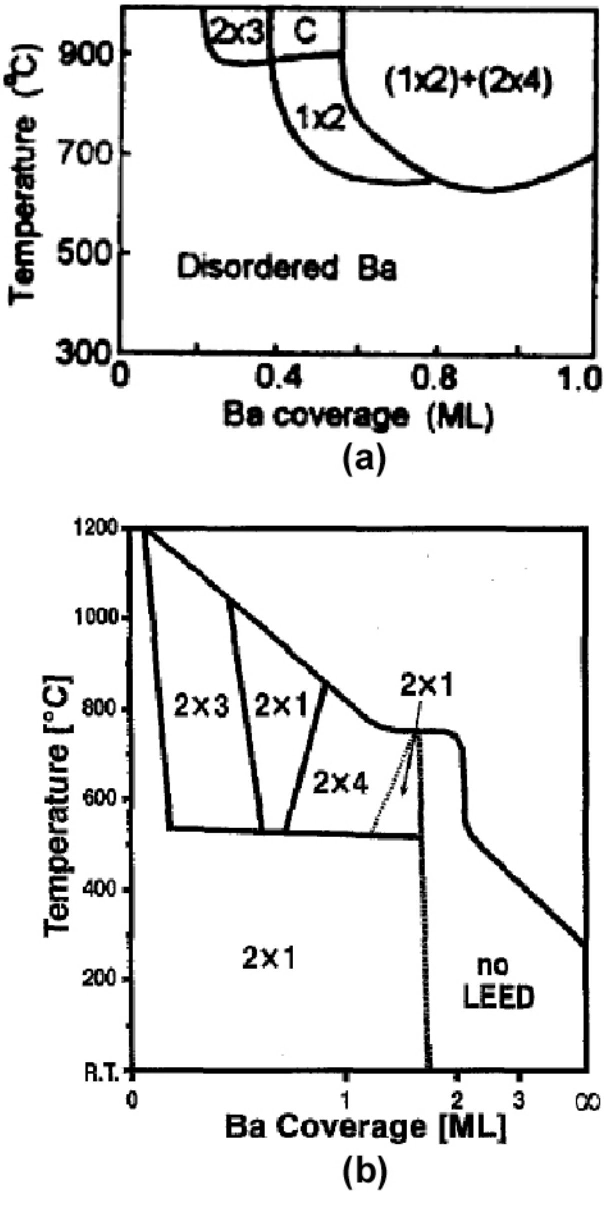

Fig. 2.8. Graphical representations of the reported relationships between substrate temperature, Ba coverage and surface periodicity for Ba/Si(001). Figures taken from Refs. [52] and [41].

Site	1/16 ML	1/4 ML	1/2 ML
Valley-bridge	4.34	4.18	3.90
Pedestal	3.85	3.76	3.38
Cave	3.42	3.60	2.66
Bridge	3.43	3.09	2.14

Table 2.2. Energies of Ba adsorption on high symmetry sites on dimerized Si(001) at three different coverages, as calculated by DFT [44]. Here, net energy of the system *decreases* with increasing adsorption energy.

Just as they had for Sr/Si(001), DFT calculations [33; 36; 44] have suggested that stable (2x3) Ba/Si(001) surfaces could form with Ba atoms occupying either 1/3 or 2/3 of the valley-bridge sites, resulting in Ba coverages of either 1/6 ML or 1/3 ML. The adsorption energies(calculated by DFT [44])of Ba adsorbed onto each of the two-fold symmetry sites on dimerized Si(001) at Ba coverages of 1/16 ML, 1/4 ML and 1/2 ML are listed in Table 2.2. Variations in the intensities of RHEED spots monitored during Ba deposition onto heated Si(001) suggests a single (2x3) saturation coverage of 1/6 ML [58] (again, just as other RHEED studies [30; 31] reported for Sr). Based on XSW measurements, Herrera-Gómez *et al.* [59] claimed that the (2x3) Ba/Si(001) surface contained 1/3 ML Ba occupying valley-bridge sites. Kim *et al.* [50] also proposed a 1/3 ML model for a (2x3) Ba/Si(001) phase, but used angle-integrated ultraviolet photoelectron spectroscopy (AIUPS) measurements to argue that Ba atoms occupied cave sites. Images from room-temperature STM measurements [60] made after depositing < 0.1 ML Ba onto a dimerized Si(001) surface held at 900°C of (2x3) Ba/Si(001) surfaces are shown in Fig. 2.9. Most of the surface in shown in these images contains clean, dimerized Si atoms. There are some regions exhibiting (2x3) periodicity as well as other features that appear to be the same as those attributed to Ba occupying valley-bridge sites

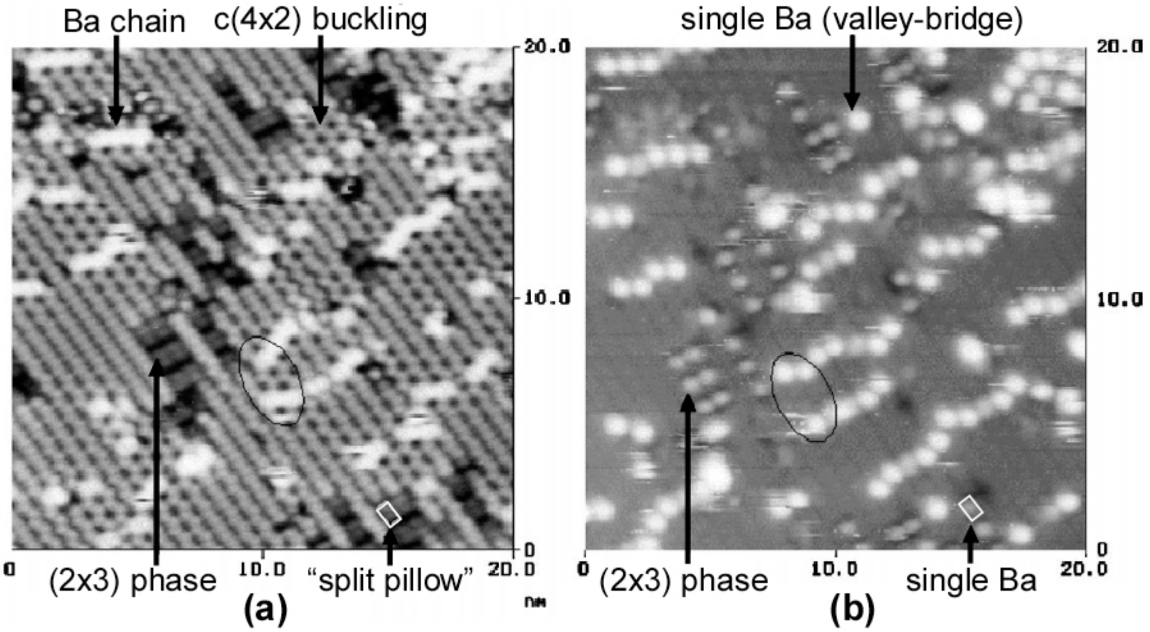

Fig. 2.9: (a) Filled and (b) empty state STM images of Ba deposited onto Si(001)-(2x1) held at 900°C. STM images were taken at room-temperature. Figures taken from Ref. [60].

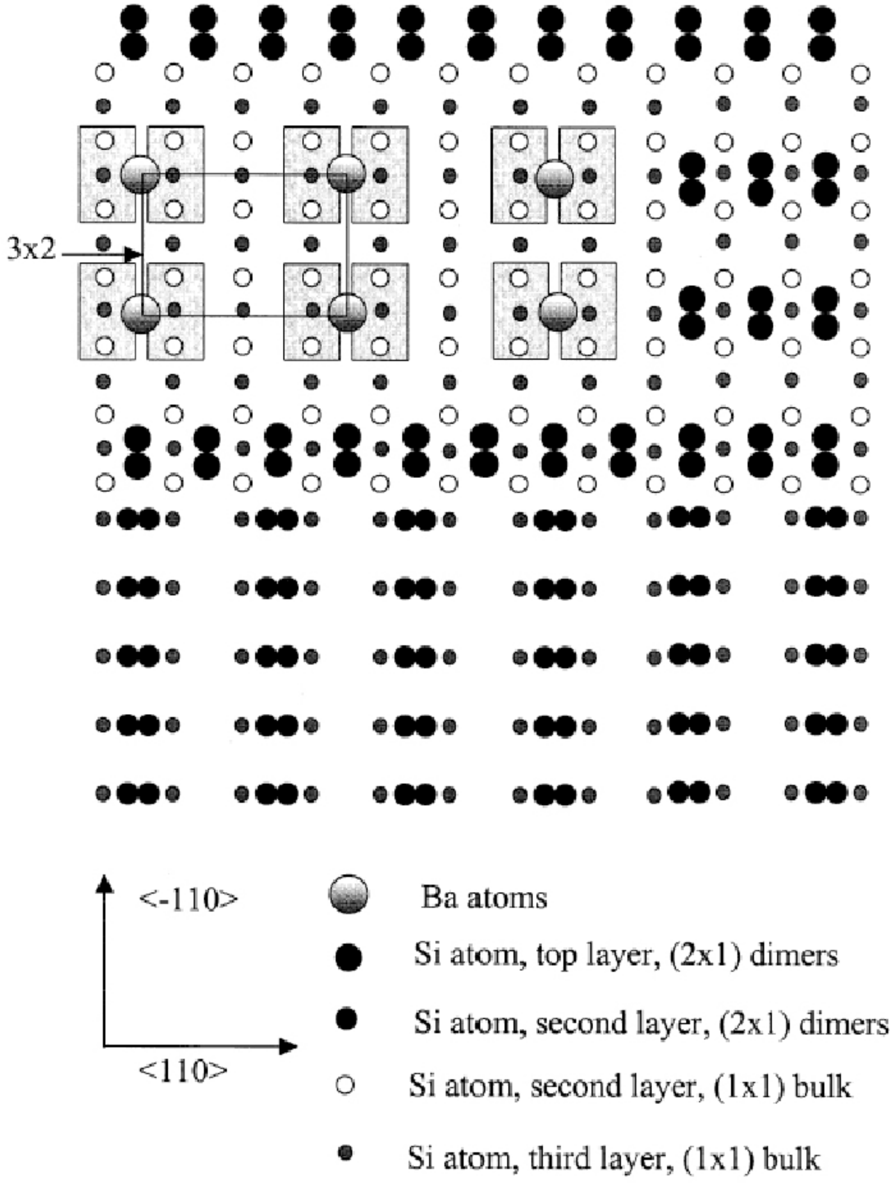

Fig. 2.10: Model of 1/6 ML Ba (2x3) surface proposed by Hu *et al.* [60]. The shaded rectangles correspond to the "split pillows" observed in the filled state STM image in Fig. 2.9(a). Areas where dimers remain and no Ba has adsorbed (including part of a terrace one atomic step lower than that containing the Ba atoms) are also shown for reference. Figure taken from Ref. [60].

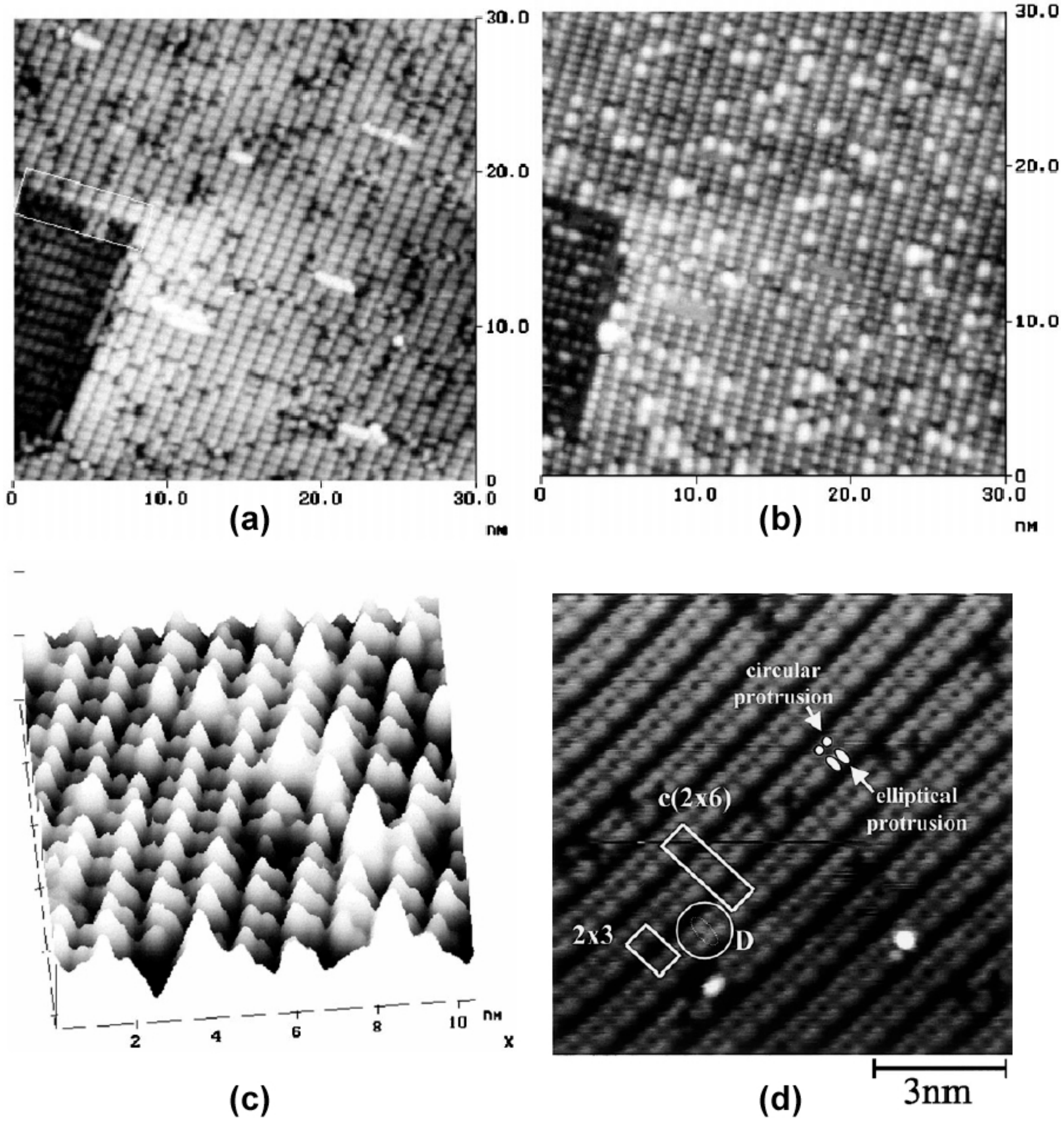

Fig. 2.11. STM images attributed to 1/3 ML (2x3) Ba/Si(001) surfaces. (a) Filled and (b), (c) empty state images taken by Hu *et al*. [60]. (d) Filled state image taken by Ojima *et al*. [57].

in Fig. 2.7(a). The fact that the local density of states (LDOS) of (2x3) Ba/Si(001) surfaces is markedly different from that of surface regions where Ba is presumably adsorbed at valley-bridge sites has been interpreted as evidence that Ba atoms in the (2x3) phase may not occupy valley-bridge sites as DFT [33; 36; 44] calculations and XSW measurements [59] have suggested. Based on their STM images, Hu *et al.* [60] argued that formation of a 1/6 ML (2x3) Ba/Si(001) surface involves the removal of all of the dimerized top layer Si atoms and that Ba atoms in this phase end up occupying 1/3 of the sites formerly occupied by Si dimers. A model of this proposed surface is shown in Fig. 2.10.

Fig. 2.11 contains several different STM images that have all been attributed to 1/3 ML (2x3) Ba/Si(001) surfaces. Filled and empty state images (of the same region) taken by Hu *et al.* [60] are shown in Figs. 2.11(a) and 2.11(b). Fig. 2.11(c) shows an enlarged, rendered portion of the image in 2.11(b) and clearly shows features that appear as asymmetric protrusions in the filled-states. Based on these images, Hu *et al.* proposed that a 1/3 ML (2x3) Ba/Si(001) phase consists of pairs of Ba atoms centered about 1/3 of the former Si dimer sites and that the heights of the Ba atoms within a given pair differed by ~0.8 Å. This proposed model is shown in Fig. 2.12(a).

Fig. 2.11(d) shows a filled-state image taken by Ojima *et al.* who interpreted this image to show a 1/3 ML (2x3) Ba/Si(001) surface and also argued the (2x3) Ba/Si(001) surface only occurs at 1/3 ML. It was suggested that the (2x3) regions Hu *et al.* had attributed to a 1/6 ML phase (see Fig. 2.9) were actually identical to the surface regions

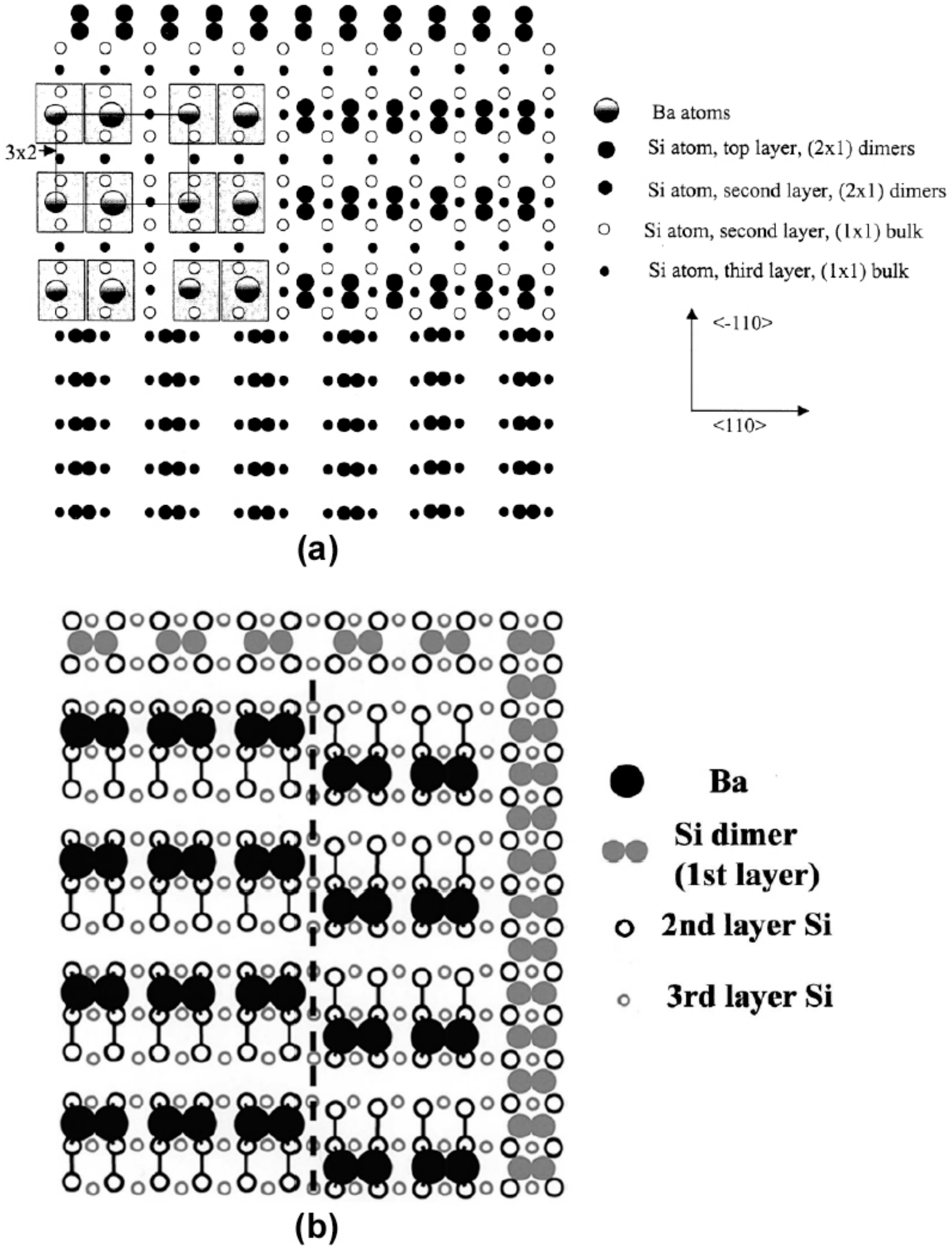

Fig. 2.12: (a) “Buckled Ba dimer” model of 1/3 ML Ba (2x3) surface proposed by Hu *et al*. [60] Shaded areas represent regions of elevated charge density detected in filled state STM image in Fig. 11(a). (b) Symmetric Ba dimer model proposed by Ojima *et al*. [57] In both (a) and (b), surrounding areas where Ba has not adsorbed and intact Si dimers remain are shown for reference.

that Hu *et al*. and Ojima *et al*. had attributed to 1/3 ML (2x3) phases. Ojima *et al*. reported that during their own experiments, Ba atoms on (2x3) surfaces always appeared as double protrusions in each unit cell in empty-state images taken with a sample bias ≤ ~1.5 V, and always appeared as single protrusions in empty-state images using biases ≥~1.5 V. It was argued that Hu *et al*.'s observation of one protrusion per unit cell in some empty-state images and two protrusions in others was due to this sample bias effect. The empty-state images that Hu *et al*. interpreted as having one protrusion per unit cell in Ref. [60] were taken at +2.2 V and +2.3 V, while that believed to have two protrusions per unit cell was taken at +2.0 V.

Formation of the 1/3 ML (2x3) Ba/Si(001) phase proposed by Ojima *et al*., like both of the (2x3) models proposed by Hu *et al*., involved the removal of an entire top layer of Si atoms and, like Hu *et al*.'s 1/3 ML model, consisted of Ba dimers. However, in Ojima *et al*.'s model, shown in Fig.2.12(b), the Ba dimers were proposed to be symmetric, and the direction of the Ba dimer "bond" was perpendicular to the direction of the Si dimer rows that presumably had been removed. The in-plane separation between dimerized Ba atoms in Hu *et al*.'s "buckled dimer" model on the other hand, was parallel to this direction. It is worth noting that in DFT calculations, Ashman *et al*. [24] and Ciani *et al*. [44] explicitly tested for the possibility AEM dimer formation on Si(001), but these structures were found to be unstable for both Sr/Si(001) and Ba/Si(001) surfaces.

Typically, the translation of STM images into atomic-scale models relies on the assumption that the center of a protrusion in a LDOS map corresponds to the center of an atom. However, Hu et al. [60] and Ojima et al. [57] argued that some protrusions corresponded to bonding electrons between Ba and Si. The differences between the conclusions reached by these two groups are largely due to differences in the assignment of protrusions due to atomic nuclei and bonding electron charge density in filled state images.

Several groups have reported a c(2x6) phase co-existing with a (2x3) Ba/Si(001) phase [50; 55-57]. Surfaces that exhibited mixed c(2x6) + (2x3) periodicity at room-temperature showed a pure (2x3) pattern at temperatures above ~550°C [56]. The total Ba coverage reported for mixed c(2x6) + (2x3) surfaces (1/3 ML – 1/2 ML) is typically greater than that reported for pure (2x3) surfaces (1/6 ML – 1/3 ML). STM images of a mixed c(2x6) + (2x3) surface [57] seemed to indicate that the c(2x6) and (2x3) phases actually have the same coverage and that Ba atoms occupy the same type of site in both of these phases. From this images, it appeared that a (2x3) phase could transform to a c(2x6) phase by shifting every other Ba atom (or Ba dimer, if the (2x3) phase does in fact contain Ba dimers) in a row of Ba atoms/dimers aligned along the 3-fold direction by a distance of a_{1x1} = 3.84 Å in the 2-fold direction. Regions exhibiting c(2x6) periodicity are indicated in the STM image in Fig.2.11(d).

Ojima *et al.* [61] also proposed a model based on Ba dimers to explain STM images of a 2-D "wavy" Ba/Si(001) structure. This model for a 1/2 ML "1x2" phase, consisted of a mixture of two mirror-symmetric unit cells: $\begin{pmatrix} 4 & 0 \\ 1 & 2 \end{pmatrix}$ and $\begin{pmatrix} 4 & 0 \\ 1 & -2 \end{pmatrix}$. Here, "1x2" is written in quotes to indicate that the basic translation vectors of the surface unit cells cannot be aligned along the bulk symmetry axes by any rotation; a rigorous description of the surface unit cells requires matrix notation [62]. Ashman *et al.* [24] noted that the wavy Ba/Si(001) structure observed by Ojima *et al.* [61] could be explained by a 1/4 ML condensed phase of zigzag chains (of individual, not dimerized Ba atoms) like the one that had been predicted for Sr/Si(001).

At a Ba coverage of 1/2 ML, most DFT calculations [33; 36] have predicted a (2x1) phase consisting of individual Ba atoms occupying valley-bridge sites. In a XSW study, Herrera-Gómez *et al.* [59] also concluded that Ba atoms in the (2x1) phase occupy valley-bridge sites, just as they had concluded for a (2x3) surface, but the out-of-plane position Ba atoms in the (2x1) phase was determined to be 0.33 Å lower than that of Ba atoms in the (2x3) phase. An AIUPS study [50] suggested that Ba occupied cave sites, rather than valley-bridge sites, in the (2x1) phase. Some DFT calculations [44] have indicated that the minimum energy configuration of a 1/2 ML Ba/Si(001) surface may actually exhibit (2 x n) symmetry, where the most likely values of the integer, n, are from 3 to 6. (2 x n) unit cells for N = 1 – 6 are shown in Fig. 2.14. A 1/2 ML (2 x 1) surface with Ba atoms occupying all of the valley-bridge sites can be converted to a (2 x n) surface by moving every n^{th} ($n \neq 1$) Ba atom from a valley-bridge site into an adjacent pedestal site. It was suggested that the presence of some vacant valley-bridge sites along the trough between dimer rows helped accommodate the size and charge of Ba adatoms. The cell with $n = 3$ was calculated to be the most stable, but only by 0.02 eV, 0.03 eV and 0.05 eV relative to n = 4, 5 and 6, respectively.

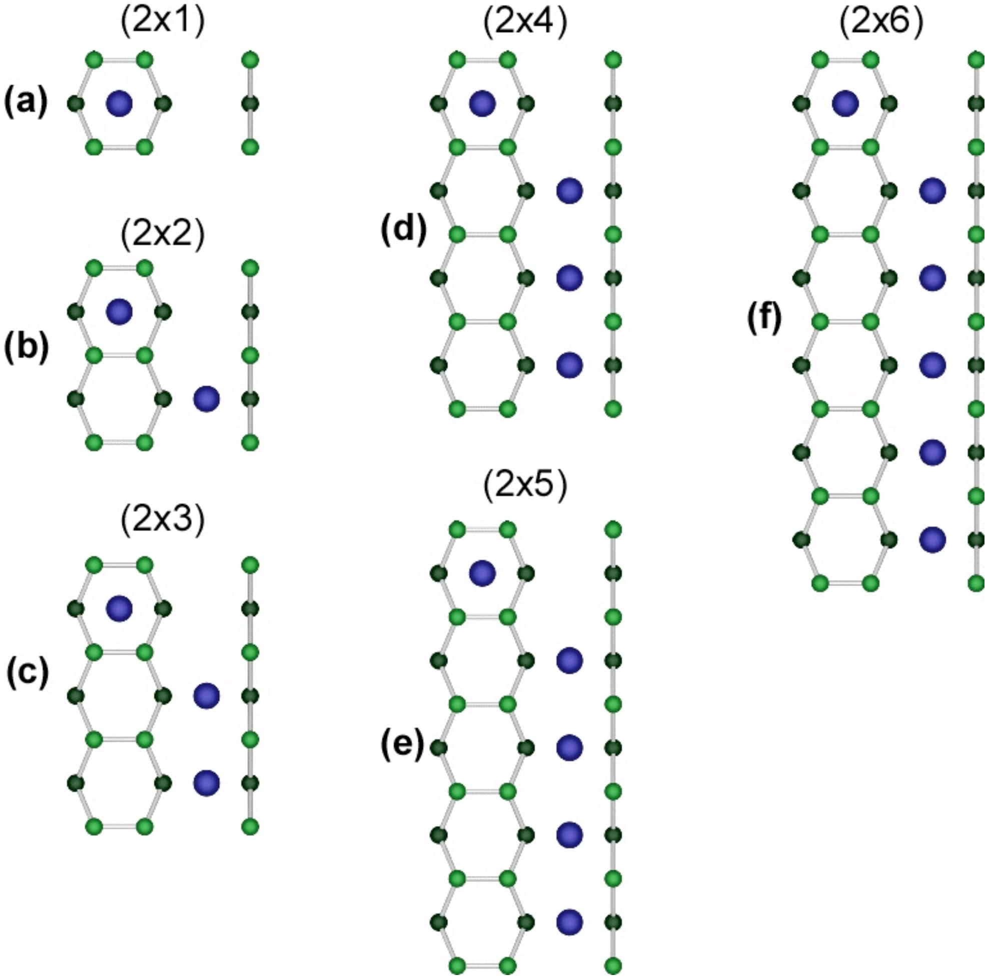

Fig. 2.14: 1/2 ML (2 x n) Ba/Si(001) unit cells tested by Ciani *et al.*'s DFT calculations [44]. (a) n = 1, (b) n = 2, (c) n = 3, (d) n = 4, (e) n = 5, and (f) n = 6.

Relatively little work has been done to investigate the atomic-scale structural details of the (2x4) Ba/Si(001) phase(s) observed at Ba coverages above 0.5 ML. LEED studies [55] of Ba deposited on single domain Si(001)-(2x1) surfaces reportedly confirmed that the 2-fold direction of the (2x4) Ba/Si(001) unit cell [as well as that of the (2x3) unit cell] was parallel to the Si dimer bond direction on the clean Si(001) surface, although the published LEED image used to support this claim appeared to be a two-domain (2x4) pattern. Ciani *et al.* [44] used DFT calculations to test the stability of a 3/4 ML (2x4) phase, but found that the 3/4 ML (2x2) phase was more stable. While the coverages reported along with (2x4) Ba/Si(001) LEED patterns are typically above 1/2 ML, Fan *et al.* did report a mixed (2x1) + (2x4) pattern at coverages as low as 0.4 ML when 900 – 1000°C anneal temperatures were used. It is possible that these anneal conditions produced the 1/2 ML (2 x n) phase (with $n = 4$) predicted by DFT [44].

2.4 $SrTiO_3$ / Si(001)

2.4.1 Technological Motivation for High-κ Dielectrics

Amorphous SiO_2, with a dielectric constant $\kappa = 3.9$ has been the standard gate dielectric material since the 1960s. Traditionally, the development of each new generation of smaller, faster devices has been accompanied by a reduction in the SiO_2 gate dielectric thickness because the operating speed of a FET can be increased by increasing the capacitance across the gate dielectric. At thicknesses below ~10 Å, leakage currents (due to electron tunneling) across the SiO_2 gate becomes prohibitively large. One way to work around this problem would be to replace SiO_2 with a "high K" dielectric material (i.e. one with a κ value greater than that of SiO_2) that would allow sufficiently high capacitance values to be obtained using film thicknesses much larger than those used to achieve the same capacitance across a SiO_2 film. A recent short-term solution has been to use amorphous SiO_xN_y "oxynitrides" and stacked Si_xN_y/SiO_2 films in place of pure SiO_2 in order to achieve marginal increases the capacitance obtained at a given film thickness [63; 64]. Pure $Si_3N_4\kappa$ has $\kappa = 7$ compared to $\kappa = 3.9$ for pure SiO_2. Amorphous films of oxides such as Ta_2O_5 ($\kappa = 26$), or $HfSiO_4$ ($\kappa = 17$) will likely provide a medium-term solution [65; 66].

The even higher dielectric constant of $SrTiO_3$ ($\kappa = 300$), combined with McKee *et al.*'s evidence [6] that $SrTiO_3$ could be grown on Si(001) with an atomically sharp oxide-semiconductor interface, seemed especially promising for a long-term gate dielectric solution. Although numerous oxide materials possess dielectric constants high enough to satisfy requirements for future gate dielectric applications, most of these materials are not suitable for use as gate dielectrics because they are not thermodynamically stable in contact with Si. Chemical reactions between a silicon substrate and overlying oxide used as a gate dielectric tend to increase the roughness of the oxide-Si interface and can be detrimental to FET device operation for a variety of reasons. If the chemical reaction results in the formation of a "low K" reaction product at the interface, the capacitance across the now multi-layered gate dielectric will be reduced. A rough oxide-Si interface would reduce the mobility of charge carriers in the FET's active channel region (and would consequently reduce the overall device speed) due to increased phonon scattering. A rough interface would also be likely to have a high density of trap states that would increase the concentration of fixed charge at the oxide-Si boundary leading to problems such as inconsistent capacitance-voltage behavior and dielectric breakdown of the oxide.

At this point, it may be unclear why an epitaxial $SrTiO_3$ film is desirable for gate dielectric applications when, as mentioned above, the materials currently used for gate dielectrics are in amorphous form. First, it is unlikely that the thermodynamically stable $Si(001) - Sr - SrO - TiO_2 \cdots$ atomic layering sequence would be present throughout the entire interface between Si and an amorphous film, but even if this problem were overcome, epitaxy of the $SrTiO_3$ film would still be required for other reasons. Defects such as grain boundaries within the interior of a gate dielectric film can lead to problems similar to those caused by trap states at the oxide-Si interface. Grain boundaries within the gate dielectric can also act as diffusion pathways for contaminants such as B and P atoms from the highly doped overlying polycrystalline Si gate electrode. Thus, any gate dielectric film, regardless of what material it is, should be in either amorphous or single-crystal (epitaxial) form. For $SrTiO_3$ gate dielectrics however, an epitaxial film is the only viable option because amorphous $SrTiO_3$ films are known to crystallize at 450°C [67; 68] (well below the temperatures used during the back-end processing of Si based microelectronic devices). Also, the dielectric constant of epitaxial $SrTiO_3$ significantly greater than that measured for amorphous or polycrystalline $SrTiO_3$ films [68-70].

2.4.2 Review of $SrTiO_3$/Si(001) Research

A great deal of effort has been put into understanding the synthesis, atomic-scale structure and electronic properties of $SrTiO_3$/Si(001). Thin films of $SrTiO_3$ have been grown on single crystal Si(001) substrates using a variety of deposition techniques including sputtering [67; 71-74], sol-gel processing [75-77], metal-organic chemical vapor deposition (MOCVD) [78], electron beam evaporation [4; 79]and molecular beam epitaxy (MBE) [32; 34; 35; 80-82]. So far, only MBE-based techniques have demonstrated the ability to form $SrTiO_3$ films that are both epitaxial and (apparently) free of unwanted secondary phases at the $SrTiO_3$-Si interface as indicated by TEM [6; 33; 36; 82-87] and x-ray photoemission spectroscopy (XPS) studies [88].

The primary tool used for in-situ characterization during the MBE growth of $SrTiO_3$ (as well as the Sr/Si(001) and SrO precursors) is reflection high energy electron diffraction (RHEED). This technique provides information about the surface periodicity and is also used (somewhat empirically) to determine when the growth of a particular atomic layer is complete and obtain information about surface morphology. As mentioned above, TEM has been widely used for post-growth studies of atomic-scale structure of $SrTiO_3$/Si(001). Additional information on the arrangement and chemical states of atoms at the interface and in the film has been obtained by extended x-ray absorption fine-structure (EXAFS) [89], grazing-incidence X-ray diffraction (GIXD)

[90], Rutherford backscattering spectrometry (RBS) [91], UV-Raman spectroscopy [92], XPS [34; 86; 88; 91; 93-97], atomic force microscopy [98] (AFM) and STM [34].

Much of the electrical properties information on $SrTiO_3$/Si(001) has been obtained in the form of current-voltage (I-V) and capacitance-voltage (C-V) measurements of metal-oxide-semiconductor (MOS) capacitors [6; 98; 99] and actual FETs with $SrTiO_3$ gates [100]. Schaadt *et al.* [101] used conductive atomic force microscopy (CAFM) to image the leakage current through $SrTiO_3$/Si(001) films and detect the presence of e "dead" interface layer that caused some $SrTiO_3$ films to have a significantly lower κ value than that of bulk $SrTiO_3$. XPS investigations of the band offsets between epitaxial $SrTiO_3$ and the underlying Si(001) have reported that the $SrTiO_3$ valence band maximum is 2.1 – 2.6 eV below the Si valence band maximum. Values reported for the conduction band offsets have ranged from the $SrTiO_3$ conduction band minimum being 0.5 eV below to 0.1 eV above the Si conduction band minimum. This latter finding revealed a significant obstacle that could prevent $SrTiO_3$ from being a useful gate dielectric material. The rather small (or even negative) offset between the $SrTiO_3$ and Si conduction bands would most likely allow unacceptably large tunneling currents across a $SrTiO_3$ gate dielectric. A negative conduction band offset refers to the case of the $SrTiO_3$ conduction band minimum being lower than that of Si.

A number of theoretical studies have investigated the band $SrTiO_3$-Si band offsets as well. Pseudopotential calculations using bulk parameters have predicted a conduction band offset of -0.1 eV [102; 103]. Studies that have considered atomic arrangements and bonding at the interface found that the band offsets are highly sensitive to these factors. Density Functional Theory (DFT) calculations of interface structures containing a single SrO atomic layer between the Sr/Si(001) layer and the bottom TiO_2 layer in the $SrTiO_3$ film typically estimate a conduction band offset between 0 and +1 eV. [104-107], although Forst *et al.* [104] noted that due to the fact that DFT calculations tend to underestimate band gaps, the actual conduction band offset would likely be somewhat smaller than the value predicted by their calculations (and consequently revised their calculated value of a +0.7 – +0.8 eV offset for a Si(001) – Sr – SrO – TiO_2 – SrO – TiO_2··· interface to 0.1 – 0.2 eV).

Both theoretical [38; 39; 104] and experimental [31; 40] studies have indicated that a tunneling barrier may be achieved by increasing the number of SrO atomic layers present at the interface and/or by alloying these layers with binary oxides of other alkaline-earth metals. For example, Forst *et al.* [104] predicted that the presence of two interfacial atomic layers of SrO would result in a (corrected) conduction band offset of +1.2 – +1.3 eV, and Junquera *et al.* [39] predicted an offset of +2.7 eV for an interface with 5 SrO layers. It is generally accepted that an offset of at least +1.0 eV is needed for gate dielectric applications.

While the possibility of using “interface engineering” to overcome the conduction band offset problem of $SrTiO_3$ has generated academic interest, industry seems to have given up (for now, at least) on the prospect of using $SrTiO_3$ as a gate dielectric. Doubts about the robustness of such a solution as well as questions about the chemical stability of any $SrTiO_3$-Si interface against some SiO_2 formation at the ~1000°C currently used in some semiconductor processing steps currently outweigh the potential benefits of using $SrTiO_3$ as a gate dielectric.

While it appears that the recent surge of research efforts into $SrTiO_3$/Si(001) will not lead to $SrTiO_3$ being used as a gate dielectric, there are still both scientific and technological gains to be made from these endeavors. Since investigations of $SrTiO_3$/Si(001) have included both experimental and theoretical work, this materials system has provided a platform for many experimentalists and theoreticians to share and test their results. Also, progress in the epitaxial growth of $SrTiO_3$/Si(001) has resulted in heterostructures that are still useful for other applications. As mentioned at the beginning of this chapter, $SrTiO_3$/Si(001) was used as a template for growing high-T_C oxide films before it was ever seriously considered as a gate dielectric. In the past few years, epitaxial $SrTiO_3$/Si(001) has been successfully used as a “template” for growing epitaxial films of other materials that are not stable in direct contact with Si, but have properties that may be useful in device applications. In addition to high-T_C superconductors [108], the functional materials that have been grown epitaxially $SrTiO_3$/Si(001) include another high-T_C superconductor, a piezoelectric, $Pb(Zr,Ti)O_3$ [109-111]; a conducting oxide, $(La_{0.5}Sr_{0.5})CoO_3$ [112]; and a direct bandgap semiconductor, GaAs [113].

CHAPTER 3

X-ray Standing Waves

3.1 Introduction

The interference field that results from the superposition of two coherently related traveling plane waves takes the form of a standing wave. An X-ray standing wave (XSW) can be generated by a variety of X-ray reflection conditions including Bragg diffraction from a single crystal; Bragg diffraction from a layered, synthetic, periodic microstructure (e.g. a Si-Mo multilayer); and total external reflection from a smooth solid-vacuum interface. Both the theory and application of the XSW technique in the characterization of distributions of atoms within the bulk and (more commonly) on the surface of solid-state materials have been described extensively in Refs. [114-119]. This chapter reviews some of the fundamental principles involved in using an XSW generated by Bragg diffraction from a bulk single crystal in the Bragg (rather than Laue) geometry to study adsorbates and thin films deposited on single crystal substrates.

An XSW formed by satisfying the Bragg condition for a set of bulk single crystal diffraction planes and a monochromatic X-ray beam is shown schematically in Fig. 3.1. The XSW along with the incident and diffracted X-ray beams are all plane waves. The XSW field is present above and below the crystal surface, and its period *D*, given by:

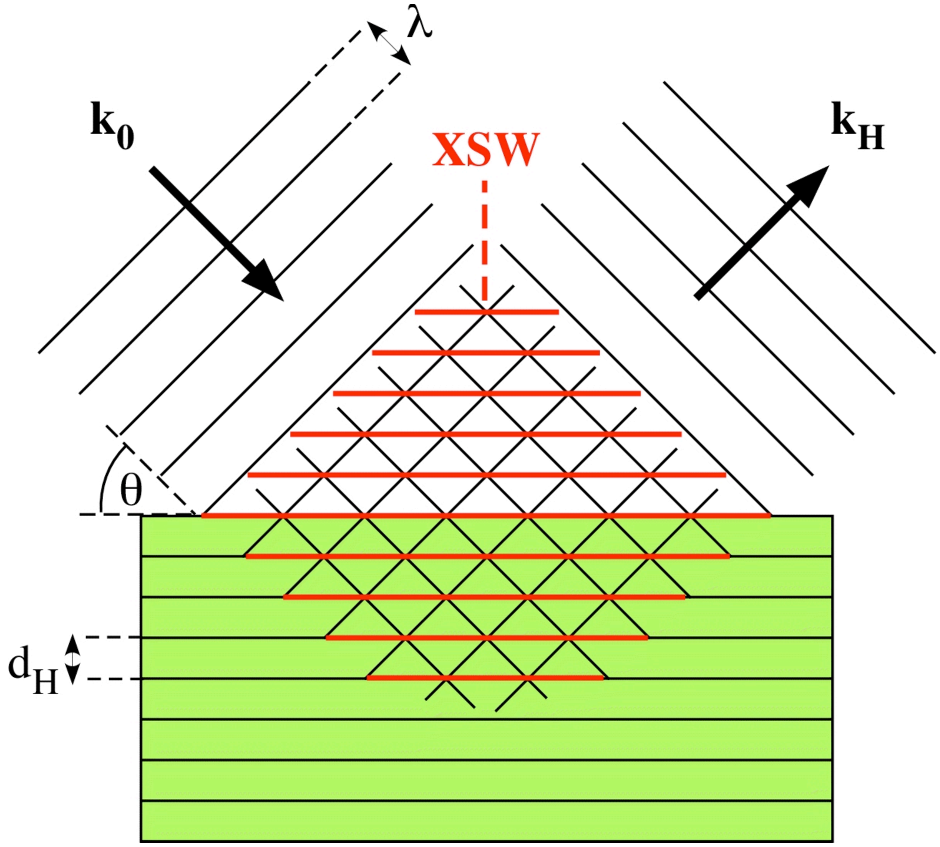

Fig. 3.1. X-ray standing wave generated by interference between incident and diffracted plane waves with respective external wave-vectors $\boldsymbol{k_0}$ and $\boldsymbol{k_H}$ when diffraction condition is satisfied for the ***H*** diffraction planes of a bulk single-crystal.

(3.1) $$D = \frac{\lambda}{2\sin\theta_B} = \frac{2\pi}{|\boldsymbol{H}|}.$$

is equal to the interplanar spacing d_H of the diffraction planes. λ is the X-ray wavelength, θ_B is the geometrical Bragg angle, and $\boldsymbol{H}$ is the reciprocal lattice vector of the diffraction planes. The phase of the XSW (i.e. the position of the XSW antinodes relative to the diffraction planes) can be controlled by changing either λ or the incident angle, θ. Atoms residing within the XSW field can undergo photoelectric transitions and emit photoelectrons, auger electrons, and X-ray fluorescence with element-specific energies. Together, these qualities allow the XSW to be used as an element-specific probe to study distributions of atoms with sub-Angstrom resolution.

3.2 XSW Generation

The formalism used to describe the existence and behavior of an XSW generated by diffraction from a bulk single crystal comes from dynamical diffraction [120] theory which involves solving Maxwell's equations for a triply periodic dielectric medium. The respective wave vectors of the incident and diffracted X-ray beams in Fig. 3.1 are $\boldsymbol{k_0}$ and $\boldsymbol{k_H}$ outside of the crystal and $\boldsymbol{K_0}$ and $\boldsymbol{K_H}$ inside the crystal. The complex internal wave vectors can be related to the purely real external wave vectors by applying the boundary conditions that the tangential component of the wave vectors must be continuous at the crystal surface.

Inside the crystal, the electric fields of the incident and diffracted beams (traveling X-ray plane waves) can be written as:

$$\boldsymbol{\mathring{a}_0} = \boldsymbol{E_0} \exp\left[i\left(\omega t - \boldsymbol{K_0} \cdot \boldsymbol{r}\right)\right] \tag{3.2}$$

for the incident beam and:

$$\boldsymbol{\mathring{a}_H} = \boldsymbol{E_H} \exp\left[i\left(\omega t - \boldsymbol{K_H} \cdot \boldsymbol{r}\right)\right] \tag{3.3}$$

for the diffracted beam.

ω is the X-ray angular frequency, and ***r*** is a coordinate vector relative to the same origin as that used to define the atomic positions of the single crystal unit cell. When the Bragg condition is satisfied, $\boldsymbol{K_0}$ and $\boldsymbol{K_H}$ are related by the Laue condition:

$$\boldsymbol{K_H} - \boldsymbol{K_0} = \boldsymbol{H} \tag{3.4}$$

The amplitudes $\boldsymbol{E_0}$ and $\boldsymbol{E_H}$ of the incident and diffracted beams contain a phase factor and therefore are complex. Treating the cases of σ and π polarized X-rays separately allows the complex ratio of the electric field amplitudes to be expressed in scalar form for each case as:

$$\frac{E_H}{E_0} = \left|\frac{E_H}{E_0}\right| \exp\left(i\phi\right), \tag{3.5}$$

where ϕ is the difference in phase between E_H and E_0.

The normalized electric field intensity that results from superimposing the incident and diffracted X-ray beams is:

$$I = \frac{\left|\boldsymbol{\mathring{a}_0} + \boldsymbol{\mathring{a}_H}\right|^2}{\left|E_0\right|^2}. \tag{3.6}$$

Using Eqs. (3.2) – (3.6) allows I to be written as:

$$I = \left[1 + \left|\frac{E_H}{E_0}\right|^2 + 2P\left|\frac{E_H}{E_0}\right|\cos(\phi - \boldsymbol{H}\cdot\boldsymbol{r})\right] \times \begin{cases} 1;\ \text{above the surface} \\ e^{-\mu_z z};\ \text{at depth z below surface} \end{cases} \tag{3.7}$$

This equation describes a standing wave that is periodic in the direction of $\boldsymbol{H}$ and has a period of d_H. The polarization factor, P is equal to 1 for σ polarization and $cos(2\theta_B)$ for π polarization. μ_z is the effective absorption coefficient of the incident X-ray beam. μ_z, ϕ, and $\left|\frac{E_H}{E_0}\right|$ are all functions of θ.

Before discussing the details of how these parameters (and consequently, I) vary with θ, it is useful to introduce the normalized angle parameter η defined as:

$$\eta = \frac{b\Delta\theta\sin(2\theta_B) + \Gamma F_0}{|b|\Gamma\sqrt{F_H F_{\overline{H}}}}. \tag{3.8}$$

The relative incident angle $\Delta\theta$ is given by:

$$\Delta\theta = \theta - \theta_B. \tag{3.9}$$

The constant Γ is:

$$\Gamma = \frac{r_e\lambda^2}{\pi V_C}, \tag{3.10}$$

where $r_e = 2.818\times10^{-5}$ Å is the classical electron radius, and V_C is the volume of the crystal unit cell.

The $\boldsymbol{H}$ structure factor, F_H, can be calculated by:

$$F_H = \sum_{n=1}^{N}\left[f_n^0(\boldsymbol{H}) + \Delta f_n'(\lambda) + i\Delta f''(\lambda)\right]\exp(i\boldsymbol{H}\cdot\boldsymbol{r_n})D_n(\boldsymbol{H}). \tag{3.11}$$

This summation is over all *N* atoms in the unit cell. f_n^0 is the atomic form factor of the n^{th} atom in the unit cell, while $\Delta f_n'$ and $\Delta f_n''$ are the respective real and imaginary anomalous dispersion corrections. Throughout this chapter, a complex number *X* is considered to be of the form $X = X' + iX''$. $D_n(\boldsymbol{H})$ is the Debye-Waller factor due to thermal vibrations of the n^{th} atom and is given by:

$$D_n(\boldsymbol{H}) = \exp(-M_n), \tag{3.12}$$

where

$$M = \frac{2\pi^2 \left\langle u_H^2 \right\rangle_n}{d_H^2}, \tag{3.13}$$

and $\left\langle u_H^2 \right\rangle_n$ is the mean square vibration amplitude of the n^{th} atom along the direction of $\boldsymbol{H}$.

It can be shown by dynamical diffraction theory that the ratio of the electric field amplitudes varies with η as:

$$\frac{E_H}{E_0} = -\sqrt{|b|}\frac{|P|}{P}\sqrt{\frac{F_H}{F_{\overline{H}}}}\left(\eta \pm \sqrt{\eta^2 - 1}\right). \tag{3.14}$$

Eq. (3.14) is a piece-wise function in which the factor inside the parentheses is $\left(\eta + \sqrt{\eta^2 - 1}\right)$ when $\eta' < 1$ and is $\left(\eta - \sqrt{\eta^2 - 1}\right)$ when $\eta' \geq 1$. The asymmetry factor, *b*, is defined as:

$$b = \frac{\gamma_0}{\gamma_H}, \tag{3.15}$$

where

(3.16) $$\gamma_0 = \hat{\boldsymbol{n}} \cdot \hat{\boldsymbol{s}}_{\boldsymbol{0}},$$

and

(3.17) $$\gamma_H = \hat{\boldsymbol{n}} \cdot \hat{\boldsymbol{s}}_{\boldsymbol{H}}.$$

$\hat{\boldsymbol{s}}_{\boldsymbol{0}}$ and $\hat{\boldsymbol{s}}_{\boldsymbol{H}}$ are unit vectors parallel to $\boldsymbol{k}_{\boldsymbol{0}}$ and $\boldsymbol{k}_{\boldsymbol{H}}$, respectively, and $\hat{\boldsymbol{n}}$ is a unit vector along the outward direction of the crystal surface normal. γ_0 and γ_H can be thought of as the direction cosines of the incident and diffracted beam directions with respect to the surface normal.

The physically measurable reflectivity, R, is given by:

(3.18) $$R = \left|\frac{E_H}{E_0}\right|^2.$$

A plot of R as a function of $\Delta\theta$ (or η') in the vicinity of the $\boldsymbol{H}$ Bragg reflection is referred to as the $\boldsymbol{H}$ "rocking curve." Eqs. (3.8), (3.14) and (3.18) can be used to show that R approaches 1 over a range of $\Delta\theta$ values known as the "Darwin width," given by:

(3.19) $$\omega = \Delta\theta_{\eta'=-1} - \Delta\theta_{\eta'=1} = \frac{2\Gamma\sqrt{F_H' F_{\overline{H}}' + F_0''^2 - F_H'' F_{\overline{H}}''}}{\sin(2\theta_B)\sqrt{|b|}}.$$

A simulated Si(004) rocking curve calculated using 18.5 keV X-rays and assuming a symmetric reflection geometry (i.e. b = -1) are shown in Fig 3.2.

From Eq. (3.5), it can be seen that:

(3.20) $$\phi = \arg\left(\frac{E_H}{E_0}\right),$$

and eq. (3.7) indicates that in addition to being the difference between the phases of E_H and E_0, ϕ is also the phase of the XSW. The normalized phase, $\phi/(2\pi)$ is plotted along with the rocking curve in Fig. 3.2. It can be seen from this plot that as $\Delta\theta$ is scanned from the low-angle side to the high-angle side of the rocking curve, ϕ decreases by π radians. The $-\pi$ shift in ϕ corresponds to the XSW antinodes moving a distance of $d_H/2$ in real space along the ***–H*** direction. Hence, the electric field intensity at a given point within the XSW field can change dramatically as the crystal is scanned through the rocking curve.

The factor $e^{-\mu_z z}$ in eq. (3.7) is due to attenuation of the electric-field intensity inside the crystal. The effective absorption coefficient μ_z is defined as:

(3.21)
$$\mu_z(\theta) = \frac{\mu_0}{\sin\theta_B}\left[1 + \frac{F'_{\bar{H}}}{F''_0}\left(\frac{E_H}{E_0}\right)'' + \frac{F''_{\bar{H}}}{F''_0}\left(\frac{E_H}{E_0}\right)'\right].$$

μ_0 is the linear absorption coefficient and can be expressed as:

(3.22)
$$\mu_0 = \frac{2\pi}{\lambda}\Gamma F''_0$$

μ_z is maximized (and consequently the penetration depth of the incident X-ray beam is minimized) when $\eta' = 0$. The value taken on by μ_z^{-1} when $\eta' = 0$ is referred to as the extinction length, Λ_{ext}, and is given by:

(3.23)
$$\Lambda_{ext} = \frac{V_C}{4 d_H r_e\left(F''_0 + \sqrt{|F_H||F_{\bar{H}}|}\right)}$$

Atoms located within the XSW field can undergo photoelectric transitions and

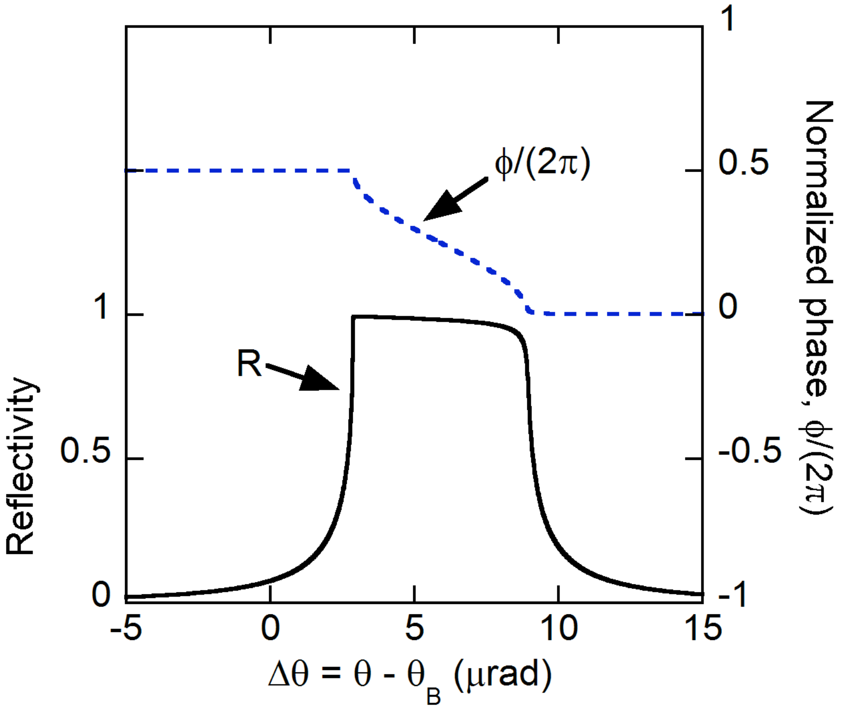

Fig. 3.2: Calculated rocking curve and normalized phase of the XSW for Si(004) reflection with 18.5 keV X-rays.

consequently emit signals including photoelectrons, Auger electrons and X-ray fluorescence. As $\Delta\theta$ is scanned through the rocking curve, the probability that an atom within the XSW field will undergo a photoelectric transition modulates due to the change in the atom's local electric field intensity brought about by the XSW phase shift. For most XSW experimental conditions, it is valid to use the dipole approximation when calculating an atom's photoelectric cross-section. In this approximation, the photoelectric cross-section is proportional to the electric field intensity at the atom's center.

The photoelectric signals measured in the experiments presented in this thesis were limited to X-ray fluorescence. If a characteristic X-ray fluorescence signal is initiated exclusively by the XSW, then in the dipole approximation, the normalized fluorescence yield of that fluorescence signal can be written as:

$$Y(\theta) = \int I(\theta, \boldsymbol{r})\rho(\boldsymbol{r})\exp\left[-\mu_f(\alpha)z\right]d\boldsymbol{r}. \tag{3.24}$$

ϱ(r) is the normalized distribution function of the atomic species responsible for the particular fluorescence signal. The ***H*** Fourier component of ϱ(r) is:

$$G_{\mathrm{H}} = \int \rho(\boldsymbol{r})\exp(i\boldsymbol{H}\cdot\boldsymbol{r})d\boldsymbol{r} = f_H \exp(2\pi i P_H). \tag{3.25}$$

For reasons explained later, the amplitude, f_H, of G_H is referred to as the *coherent fraction*, and the phase, P_H, is called the *coherent position*. μ_f is the effective absorption coefficient of the fluorescent X-rays and is a function of α, the "takeoff" angle between a fluorescent photon's direction of travel and the crystal surface. μ_f is given by:

(3.26) $$\mu_f(\alpha) = \frac{2\sqrt{2}\pi}{\lambda_f}\left[\sqrt{\left(2\delta - \alpha^2\right)^2 + 4\beta^2} + 2\delta - \alpha^2\right]^{\frac{1}{2}},$$

where:

(3.27) $$\delta = \frac{\Gamma F_0'}{2},$$

and:

(3.28) $$\beta = \frac{\Gamma F_0''}{2}$$

(where δ and β are related to the average index of refraction, *n*, through: $n = 1 - \delta - i\beta$).

Using Eqs. (3.7) and (3.17) and integrating Eq. (3.19) allows *Y(θ)* to be written as:

(3.29) $$Y(\theta) = Y_{OB}\left[1 + R(\theta) + 2\sqrt{R(\theta)}f_H \cos\left(\phi(\theta) - 2\pi P_H\right)\right]Z(\theta).$$

The off-Bragg yield, Y_{OB} is the fluorescence yield when θ is far away from the Bragg condition. *Z(θ)* is the effective-thickness factor and accounts for absorption / extinction of the incident X-ray beam as well as absorption of the emitted photoelectric signal. If the distribution of atoms responsible for a particular fluorescence signal is located on or above the crystal surface, then $Z(\theta) = 1$. The approximation that $Z(\theta) \approx 1$ can be made for fluorescing species located below the crystal surface if they are at a depth $z << \Lambda_{ext}$. If the fluorescing atoms are distributed evenly throughout the crystal, then:

(3.30) $$Z(\theta) = \frac{\mu_0\left(\sin\theta_B\right)^{-1} + \mu_f(\alpha)}{\mu_z(\theta) + \mu_f(\alpha)}.$$

3.3 Using XSWs for Atomic-scale Structural Analysis

3.3.1 Coherent Position and Coherent Fraction

In an actual XSW experiment, the reflectivity and fluorescence spectra are measured simultaneously while scanning through the ***H*** rocking curve. The measured reflectivity curve is fit to dynamical diffraction theory using Eqs. (3.8) and (3.14). The fluorescence yield emitted by a particular atomic species can then be fit to Eq. (3.29) using Y_{OB}, f_H and P_H as fitting parameters.

f_H can be separated into three factors as:

(3.31) $$f_H = C a_H D_H .$$

Here, the C is the fraction of the fluorescence-selected atoms that are ordered with respect to the crystal lattice. The quantity $(1 - C)$ is often referred to as the "disordered fraction." a_H and D_H are the respective geometrical and Debye-Waller factors of the ordered fluorescence-selected atoms; the value of these quantities is not affected by the disordered population. D_H is of the form:

(3.32) $$D_H = \exp\left(\frac{-2\pi^2 \left\langle u_H^2 \right\rangle}{d_H^2} \right).$$

The geometrical factor a_H is the modulus of the normalized geometrical structure factor, S_H, of the atomic species responsible for the fluorescence signal of interest. S_H is given by:

(3.33) $$S_H = \frac{1}{C}\sum_{j=1}^{N}\left[c_j \exp\left(i\boldsymbol{H}\cdot\boldsymbol{r}_j\right)\right],$$

and a_H is:

(3.34) $$a_H = \left|S_H\right|.$$

The summation in Eq. 3.33 is over the N ordered sites occupied by the XRF selected atom relative to the bulk unit cell. c_j is the fraction of the XRF selected atoms occupying site j (i.e. C = $\sum_{1}^{N} c_j$), and r_j is the position vector of site j relative to the bulk unit cell.

Examination of Eq. 3.31 helps to illustrate why f_H is called the *coherent fraction.* It is evident from this equation that f_H is proportional to the ordered fraction. If the atomic species of interest occupies only one site with respect to the single crystal unit cell and thermal vibrations are ignored (i.e. a_H and D_H are both unity), then f_H is equal to the ordered fraction.

P_H is the phase of the normalized geometrical structure factor and can be written as:

(3.35) $$P_H = \frac{\arg\left[S_H\right]}{2\pi}$$

If $a_H = 1$, then P_H is equal to the position of the occupied site (as a fraction of d_H) relative to the diffraction planes defined by the reciprocal lattice vector $\boldsymbol{H}$ (e.g. if the occupied site is half way between two adjacent diffraction planes, then $P_H = 0.5$). The *3D* position(s) of the occupied site(s) can be triangulated by making multiple XSW measurements (using different $\boldsymbol{H}$ reflections for each measurement).

3.3.2 XSW Triangulation of Adatoms on Dimerized Si(001)

The ordered fraction, *C*, in Eq. 3.31 can be comprised of atoms exhibiting long- and/or short-range order. Based on symmetry arguments, it can be shown that if a long-range ordered phase of adsorbate atoms on dimerized Si(001) contains just one adatom per unit cell, then the adatom must occupy one of the four high symmetry sites indicated in Fig.2.3. If the unit cell contains more than one adatom, then each adatom would not necessarily occupy a high symmetry site, but in order to maintain long-range order, any adatom not occupying a high symmetry site would need to be part of a group of atoms centered about a high symmetry site. Short-range ordered adatoms could also be distributed onto the surface as individual atoms occupying high symmetry sites, or as groups of atoms centered about high symmetry sites. Although the minimum energy position for an isolated adatom is typically located on a high-symmetry site, it would even be possible for short-range ordered adatoms to be present as individual adatoms occupying non-high-symmetry sites. In this last case, the position of the short-range ordered adatoms averaged over the large area (~0.1 – 1 mm^2) probed in a typical XSW experiment would still be centered about one or more high symmetry site.

If it is assumed that the ordered AEM atoms occupy only one type of site (and that this site is a high symmetry site), the AEM adatom position relative to the bulk primitive unit cell of the Si lattice can be uniquely determined in three dimensions using less than three P_H values. Most of the XSW measurements conducted in this thesis work were made by scanning either the Si(004) or Si(022) Bragg condition. If the ordered adatoms are centered on just one type of high-symmetry site, then it turns out that P_{004} and P_{022} must satisfy one of the following two symmetry rules:

$$P_{022} = \frac{P_{004}}{2}, \tag{3.36}$$

or

$$P_{022} = \frac{(1 + P_{004})}{2}. \tag{3.37}$$

Fig. 3.3(a) shows a [010] “side-view” projection of a Si(001) crystal with the bulk (004) and (022) diffraction planes drawn as solid lines. On the left-hand side of the figure, the terminating top-layer of dimerized Si atoms is one atomic layer higher than that on the right-hand side. The [001] projection of this same crystal in Fig. 3.3(b) reveals that the terminating top-layer on the left-hand side of Fig. 3.3(a) is an “A” domain, while that on the right-hand side of Fig. 3.3(b) is a “B” domain, as defined in section 2.2.1.

The in-plane positions of adatoms occupying bridge, cave, pedestal and valley-bridge sites are indicated by shaded circles on both the “A” and “B” terraces in Fig. 3.3(b). It can be seen from the side-view projection in Fig. 3.3(b) that all of these adatoms are sitting at the same height above the ideal bulk plane of second layer Si atoms. This height is given by:

$$h = (P_{004} + n)d_{004}. \tag{3.38}$$

In the general case, n can be any integer (since the XSW is a periodic probe, there is an inherent ‘modulo-d ambiguity’), but for all of the adatoms shown in Fig. 3.3, $n = 0$.

Since the terminating Si surface layer on terrace “B” is one atomic step lower than that on terrace “A,” the second layer bulk plane on terrace “B” is the third layer bulk plane on terrace “A.”

Adatoms occupying cave and bridge sites on both the “A” and “B” terraces are located at a distance $P_{022}^{BC}d_{022}$ along the [011] direction from a (022) diffraction plane, and the P_H values of these atoms satisfy Eq. 3.36. Adatoms occupying valley-bridge and pedestal sites in Fig. 3.3 are located a distance $P_{022}^{VP}d_{022}$, along the [011] direction from a (022) diffraction plane, and the P_H values of these atoms satisfy the relationship Eq. 3.37.

Fig. 3.3 also illustrates that if two adatoms occupy identical positions relative to the terminating Si(001) surface atoms but are located on adjacent terraces separated by a monoatomic step, these adatoms occupy equivalent positions relative to the bulk Si(004) and Si(022) Bragg diffraction planes.

Figs. 3.4 (a) and (b) show the same crystallographic projections as those shown in Fig. 3.3. However, in these figures, the height of the adatoms above the ideal bulk plane of second layer Si atoms is given by Eq. 3.38 with $n = 1$ (instead of $n = 0$). Since the height of each adatom in this figure is an integer number of Si(004) d-spacings higher than what it was in Fig. 3.3, P_{004} has not changed. It should also be pointed out that relative to the Si(022) diffraction planes, the position adatoms occupying bridge and cave sites in Fig. 3.4 is the same as that of adatoms occupying valley-bridge and pedestal sites in Fig. 3.3. Likewise, adatoms occupying valley-bridge and pedestal sites in Fig. 3.4 are in the same position relative to the Si(022) diffraction planes as atoms occupying bridge and cave sites in Fig. 3.3. Thus, for $n = 1$, the P_H values of adatoms occupying cave and bridge sites satisfy Eq. 3.37, while adatoms in valley-bridge and pedestal sites satisfy Eq. 3.36.

Under the assumption of single-site occupancy, measuring P_{004} and P_{022} values that satisfy Eq. 3.36 would be consistent with cave or bridge site occupancy with $n = odd$, but would also be consistent with valley-bridge or pedestal site occupancy with $n = even$. Similarly, experimentally measured P_{004} and P_{022} values satisfying Eq. 3.37 would be consistent with cave or bridge site occupancy with $n = even$, but would also be consistent with valley-bridge or pedestal site occupancy with $n = odd$. Part of this ambiguity is due to the fact that for a given value of n, each of the four high-symmetry sites represents a unique position relative to the dimerized Si surface atoms, but the cave and bridge sites represent a single position relative to the bulk primitive Si unit cell, and the valley-bridge and pedestal sites represent another (single) position relative to the bulk primitive unit cell. The inability to distinguish between cave and bridge site occupancy as well as the inability to distinguish between valley-bridge and pedestal site occupancy would be inherent in any XSW measurement utilizing bulk Si diffraction planes, regardless of which (and how many) $\boldsymbol{H}$ reflections were used.

The additional ambiguity that a particular pair of P_H values cannot distinguish between cave / bridge site occupancy at a height h and valley-bridge / pedestal site

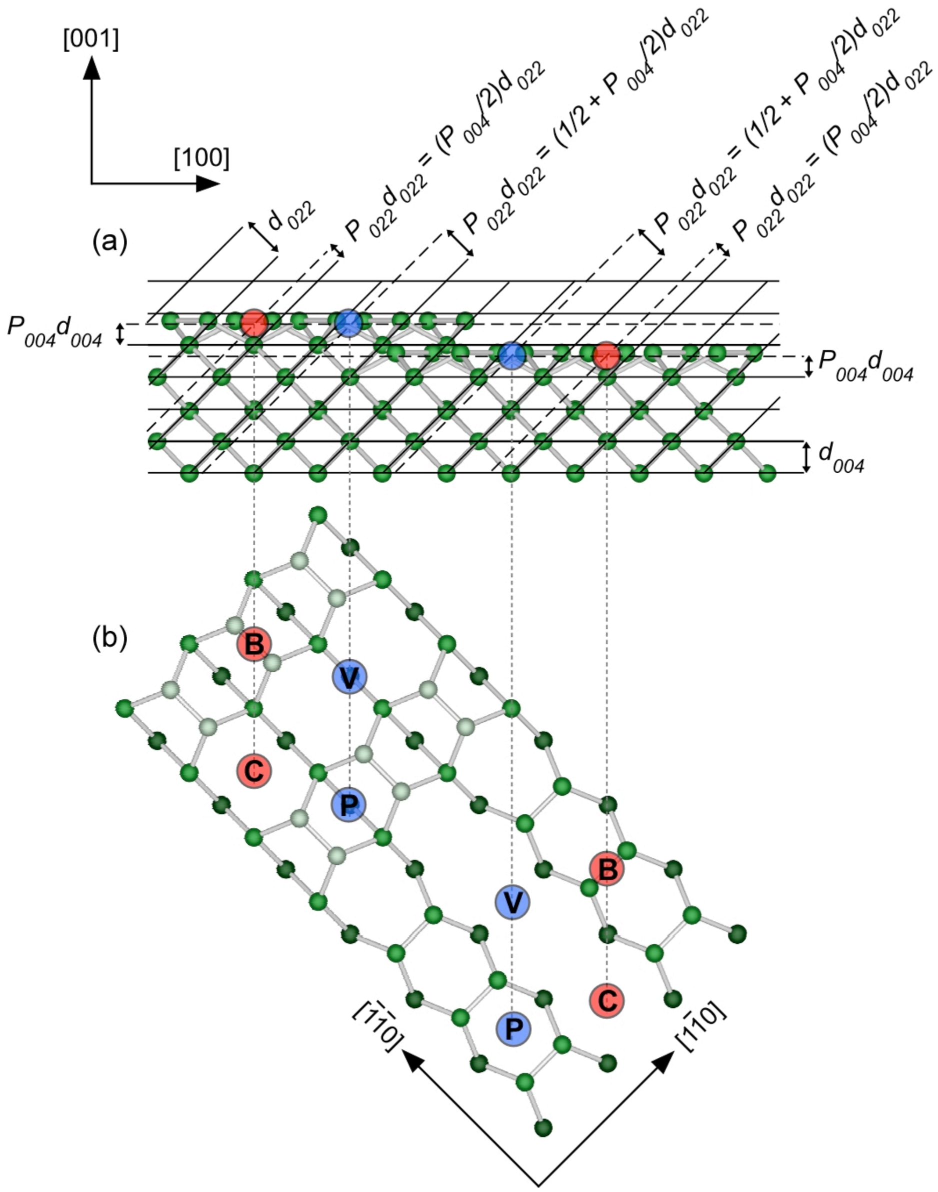

Fig. 3.3. (a) [010] and (b) [001] projections of atoms occupying high symmetry sites on "A" and "B" domains of a dimerized Si(001) surface at heights corresponding to $n = 0$ in Eq. 3.38. The (004) and (022) diffraction planes are drawn as solid lines. The top-layer of atoms on the left-hand side of (a) forms an "A" domain, while that on the right-hand side forms a "B" domain.

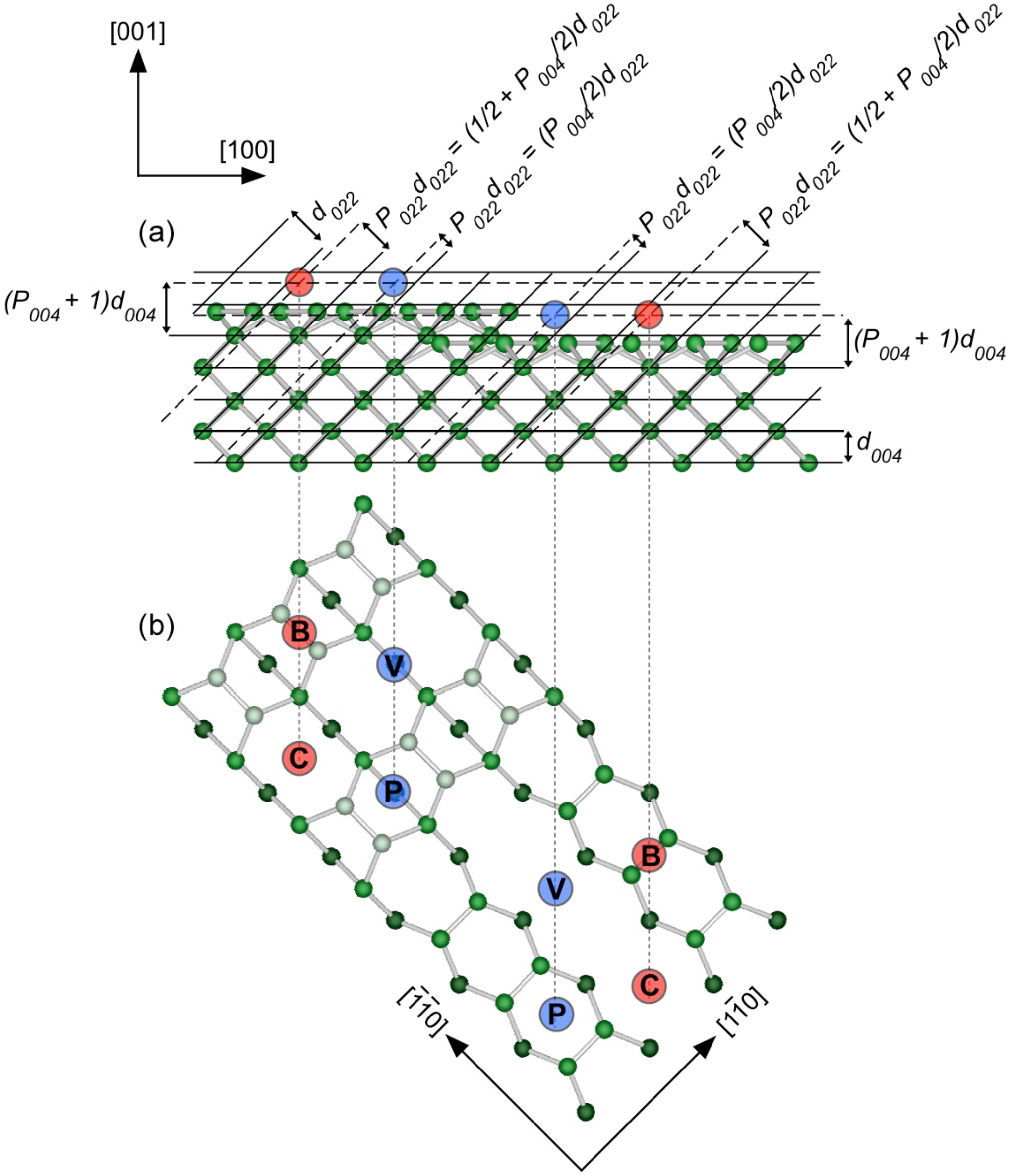

Fig. 3.4. (a) [010] and (b) [001] projections of atoms occupying high symmetry sites on "A" and "B" domains of a dimerized Si(001) surface at heights corresponding to *n* = 1 in Eq. 3.38. The (004) and (022) diffraction planes are drawn as solid lines. The top-layer of atoms on the left-hand side of (a) forms an "A" domain, while that on the right-hand side forms a "B" domain.

occupancy at a height $(h \pm md_{004})$, where m can be any odd integer, is not inherent in all pairs of P_H values if the XSW measurements are made using a single-domain Si(001) surface. In the remainder of this section, it will be explained how results of Si(004) and Si(111) measurements on a single domain surface would remove a certain amount of ambiguity, but on a two-domain Si(001) surface, the positional ambiguity that remains after specifying P_{004} and P_{022} (for a surface with single site occupancy) cannot be removed by measuring any number of additional P_H.

While only *two* relationships [Eqs. 3.36 and 3.37] between P_{004} and P_{022} are possible for ordered adatoms occupying a single type of site on dimerized Si(001), the relationship between P_{004} and P_{111} must follow one of the *four* following equations:

$$P_{111} = \frac{P_{004}}{4}, \tag{3.39}$$

$$P_{111} = \frac{(1 + P_{004})}{4}, \tag{3.40}$$

$$P_{111} = \frac{(2 + P_{004})}{4}, \tag{3.41}$$

or

$$P_{111} = \frac{(3 + P_{004})}{4}. \tag{3.42}$$

Fig. 3.5 shows (a) a [011] “side-view” projection and (b) a [001] “top-view” projection of a Si(001) crystal terminated with both “A” and “B” domains. The bulk (004) and (111) diffraction planes are drawn as solid lines. The out-of-plane position of all of the adatoms shown occupying high-symmetry sites in Fig. 3.5 is given by Eq. 3.38

with $n = 0$. Adatoms that occupy identical sites relative to the Si(001) surface atoms but are separated by a monoatomic step are in nonequivalent positions relative to the bulk Si(111) diffraction planes, so the relationship between P_{111} and P_{004} for a given type of high-symmetry site must be considered separately for "A" and "B" domains. For all of the high-symmetry sites on the "A" domain in Fig. 3.5, P_{004} and P_{111} are related by Eq. 3.40. On the "B" domain, Eq. 3.41 is followed for cave and bridge sites, while Eq. 3.39 is followed for valley-bridge and pedestal sites.

Fig. 3.6 (a) and (b) show the same crystallographic projections shown in Fig. 3.5, but, in Fig. 3.6 the adatom height relative to the ideal bulk plane of second layer Si atoms is given by Eq. 3.38 with $n = 1$ (instead of $n = 0$). For all of the high-symmetry sites on the "A" domain in Fig. 3.6, P_{004} and P_{111} follow eq. (3.41). On the "B" domain, Eq. (3.42) is followed for cave and bridge sites and Eq. (3.40) is followed for valley-bridge and pedestal sites.

The relationships between P_{111} and P_{004} for cave / bridge and valley-bridge / pedestal occupancy with $n = 0$ and $n = 1$ are summarized in Table 3.1. If the dimerized Si(001) surface were terminated exclusively by "B" domains, then the P_{004} and P_{111} values for adatoms ordered onto a single high-symmetry site would be consistent with just one of the four possible adsorption arrangements (cave / bridge, $n = 0$; valley-bridge / pedestal, $n = 0$; cave / bridge, $n = 1$; or valley-bridge / pedestal, $n = 1$) listed in Table 3.1. If the surface were terminated exclusively by "A" domains, then the relationship between the P_{004} and P_{111} values of adatoms ordered onto a single high-symmetry site would be consistent with two of the four possible adsorption arrangements in listed in Table 3.1, but for each of the four possible adsorption arrangements in Table 3.1, there would be a unique relationship between the (004) and $(\bar{1}11)$ coherent positions.

In-plane sites	***n* in Eq. 3.38**	**Domain "A" P_{111}**	**Domain "B" P_{111}**
Cave / Bridge	0	$(1 + P_{004})/4$	$(2 + P_{004})/4$
Valley-bridge / Pedestal	0	$(1 + P_{004})/4$	$P_{004}/4$
Cave / Bridge	1	$(2 + P_{004})/4$	$(3 + P_{004})/4$
Valley-bridge / Pedestal	1	$(2 + P_{004})/4$	$(1 + P_{004})/4$

Table 3.1. P_{111} for single-site occupancy of high symmetry sites on "A" and "B" domains on dimerized Si(001) surface with $n = 0$ and $n = 1$ in Eq. 3.38. If both domains are present, then the overall P_{111} would be given by Eqs. 3.33 and 3.35 with $c_1 = c_2 = 0.5$, $\boldsymbol{H \cdot r_1}/(2\pi)$ equal to P_{111} for the "A" domain, and $\boldsymbol{H \cdot r_2}/(2\pi)$ equal to P_{111} for the "B" domain.

On a surface terminated with equal amounts of "A" and "B" domains, P_{111} would be given by Eqs. 3.33 and 3.35, with two terms (one for the "A" domain and one for the "B" domain) in the summation of Eq. 3.33. c_1 and c_2 would each be equal to 1/2. $\boldsymbol{H \cdot r_1}/(2\pi)$ would be the P_{111} value expected for adsorption onto a particular site on a surface consisting of only "A" domains, and $\boldsymbol{H \cdot r_2}/(2\pi)$ would be the P_{111} value expected for adsorption onto the same type of site on a surface consisting entirely of "B" domains. Examining Table 3.1, it is clear that on a two-domain surface (with equal amounts of each domain), cave / bridge site occupancy with $n = 0$ and valley-bridge / pedestal site occupancy with $n = 1$ would result in the same value for P_{111} since $\boldsymbol{H \cdot r_1}/(2\pi)$ in the latter case would be equal to $\boldsymbol{H \cdot r_2}/(2\pi)$ in the former and vice-versa. Although it may not be

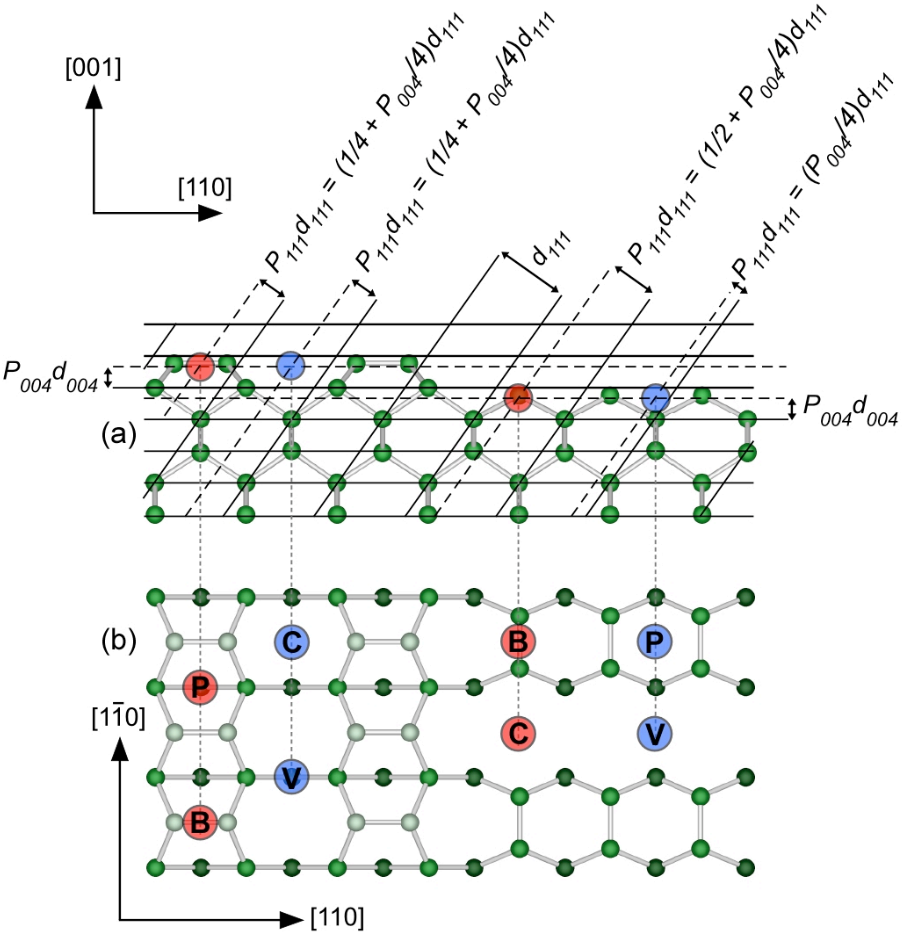

Fig. 3.5. (a) [110] and (b) [001] projections of atoms occupying high symmetry sites on "A" and "B" domains of a dimerized Si(001) surface at heights corresponding to $n = 1$ in Eq. 3.38. The (004) and (022) diffraction planes are drawn as solid lines. The terminating surface on the left-hand sides of both figures forms an "A" domain, and that on the right-hand sides forms a "B" domain.

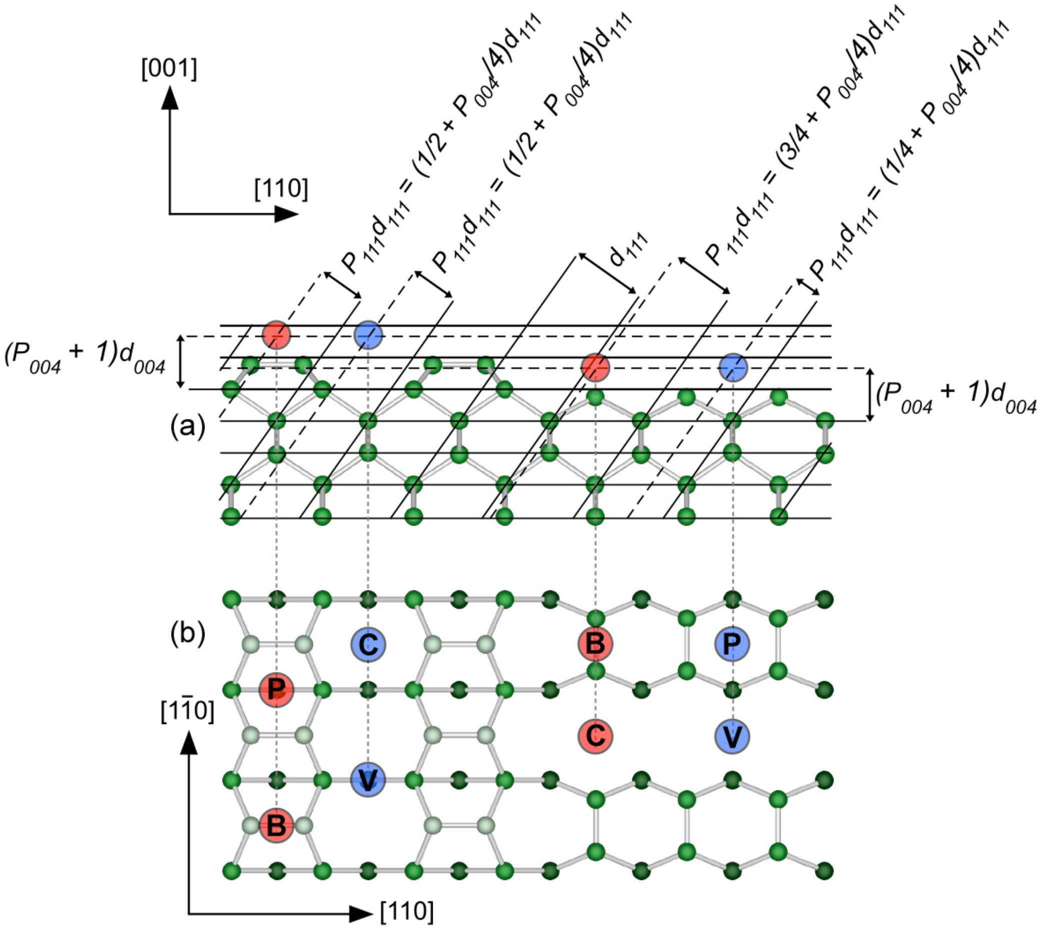

Fig. 3.6. (a) [010] and (b) [001] projections of atoms occupying high symmetry sites on "A" and "B" domains of a dimerized Si(001) surface at heights corresponding to $n = 1$ in Eq. 3.38. The (004) and (022) diffraction planes are drawn as solid lines. The terminating surface on the left-hand sides of both figures forms an "A" domain, and that on the right-hand sides forms a "B" domain.

immediately obvious from examining Table 3.1, the P_{111} value due to cave / bridge site occupancy with $n = 1$ would be the same as that due to valley-bridge / pedestal site occupancy with $n = 0$. In the latter case, S_{111} would simplify to:

$$S_{111} = \frac{1}{2}\exp\left(\frac{\pi i P_{004}}{2}\right)\left[i+1\right], \tag{3.43}$$

and in the former case S_{111} would be:

$$S_{111} = -\frac{1}{2}\exp\left(\frac{\pi i P_{004}}{2}\right)\left[i+1\right]. \tag{3.44}$$

Since Eq. 3.44 is just the negative of Eq. 3.43, and:

$$Arg\left[-X\right] = Arg\left[X\right], \tag{3.45}$$

the P_{111} value computed [using Eq. 3.35] would be the same for both cases.

3.3.3 Resolving Structural Ambiguity of XSW Results

In order to translate XSW results into an atomic-scale model of a particular surface phase, it is necessary to consider information from other experimental techniques such as XPS, STM and X-ray Absorption Fine Structure (XAFS) and/or general knowledge about expected bond-lengths, expected valence configurations, etc.

There are two main reasons for this requirement. The first general reason is the ambiguity inherent in using structural information relative to the bulk-primitive unit cell to describe a surface unit cell that may be significantly larger than the bulk-primitive cell and may be present in multiple orientations relative to the bulk (as demonstrated by the discussion in section 3.3.2). The second reason is that XSW measurements do not provide high-resolution structural information about the substrate atoms in the surface region. Any photoelectric signal originating from substrate surface atoms is typically overwhelmed by the signal (of the same energy) originating from bulk substrate atoms. It is possible to enhance the sensitivity to surface substrate atoms by analyzing only fluorescent photons emitted at very low take-off angles (and thus increasing μ_f in Eq. 3.24), but experimentally, it would not be feasible to collect fluorescence from just a single (top) atomic layer of substrate atoms.

It is often the case that many of the possible arrangements consistent with a particular set of XSW results can be ruled out by comparison with other experimental results and/or consideration of bond lengths and directions. While the previous section has focused on the use of P_H values to triangulate atomic positions, it is also important to note that XSW results are not limited to simply determining atomic positions. They can also reveal other atomic-scale structural information about thermal vibrations and the extent of order vs. disorder via Eqs. (3.31) – (3.33).

CHAPTER 4

Experimental Apparatus

The XSW measurements presented in Chapters 5 – 7 were conducted at the 12ID-D undulator experimental station at Argonne National Laboratory's Advance Photon Source (APS). The X-ray optics and detection equipment used in these experiments are described in Section 4.1. Details of the UHV chamber used at 12ID-D, along with an UHV system used for LEED, AES and XPS measurements at Northwestern University are provided in Section 4.2.

4.1 X-ray Optics and Detection Equipment at APS 12ID-D

A schematic diagram of the X-ray optical components and detectors used at12ID-D are shown in Fig. 4.1. X-rays produced by the undulator source are filtered (to select the X-ray energy to be used for a particular experiment) using a "high heat load," liquid N_2 cooled Si(111) double crystal monochromator. Further narrowing of the energy and angular divergence of the X-ray beam is achieved by passing it through a pair of detuned nondispersive Si channel-cut crystals. For almost all XSW measurements reported in this thesis, the same (hkl) diffraction planes were used for the channel cut crystals and sample, although some Si(022) XSW measurements were made using Si(004) diffraction

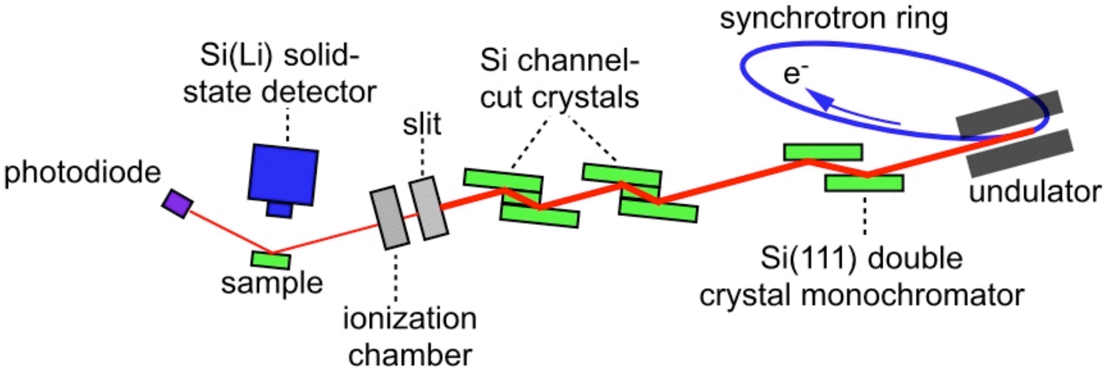

Fig. 4.1. Schematic diagram of experimental setup at APS station 12ID-D. The sample and photodiode are located inside the UHV chamber.

planes for the channel-cuts. Horizontal and vertical slits placed between after the second channel cut define the size of the impinging on the sample. The typical horizontal and vertical slit sizes were ~0.2 mm and ~0.1 mm, respectively. Ionization chambers placed before and after each optical component are used to monitor the X-ray beam intensity.

The second crystal of the Si(111) double crystal monochromator and both of the channel-cut crystals are "detuned" in angle so that the intensity of X-rays diffracted off each of these crystals is lower than the maximum intensity observed when scanning the rocking curve of the diffraction planes. The second crystal of the Si(111) monochromator and the first channel cut crystal are both typically detuned to ~80% of the peak value. Detuning of these crystals is done for stability purposes (it is easier for a feedback loop to "lock on" to the side of a rocking curve rather than the peak) and to reject higher order harmonics diffracted off the first crystal of the Si(111) monochromator. The second channel cut crystal is usually detuned to ~25% so that the angular divergence of the incident beam is significantly smaller than the angular width of the sample rocking curve.

Detuning and stabilization of the monochromator and channel-cut crystals was achieved using monochromator stabilizer (MOSTAB) [121] feedback systems. A MOSTAB control unit accepts the outputs from ionization chambers located immediately upstream and downstream of a particular crystal (a voltage proportional to the synchrotron ring current was used instead of an ionization chamber reading as the upstream signal for the high heat load monochromator). In order to maintain a constant ratio between these two values and consequently keep the crystal at the same point on the rocking curve, the controller adjusts the voltage sent to a piezoelectric actuator that can adjust the crystal angle with sub-microradian resolution.

XSW measurements were performed by scanning single crystal Si(001) substrates in angle through the (004), (022) and (111) rocking curves. During each XSW scan, the diffracted beam intensity was monitored with a photodiode, and the X-ray fluorescence spectra were collected by a single-element Si(Li) solid state detector (Princeton Gamma Tech).

Signals corresponding to detected X-ray events are output from the solid-state detector as sharp voltage increases with ~50 – 100 ns rise times. The magnitude of a particular voltage change is proportional to the energy of the detected photon. The proportionality constant between photon energy and voltage change depended on the pre-amplifier gain setting and was typically 1.5 – 2.0 mV/keV. Two different X-ray pulse processing schemes were used to convert signals output by the solid state detector pre-amplifier into fluorescence spectra like that shown in Fig. 4.3. During some beam times, the pre-amplifier output was sent to an analog spectroscopy amplifier (Tennelec TEC 244). This amplifier converts signals due to individual X-ray events into (0 – 10 V) Gaussian shaped pulses proportional in height to the photon energy. These pulses are then sent to a PCAIII multi-channel analyzer (Oxford / Nucleus) card installed on a Linux PC to be converted into a fluorescence spectrum. During other beam times, the output of the solid state detector pre-amplifier was processed digitally using a DXP-2X unit (X-ray

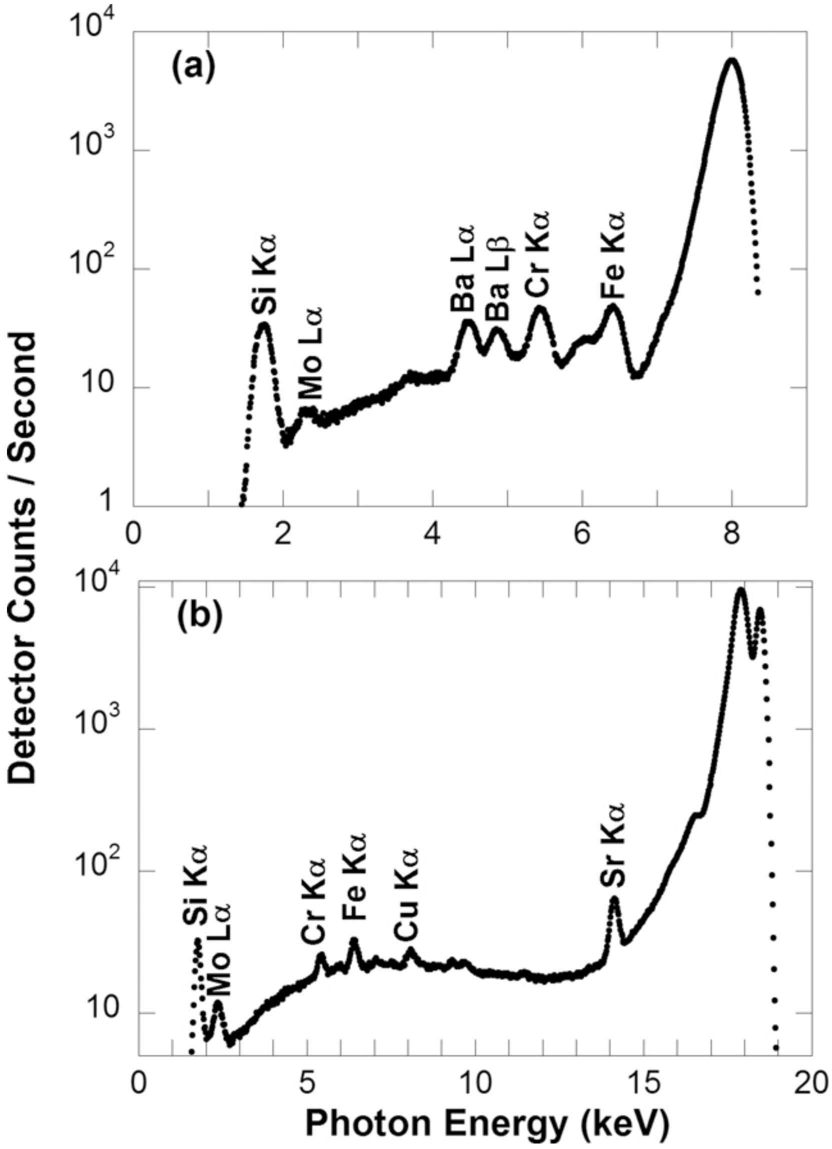

Fig. 4.2. Fluorescence spectra collected from (a) a Sr/Si(001) sample with an incident beam energy of 18.5 keV and (b) a Ba/Si(001) sample with an incident beam energy of 8.0 keV. The Mo, Cr, Fe and Cu are not on the sample. These signals are due to secondary emission from the surrounding chamber and sample-holder hardware. Data collected at 12ID-D.

Instrumentation Analysis) installed on a CAMAC crate. A Labview program called MESA controls and acquires fluorescence spectra from the DXP-2X board.

Overall control and data acquisition of an XSW experiment was carried out using a program called SPEC, installed on the same Linux PC running the PCAIII card or MESA. In addition to controlling motors that move the X-ray optics and diffractometers, SPEC can collect and write data produced by all of the X-ray detection equipment (ionization chambers, solid state detectors, photodiodes, scintillation detectors, etc.) used in an XSW experiment. Data from an XSW measurement is written to files in the form of arrays, with each column corresponding to an angular step in the rocking curve scan and each row corresponding to a channel in the fluorescence spectrum (although the first 20 – 30 rows are typically reserved for scalar data output from other detection equipment).

4.2 UHV Equipment

Two different UHV systems were used in this thesis work. One chamber, located at the APS 12ID-D station, was used to make LEED, AES and XSW measurements on Sr/Si(001) and Ba/Si(001) surfaces. The other chamber, located at Northwestern University (Cook Hall, Room 1008), was used for XPS as well as additional LEED and AES measurements of Sr/Si(001) surfaces.

4.2.1 12ID-D UHV / XSW Chamber

An overhead view diagram of the UHV system at 12ID-D is shown in Fig 4.4. Within this system, there are five different stations where samples can be placed: the introductory “load lock,” the “MBE chamber” used for sample preparation, the storage carousel, the analytical stage used during LEED and AES studies, and the “X-ray chamber” used for the actual XSW measurements. Samples are moved from one station to another (without being removed from the UHV environment) using the radial and rotary motions of a transfer arm in the central “R2P2” chamber (Vacuum Generators LTD). The base pressure of the entire system (except the introductory load lock compartment) is ~1.5 x 10^{-10} Torr.

The MBE chamber is equipped with Knudsen cell sources used for depositing Ba and Sr, a quartz crystal thickness monitor, a leak valve (Varian) for the introduction of high purity gases, and a sample manipulator (Perkin-Elmer) with three translational and one rotational degree of freedom. The resistive tungsten filament heater on this manipulator can heat samples up to ~1000°C. The sample temperature is monitored with an optical pyrometer and also with a K-type thermocouple mounted inside the sample stage.

XSW measurements are performed with the sample sitting in the X-ray chamber which has Be windows that allow X-rays to pass in and out of the chamber. The sample manipulator (Perkin-Elmer) in this chamber has three translational and two rotational

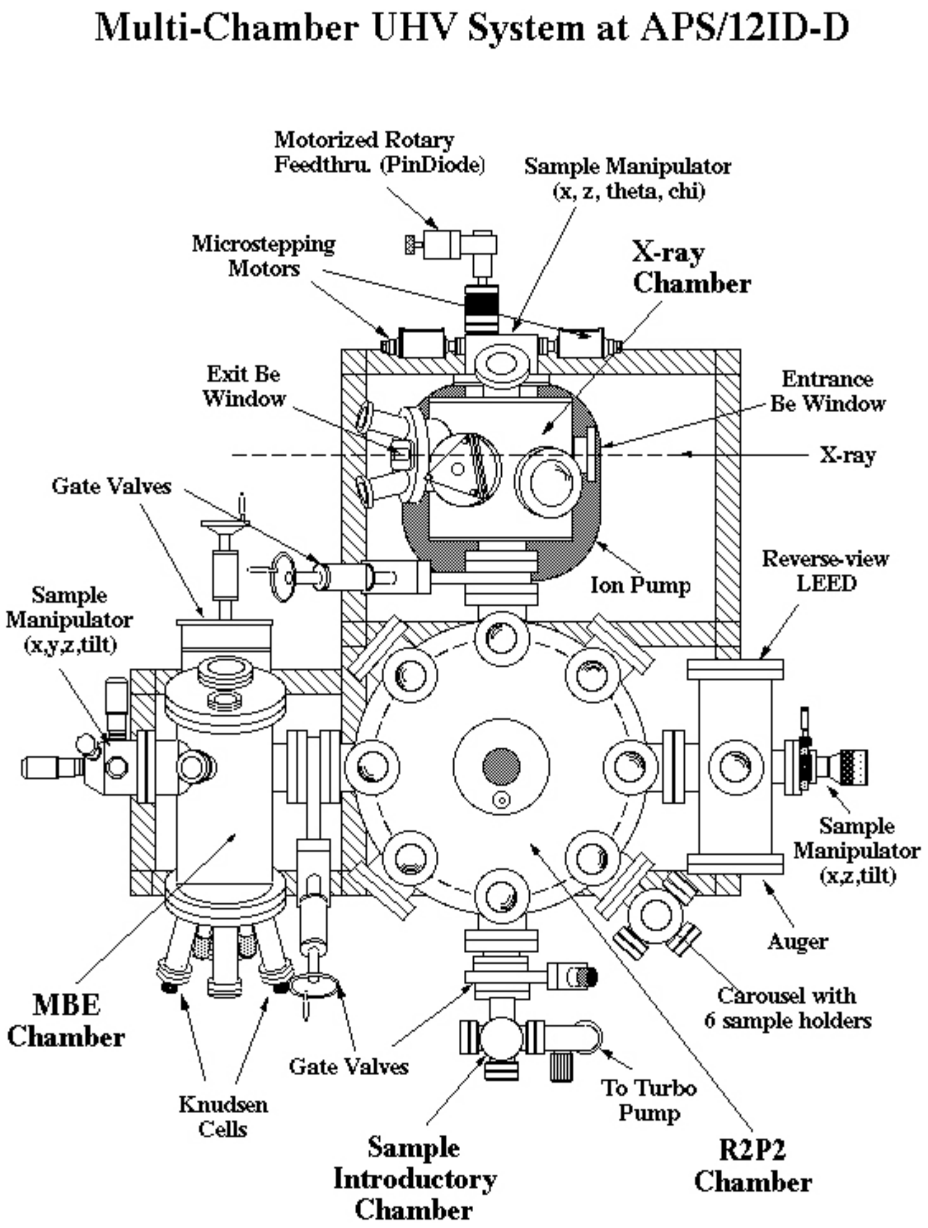

Fig. 4.4. “Top-view” schematic diagram of UHV chamber at APS station 12ID-D.

degrees of freedom. These motions are used to align a sample into the Bragg condition for a particular reflection, but the mechanical accuracy of the manipulator and the rotary feedthroughs that accompany it is insufficient to reproducibly scan through the narrow (on the order of ~10 μrad) rocking curves scanned in a typical single crystal XSW experiment. The rocking curve scans performed during XSW data collection are made by tilting the entire UHV system using the vertical motions of three translational stages mounted beneath the chamber frame. As the sample is scanned in angle, reflectivity of the diffracted beam is monitored using a Si photodiode (Hammamatsu) on a rotary manipulator (Thermionics) located inside the X-ray chamber. X-ray fluorescence is collected by a Si(Li) solid state detector located outside of the chamber. The chamber design allows the solid state detector element to be placed ~2 mm outside of a Be window that is ~20 mm from the sample during data collection.

A sample sitting on the analytical stage can be analyzed using a reverse-view LEED system (PHI) as well as an AES electron gun and analyzer (PHI). These apparatus were used to study the composition and long-range ordering of AEM/Si(001) surfaces. The theory and application of LEED and AES as surface analytical tools are reviewed in Refs. [122] and [123]. A more detailed description of the 12ID-D UHV system is provided in Ref. [124].

Of the two UHV systems used in this thesis work, the chamber at 12ID-D resulted in higher contamination levels (mainly consisting of O in some form) on the surface. One major source of O contamination during some Sr/Si(001) experiments was the Sr

Knudsen cell. It was eventually learned that contamination from this source could be minimized by out gassing the Sr Knudsen cell source for ~5 days at 400 – 450°C. Out gassing for longer times and/or at higher temperatures did not seem to result in any further reduction in the contamination apparently introduced by the Sr source. It is possible that this minimum attainable contamination level was not necessarily due to the Sr source but was instead due to the level of residual gases (namely H_2O) present in the 12ID-D chamber.

4.2.2 Multi-purpose UHV Surface Science System at Northwestern University

A photograph of the Multi-purpose UHV surface science system used for LEED, AES and XPS measurements at Northwestern University is shown in Fig. 4.5. The base pressure of this system, ~5 x 10^{-11} Torr is noticeably lower than that of the UHV chamber at 12ID-D. Sr/Si(001) surfaces prepared in this chamber accumulated contaminants much more slowly than those prepared at 12ID-D.

The UHV system shown in Fig. 4.5 is divided into two sections separated by a gate valve. The chamber on the right hand side of the photograph is equipped with reverse-view LEED (Omicron), an electron gun and cylindrical mirror analyzer (PHI) for AES measurements, Knudsen cell sources, and a quartz crystal thickness monitor. The left-hand side contains a soft X-ray source (Mg $K\alpha$ and Al $K\alpha$) and Hemispherical Analyzer (PHI) for XPS measurements; and a leak valve for introducing molecular O_2. Other equipment (not used in this thesis work) on the chamber includes a STM; an atomic-force microscope (AFM); and a gas “cracker” cell for the introduction of atomic O.

Each of the two sections of this UHV system has a load-lock and magnetic linear transfer arm for sample introduction. One of the transfer arms also allows for a sample to be transferred between the two chambers without being removed from UHV. Each chamber is equipped with a sample manipulator with three translational motions and one rotational axis. These manipulators are equipped with wiring to heat samples “directly” – i.e. by passing current through the sample – and each also has a tungsten filament used for “indirect” heating.

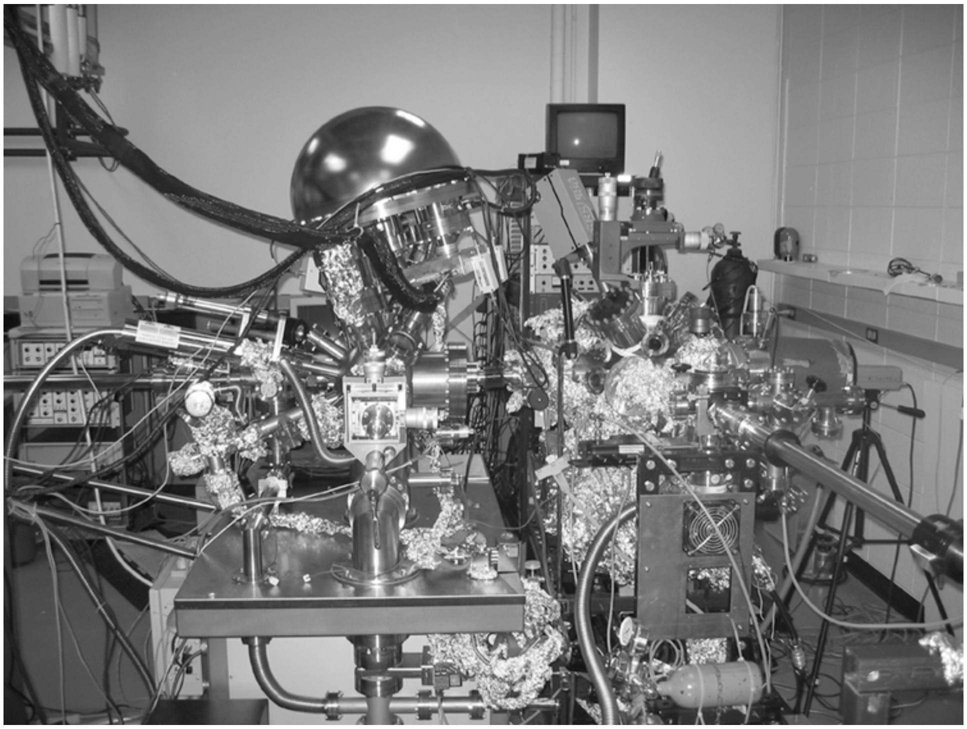

Fig. 4.5. Photograph of UHV system at Northwestern University (Cook Hall, Room 1008).

CHAPTER 5

Studies of Sub-monolayer Surface Phases of Strontium on Si(001)

This chapter discusses XSW, LEED and AES measurements made on Sr/Si(001) surfaces. Experiments performed using the UHV system at the APS station 12ID-D are discussed in Sections 5.1 – 5.3. These sections include results and discussions of XSW measurements made on (2x1), (2x3) and (3x1) Sr/Si(001) surfaces. Results of additional LEED and AES measurements are discussed in Section 5.4.

5.1 Sr/Si(001) Surface Preparation for XSW Studies

XSW measurements of sub-monolayer Sr/Si(001) surfaces were carried out in the 12ID-D UHV/XSW chamber at the APS. Samples were prepared using custom cut single-crystal Si(001) substrates. The Si(001) substrates were first treated ex-situ with a modified version of the Shiraki etch [125]. This wet chemical procedure has been shown to produce a 5 – 8 Å thick SiO_2 layer on the Si surface [125]. This thickness is less than the ~20 Å thickness of a typical Si native oxide. SiO_2 layers grown by the Shiraki etch technique also tend to have significantly less C contamination than conventional Si native oxide layers.

Samples were then mounted in a strain free manner onto Mo sample holders and introduced into the UHV system. After degassing ~12 hours at 400 – 600°C, samples were annealed for 15 minutes at 850 – 900°C to remove the chemically grown SiO_2 film. The maximum chamber pressure observed during these anneals was typically $2x10^{-9}$ Torr, and the pressure remained below $1x10^{-9}$ Torr during most of the anneal time. This procedure resulted in a two-domain (2x1) surface reconstruction as observed by LEED. Auger electron spectroscopy (AES) measurements of the clean Si(001)-(2x1) surface typically showed C and O contamination levels to be less than 0.02 ML.

A Knudsen cell evaporation source was then used to deposit Sr onto the Si(001) substrate. Two different AEM deposition and sample heating schemes were used to prepare Sr/Si(001) surfaces in the 12ID-D chamber. Most samples were prepared by depositing 0.7 – 0.8 ML Sr onto a clean, room-temperature Si(001)-(2x1) surface and subsequently annealing the sample at 700 – 800 °C. Some Sr/Si(001) surfaces were prepared by depositing Sr onto Si(001)-(2x1) surfaces held at elevated temperatures (615 – 715°C).

In the room-temperature deposition process, a Knudsen cell temperature of 353°C was used (resulting in a deposition rate of ~0.07 ML/min). The as-deposited surfaces were then annealed at 700 – 800°C for 1 – 25 min. AES and LEED measurements were made before and after each anneal and revealed that the heat treatments had caused portions of the AEM atom coverage to desorb and had also induced changes in surface periodicity. The Sr coverage was determined in UHV by comparing the intensity of the Sr Kα fluorescence signal from the samples to that of a Sr-implanted Si standard calibrated by RBS.

After Sr deposition onto the room-temperature substrate, samples exhibited (3x1) LEED patterns like that shown in Fig. 5.1(a). The lowest and highest coverages measured for these (3x1) Sr/Si(001) surfaces were 0.67 and 0.78 ML. The possibility of (3x1) phase formation on Sr/Si(001) surfaces at coverages above and below this range was not investigated, so these values are not necessarily limits on the coverage range over which the (3x1) phase can form. All previously reported sub-monolayer Sr/Si(001) surface phases exhibiting long-range order have been prepared by annealing the surface during (or after) at least part of the deposition process. There has been one report of a 7/8 ML (3x1) phase formed by depositing the final 3/8 ML onto RT Si(001), but this process was preceded by the deposition of 1/2 ML Sr onto a Si(001) substrate held at 700°C to form a well-ordered (2x1) phase [30].

Anneals of as-deposited (3x1) Sr/Si(001) surfaces resulted in (2x1) surfaces with Sr coverages ranging from 0.47 ML to 0.57 ML and (2x3) surfaces with Sr coverages ranging from 0.13 ML to 0.24 ML. Table 5.1 summarizes the heat treatments as well as the resulting Sr coverage and surface periodicity for a number of Sr/Si(001) surfaces prepared by depositing Sr onto room-temperature substrates and then annealing. In many cases, a particular Si substrate was annealed multiple times after a single deposition procedure. In Table 5.1, surfaces that were prepared after the same deposition have the same first three characters in their sample name. The final character in the sample name indicates the total number of post-deposition anneals (a = 0, b = 1, and c = 2) that had been performed on a given substrate at the time a particular surface was measured. For

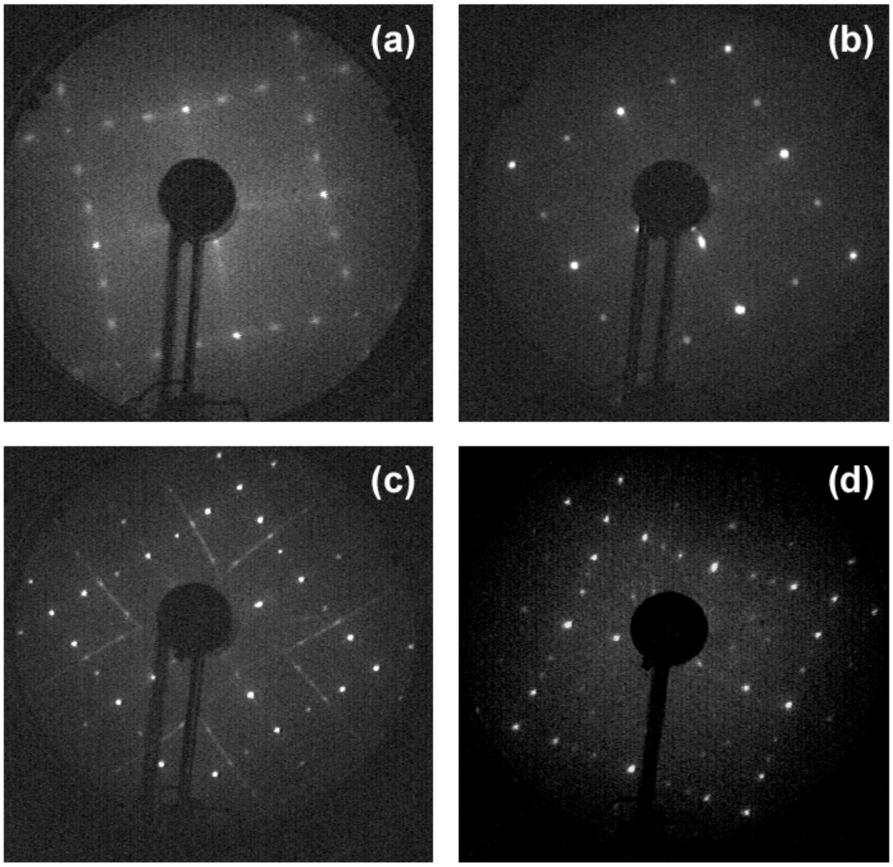

Fig. 5.1 (a) (3x1) LEED pattern observed after depositing 0.78 ML Sr onto room-temperature (2x1) Si(001) surface. (b) (2x1) LEED pattern of surface containing 0.47 ML Sr after annealing a (3x1) surface for 10 minutes at 700°C. (c) (2x3) LEED pattern accompanied by c(2x6) streaks observed on a surface with 0.19 ML Sr after annealing a (3x1) surface for 25 minutes at 750°C. (d) (2x3) LEED pattern surface containing 0.15 ML Sr that resulted after annealing the surface responsible for the pattern in (c) for 2.5 minutes at 800°C. Data collected at 12ID-D.

Sample Name	LEED Pattern	Anneal Temp. °C	Anneal Time (min)	Sr Coverage (ML)	P_{004}	f_{004}	P_{022}	f_{022}
A09a	(3x1)	25	n.a.	0.68	-	-	-	-
A09b	(2x1)	700	10	0.48	0.74(1)	0.46(2)	0.35(1)	0.69(3)
A09c	(2x3)	800	1	0.14	0.87(3)	0.39(4)	0.42(3)	0.59(6)
A11a	(3x1)	25	n.a.	0.67	0.86(2)	0.19(2)	-	-
A11b	(2x3)	750	10	0.24	0.80(1)	0.40(1)	0.37(1)	0.60(5)
B02b	(2x1)	750	1	0.57	0.86(2)	0.26(3)	0.45(2)	0.29(3)
B02d	(2x3)	800	1	0.13	0.86(1)	0.56(2)	-	-
D05a	(2x1)	615[*]	n.a.	0.34	0.82(1)	0.33(2)	0.40(2)	0.38(4)
E02b	(2x3)	750	25	0.19	0.93(3)	0.24(3)	0.53(2)	0.38(2)
E02c	(2x3)	800	2.5	0.15	0.90(2)	0.38(4)	-	-
E03a	(3x1)	25	n.a.	0.79	-	-	-	-
E03b	(2x1)	700	10	0.47	0.89(2)	0.29(3)	0.55(1)	0.32(2)

[*] Since this sample was prepared by depositing Sr directly onto a Si substrate held at 615°C, the heat treatment was not an "anneal" in a strict sense.

Table 5.1. Summary of preparation conditions, LEED pattern, Sr coverage and XSW results of Sr/Si(001) samples studied at 12ID-D.

example, the 0.68 ML (3x1) surface observed after room-temperature deposition onto substrate A09 is referred to as "A09a." The 0.48 ML (2x1) surface observed after this substrate was annealed for 10 minutes at 700°C is referred to as "A09b," and the 0.14 ML (2x3) surface observed after annealing the same substrate for an additional 1 minute at 800°C is referred to as "A09c."

In general, increasing the anneal temperature increased the extent of Sr desorption. The surface periodicity and Sr coverage that remained after annealing an as-deposited (3x1) surface depended on both the temperature and duration of the heat treatment. For example, sample E02b, a 0.19 ML (2x3) surface, was prepared by annealing an as-deposited (3x1) surface for 25 minutes at 750°C. However, annealing another as-deposited (3x1) surface at 750°C for just 1 minute resulted in a (2x1) surface with 0.57 ML Sr (sample B02b).

Figs. 5.1(b) – (d) show LEED patterns measured on three different annealed Sr/Si(001) surfaces. Fig. 5.1(b) shows the (2x1) LEED pattern observed on sample E03b. Figs. 5.2(c) and (d) both show (2x3) LEED patterns. However, the pattern in Fig. 5.2(c) contains streaks passing through the (1, 1/2) spots, but similar streak features are not present in Fig. 5.1(d). The pattern in Fig. 5.1(c) was measured on sample E02b, a 0.19 ML surface produced by annealing an as-deposited (3x1) surface for 25 minutes at 750°C, while the pattern in Fig. 5.1(d) was measured on sample E02c, a 0.15 ML surface that resulted after annealing sample E02b for an additional 2.5 minutes at 800°C. The streaks in Fig. 5.1(c) are similar to features that Hu *et al.* [26] indexed as c(2x6) streaks co-existing with a (2x3) Sr/Si(001) LEED pattern. A number of groups [50; 55-57] have reported the co-existence of sharp c(2x6) diffraction spots with some of the (2x3) LEED patterns of Ba/Si(001) surfaces with Ba coverages between 1/6 ML and 1/3 ML, but the streaky c(2x6) features published by Hu *et al.* constitute the only known report of this periodicity on a Sr/Si(001) surface. The c(2x6) Sr/Si(001) and Ba/Si(001) surface phases are discussed in further detail in Section 5.4.

For the Sr/Si(001) surfaces prepared by depositing onto heated Si, a Sr Knudsen cell temperature of 400°C was used, resulting in a flux of 0.2 ML/min. The (2x1) Si(001) substrate was maintained at a constant temperature (between 600°C and 715°C) while being exposed to the Sr flux. Deposition temperatures between 600°C and 715°C and exposure times ranging from 29 seconds to 244 seconds were used. Following exposure to the Sr flux, samples were annealed at the deposition temperature for an additional 1 – 15 min. The resulting Sr coverage of samples prepared using this method ranged from 0.13 ML to 0.78 ML. Since thermal desorption processes competed with Sr accumulation on the surface, the net amount of Sr coverage depended on the duration of exposure to Sr flux as well as the substrate temperature and post-deposition anneal time.

5.2 Sr/Si(001) XSW Measurements

XSW measurements of samples prepared by both of the deposition schemes described above were performed in UHV using the equipment and methods described in chapter 4. The incident photon energy used for these measurements was 18.5 keV. For a given measurement, the incident beam energy was known to within 0.01 keV, but among different experimental runs (a.k.a. "beam times"), the incident beam energy varied from 18.46 keV to 18.50 keV. Most of the Sr/Si(001) samples studied by XSW were characterized using Si(004) and Si(022) Bragg reflections, although for some samples, only the (004) measurement was made. A Si(111) XSW measurement was made on one sample. The experimentally determined f_H and P_H values along with sample preparation conditions, Sr coverage and LEED periodicity of Sr/Si(001) samples are summarized in Table 5.1

5.2.1 (2x1) Sr/Si(001): Room Temperature Deposition Followed by Annealing

Experimental data and the corresponding theoretical fits from normal Si(004) and off-normal Si(022) XSW measurements of sample B02b, a (2x1) surface with an XRF measured Sr coverage of 0.57 ML, are shown in Fig. 5.2(a) and (b). Assuming the ordered Sr adatoms on this sample occupy only one type of site, then via Eq. 3.38, the experimentally measured $P_{004} = 0.86 \pm 0.02$ indicates that the ordered Sr atoms are located (1.17 Å + nd_{004}) above the ideal bulk plane of second-layer Si atoms. Within the experimental error, the measured P_{022} and P_{004} satisfy Eq. 3.36 which is consistent with ordered Sr atoms occupying bridge or cave sites if $n = even$ and with ordered Sr atoms occupying valley-bridge or pedestal sites if $n = odd$. The XSW measurements alone are consistent with many adsorption geometries of ordered Sr atoms – especially if no upper and/or lower bounds are placed on the possible values of n.

A lower bound of $n = -1$ can be introduced by the assumption that the ordered Sr atoms are not underneath any Si atoms. STM images of ordered sub-monolayer AEM/Si(001) surfaces support this assumption. While this restriction still leaves many possible choices, each particular position (specified by one of the four high symmetry sites and a single value of n) that is consistent with the measured P_{004} and P_{022} would result in a distinct set of Sr-Si bond lengths.

Table 5.2 shows the first and second nearest neighbor AEM-Si bond lengths that would result from Sr atoms occupying each of the high symmetry sites consistent with the Sr coherent positions measured on sample B02b for n = -1, 0, 1 and 2. The Si atomic positions given by Roberts *et al.*'s model for a symmetrically dimerized Si(001)-(2x1) surface [126] are used when calculating the Sr-Si bond lengths in order to approximate the presumably symmetric structure [21; 24] of Si dimers in the Sr/Si(001) surface reconstructions. Since no accommodation was made for the relaxation of Si atoms away from these assumed positions when calculating the bond lengths listed in Table 5.2, these values should only be considered accurate to within 0.2 Å (DFT calculations [44] have predicted that the presence of AEM atoms on Si(001) would cause an increase in the height of top layer Si dimers, and the magnitude of this height change was found to depend on both the in-plane position and total coverage of the AEM atoms).

n	**Site**	**1st n.n. Si [#]: distance (Å)**	**2nd n.n. Si [#]: distance (Å)**
-1	pedestal	[1]: 1.05	[2]: 1.83
-1	valley-bridge	[1]: 1.31	[4]: 2.03
0	bridge	[2]: 1.12	[4]: 2.89
0	cave	[2]: 2.73	[4]: 3.02
1	pedestal	[4]: 2.68	[2]: 3.11
1	valley-bridge	[2]: 3.23	[4]: 3.66
2	bridge	[2]: 3.07	[4]: 4.70
2	cave	[2]: 3.95	[4]: 4.78

Table 5.2 [Coordination number] and distance of first and second nearest-neighbor Si atoms that would result from Sr occupying positions consistent with coherent positions measured on sample B02b.

Both possible positions for *n* = -1 as well as the bridge site for *n* = 0 can immediately be ruled out due to steric hindrance since the nearest neighbor Sr-Si distances for Sr atoms occupying this site would be more than 50% shorter than the 3.2 – 3.4 Å Sr-Si nearest neighbor distances found in bulk Sr-Si compounds [127-134]. The nearest neighbor Sr-

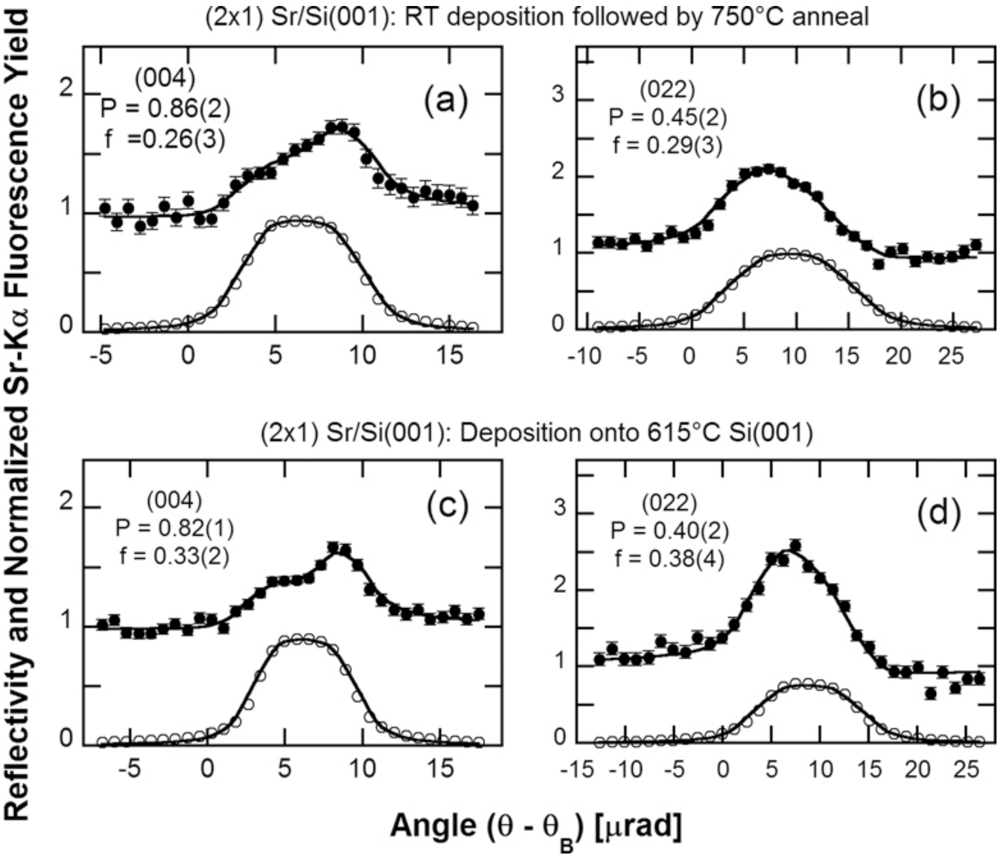

Fig. 5.2. Angular dependence of X-ray reflectivity (open circles) and normalized fluorescence yield (filled circles) data fit to dynamical diffraction theory for (a) Si(004) and (b) XSW Si(022) measurements of a (2x1) surface prepared by depositing Sr onto room-temperature Si and then annealing at 750°C; as well as (c) Si(004) and (d) Si(022) XSW measurements of a (2x1) Sr/Si(001) surface prepared by depositing Sr onto Si(001) held at 615°C. Data collected at 12ID-D.

Si distances for adatoms located at cave sites for $n = 0$ and pedestal sites for $n = 1$ would be 0.5 – 0.7 Å shorter than bulk AEM-Si nearest neighbor distances, and the nearest neighbor distances for cave site occupancy with $n = 2$ would be 0.5 – 0.7 Å longer than typical bulk distances. The distances resulting from any $n > 2$ would be even greater. The only nearest neighbor distance in Table 5.2 that falls within the range of distances observed in bulk compounds is that for valley-bridge site occupancy with $n = 1$. The neighbor Sr-Si distance for bridge site occupancy with $n = 2$ is shorter than the smallest distances reported by ~0.1 Å, but this difference is less than the uncertainty introduced by assuming fixed Si positions. However, if the interaction between the Sr *5s* electrons and the *2p* dangling bonds of dimerized Si atoms possesses a significant amount of covalent character, as many experimental and theoretical studies have suggested [22; 23; 43; 46; 49], then the 42.6° Si – Sr – Si and 68.7° Sr – Si – Si bond angles that would result from bridge site occupancy with $n = 2$ are vastly different from the ideal 180° angle for sp hybridization. Based on these bonding considerations, the most plausible location of the ordered Sr atoms is on the valley-bridge site at a height 2.53 Å above the ideal bulk plane of second layer Si atoms.

Side-view [100] and [110] projections of Sr atoms occupying valley-bridge sites with $n = 1$ and bridge sites with $n = 2$ are shown in Fig. 5.3(a) and (b), respectively. The top-view [001] projection in Fig. 5.3(c) shows Sr atoms occupying all of the valley-bridge sites to form a 1/2 ML (2x1) Sr/Si(001) phase.

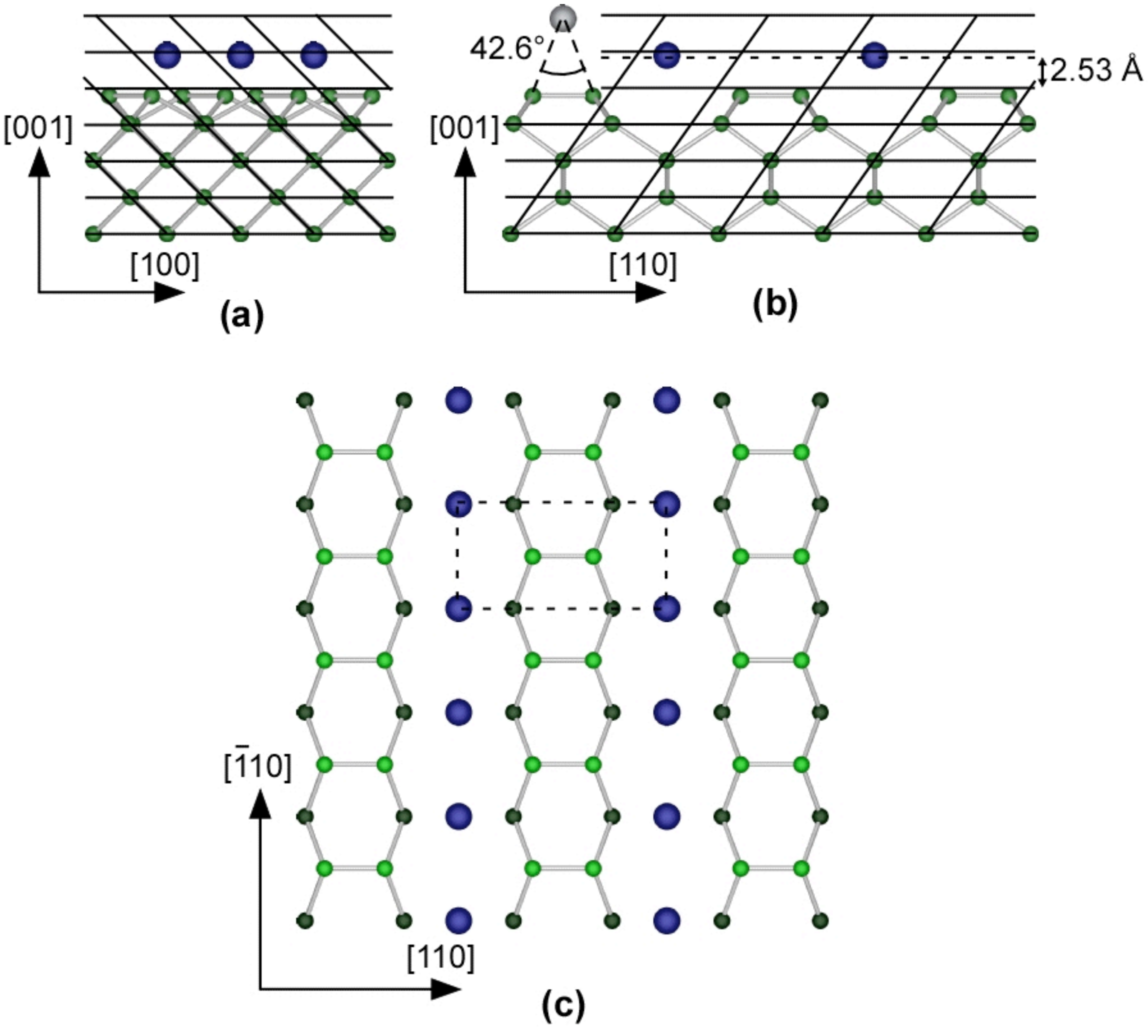

Fig. 5.3. (a) [100] and (b) $[\bar{1}10]$ projections of Sr atoms occupying valley-bridge sites at position consistent with $n = 1$ in Eq. 3.38 and the P_H values determined from data in Figs. 5.2(a) and (b). One Sr atom occupying a bridge site with $n = 2$ is also shown in Fig. 5.3(b). (c) Top-view [001] projection showing AEM atoms at valley-bridge sites to form a 1/2 ML (2x1) phase. The dashed rectangle indicates a (2x1) unit cell.

5.2.2 (2x1) Sr/Si(001): Deposition onto Heated Si

Figs. 5.2(c) and (d) show the experimental data and theoretical fits from Si(004) and Si(022) XSW measurements of sample D05a, a 0.34 ML (2x1) Sr/Si(001) surface prepared by depositing Sr onto a Si(001)-(2x1) surface held at 615°C. The measured coherent positions, $P_{004} = 0.82 \pm 0.01$ and $P_{022} = 0.40 \pm 0.02$, for this surface are in close agreement with Eq. 3.36 (and thus restrict the possible in-plane Sr adsorption configurations to those considered in Table 5.2), but both are ~ 5 – 10% lower than the corresponding P_H values measured on the (2x1) surface B02b (discussed in the previous section) which was prepared by depositing Sr onto room-temperature Si(001)-(2x1) and then annealing. These differences are roughly 2 – 3 times larger than the experimental error, but as indicated in Table 5.1, are actually smaller than the sample-to-sample variation among the P_H values measured for all of the (2x1) Sr/Si(001) surfaces prepared by depositing Sr at room-temperature and then annealing. In Chapter 6, it will be argued that the primary source of these variations is due to variations in the amount of oxygen contamination on different samples. Thus, the marginal differences between the P_H values measured for samples D05a (prepared by depositing onto a heated substrate) and B02b (prepared by depositing onto a room-temperature substrate and then annealing) is not considered to be evidence of any fundamental difference between the position of Sr atoms on (2x1) surfaces prepared by the two different methods.

Sr/Si(001) surfaces used as “template layers” for growing $SrTiO_3$ films on Si are typically formed by depositing Sr onto a heated Si(001) substrate [6; 36]. It has been reported that oxide growth on Sr/Si(001) surfaces prepared by this method results in oxide-Si interfaces that are of higher quality (i.e. have less or no amorphous phase formation at the interface) than the interfaces that are formed when $SrTiO_3$ is grown on Sr/Si(001) surfaces prepared by depositing Sr onto room-temperature Si(001) and then annealing. This observation has led to some claims that the local atomic arrangement of ordered Sr atoms in (2x1) Sr/Si(001) surfaces prepared by depositing onto heated Si(001) differs from that in surfaces prepared by room-temperature deposition followed by annealing [6]. Based on XSW measurements of these two types of surfaces however, it appears that they are equivalent phases. There may be other causes for the differences in the oxide-Si interface and oxide film quality of $SrTiO_3$ films grown on the two types of surfaces. The high-temperature deposition process may facilitate improved control of the actual Sr coverage and the amount of Sr that actually orders into the (2x1) phase. These parameters would presumably affect the quality of a subsequently grown $SrTiO_3$ film.

The Si temperatures that have been used by various groups to form (2x1) Sr/Si(001) phases via a high-temperature deposition process range from 500°C to 800°C. Temperatures near 700°C are used most often [30; 35]. Si(004) XSW measurements were made on a number of (2x1) Sr/Si(001) surfaces prepared by depositing 0.3 – 0.7 ML Sr onto Si(001)-(2x1) surfaces held at temperatures ranging from 690°C to 715°C. The f_{004} values measured on all of these samples were < 0.1. Thus, the main conclusion that can be made from measurements of these samples is that they contained a higher disordered fraction of Sr than other Sr/Si(001) samples. This disorder was most likely due to problems with sample preparation during the particular beam time in which these samples were measured. During the same beam time, a (2x1) Sr/Si(001) surface was also prepared by depositing Sr onto a room-temperature substrate and then annealing. The f_H value measured for this sample was also < 0.1.

5.2.3 (2x3) Sr/Si(001)

Experimental data and the corresponding theoretical fits from normal Si(004) and off-normal Si(022) XSW measurements of a (2x3) Sr/Si(001) surface, sample A09b, are shown in Figs. 5.4(a) and (b). The $P_{004} = 0.87 \pm 0.03$ and $P_{022} = 0.42 \pm 0.03$ measured on this sample are in close agreement with the $P_{004} = 0.86 \pm 0.02$ and $P_{022} = 0.45 \pm 0.02$ measured on sample E03b, the (2x1) Sr/Si(001) surface discussed in section 5.2.1. The similarity between the P_H values measured for these two surfaces provides strong evidence that the ordered fraction of adatoms occupies the same site in the (2x3) and (2x1) Sr/Si(001) surfaces. Based on the Sr-Si bonding considerations in section 5.2.1, this site is most likely the valley-bridge site. While the conclusion that Sr atoms occupy the valley bridge site, with $n = 1$ in Eq. 3.38, must be qualified with several assumptions (that the ordered fraction of Sr atoms occupies a single type of site, that XPS evidence showing that the top layer Si atoms remain dimerized is correct, and that the Sr-Si bond lengths in a surface phase ought to be reasonably close to those found in bulk Sr-Si compounds), the conclusion that Sr occupies the same type of site (whatever that site may

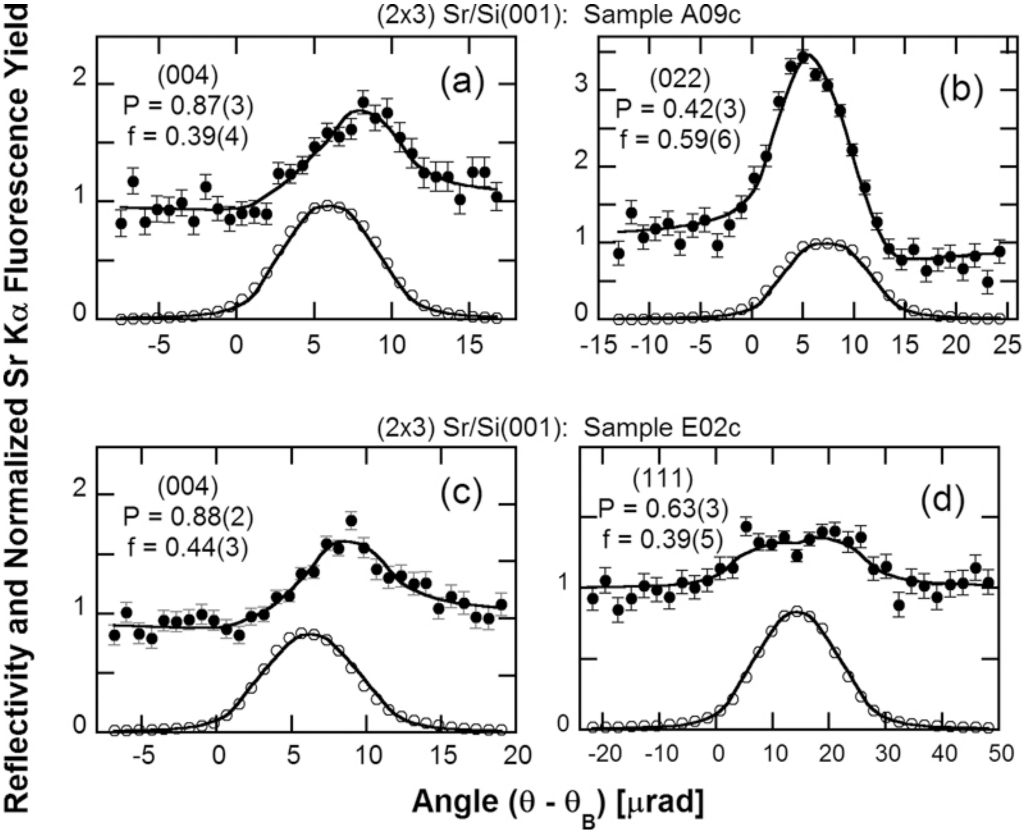

Fig. 5.4. Angular dependence of X-ray reflectivity (open circles) and normalized fluorescence yield (filled circles) data fit to dynamical diffraction theory for (a) Si(004) and (b) XSW Si(022) measurements of sample A09c, a (2x3) Sr/Si(001) surface; as well as well as (c) Si(004) and (d) Si(111) XSW measurements of a sample E02c, another (2x3) Sr/Si(001) surface. Data collected at 12ID-D.

be) in the (2x3) and (2x1) phases is essentially unqualified. It would be a highly unlikely coincidence for the ordered adatoms in each phase to occupy the same 3D position relative to the bulk-primitive unit cell (as the XSW results in Figs. 5.2 and 5.4 demonstrate) but occupy different surface sites in each phase.

Experimental data and the corresponding theoretical fits from normal Si(004) and off-normal Si(111) XSW measurements of another (2x3) Sr/Si(001) surface, sample E02c, are shown in Figs. 5.4(c) and (d). A P_{004} value of 0.88 ± 0.02 was determined for this sample. Using Eqs. (3.30), (3.34), (3.39) and (3.41) the expected P_{111} value for with Sr occupying valley-bridge (or pedestal) sites with $n = 1$ would be 0.60. The measured $P_{111} = 0.63 \pm 0.03$ determined from the data in Fig. 5.4(d) is in close agreement with this expected value. As expected, Sr atoms were triangulated to the same position using a (004) and (111) measurements on sample E03c as they were using (004) and (022) measurements on other (2x3) Sr/Si(001) surfaces.

The top-view [001] projection of the (2x3) Sr/Si(001) surface model in Fig. 5.5 shows AEM atoms occupying 1/3 of the valley-bridge sites for a net Sr coverage of 1/6 ML. Dotted circles are drawn over an additional 1/3 of the valley-bridge sites in this figure. If these sites were also occupied (resulting in a coverage of 1/3 ML), the surface would still exhibit (2x3) periodicity. As discussed in chapter 2, there is some disagreement regarding whether (2x3) Sr/Si(001) and Ba/Si(001) surface phases occur at 1/6 ML (with one AEM atom per unit cell) and/or 1/3 ML (with two AEM atoms per unit cell). XSW results for six different (2x3) Sr/Si(001) surfaces are included in Table 5.1.

The average of the Sr coverage values measured on these samples was 0.17 ± 0.02 ML. While this value is suggestive of the 1/6 ML model with one atom per unit cell shown in Fig. 5.5, it does not provide entirely conclusive evidence that all (or any) (2x3) Sr/Si(001) surfaces have just one Sr atom per unit cell.

There are multiple scenarios in which the local coverage of Sr in the ordered (2x3) phase would not necessarily be equal to the global coverage measured by XRF. A surface exhibiting a (2x3) LEED pattern and a total coverage of 1/6 ML could conceivably have 50% of its area covered by a 1/3 ML (2x3) phase with two Sr atoms per unit cell and have a clean Si(001)-(2x1) reconstruction covering the other 50%. Since all the diffraction spots of a (2x1) LEED pattern coincide with spots in a (2x3) pattern, it is possible that the LEED pattern of a surface with a mixture of (2x1) and (2x3) periodicity could be interpreted as a "pure" (2x3) pattern. Also, it may not necessarily be the case that the local coverage in regions where disordered Sr is present is the same as the local coverage in the ordered phase. It should be noted that the error associated with this average coverage value is due to error associated with the coverage measurement on a given sample as well as differences among the actual coverages of the samples studied since the preparation conditions (anneal time and temperature) varied significantly from sample to sample. The measured Sr coverages on these surfaces ranged from 0.13 ML to 0.24 ML. A global Sr coverage greater than 1/6 ML on a surface with (2x3) periodicity does not necessarily indicate that any (2x3) phase with two atoms per unit cell is present

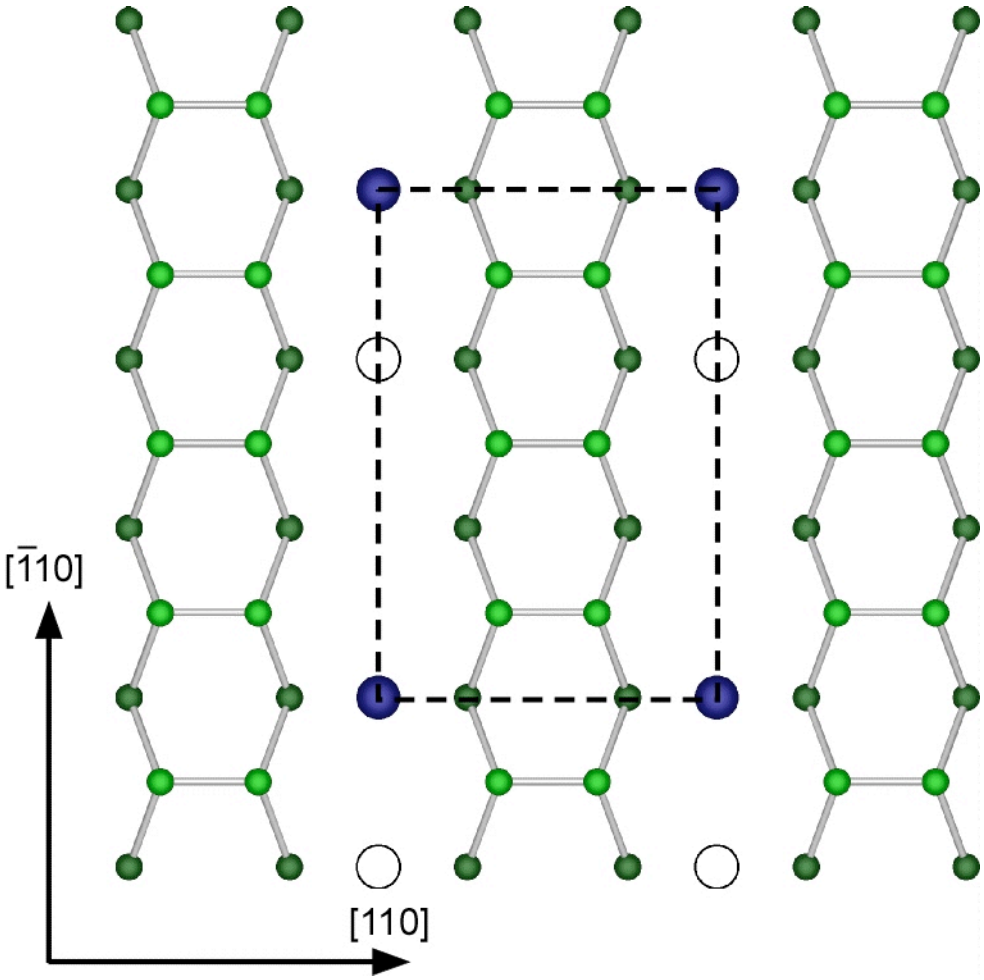

Fig. 5.5. Top-view [001] projection showing AEM atoms at valley-bridge sites to form a 1/6 ML (2x3) phase. The dashed line indicates a (2x3) unit cell. The additional occupation of sites marked with open circles would result in a 2/3 ML (2x3) phase.

since the “excess” Sr could just be part of the disordered fraction. The coverage of (2x3) AEM/Si(001) phases will be discussed further in Section 5.4.2.

The finding that Sr heights in the (2x3) and (2x1) phases are essentially identical position (within ~0.02 Å) is somewhat surprising. A top-layer Si atom adjacent to an occupied valley-bridge site in the (2x3) model shown in Fig. 5.5 would have just one Sr nearest-neighbor. However, every top-layer Si atom in the (2x1) model shown in Fig. 5.3 would have two Sr nearest-neighbors. Thus, the interaction between a particular Sr-Si pair would presumably be weaker in the (2x1) phase than it would be in the (2x3) phase. This difference would be expected to result in some difference between the Sr heights in the two phases. Examination of Table 5.1 reveals that the Sr P_{004} and P_{022} values measured on Sr/Si(001) surfaces did vary from sample-to-sample by as much as ~0.2 for P_{004} and ~0.1 for P_{022}. However, these variations did not correlate with the surface periodicity, but instead, were primarily due to variations in the amount of O contamination on the surface. The effects of O contamination on AEM/Si(001) surfaces will be discussed in Chapters 6 and 7. While a real difference may exist between the height of Sr atoms in the (2x1) and (2x3) phases, it is possible that this difference is small compared to changes in the measured P_H values induced by contamination effects.

5.2.4 (3x1) Sr/Si(001)

Fig. 5.6 shows experimental data and theoretical fits from a Si(004) XSW measurement performed on sample A11a, a 0.67 ML Sr/Si(001) surface exhibiting (3x1) periodicity. Although no Si(004) XSW measurement was made on this sample, the fact that the measured coherent position $P_{004} = 0.86 \pm 0.02$ of this surface is in close agreement with the values measured for (2x1) Sr/Si(001) surfaces is consistent with the DFT calculations of Ashman *et al.* [24]. Models of the stable 1/2 ML (2x1) and 2/3 ML (3x1) Sr/Si(001) surfaces predicted by these calculations are shown in Fig. 5.7. In the predicted (2x1) phase, Sr atoms occupy valley-bridge sites on a dimerized Si(001) surface. In the predicted (3x1) phase, 1/3 of the top layer Si atoms are no longer dimerized. For every Si dimer row along the [110] direction, there is a row of individual (undimerized) Si atoms. Due to this rearrangement of top layer Si atoms, the valley-bridge sites occupied in the (2x1) phase are no longer present, and Sr atoms in the (3x1) phase occupy sites in between rows of dimerized and undimerized Si atoms. Relative to the bulk Si lattice however, the positions of Sr atoms in the predicted (2x1) and (3x1) phases appear to be identical. The XSW data in Figs 5.2 and Fig. 5.6 provides experimental evidence that, at least relative to the bulk Si(004) diffraction planes, ordered Sr atoms are in essentially the same position in the (2x1) and (3x1) phases.

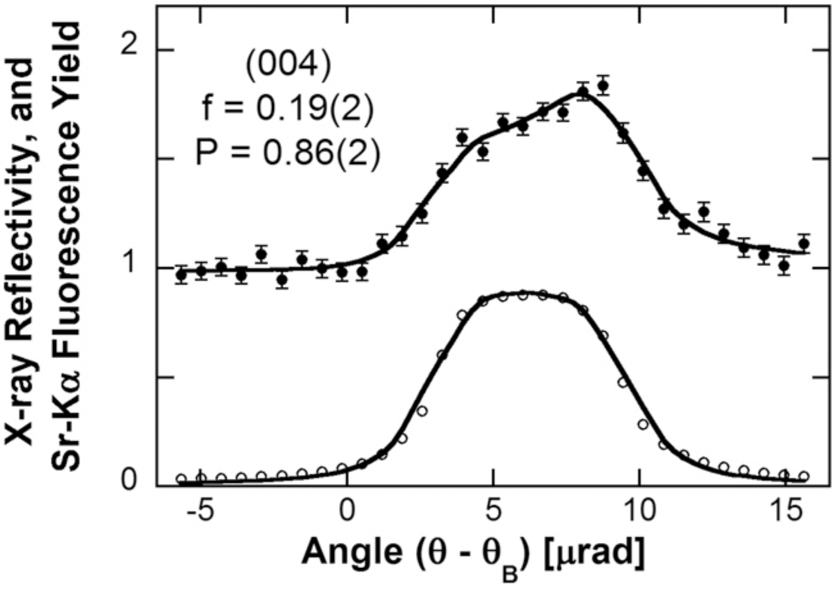

Fig. 5.6. Angular dependence of X-ray reflectivity (open circles) and normalized fluorescence yield (filled circles) data fit to dynamical diffraction theory for Si(004) XSW measurement of a (3x1) Sr/Si(001) surface. Data collected at 12ID-D.

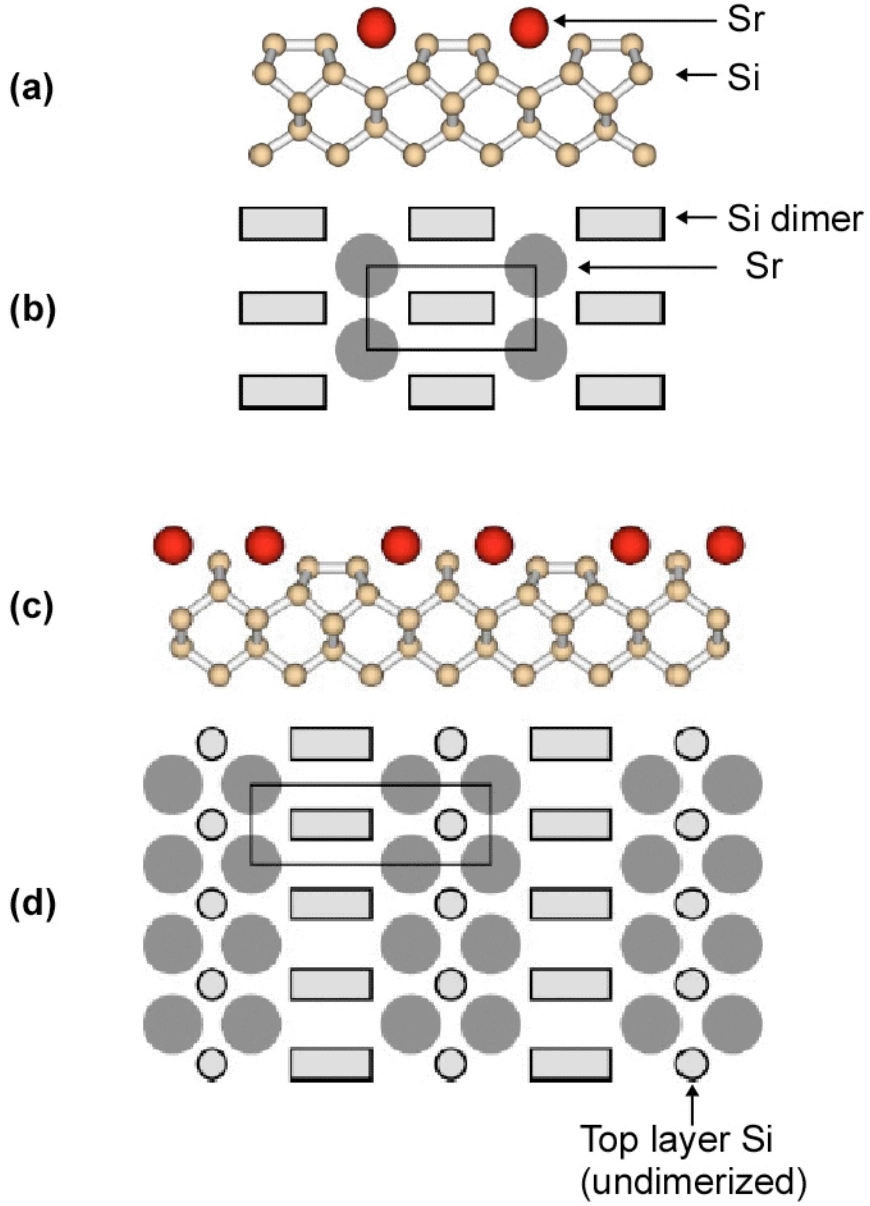

Fig. 5.7. (a) Side-view [110] and (b) top-view [001] projections of 1/2 ML (2x1) Sr/Si(001) phase proposed by Ashman *et al.* (c) Side-view [110] and (d) top-view [001] projections of 2/3 ML (3x1) proposed by the same authors. Figures taken from Ref. [24].

5.3 Coherent Fractions Measured Sr/Si(001) Surfaces

5.3.1 Disordered Fraction

So far, most of the discussion of the XSW measurements of Ba/Si(001) and Sr/Si(001) surfaces has focused on interpreting the coherent positions determined from the XSW data, and little attention has been paid to the coherent fractions. Compared to other metal-on-silicon surface phases studied in the 12ID-D UHV / XSW chamber using surface preparation and characterization methods similar to those employed in this thesis work, the coherent fractions measured for Sr/Si(001) surfaces tend to be rather low.

The low (i.e. $f_{004} = 0.19$) coherent fraction measured for the (3x1) Sr/Si(001) surface prepared by depositing Sr onto room-temperature Si without any subsequent annealing should not be surprising. Due to limited surface diffusion at this temperature, it is understandable that a significant amount of Sr atoms would be unable to “find” a minimum energy adsorption site. The LEED patterns of (3x1) surfaces also indicated that long-range ordering of Sr on these samples was not complete. These patterns tended to have diffraction spots that were more diffuse and backgrounds that were higher than those observed in the LEED patterns of (2x1) and (2x3) Sr/Si(001) surfaces. The XSW measurement of the (3x1) surface phase indicated that short range ordering of Sr was also incomplete.

Somewhat more surprisingly, XSW has also indicated that a significant amount (typically more than half) of the Sr atoms on surfaces exhibiting sharp (2x1), (2x3) LEED patterns can be disordered. This apparent disorder could be due to a variety of causes. It is likely that the presence of various surface defects such as step edges, dimer vacancies and contaminants cause AEM atoms to adsorb onto a variety of different positions (other than those occupied by AEM atoms in the long-range ordered phases) relative to the Si lattice. The comparatively high reactivity of AEM atoms compared to that of most other elements would make Ba and Sr particularly susceptible to becoming "trapped" at various surface defects. It is fairly easy to imagine how a surface defect with an amorphous structure (e.g. regions of amorphous SiO_2 that were not completely removed during the pre-deposition anneal) would cause an XSW measurement to detect a significant disordered fraction. However, some types of defects might cause AEM atoms to occupy particular positions relative to the Si lattice, and thus result in additional terms in the summation in Eq. 3.33. Adatoms occupying such defects can still be thought of as part of the disordered fraction provided that they are distributed relatively evenly among many different types of defects (resulting in many different AEM positions distributed throughout the Si unit cell).

A number of factors appeared to affect the measured f_H. In general, increasing the temperature and/or duration of a post-deposition anneal caused f_{004} and f_{022} to increase. This effect is most likely due to enhanced surface mobility of AEM atoms and possibly to the preferential desorption of disordered adatoms. The measured f_H values tended to decrease with increasing time between surface preparation and the XSW measurement. This apparent deterioration was accompanied by a gradual increase in the amount of oxygen on the surface (as observed by AES) and occurred more rapidly on Ba/Si(001) surfaces than it did on Sr/Si(001) surfaces. A higher rate of deterioration on Ba/Si(001) than on Sr/Si(001) is in some ways consistent with Lettieri *et al.*'s finding [30] that the O_2 partial pressure necessary to fully oxidize Ba deposited onto a quartz crystal microbalance is lower than that necessary to fully oxidize Sr.

5.3.2 Thermal Distribution of Sr in (2x1) and (2x3) Phases

It is noteworthy that for all the samples on which both Si(004) and Si(022) XSW measurements were performed, $f_{022} > f_{004}$. This inequality could be due to differences in the Sr Debye-Waller factors, D_{004} and D_{022}. The ratio of the (004) coherent fraction to the (022) coherent fraction can be expressed as:

$$\frac{f_{004}}{f_{022}} = \frac{C_1 a_{004} D_{004}}{C_2 a_{022} D_{022}}, \tag{5.1}$$

where C_1 and C_2 are the respective ordered fractions at the time the (004) and (022) XSW measurements are made. If the sample does not change (e.g. deteriorate) significantly between the times when the (004) and (022) measurements are performed, it can be assumed that $C_1 = C_2$. If this assumption is made, then for the case of single site occupancy (*i.e.* $a_{004} = a_{022} = 1$) and isotropic thermal vibrations with mean square amplitude $\langle u^2 \rangle$, the ratio f_{004} / f_{022} becomes:

$$\frac{f_{004}}{f_{022}} = \frac{D_{004}}{D_{022}} = \exp\left[2\pi^2\left(\frac{\langle u^2 \rangle}{d_{022}^2} - \frac{\langle u^2 \rangle}{d_{004}^2}\right)\right]. \tag{5.2}$$

This ratio is less than unity since $d_{004} < d_{022}$. In the case of an anisotropic thermal distribution, f_{004} / f_{022} is given by:

$$\frac{f_{004}}{f_{022}} = \frac{D_{004}}{D_{022}} = \exp\left[2\pi^2\left(\frac{\langle u_{022}^2\rangle}{d_{022}^2} - \frac{\langle u_{004}^2\rangle}{d_{004}^2}\right)\right], \tag{5.3}$$

$\langle u_{004}^2\rangle$ and $\langle u_{022}^2\rangle$ are the respective mean square vibration amplitudes parallel to the (004) and (022) diffraction vectors. The ratio given by Eq. 5.3 is even smaller than that of the isotropic case if:

$$\frac{\langle u_{004}^2\rangle}{d_{004}^2} > \frac{\langle u_{022}^2\rangle}{d_{022}^2}. \tag{5.4}$$

While all of the samples that were characterized using both Si(004) and Si(022) XSW measurements satisfied the inequality, $f_{022} > f_{004}$, the ratio f_{004} / f_{022} tended to be significantly higher for (2x1) Sr/Si(001) surfaces than it was for (2x3) Sr/Si(001) surfaces. The average value of f_{004} / f_{022} was 0.83 ± 0.06 for (2x1) Sr/Si(001) surfaces and 0.65 ± 0.02 for (2x3) Sr/Si(001) surfaces. The difference between the observed f_{004} / f_{022} ratios in the two different phases could be due to the thermal distribution of Sr atoms in the (2x3) phase being more elongated along the [001] direction and/or confined along the [011] direction than the distribution in the (2x1) phase.

If XSW measurements using multiple reflections with parallel diffraction vectors [e.g. (004) and (008)] are made, then it is possible to experimentally determine the thermal vibration amplitude of atoms along the direction parallel to the diffraction vectors. While attempts were made to make Si(008) XSW measurements of Sr/Si(001) surfaces, the mechanical stability required of both the x-ray optics and sample to reproducibly scan through the 1.65 μrad width of a Si(008) rocking curve using 18.5 keV x-rays was beyond the limits of the experimental setup at 12ID-D. Although the XSW data collected for Sr/Si(001) surfaces does not contain all of the information necessary to determine the actual values of $\langle u_{004}^2 \rangle$ and $\langle u_{022}^2 \rangle$, fixing f_{004} / f_{022} at a specific value still places a restriction on the relationship between $\langle u_{004}^2 \rangle$ and $\langle u_{022}^2 \rangle$ via the equation:

$$\langle u_{022}^2 \rangle = \frac{d_{022}^2}{d_{004}^2} \langle u_{004}^2 \rangle + \frac{d_{022}^2}{2\pi^2} \ln\left[\frac{f_{004}}{f_{022}}\right] \tag{5.5}$$

which is just a rearranged version of Eq. 5.3.

Assuming that the 50% equal-probability surface of the thermal distribution of ordered Sr atoms takes the form of an ellipse when viewed along the [010] direction, the in-plane mean square vibration amplitude $\langle u_{100}^2 \rangle$ is given by:

$$\langle u_{100}^2 \rangle = \frac{\langle u_{004}^2 \rangle \langle u_{022}^2 \rangle}{2\langle u_{004}^2 \rangle - \langle u_{022}^2 \rangle} \tag{5.6}$$

Fig. 5.8 shows plots of the (100) root mean square (rms) vibration amplitude, u_{100}, as a function of the (004) rms vibration amplitude, u_{004} for two different cases: $f_{004} / f_{022} = 0.83$, the average ratio for (2x1) Sr/Si(001) surfaces; and $f_{004} / f_{022} = 0.65$, the average ratio determined for (2x3) Sr/Si(001) surfaces. Note that:

$$u_H = \left| \sqrt{\langle u_H^2 \rangle} \right|. \tag{5.7}$$

For illustrative purposes, consider u_{004} = 0.22 Å for both $f_{004} / f_{022} = 0.65$ and $f_{004} / f_{022} = 0.83$. In the latter case, u_{100} = 0.29 Å (the in-plane thermal distribution is wider than the out-of-plane distribution), but in the former case, u_{100} = 0.10 Å (the in-plane distribution is narrower than the out-of-plane distribution). Ellipses representing [010] projections of the 50% equal-probability surfaces of the thermal distribution for each of these cases are shown in Fig. 5.9. These projections demonstrate graphically how the lower value of f_{004}/f_{022} observed for the (2x3) Sr/Si(001) surface could correspond to a greater degree of lateral Sr confinement in the (2x3) phase than in the (2x1) phase.

Some physical basis for this apparent difference between the thermal distributions of ordered adatoms in these two phases can be found by considering differences in the restrictions that the symmetry of each phase places on the bonding environment of adatoms occupying valley-bridge sites. STM images of isolated Ba atoms adsorbed onto valley-bridge sites have shown that the four Si surface atoms nearest an occupied valley-bridge site were found to be locked in the “up” position. This constraint determined the tilt direction of surrounding dimers (which would otherwise be oscillating). DFT calculations [36; 43] have found that in addition to affecting the vertical positions of

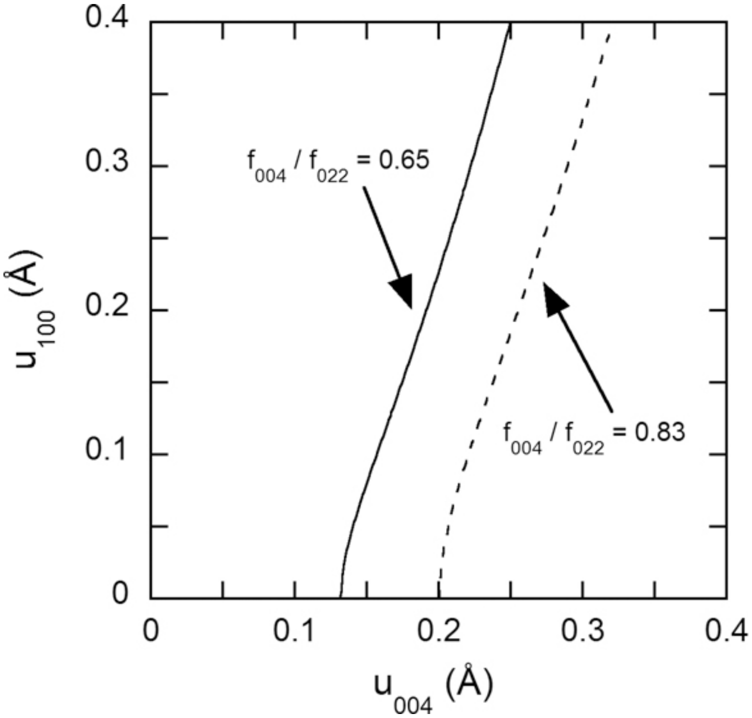

Fig. 5.8 Plots of in-plane thermal vibration amplitude u_{100} as a function of out-of-plane amplitude u_{004} with f_{004}/f_{022} fixed at 0.65, the average f_{004}/f_{022} value measured for (2x3) Sr/Si(001) surfaces; and with f_{004}/f_{022} fixed at 0.83, the average f_{004}/f_{022} value measured for (2x1) Sr/Si(001) surfaces.

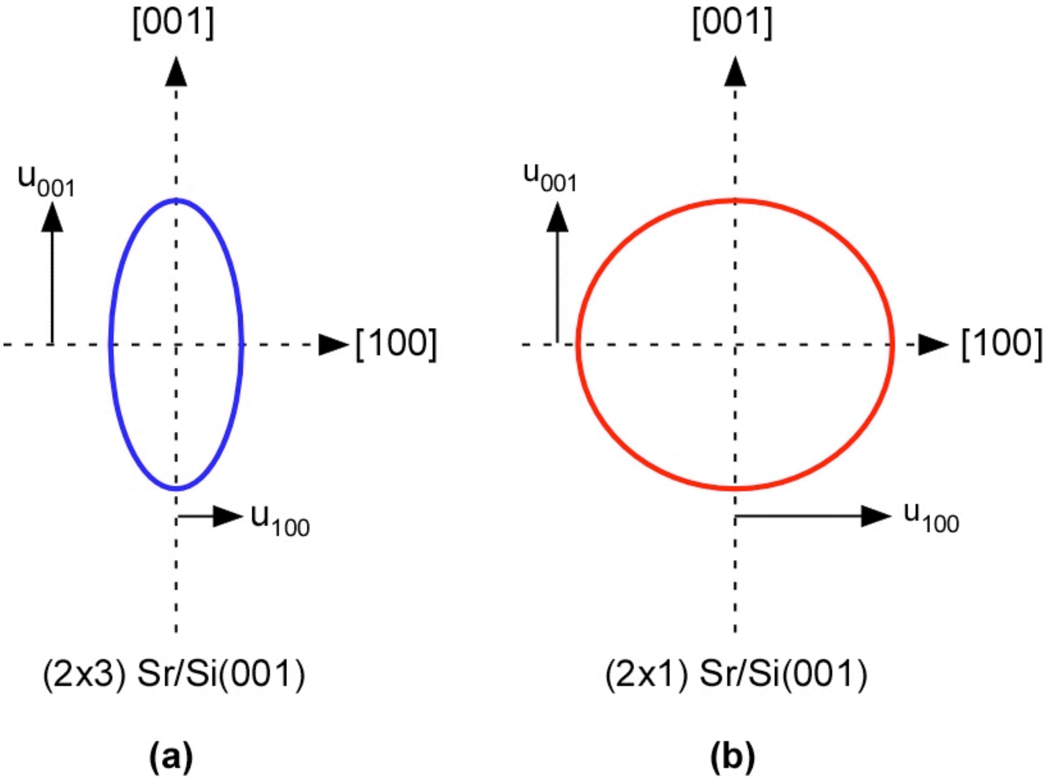

Fig. 5.9. [010] projections of 50% equal probability surface of thermal distribution of Sr that would result if $u_{001} = 0.22$ Å in both the (a) (2x3) and (b) (2x1) Sr/Si(001) surface phases assuming that for the (2x3) phase, the relationship between u_{100} and u_{004} follows the solid curve in Fig. 5.8 and that for the (2x1) phase, u_{100} and u_{004} lie on the dashed curve (Note that $u_{004} = u_{001}$ since u_H is defined as a distance and does not depend on d_H).

surrounding Si surface atoms, attractive forces between Ba and Si would also cause the four top layer Si atoms surrounding the occupied valley-bridge site to be pulled laterally along the [110] and $[1\bar{1}0]$ directions toward the center of the valley-bridge site, as indicated in Fig. 5.10.

Based on the similarities between both the size and electronic configuration of Sr and Ba, it is reasonable to assume that Sr atoms occupying valley-bridge sites would affect surrounding Si atoms in a manner very similar to that observed for Ba. Some experimental and theoretical evidence does support this assumption. STM images of Sr adsorbed onto room-temperature Si(001) in Refs. [22; 23] do appear to show the same type of dimer buckling induced by Ba atoms occupying valley bridge sites, although the authors do not discuss this apparent bucking. DFT calculations of Sr on Si(001) found that a single Sr atom occupying a valley-bridge determined the tilt state of surrounding Si dimers, locking three out of the four nearest neighbor Si atoms into the “up” position. According to these calculations [24], the fourth Si atom would accept all of the Sr valence electrons and the dimer to which this atom belonged would become symmetric, but in a time averaged sense, all four Si nearest neighbors would be in the “up” position because the Sr valence electrons would rapidly move from one Si nearest-neighbor to another. Lateral shifts in the surrounding Si atomic positions toward the center of the occupied valley-bridge sites were not reported in this work, but it appears that these calculations did not consider the possibility of horizontal shifts (other than the Si atom movement that

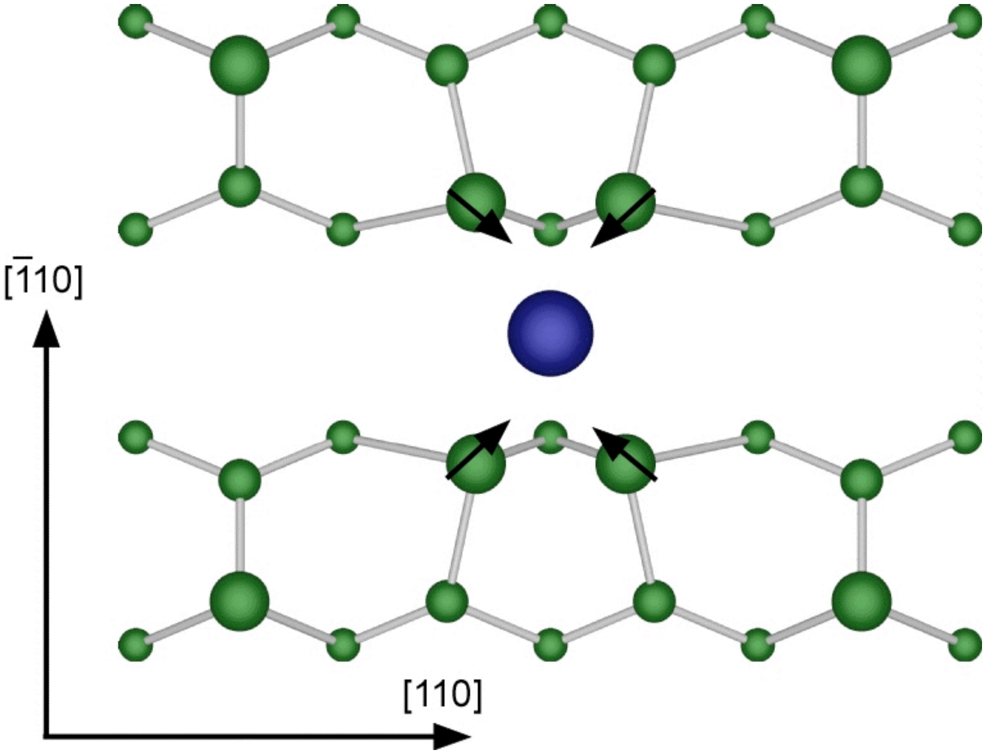

Fig. 5.10. Local Si dimer buckling induced by isolated AEM atom adsorbed at a valley-bridge site. Arrows indicate directions of in-plane shifts (predicted by DFT calculations) of Si atoms toward the center of the occupied valley-bridge site.

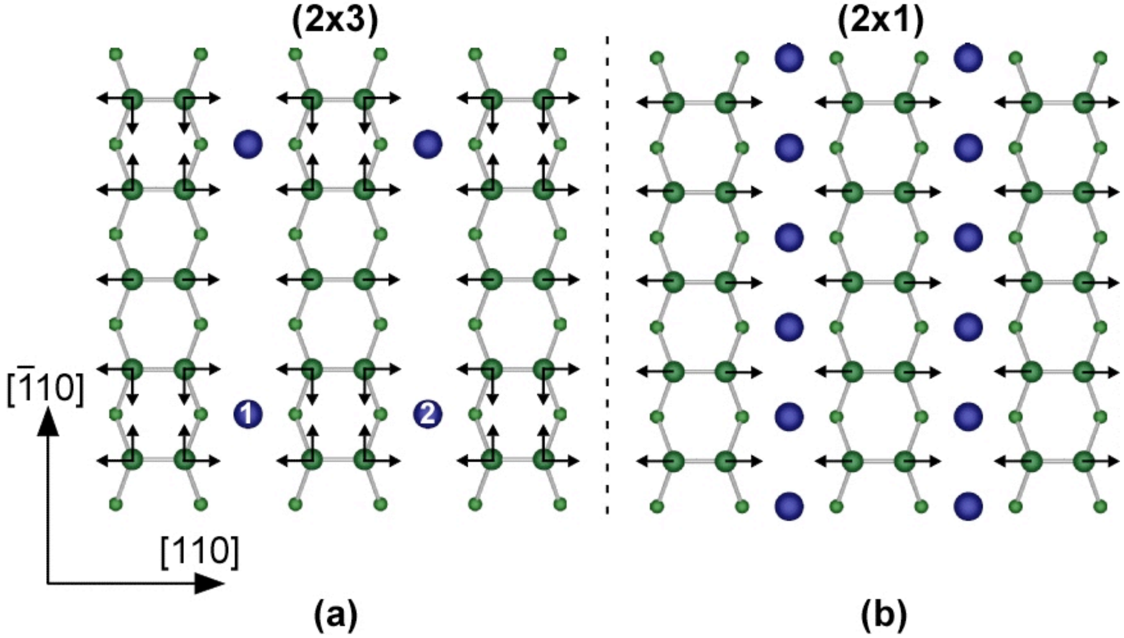

Fig. 5.11. Allowed [110] and [$\bar{1}$10] components of lateral relaxations of top layer Si atoms toward occupied valley bridge sites in (a) 1/6 ML (2x3) and (b) 1/2 ML (2x1) surface phases.

occurs perpendicular to the dimer row direction when any Si dimer – even on a clean Si surface – changes its tilt state).

In a 1/6 ML (2x3) AEM/Si(001) phase, the tilt direction of the dimers surrounding the occupied valley-bridge sites could not be locked into any particular position (other than that of an untilted, symmetric dimer) without reducing the surface symmetry [without changing to something other than (2x3)]. Also, from a bonding point of view, locking these dimers into a particular asymmetric state would not make sense – if the four Si atoms surrounding one occupied valley-bridge site [e.g. the site labeled "1" in Fig. 5.11(a)] were all locked into an up position, then the four Si atoms surrounding an occupied site located ±[110] away from this site [e.g. the site labeled "2" in Fig. 5.11(a)] would necessarily be locked in a "down" position. However, the four Si atoms surrounding an occupied valley-bridge site would be allowed to shift horizontally along the [110] direction (defined perpendicular to the dimer rows in Fig 5.11) as well as the $[\bar{1}10]$ direction (defined parallel to the dimer rows in Fig. 5.11) without reducing the surface symmetry. Si atoms adjacent to an unoccupied valley-bridge site in the (2x3) phase would only be allowed to shift perpendicular to the dimer rows. The directions in which each top layer Si atom in a (2x3) Sr/Si(001) phase would be allowed to shift are indicated by arrows in Fig. 5.11(a). The two Si atoms in a given dimer would need to move by equal amounts in the same direction for shifts parallel to the dimer rows and would be required to move by equal amounts in opposite directions for shifts perpendicular to the dimer rows. Out-of-plane shifts would also be allowed provided that the dimers remain symmetric.

In a 1/2 ML (2x1) AEM/Si(001) phase with AEM atoms occupying all of the valley-bridge sites, top-layer Si atomic position shifts along the dimer row direction (as well as locking of dimers into any particular asymmetric state) could not occur without reducing the surface symmetry. Again, from a bonding perspective, these symmetry breaking shifts would be unreasonable – movement of a top layer Si atom along the dimer row direction would move that Si atom closer to one of its AEM nearest-neighbors, but would also move it further from its other AEM nearest neighbor (and since neither group II nor group IV elements have any *d-shell* valence electrons, crystal field splitting would not be expected for AEM-Si bonding). For the 1/2 ML (2x1) phase, only vertical shifts of the top layer Si atoms and changes in the Si dimer bond length would be allowed. The allowed shifts of top layer Si atoms in a (2x1) Sr/Si(001) phase are indicated by arrows in Fig. 5.11(b).

It is likely that relaxation of top-layer Si atoms toward the center of a valley-bridge site occupied by an AEM atom could place considerable restrictions on the in-plane thermal motion of the AEM atom occupying that site. Since top layer Si atoms in the 1/2 ML (2x1) phase have considerably less freedom in their ability to move toward the center of an occupied valley-bridge site than that possessed by top layer Si atoms in the 1/6 ML (2x3) phase, it is reasonable that in-plane confinement of the thermal distribution of AEM atoms would be more pronounced for the 1/6 ML (2x3) phase than it would be for the 1/2 ML (2x1) phase. This effect would explain why the observed value of f_{004} / f_{022} tended to be larger for (2x1) Sr/Si(001) surfaces than it was for (2x3) Sr/Si(001) surfaces.

While the f_H values measured for Sr/Si(001) surfaces are qualitatively consistent with the proposal that there is a significant difference between the shapes of the Sr thermal distributions in the (2x3) and (2x1) Sr/Si(001) phases, a certain amount of caution needs to be used when considering these results quantitatively. A change of ~0.1 in the ratio of two f_H values would cause the x-axis intercepts of the plots in Fig. 5.8 to change by a similar amount. An overestimation of f_{004}/f_{022} would cause the curves plotted in Fig. 5.8 to shift to lower values of u_{004}, while an underestimation would have the opposite effect. Since the $\frac{du_{100}}{du_{001}} > 1$, such shifts in the intercept would cause even greater changes in the out-of-plane vibration amplitude expected for a given value of u_{004}.

There are a number of sources of error in the f_{004} / f_{022} ratios used to plot the curves in Fig. 5.8. Each measured f_H value is subject to error due to (fluorescence) counting statistics as well as some uncertainty in the appropriate asymmetry factor, *b*, to use when fitting the rocking curve reflectivity to Eqs. 3.14 and 3.18. Systematic errors are possible if the assumptions that the ordered fraction occupies only one site (i.e. $a_{004} = a_{022} = 1$) and that a sample does not deteriorate over time (i.e. $C_1 = C_2$) are not entirely valid. For the samples studied in this work, any breakdown in the first of these approximations generally resulted in $a_{004} < a_{022}$, and consequently caused an underestimation of f_{004} / f_{022}. On most samples, the Si(022) XSW measurement was performed after the Si(004), so a breakdown in the latter approximation tended to result in an overestimation of f_{004} / f_{022}. Examples of each of these cases will be provided in Chapters 6 and 7.

5.4 Additional Investigations of Sr/Si(001) Surface Phases

5.4.1 Surface Preparation

Additional investigations of Sr/Si(001) surfaces were carried out in the MBE surface science chamber described in Section 4.2.2. Samples for this work were prepared on ~7mm x 12mm pieces of 300μm thick n-type (P doped) Si(001) wafers (Virginia Semiconductor) with resistivities of 0.034 – 0.040 Ω-cm. Samples were sonicated in acetone and methanol, rinsed with deionized water and blown dry with dry N_2 prior to introduction into the UHV chamber.

Heating of these samples was achieved by passing current directly through the Si. Samples were degassed for ~12 hours at 600°C and then annealed for 15 minutes at 1200°C. The maximum chamber pressure observed during these anneals was $6x10^{-10}$ Torr. The resulting surface exhibited a (2x1) LEED pattern and had C and O contamination levels that were undetectable by AES. The Shiraki etch used to pre-treat Si(001) substrates studied in the 12ID-D UHV chamber was not necessary for preparing clean Si(001)-(2x1) surfaces in the NU MBE chamber because the 1200°C anneal temperature was sufficient to remove both SiO_2 and SiC from the Si(001) surface.

With the clean Si(001)-(2x1) surface at room-temperature, Sr was then deposited at a deposition rate of ~0.051 ML/min from a Knudsen cell source set to a nominal temperature of 400°C. The sample then underwent a series of 15 minute anneals at temperatures between 600°C and 820°C. The temperature used for a given anneal was always higher than the temperature of the preceding anneal. The surface was measured with LEED and AES after each anneal.

The C contamination levels of these surfaces were undetectable by AES throughout the characterization process. O contamination levels were also below the detectable limit of AES on most of these surfaces. The O contamination on the few samples that did have a detectable amount was always less than 0.02 ML.

5.4.2 LEED and AES Results

The (2x1) LEED pattern observed for a clean Si(001) surface after annealing at 1200°C in the NU MBE chamber is shown in Fig. 5.12(a). The LEED pattern in Fig. 5.12(b) showing no diffraction spots was taken after depositing ~5 ML Sr onto the room-temperature Si(001)-(2x1) surface. Figs. 5.12(c) – (i) show LEED images taken after annealing this sample at temperatures between 500°C and 680°C. LEED images taken after annealing the same sample at temperatures between 695°C and 832°C are shown in Figs. 5.13 (a) – (j). The duration of each anneal was 15 minutes. A plot of the ratio of the Sr_{MNN}:Si_{LMM} peak-to-peak AES intensities as a function of anneal temperature

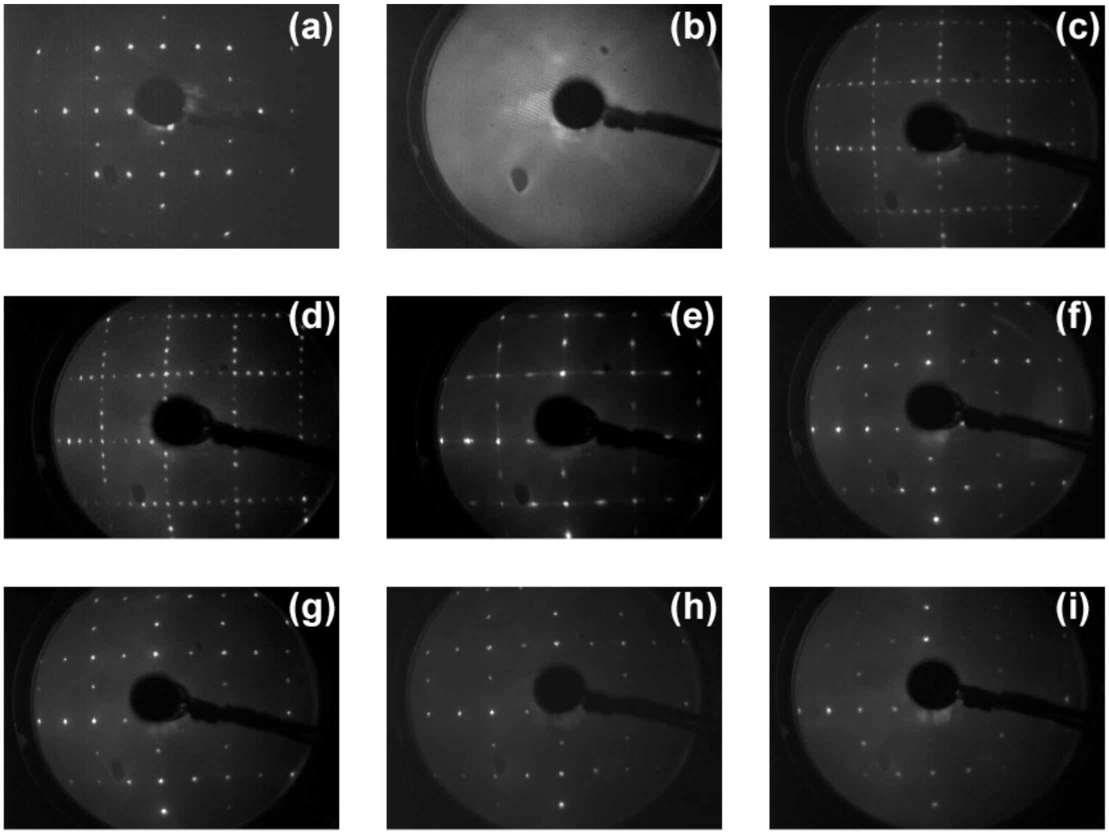

Fig. 5.12. LEED patterns of (a) clean (2x1) Si(001); (b) ~5 ML Sr deposited onto a clean (2x1) Si(001) surface held at room-temperature; (c) and (d) (5x1) Sr/Si(001) surfaces that resulted after annealing at 500°C and 565°C, respectively; and (e) – (i) (2x1) Sr/Si(001) surfaces produced by annealing at 607°C, 623°C, 643°C, 661°C and 677°C. The Sr coverages measured on the surfaces responsible for patterns (c) – (i) are indicated in the plot in Fig. 5.14. Data collected at Northwestern multi-purpose surface science chamber.

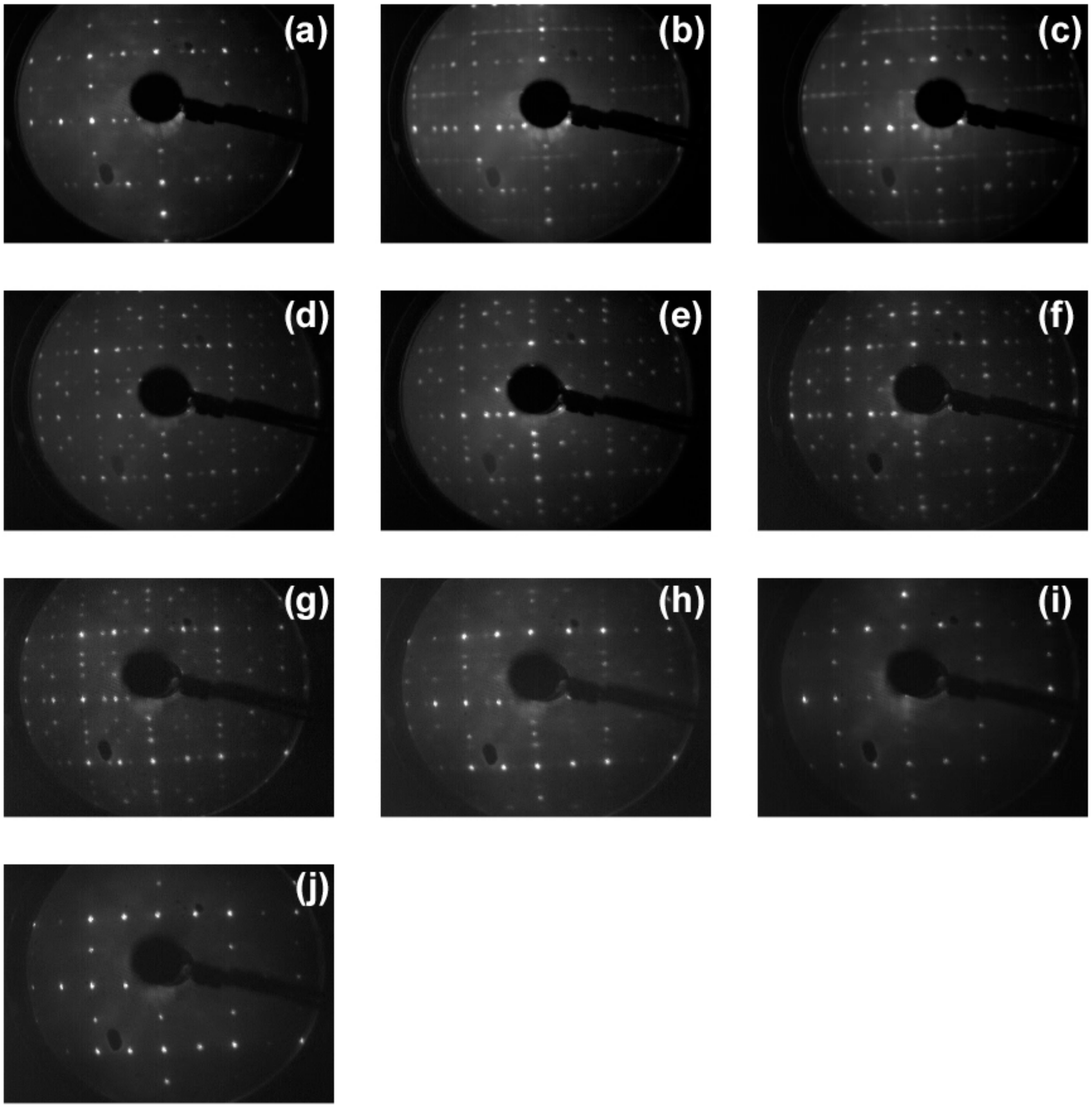

Fig. 5.13. LEED patterns of (a) (2x1) + (2x3) surface produced by annealing at 695°C; (b), (c) (2x3) + c(2x6) surfaces that resulted from annealing at 714°C and 730°C; (d) – (g) (2x3) surfaces observed after annealing at 745°C, 760°C, 775°C and 789°C; (h) mixed (2x3) Sr/Si(001) + clean (2x1) Si(001) surface produced by annealing at 806°C; (i) and (j) clean (2x1) Si(001) surfaces that resulted after annealing at 818°C and 831°C. The Sr coverages measured on all of these surfaces are indicated in Fig. 5.13(b). Data collected at Northwestern multi-purpose UHV surface science chamber.

(ranging from 25°C to 832°C) is shown in Fig. 5.14(a), and an enlarged version of this plot showing only the AES ratios measured for anneal temperatures between 500°C and 832°C is shown in Fig. 5.14(b). The y-axis in Fig. 5.14(b) is also labeled in coverage units (ML). The scale of this axis was determined by comparing the $\mathrm{Sr_{MNN}}$:$\mathrm{Si_{LMM}}$ ratios to the Sr coverage determined by XRF on samples that were measured with both AES and XRF. The decrease in Sr coverage with increasing anneal temperature is due to thermal desorption.

The type of symbol used for the data point at a given temperature and coverage in Fig. 5.14(b) corresponds to the LEED periodicity observed after annealing at that temperature. The type of symbol used to represent each of the observed LEED periodicities is indicated in the figure legend. Two different types of symbols are used to represent a (2x1) LEED pattern. One type is used for the Sr/Si(001)-(2x1) LEED pattern observed after annealing at temperatures between 600°C and 680°C, and another type is used for the clean Si(001)-(2x1) surface observed after annealing at temperatures above 810°C. No Sr remained on the surface after annealing above this latter temperature. Two different types of symbols are also used to represent a mixed (2x3) + (2x1) LEED pattern. One type is used for the pattern observed after annealing at 695°C. This temperature is higher than the anneal temperatures that resulted in pure Sr/Si(001)-(2x1) LEED patterns and is lower than those that produced (2x3) + c(2x6) patterns. Another type of symbol is used to represent the (2x3) + (2x1) LEED pattern observed at an anneal temperature above those resulting a pure Sr/Si(001)-(2x3) pattern and below the

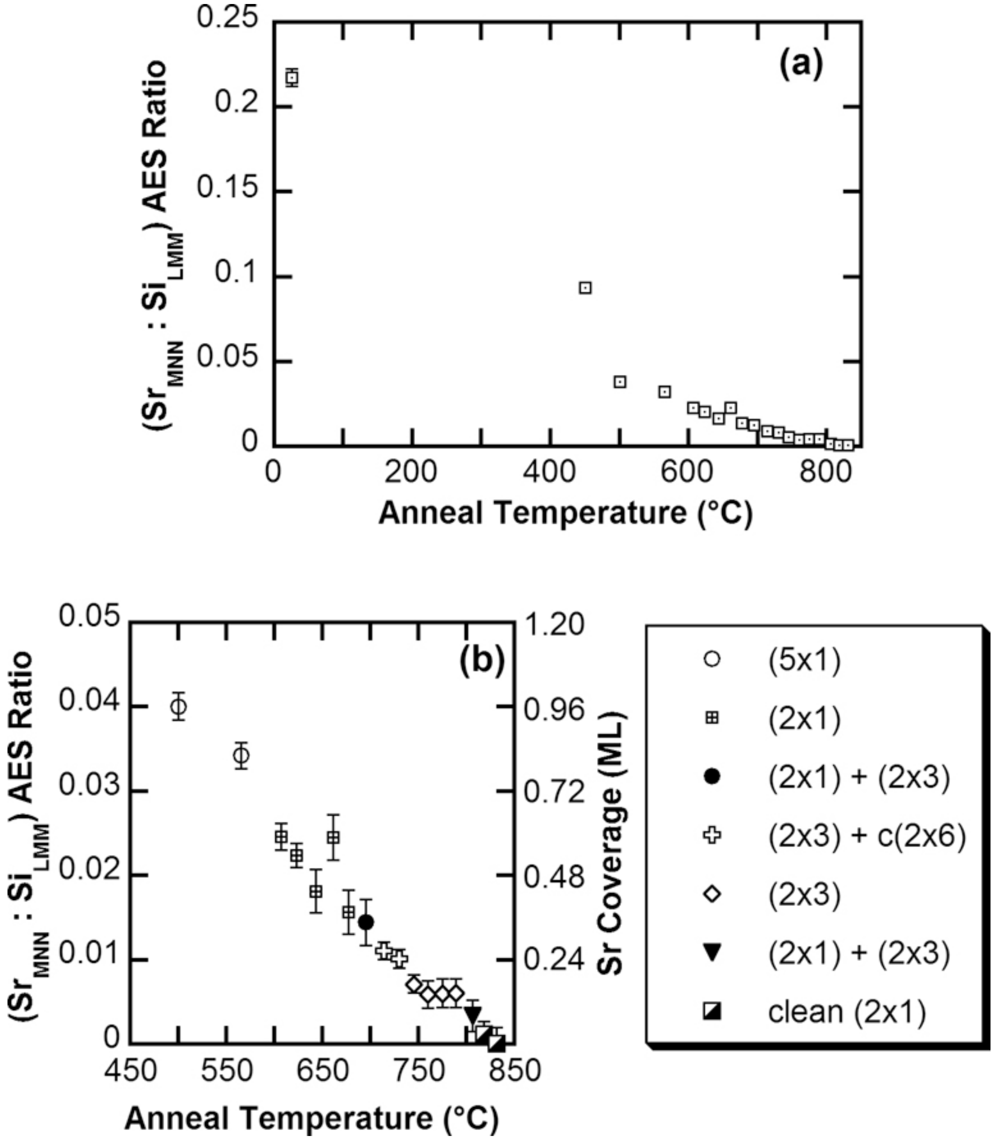

Fig. 5.14. Sr_{MNN}:Si_{LMM} AES ratio plotted as a function of anneal temperatures ranging from (a) room-temperature to 820°C and (b) 450°C to 820°C. Data collected at Northwestern multi-purpose UHV surface science chamber.

minimum temperature necessary to completely desorb all remaining Sr.

Figs. 5.11(c) and (d) show the (5x1) LEED patterns observed after annealing the sample at 500°C and 565°C. The respective coverages measured for these surfaces were 0.97 ML and 0.83 ML respectively. DFT calculations performed by Ashman *et al.* [24] predicted a stable (5x1) Sr/Si(001) surface with a coverage of 4/5 ML. Hu *et al.* [26] and Fan *et al.* [25] both observed (5x1) Sr/Si(001) LEED patterns after depositing Sr onto room-temperature Si(001) and then annealing at temperatures between 600°C and 750°C. The coverage range reported for these (5x1) surfaces was 1.0 – 1.5 ML. The discrepancy between the 600°C – 750°C anneal temperatures used by these authors to produce the (5x1) phase and the 500°C – 565°C anneals used in the present work is likely due to differences in the duration of the anneals. Fan *et al.*'s post-deposition anneals lasted 1 minute, while 15 minute anneals were employed to produce the (5x1) LEED patterns in Figs. 5.11(c) and (d). Also, as mentioned in Chapter 2, the Sr coverage values reported by Fan *et al.* corresponded to the amount of Sr deposited prior to annealing and did not account for thermal desorption of Sr.

Section 5.2.4 described the results of XSW measurements of a (3x1) surface that resulted after depositing 0.67 ML Sr onto a room temperature Si(001)-(2x1) surface. The fact that no (3x1) phase was observed among the series of LEED patterns in Figs. 5.12 and 5.13 may simply be due to the fact that none of the post-deposition anneals used to produce these surfaces resulted in a Sr coverage at which the presence of a significant amount the (3x1) phase is stable. The amount of Sr (> 5 ML) deposited was much greater than Sr coverages at which (3x1) periodicity has been reported, and the lower coverages that resulted after post-deposition anneals may have "skipped over" any coverage range that would have resulted in a (3x1) phase. If the (3x1) phase responsible for the LEED pattern in Fig. 5.1(a) is the 2/3 ML (3x1) phase predicted by Ashman *et al.*'s DFT calculations [24], the 0.82 ML Sr coverage measured after annealing at 565°C and the 0.59 ML measured after the subsequent anneal (607°C) may have been above and below the coverage range for stable (3x1) phase formation. The presence of faint streaks passing through both the integer and half-order spots of the (2x1) pattern in Fig. 5.12(e) could be due to the presence of small regions of a (3x1) phase, but could also be due to (5x1) and/or other (*n* x 1) phases.

Surfaces exhibiting the (2x1) LEED patterns in Figs. 5.12(e) – (i) had Sr coverages ranging from 0.60 ML down to 0.38 ML. This range is consistent with the (2x1) phase having a local coverage of 1/2 ML. The LEED pattern in Fig. 5.13(a) shows (2x1) spots along with comparatively weak (2x3) spots. The 695°C anneal temperature that resulted in the 0.35 ML surface responsible for this mixed (2x1) + (2x3) pattern is significantly lower than the 800 – 850°C anneal temperatures previously reported as the minimum temperatures necessary to form the (2x3) Sr/Si(001) surface phase after depositing Sr onto room-temperature Si(001). This discrepancy, like the differences in minimum temperatures reported for (5x1) phase formation, is likely due to differences in the durations of anneals.

Figs. 5.13(b) and (c) show mixed c(2x6) + (2x3) LEED patterns. Unlike the streaks in Fig. 5.1(c) [and similar streaks accompanying a (2x3) LEED pattern reported Hu *et al.*] that were attributed to a small fraction of the surface exhibiting c(2x6) periodicity, the c(2x6) features in Figs. 5.13(b) and (c) are comparatively sharp diffraction spots. The diagram in Fig. 5.15 shows which spots in a c(2x6) + (2x3) LEED pattern are due to c(2x6) periodicity and which are due to (2x3) periodicity. Based on the relative intensities of spots due exclusively to c(2x6) and those due exclusively to (2x3) periodicity in Figs. 5.13(b) and (c), it appears that the c(2x6) + (2x3) surfaces had comparable amounts of each phase.

LEED patterns of Sr/Si(001) surfaces exhibiting pure (2x3) periodicity are shown in Figs. 5.13(d) – (g). The data points corresponding to these surface in the anneal temperature vs. coverage plot in Fig. 5.14 form a plateau near 1/6 ML in coverage and 760 – 790°C in temperature. This plateau supports the McKee *et al.*'s claim [31] that the (2x3) phase is a stoichiometric line compound as shown in the proposed phase diagram in Fig. 2.5(c). This proposed phase diagram also shows (2x1) and (3x1) phases as line compounds at respective coverages of 1/4 ML and 5/8 ML.

As mentioned in Chapter 2, the local Sr coverage in a (2x1) Sr/Si(001) phase must be at least 1/2 ML because the areal number density of (2x1) unit cells is 1/2 ML (with the units on the definition of 1 ML in Section 2.2.2 changed from *atoms*□*nm*$^{-2}$ to *unit cells·nm*$^{-2}$). The fact that the data points corresponding to the (2x1) phase in Fig. 5.14 do not appear to form a plateau similar to that observed for the (2x3) phase suggests that the

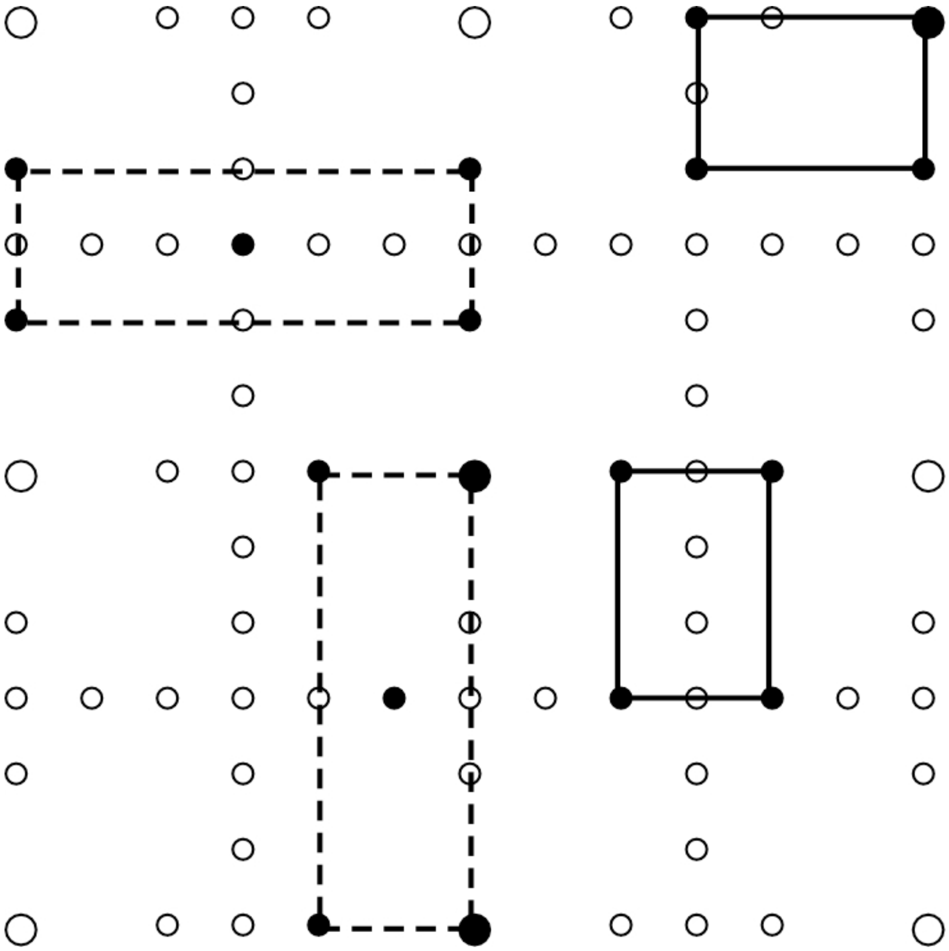

Fig. 5.15. Schematic diagram of mixed c(2x6) + (2x3) LEED pattern. The spots belonging to each outlined c(2x6) [dashed] and (2x3) [solid] unit cell are filled.

(2x1) Sr/Si(001) phase may not be a line compound, but instead is better described as a surface solution phase that is stable of a range of coverage values. The presence of a single phase over a range of Sr coverage values could be due to the formation of Sr vacancies that would allow for variable occupancy of the valley-bridge site in the (2x1) Sr/Si(001) phase. However, the observation of only (2x1) periodicity over a range of coverage values could also be explained by regions of vacancy-free (2x1) Sr/Si(001) phase coexisting with separate regions of clean (2x1) Si(001) surface.

The fact that pure (2x3) periodicity was not observed in the LEED patterns of any surfaces with Sr coverages in the vicinity of 1/3 ML supports the claim by Hu *et al.* that the Sr/Si(001) system does not form a stable (2x3) phase with two Sr atoms per unit cell. The presence of (2x1) and (2x3) diffraction spots in the LEED pattern [Fig. 5.13(a)] of a 0.35 ML surface is most likely due to the presence of 1/2 ML (2x1) and 1/6 ML (2x3) phases. The coexistence of c(2x6) and (2x3) phases for coverage values between 1/6 ML and 1/3 ML suggests that the c(2x6) Sr/Si(001) phase has a local coverage of 1/3 ML as Ojima *et al.* [57] proposed for the c(2x6) Ba/Si(001) surface.

Fig. 5.14(b) indicates that as the anneal temperature was increased (and the coverage consequently decreased) (2x3) diffraction spots were first observed on a 0.35 ML surface resulting from a 695°C anneal, but c(2x6) spots were not observed until after an anneal at 714°C that resulted in a Sr coverage of 0.27 ML. This apparent contradiction with the proposal that the local coverage of the c(2x6) phase is higher than that of the (2x3) phase could be explained by the energy barrier for nucleation the c(2x6) phase being greater than that of the (2x3) phase. The fact that most of the previous studies of Sr/Si(001) surface phases have “missed” the (2x3) phase is probably due to a certain amount of time required for the surface to reach equilibrium.

It is evident from the 1/6 ML (2x3) surface model shown in Fig. 5.5 that the formation of a phase with (2x3) periodicity does not require a change in the symmetry of the top-layer Si atoms. In this figure, the positions of Si atoms drawn in this figure are identical to those on a clean Si(001)-(2x1) surface. However, it can be shown by symmetry arguments that regardless of the type and number of site(s) occupied by adatoms, the formation of a surface phase with c(2x6) periodicity on Si(001) requires that the symmetry of the top Si atoms differ from that of a clean (2x1) Si(001) surface. Symmetrically dimerized Si atoms arranged in the same row pattern observed on a clean (2x1) Si(001) surface could – with a proper arrangement of adsorbate atoms – result in a primitive (2x6) unit cell, but not a c(2x6) unit cell. Various arrangements involving dimers in locked tilt states, like those in the low temperature c(4x2) Si(001) unit cell shown in Fig. 2.4, could result in c(2 x n) cells for $n/2 = even$, but not for $n/2 = odd$. Formation of any c(2 x 6) surface phase on Si(001) requires breaking of at least some of the Si dimer bonds. It would be possible for new Si dimers to form in order to satisfy bonding requirements, but the resulting arrangement could not be in the form of continuous dimer rows along <110> directions.

This rearrangement would most likely present a significant energy barrier to nucleation and could explain why c(2x6) periodicity has rarely been observed on

Sr/Si(001) surfaces. The intermediate (and possibly final) undimerized state(s) of Si atoms involved in the formation of a c(2x6) AEM/Si(001) phase could be stabilized by valence electrons of AEM atoms satisfying the dangling bonds of undimerized Si atoms. While anneals as brief as 1 minute have been used to form (2x3) and (2x1) Sr/Si(001) phases, the c(2x6) Sr/Si(001) surfaces observed in this thesis work were only observed after annealing for at least 15 minutes. However, as will be presented in Chapter 7, the c(2x6) Ba/Si(001) surface has been observed after annealing for just 5 minutes. Anneal times less than 5 minutes were never employed for Ba/Si(001) surfaces, so this amount of time does not necessarily represent a lower limit required for c(2x6) Ba/Si(001) nucleation. The fact that a c(2x6) phase seems to form more readily for Ba/Si(001) than it does for Sr/Si(001) may be due to the fact that Ba is more electropositive than Sr is. The greater electropositivity of Ba would enhance its ability to donate charge to the dangling bond orbitals of Si.

The difference between the electronegativities of Ba and Sr could also explain why STM images seemed to indicate that the formation of (2x3) Ba/Si(001) surfaces involves the removal of all of the top layer Si atoms while STM images of a (2x3) Sr/Si(001) surface suggested that the top layer Si dimers remained intact. The greater extent of charge transfer possible in the Ba/Si(001) system may be just enough to stabilize undimerized Si atoms in a 1/6 ML (2x3) phase.

5.5 Summary

XSW measurements have shown that Sr atoms are located in the same type of site in the (2x1) and (2x3) Sr/Si(001) surface phases. Consideration of AEM bonding environments in conjunction with the XSW results points to the valley-bridge site as the most likely adsorption site for Sr in these long-range ordered phases, in agreement with DFT calculations. There does not appear to be any difference between the position of Sr atoms in a (2x1) phase prepared by depositing onto a room temperature substrate followed by annealing and the position of Sr in a (2x1) phase prepared by depositing Sr directly onto a heated Si substrate.

It needs to be emphasized that the XSW results are consistent with many possible Sr positions. The proposal that Sr occupies the valley-bridge site relies on indications from XPS [21] and STM [22; 23] studies that the top-layer Si atoms remain dimerized in the (2x1) and (2x3) phases. While this arrangement of top-layer Si does make sense in terms of bonding requirements, the STM and XPS evidence in provided in Refs. [21], [22] and [23] is not entirely conclusive.

Differences between the ratios of the (004) and (022) coherent fractions measured for (2x1) and (2x3) Sr/Si(001) surfaces could be due to differences in the shape of the thermal distribution of Sr atoms in these phases. Consideration of the different requirements placed on allowed displacements of Sr atomic positions in these two phases reveals a possible atomic-scale explanation for differences in the thermal vibration anisotropies of the (2x1) and (2x3) phases.

XRF and AES measurements of Sr/Si(001) surfaces are consistent with the Sr coverages of the (2x3) and (2x1) phases being 1/6 ML and 1/2 ML. However, since the XRF detects the global coverage on the sample and not the local coverage in the ordered phase, these measurements do not necessarily rule out the possibility that at a 1/3 ML (2x3) Sr/Si(001) phase might exist.

Sharp c(2x6) diffraction spots were observed accompanying (2x3) spots in the LEED patterns of Sr/Si(001) surfaces with coverages between 1/6 ML and 1/3 ML. It is proposed that the c(2x6) phase has a local coverage of 1/3 ML. It is noted that c(2x6) periodicity would require top-layer Si atoms to rearrange to a configuration other than that of the continuous dimer rows found on clean (2x1) Si(001) surfaces. The ease with which this barrier can be overcome would be expected to increase with decreasing electronegativity of the adsorbate species.

CHAPTER 6

Sub-monolayer Surface Phases of Barium on Silicon (001)

Section 6.1 describes the methods used to prepare Ba/Si(001) samples and also contains LEED images of various Ba/Si(001) surfaces. The XSW measurements of a (2x1) Ba/Si(001) surface presented in Section 6.2 indicate that Ba atoms in this phase occupy the same in-plane position that Sr occupies in the (2x1) and (2x3) Sr/Si(001) phases. XSW data collected on (2x1) Ba/Si(001) surfaces within the first few hours after preparing the surface phase indicates that the position of Ba atoms is slightly higher than that occupied by Sr. However, deterioration of the Ba/Si(001) samples introduces some uncertainty (on the order of 0.1 Å) in the height of Ba atoms. Results of XSW measurements of c(2x6) + (2x3) and pure (2x3) Ba/Si(001) surfaces are briefly covered. These samples had apparently deteriorated before XSW data collection began. A previous XSW study of Ba/Si(001) by Herrera-Gómez *et al.* [59] is discussed in Section 6.3.

6.1 Ba/Si(001) Surface Preparation

A number of Ba/Si(001) surfaces were studied in the BESSRC-CAT 12ID-D UHV/XSW chamber. Using a Knudsen cell temperature of 450°C, 0.4 ML – 1.7 ML Ba was deposited at a rate of ~0.03 ML/min onto room-temperature Si(001)-(2x1) substrates prepared in the same manner as those used for Sr/Si(001) surfaces (see Section 5.1).

Subsequent anneals at 770 – 955°C for 1 – 60 minutes caused some of the Ba atoms to desorb and also resulted in changes in the surface periodicity. Samples were characterized with LEED, AES and XSW. The Ba coverage of samples studied by XSW was determined by comparing the intensity of the Ba Lα fluorescence signal from the samples to that of Ba-implanted Si standards calibrated by RBS. Many Ba/Si(001) surfaces were also prepared in the 12ID-D UHV chamber during times when the X-ray beam was unavailable (and thus could not be measured by XRF). The Ba coverage of these samples was determined by comparing their Ba_{MNN}:Si_{KLL} AES ratio to that measured on samples studied by both AES and XRF.

Fig. 6.1(a) shows the (2x1) LEED pattern of a clean Si(001)-(2x1) surface, and Figs. 6.1(b) – (d) show the LEED images taken immediately after depositing 0.38 ML, 0.76 ML and 1.52 ML onto this surface (with the substrate crystal held at room-temperature). The LEED patterns in Fig. 6.1(b) – (d), do not show any evidence of long-range ordering of Ba atoms. The intensities of the original (2x1) diffraction spots grew steadily weaker with increasing Ba coverage, and no new diffraction spots appeared on the Ba covered surfaces. Based on these LEED images, it appears that (at least for the Ba coverages studied here) the room-temperature deposited Ba atoms formed a disordered overlayer. This behavior differs from the (3x1) ordering in Fig. 6.1(a) that resulted from 0.6 ML – 0.8 ML Sr deposition onto room-temperature Si(001)-(2x1). It is unclear whether or not the top-layer Si atoms underneath the disordered Ba remained dimerized. The gradual disappearance of the half-order diffraction spots could be due to the removal

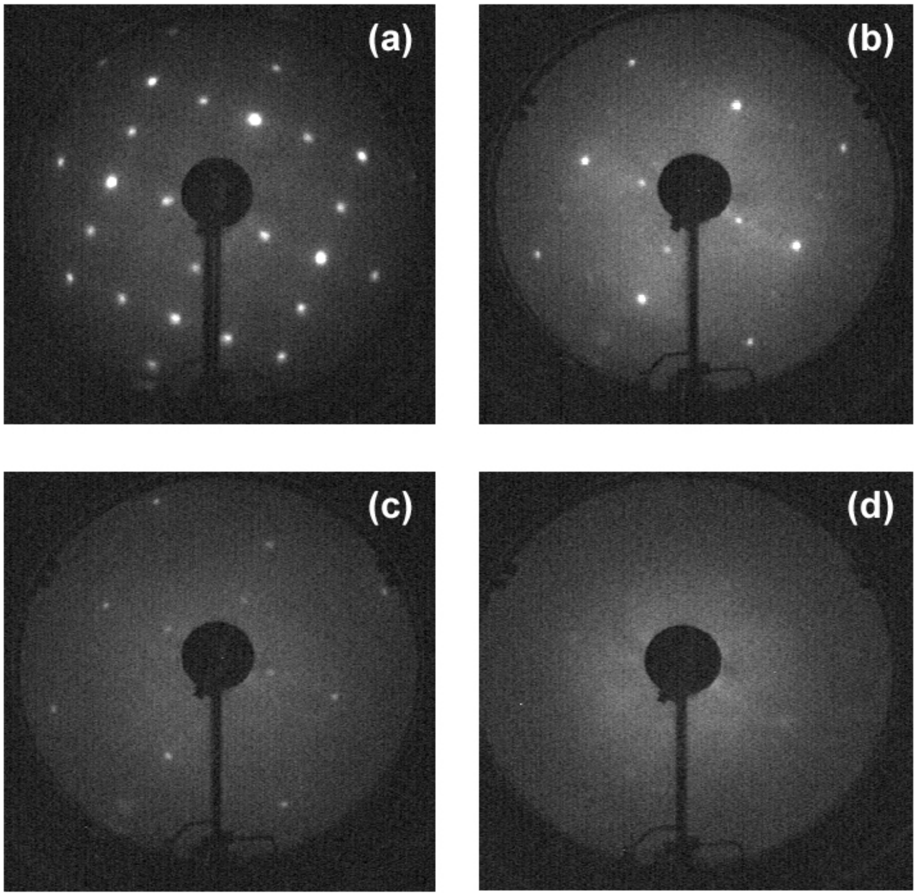

Fig. 6.1. (a) LEED pattern of clean (2x1) Si(001) surface and subsequent LEED images taken after depositing (b) 0.38 ML, (c) 0.76 ML and (d) 1.52 ML Ba onto Si(001) held at room temperature. Data collected at 12ID-D.

of Si-Si dimer bonds (and hence the loss of 2x periodicity), or it could simply be due to the half-order diffracted intensity being attenuated by the Ba overlayer.

The annealing conditions, Ba coverage and surface periodicity of a number of Ba/Si(001) samples are summarized in Table 6.1. The naming convention used for Ba/Si(001) samples in Table 6.1 is the same as that used for Sr/Si(001) samples in Table 6.1. Annealing the as-deposited, disordered Ba/Si(001) surfaces resulted in four different types of LEED patterns. (2x1) Ba/Si(001) surfaces with Ba coverages of 0.29 – 0.64 ML were formed by 5 minute anneals at 770 – 875°C. Anneals lasting 5 – 60 minutes at 900 – 955°C resulted in mixed (2x3) + c(2x6) LEED patterns. However, an anneal limited to 5 minutes at the low end of this temperature range (i.e. at 904°C) resulted in a surface containing 0.28 ML Ba and a LEED pattern with (2x1) diffraction spots accompanied by fourth order streaks. Also, annealing at the high end of this temperature range (i.e. above 930°C) for more than 30 minutes resulted in pure (2x3) surfaces with measured Ba coverages of 0.11 – 0.13 ML. (2x1), (2x1) + 4x, (2x3) + c(2x6), and (2x3) Ba/Si(001) LEED patterns are shown in Fig. 6.2.

6.2 Ba/Si(001) XSW Results

XSW measurements were performed on (2x1), (2x3) + c(2x6), and pure (2x3) Ba/Si(001) surfaces using an incident beam energy of 8.00 keV. Data from these

Sample Name	Anneal Temp. °C	Anneal Time (min)	Ba Coverage (ML)	LEED Pattern
G01a	25	n.a.	1.44	none
G01b	904	5	0.33	(2x1) + 4x
G01c	950	5	0.22	(2x3) + c(2x6)
G01d	946	15	0.17	(2x3) + c(2x6)
G01e	955	30	0.12	(2x3)
G02a	25	n.a.	1.52	none
G02b	903	30	0.23	(2x3) + c(2x6)
G02c	903	30	0.19	(2x3) + c(2x6)
G03a	25	n.a.	1.64	none
G03b	919	10	0.26	(2x3) + c(2x6)
G03c	919	10	0.23	(2x3) + c(2x6)
G03d	919	10	0.18	(2x3) + c(2x6)
G03e	936	10	0.15	(2x3) + c(2x6)
G03f	936	20	0.15	(2x3)
G03g	936	20	0.13	(2x3)
G04a	25	n.a.	1.32	none
G04b	919	10	0.19	(2x3) + c(2x6)
G04c	947	20	0.13	(2x3)
G07a	25	n.a.	1.73	none
G07b	770	5	0.56	(2x1)
G07c	857	5	0.44	(2x1)
G07d	876	5	0.37	(2x1)
G08a	25	n.a.	2.03	none
G08b	785	5	0.63	(2x1) + satellites
G08c	850	5	0.40	(2x1)
G09a	25	n.a.	1.70	none
G09b	770	5	0.51	(2x1)
G09c	797	5	0.41	(2x1)

Table 6.1 Anneal temperatures, anneal times, resulting Ba coverages and LEED periodicities of Ba/Si(001) surfaces studied at 12ID-D.

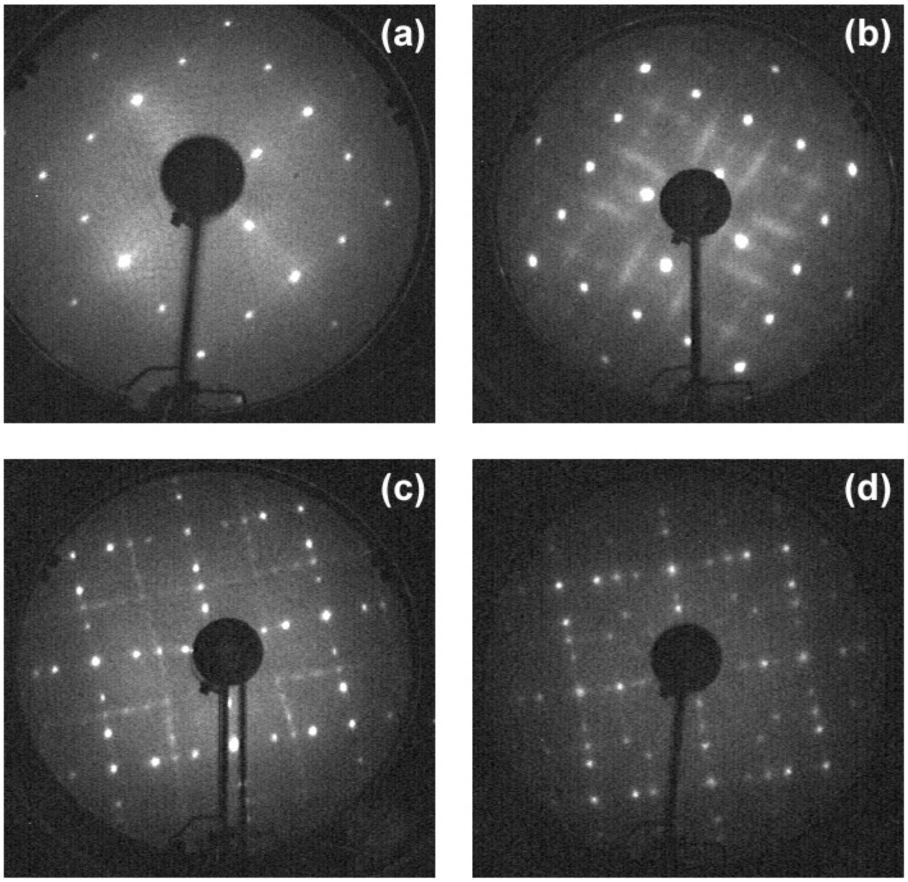

Fig. 6.2. LEED patterns of (a) 0.41 ML (2x1), (b) 0.33 ML (2x1) + 4x, (c) 0.22 ML c(2x6) + (2x3) and (d) 0.12 ML (2x3) Ba/Si(001) surfaces. Data collected at 12ID-D.

measurements was analyzed by fitting the reflectivity and Ba Lα fluorescence yield to the theory outlined in chapter 3.

6.2.1 (2x1) Ba/Si(001)

Fig. 6.3(a) shows the experimental data and theoretical fit from a Si(004) XSW measurement performed on sample G09c, a (2x1) surface with 0.41 ML Ba. Si(004) XSW data collection on this sample began approximately two hours after the completion of a 797°C anneal and continued for 144 minutes. The data shown in Fig. 6.3(a) was taken during the first 24 of these minutes. Fig. 6.4 shows all of the Si(004) XSW data collected on sample G09c, divided into groups collected over six, 24 minute time intervals. The f_{004} values determined from data collected during subsequent time intervals continuously decreased from $f_{004} = 0.44$ for data collected during the first 24 minutes to $f_{004} = 0.14$ for data collected during the final 24 minutes. This decrease in f_{004} with increasing time is manifested as decrease in the asymmetry of the fluorescence yield with respect to the Si(004) rocking curve. The measured value of P_{004} also changed over time – from 0.98 ± 0.01 in the first 24 minutes to 0.15 ± 0.04 in the final 24 minutes. The net *decrease* in this quantity is somewhat deceiving due to the fact that P_H is defined as ranging from 0 to 1. It would also be valid (and more logical, considering the sequence of P_{004} values labeled next to each fluorescence yield curve in Fig. 6.4) to describe this change as an increase from 0.98 ± 0.01 to 1.15 ± 0.04. Plots of the f_{004} and P_{004} values measured on sample G09c as a function of the amount of time elapsed after annealing are

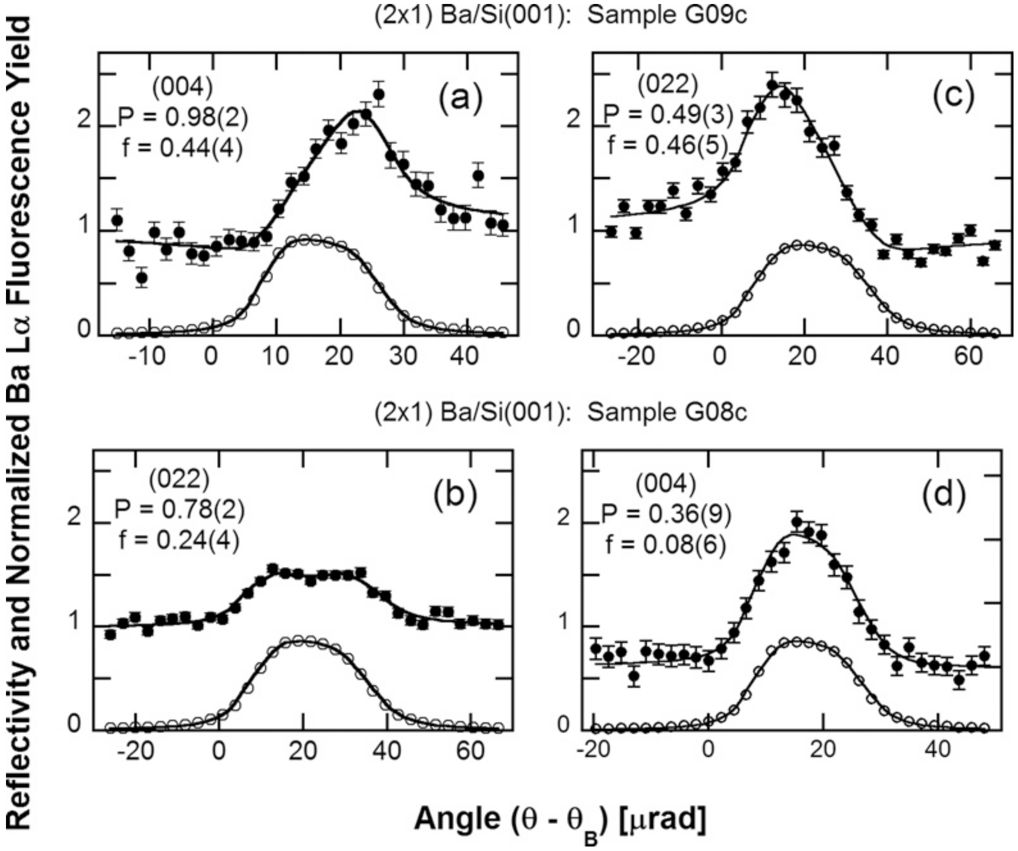

Fig. 6.3. Angular dependence of X-ray reflectivity (open circles) and normalized fluorescence yield (filled circles) data fit to dynamical diffraction theory for (a) Si(004) XSW measurement made on sample G09c ~2 hours after annealing, (b) Si(022) measurement made on sample G09c ~ 10 hours after annealing, (c) Si(022) measurement made on sample G08c ~2 hours after annealing and (d) Si(004) measurement made on sample G08c ~9 hours after annealing. Data collected at 12ID-D.

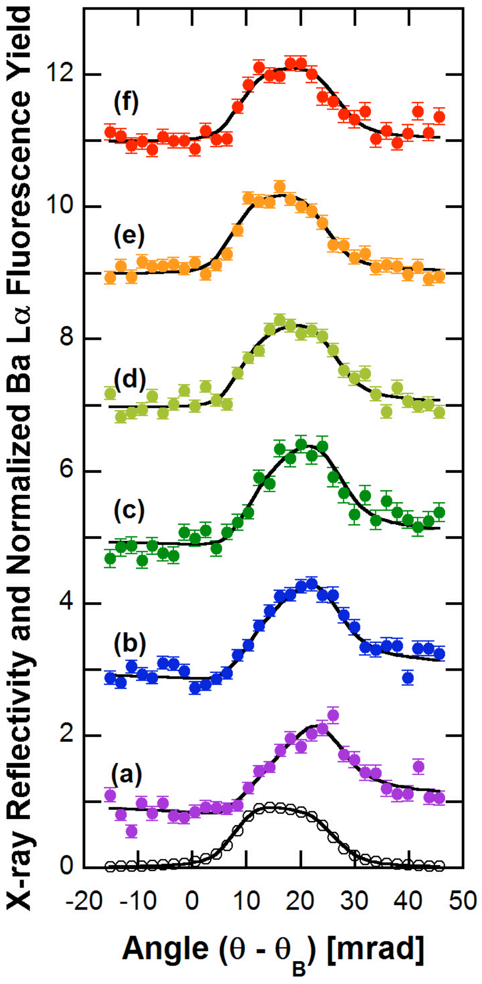

240 minutes: P = 0.15(4), f = 0.14(4)

216 minutes: P = 0.17(3), f = 0.17(3)

192 minutes: P = 0.13(2), f = 0.22(3)

168 minutes: P = 0.09(2), f = 0.38(4)

144 minutes: P = 0.04(2), f = 0.39(3)

120 minutes: P = 0.98(1), f = 0.44(2)

Fig. 6.4. Angular dependence of X-ray reflectivity (open circles) and normalized fluorescence yield (filled circles) data fit to dynamical diffraction theory for Si(004) XSW data collected in 24 minute blocks of time on sample G09c. Labels next to fluorescence yield curves indicate the amount of time that had elapsed after annealing when each yield curve was collected. Data collected at 12ID-D.

shown in Figs. 6.4(a) and (b), respectively.

Fig. 6.3(b) shows the experimental data and theoretical fits from a Si(022) XSW measurement performed on sample G09c approximately 4 hours after the completion of Si(004) data collection on this sample. Most of the time between measurements was spent changing the post-monochromator optics from Si(004) to Si(022) channel cut crystals. The data in Fig. 6.3(b) was collected over the course of 48 minutes. The P_{022} and f_{022} values determined from an additional set of Si(022) XSW data collected during the subsequent 48 minutes were statistically identical to the $P_{022} = 0.78 \pm 0.02$ and $f_{022} = 0.24 \pm 0.04$ values determined from the data in 6.3(b). This finding indicates that the time-dependent changes in P_{004} and f_{004} values observed during the Si(004) XSW measurement had ceased, or at least slowed dramatically, by the time the Si(022) data was collected.

Si(022) XSW data collected over the course of 12 minutes on another (2x1) Ba/Si(001) surface, sample G08c, are shown in Fig. 7.3(c). Collection of this data began approximately two hours after the completion of an 850°C anneal that left 0.40 ML Ba remaining on the surface. Like the P_{004} and f_{004} values measured on sample G09c, the P_{022} and f_{022} values measured on sample G08c were observed to change with time. Si(022) data was collected on sample G08c over the course of 48 minutes. P_{022} and f_{022} values determined from Si(022) data collected on this sample in four 12 minute blocks of time are plotted in Fig. 6.5(c) and (d), respectively, as a function of the time elapsed after annealing.

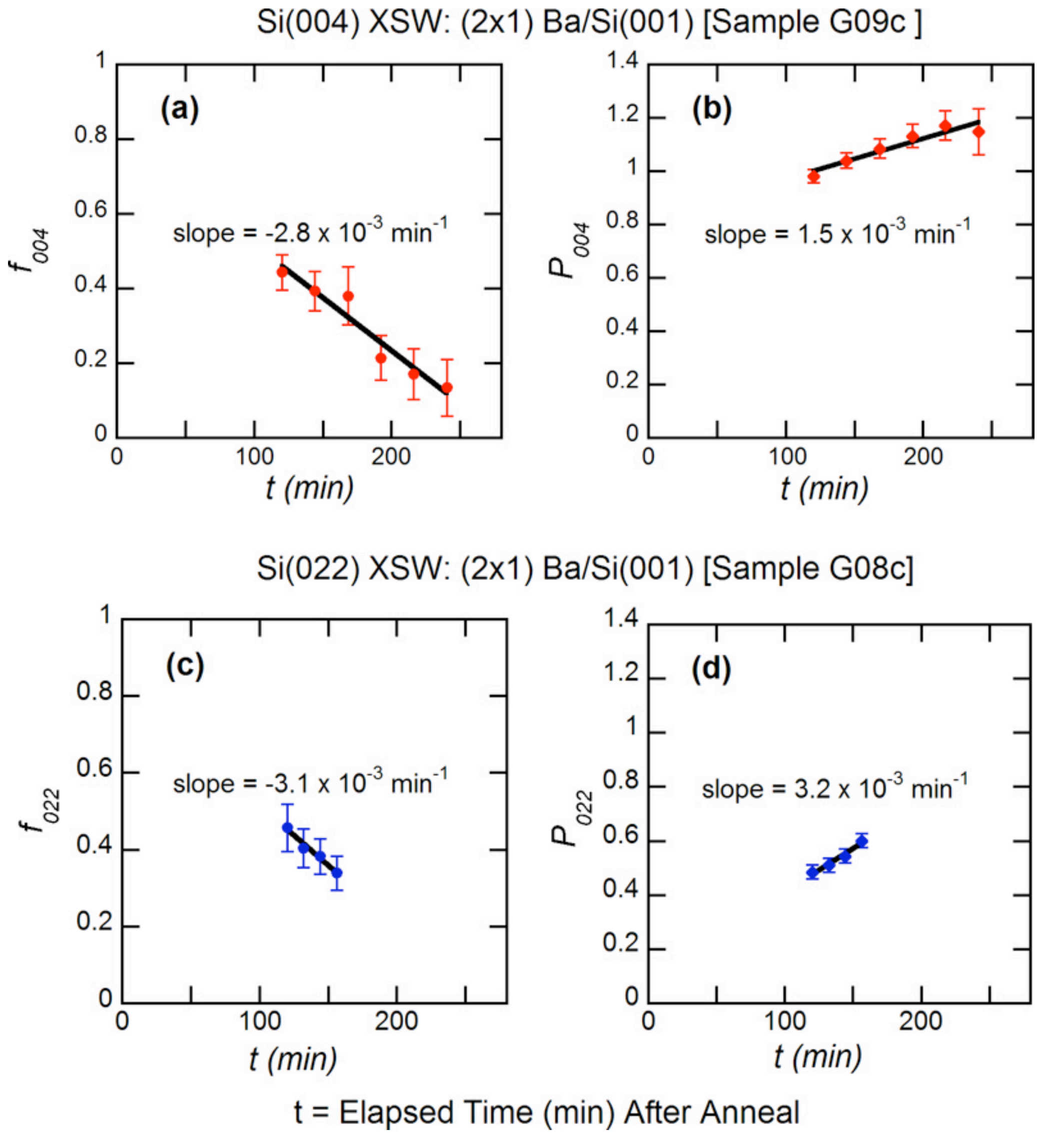

Fig. 6.5. (a) f_{004} and (b) P_{004} of sample G09c; and (c) f_{022} and (d) P_{022} of sample G08c as plotted as function of time elapsed after annealing the samples. Data collected at 12ID-D.

Fig. 6.3(d) shows the experimental data and theoretical fits from a Si(004) XSW measurement performed on sample G08c approximately 5 hours after the completion of Si(022) data collection on this sample. This data was collected over a span of 90 minutes. No time dependent variation was detectable during the course of collecting this data. As was the case for sample G09c, the processes responsible for time-dependence in the P_H and f_H values determined from XSW data collected ~2 – 3 hours after a post-deposition anneal had apparently ceased, or at least reached some sort of saturation, by the time XSW measurements using a second Bragg reflection were made (~8 hours after the anneal).

The P_{004} value measured at the beginning of Si(004) XSW data collection on sample G09c and the P_{022} value measured at the beginning of Si(022) data collection on sample G09c are in close agreement with Eq. 3.36. Assuming single site occupancy of the ordered Ba atoms, this relationship between P_{004} and P_{022} is consistent with ordered Ba atoms occupying bridge or cave sites if $n = even$ and with ordered Ba atoms occupying valley-bridge or pedestal sites if $n = odd$.

Table 6.2 lists the first and second nearest neighbor Ba-Si distances that would result from Ba occupying positions consistent with the P_H values determined from the data in Figs. 6.3(a) and (b) for n = -1, 0, 1 and 2. A comparison of these values with the 3.3 – 3.5 Å nearest neighbor distances reported for bulk Ba-Si compounds [134-138] leads to the same conclusion made for Sr – that the valley-bridge site with $n = 1$ in Eq.

3.38 is the most plausible AEM adsorption site. A 1/2 ML (2x1) Ba/Si(001) surface model consistent

n	**Site**	**1^{st} n.n. Si [#]: distance (Å)**	**2^{nd} n.n. Si [#]: distance (Å)**
-1	pedestal	[1]: 1.22	[2]: 1.82
-1	valley-bridge	[1]: 1.49	[4]: 2.02
0	bridge	[2]: 1.16	[4]: 2.97
0	cave	[2]: 2.74	[4]: 3.09
1	pedestal	[4]: 2.78	[2]: 3.26
1	valley-bridge	[2]: 3.37	[4]: 3.73
2	bridge	[2]: 3.23	[4]: 4.84
2	cave	[2]: 4.08	[4]: 4.92

Table 6.2 [Coordination number] and distance of first and second nearest-neighbor Si atoms that would result from Ba occupying positions consistent with P_{004} measured on sample G09c and P_{022} measured on sample G08c.

with the XSW data in Figs. 6.3(a) and (c) would be identical to that shown for the (2x1) Sr/Si(001) surface in Fig. 5.3, except the height of the Ba atoms above the ideal bulk height of second layer Si atoms would be 2.69 Å instead of the 2.53 Å shown for Sr.

This height difference is in good agreement with the 0.16 – 0.17 Å difference between the Ba^{2+} and Sr^{2+} ionic radii [139]. While Ba adatoms would certainly be expected to sit higher than Sr atoms occupying the same in-plane site, the fact the difference between the Ba and Sr height determined from the P_{004} values measured for the two particular samples compared here is identical to the difference in ionic radii needs to be regarded as possibly coincidental due to the fact that the condition of the Ba/Si(001) changed during the course of a given measurement.

6.2.2 Deterioration of (2x1) Ba/Si(001) Surfaces

As shown in Fig. 6.5, the rate of change of the P_H and f_H values of the (2x1) Ba/Si(001) was significant relative to the amount of time elapsed between preparation of an ordered phase and the start of XSW data collection. This time dependence may be due to accumulation of oxygen on the sample surface. AES measurements made ~1 hour after annealing (to form the ordered phase) typically indicated the presence of 0.02 – 0.04 ML O on the surface; an AES spectrum collected from sample G08c ~10 hours after annealing (i.e. after all XSW data collection) indicated that the amount of O on the surface had risen to 0.2 – 0.4 ML. Details on converting from the intensity of the O_{KLL} AES signal to O surface coverage will be discussed in Chapter 7.

Based on residual gas analyzer (RGA) measurements, the most abundant oxygen-containing gas in the 12ID-D UHV chamber was H_2O – typically at a partial pressure ~5 x 10^{-11} Torr. At this partial pressure, if every H_2O molecule impinging on the sample surface were to leave an O atom (e.g. as an –OH group bonded to Ba), then the amount of time needed for the surface to accumulate 1 ML of O would be on the order of 24 hours. Ba is sufficiently reactive that it would not be surprising for a significant fraction of the H_2O molecules impinging on the surface to react, causing an O atom in one chemical form or another to be added to the surface. Thus, the extent of O accumulation that occurred during XSW data collection seems reasonable. The accumulation of O on the surface could also be due to surface diffusion of O from the Mo sample holder onto the Si surface. Although no measurements were made to quantify the rate at which such a process was occurring on the particular samples studied, anecdotal evidence from studies of GaAs indicates that that surface diffusion can be a major contamination mechanism in UHV.

The particular brand of XSW analysis used in this thesis is not useful for obtaining any information about O atoms adsorbed on a surface. The type of photoelectric signal monitored (XRF) is an ineffective means for detecting O because Auger decay processes of photoexcited states are far more dominant than fluorescence in this relatively low Z atom. Also, any 0.53 keV O Kα fluorescent photons that do end up being emitted are severely attenuated by the Be windows located between the sample and solid-state detector crystal.

Due to its comparatively high electronegativity, an O atom adsorbing onto a Ba/Si(001) surface – perhaps directly on top of a Ba atom, perhaps on a site bridging between to neighboring Ba atoms, or perhaps elsewhere – would be expected to attract some of the electron density that had been responsible for Ba–Si bonding on the previously uncontaminated surface. This type of electron redistribution would weaken the Ba–Si bonds. Weaker Ba–Si bonding would most likely result in an increase in the height of the Ba atom(s) above the surface.

The time-dependence of the P_H and f_H values measured on Ba/Si(001) surfaces is consistent – at least qualitatively – with an increase in the height of Ba atoms. Gradual accumulation of O atoms on the surface would not be expected to cause the heights of all Ba atoms on the surface to increase uniformly. An individual O atom would only be expected to affect the heights the Ba atoms(s) adjacent to it (and possibly the first few nearest neighbors). Assuming they do not lose coherence with the Si lattice, Ba atoms bonded to O would be expected to reside at one height, while Ba atoms in uncontaminated surface regions would be at another (lower) height.

The presence of ordered Ba atoms occupying two different positions would result in two terms in the summation Eq. 3.33, so a_H, and consequently both P_H and f_H, would be affected. Since these quantities depend on the relative amounts of Ba occupying each type of site (represented by c_j in Eq. 3.33), they would be expected to change with the accumulation of O on the surface.

Since the measured P_H values were increasing during the entire time that the XSW data shown in Figs. 7.3(a) and (c) was being collected, the 2.69 Å Ba height determined using this data in conjunction with the assumption of single-site occupancy represents an upper limit on the actual height of ordered Ba atoms on uncontaminated surface regions. A linear extrapolation of the P_{004} data points in Figs. 7.5(a) would intercept the time ($t = 0$) axis at $P_{004} = 0.83$. For reasons explained below, this value, which would correspond to Ba atoms sitting 2.48 Å above the ideal bulk second layer Si plane, represents a lower limit on the P_{004} value expected for an uncontaminated surface.

The first of these reasons has to do with the fact that the sample temperature was not constant during the time between the end of an anneal and the start of data collection. After annealing, power to the sample heater was ramped down to zero over the course of ~5 minutes, and the sample temperature remained above 100°C for an additional ~20 minutes while slowly approaching room-temperature. In general, higher temperatures resulted in higher rates of O desorption from the surface. Thus, the net accumulation of O during much of the time between completion of an anneal and the start of XSW data collection was most likely occurring more slowly (and thus the overall P_H values were changing more slowly) than it was while the XSW data in Figs. 6.3(a) and (c) was being collected. It is worth mentioning that an 800°C anneal of a "deteriorated" (2x1) Ba/Si(001) that had accumulated > 0.2 ML O and exhibited $f_{004} < 0.1$ could be "regenerated" to a surface with < 0.05 ML O and $f_{004} > 0.4$ by an annealing at 800°C.

Another reason that linear extrapolations of the P_{004} value plotted in Fig. 7.5(a) and (c) would underestimate the P_H values of an uncontaminated surface is related to the form of P_H as a function of the occupancies of the Ba in the uncontaminated (c_1) and contaminated (c_2) surface regions. In order for P_{004} and P_{022} to both increase with time, as is the case in Figs. 7.5(a) and (c), the length, L, of an exclusively vertical translation of Ba induced by O adsorption would need to be:

$$(6.1) \qquad (k-1)d_{004} < L < \frac{kd_{004}}{2},$$

where k could be any odd integer. Since upward changes in the Ba position by more than d_{004} would result in unreasonably long Ba-Si bond lengths, the range of L values defined by $k = 0$ is the only one considered.

The plots in Fig. 6.6 show the calculated P_{004}, P_{022}, a_{004} and a_{022} as functions of the relative occupancy, c_2, of Ba occupying positions located distances L above the position of ordered Ba in uncontaminated surface regions. In these calculated curves, the height of Ba in the uncontaminated surface regions is fixed at 2.65 Å above the bulk ideal plane of second layer Si atoms. Using this chosen height, the value of $\boldsymbol{H}\cdot\boldsymbol{r}_1/(2\pi)$ used in Eq. 3.33 to compute S_{004} would be 0.95 (slightly lower than the $P_{004} = 0.98$ measured during the early stages of XSW data collection on sample G09c). In Fig. 6.6(a), P_{004} is plotted as a function of c_2 using four different values of L: 0.20 Å, 0.34 Å, 0.48 Å and 0.61 Å. These height differences between Ba atoms in contaminated and uncontaminated surface regions correspond to respective $\boldsymbol{H}\cdot\boldsymbol{r}_2/(2\pi)$ values of 0.1, 0.2, 0.3 and 0.4. For purposes of continuity in the plots of P_{004} as a function of c_2, it is convenient to think of these values as 1.1, 1.2, 1.3 and 1.4. At the smallest value of L used in these plots, $P_{004}(c_2)$ is well approximated by a straight line. However, at higher values of L, the slope $\frac{dP_{004}}{dc_2}$ varies considerably as a function of c_2. $\frac{dP_{004}}{dc_2}$ continuously increases over the range $0 < c_2 \leq 0.5$ and then continuously decreases for $0.5 < c_2 \leq 1$. For O accumulation with time (t), $\frac{dc_2}{dt} \geq 0$. Provided that $c_2 < 0.5$ when XSW data collection begins, then $\frac{dP_{004}}{dt}$ at the start of data collection will be greater than $\frac{dP_{004}}{dt}$ at all earlier times. Thus, even if high-temperature enhancement of O desorption is ignored, the P_{004} value obtained by extrapolating the data in Fig. 7.5(b) to $t = 0$ would be greater than or equal to the P_{004} expected for an uncontaminated surface.

The fitted slopes, $\sim\frac{dP_{004}}{dt}$ and $\sim\frac{dP_{022}}{dt}$, of the data plotted in Figs. 7.5(b) and (d) are 1.5 x 10^{-3} min^{-1} and 3.2 x10^{-3} min^{-1}. This difference between the rates of change of

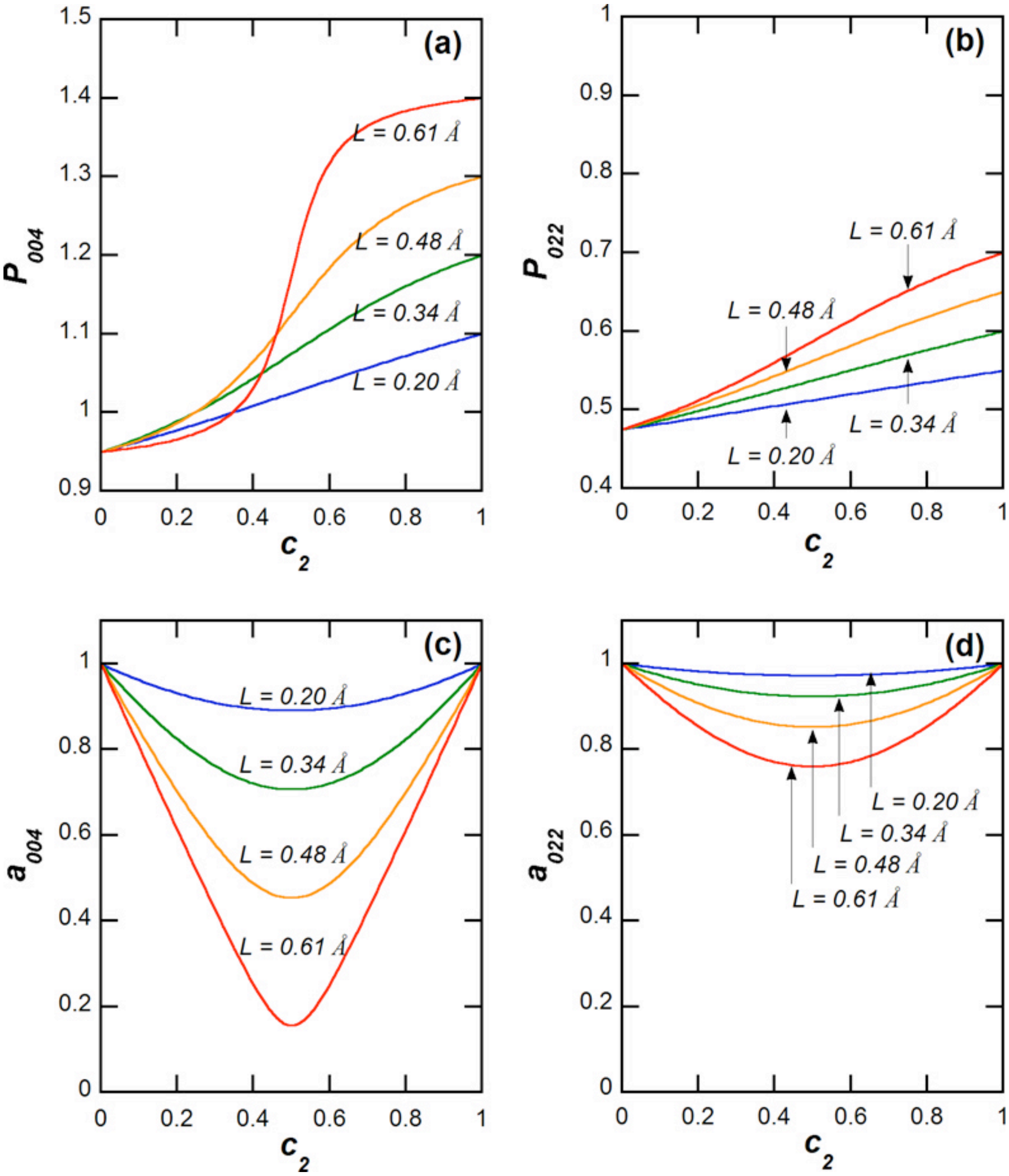

Fig. 6.6. Calculated P_{004}, a_{004}, P_{022} and a_{022} for two-site occupancy. Ba atoms with occupancy, c_1, are assumed to occupy valley-bridge sites at a height 2.65 Å above the ideal bulk height of second layer Si atoms; Ba atoms with occupancy c_2 are assumed to be located at the same in-plane position as those that make up c_1, but at a height 2.65 Å +

L above the ideal bulk height of second layer Si atoms. For any value of L that satisfies Eq. 6.1, the shape of $P_{022}(c_2)$ is more linear than that of $P_{004}(c_2)$ because atoms separated vertically by these distances are more out phase with respect to the Si(004) diffraction planes than they are with respect to the Si(022) diffraction planes (assuming the two sites have the same in-plane position).
P_{004} and P_{022} is qualitatively consistent with the curves plotted for $L = 0.61$ Å in the range $0 < c_2 \lessapprox 0.3$. For this particular case, the measured P_{004} would change by 0.04 from the P_{004} value of the uncontaminated surface as c_2 increased from 0 to 0.3; but P_{004} would begin to change much more rapidly with further increases in c_2.

The amount by which P_{004} values measured on a partially contaminated surface overestimate the height of Ba atoms on a clean Ba/Si(001) surface would grow with increasing c_2. From the plots in Figs. 6.6, it is evident that increasing this parameter would cause the difference between a_{022} and a_{004} (which are proportional to f_{022} and f_{004}) to increase. The fact that the respective f_{004} and f_{022} values measured (at the beginning of XSS data collection) on samples G09c and G08c were approximately the same at equal amounts of time after annealing indicates that c_2 was small when the XSW data collection began and that the overestimation of the height of Ba atoms on uncontaminated surface regions was minimal.

In principle, the decreases in the f_{004} and f_{022} values with time indicated in Figs. 7.5(a) and (c) could be due entirely to the decreases in a_{004} and a_{022} brought about by ordered Ba atoms occupying multiple positions. In this case, a_{004} and a_{022} would change by different amounts. If the two occupied positions have the same in-plane position and only differ in their heights above the surface and are separated by a distance L that satisfies Eq. 6.1, then $a_{004} < a_{022}$, so the change in f_{004} with O accumulation would be expected to be greater than that of f_{022}. In the calculated curves for $a_{004}(c_2)$ and $a_{022}(c_2)$ in Figs. 6.6(c) and (d), $\left|\frac{da_{004}}{dc_2}\right| \geq \left|\frac{da_{022}}{dc_2}\right|$ for a give value of L, and thus $\left|\frac{df_{004}}{dc_2}\right| \geq \left|\frac{df_{022}}{dc_2}\right|$ would also be expected. However, the slopes measured from the data in Figs. 7.5(a) and (c) indicate $\left|\frac{df_{004}}{dc_2}\right| \cong \left|\frac{df_{022}}{dc_2}\right|$. This similarity suggests that the observed decay of f_H is primarily due general disordering of Ba atoms – i.e. a decrease in C with time. In addition to causing an elongation of Ba–Si bonds, O accumulation could result in oxidation of Si atoms and cause Ba atoms to lose coherence with the Si lattice.

The observed changes in P_H and f_H indicate that the ordered fraction of Ba decreases with time and that the distribution of Ba atoms that remain part of the ordered fraction is also changing. At this point, it is unclear whether a change in the position of Ba is an intermediate step en route to loss of coherence with the Si lattice, or if the two processes occur independently of one another.

It is tempting to cite P_{004} values of ~0.4 measured on (2x1) as well as (2x3) surfaces more than 10 hours after an anneal as an indication of the height of Ba that is bonded to O (or likely in the form of –OH) and has not lost coherence with the Si lattice. However, the extremely low coherent fractions associated with these measurements would make such a conclusion highly tenuous. Further doubt would be cast by the fact that the P_{004} and P_{022} measured on these deteriorated surfaces are not in good agreement with either of the relationships (Eqs. 3.36 or 3.37) that would signify single-site occupancy (although considering the rather large errors in the deteriorated surface's P_H values, it could be argued that they are close to satisfying Eq. 3.37). However, it is possible to place upper and lower limits on the upward shift of Ba atoms that seems to occur upon O adsorption. As mentioned earlier, the separation between Ba in contaminated and uncontaminated surface regions must satisfy Eq. 6.1, and any case other than $k = 0$ in this equation would produce unreasonably large Ba-Si distances, so Ba atoms (that still remain part of the ordered fraction) on which O has adsorbed would not be any more than $d_{004}/2$ higher than ordered Ba that is not bonded to O. If P_{004} values with associated f_{004} of at least 0.2 are considered trustworthy, then it can be deduced from the data in Figs. 6.5(a) and (b) that P_{004} reaches a value of at least 1.15 (a.k.a. 0.15), corresponding to a minimum height of 2.92 Å above the ideal bulk second layer plane of Si.

6.2.3 c(2x6) + (2x3) and (2x3) Ba/Si(001) Surfaces

One Ba/Si(001) surface exhibiting mixed (2x3) + c(2x6) periodicity and another surface exhibiting pure (2x3) periodicity were also characterized using XSW. Fig. 6.6(a) shows the data from a Si(004) XSW measurement performed on sample G04b, a (2x3) + c(2x6) surface containing 0.19 ML Ba. This data was collected approximately 12 hours after the sample was annealed (at 919°C). The measured $f_{004} = 0.05 \pm 0.04$ is virtually indistinguishable from zero.

Figs. 6.6(b) and (c) show data from Si(004) and Si(022) XSW measurements of sample G04c, a 0.15 ML (2x3) Ba/Si(001) surface that resulted after annealing G04b for

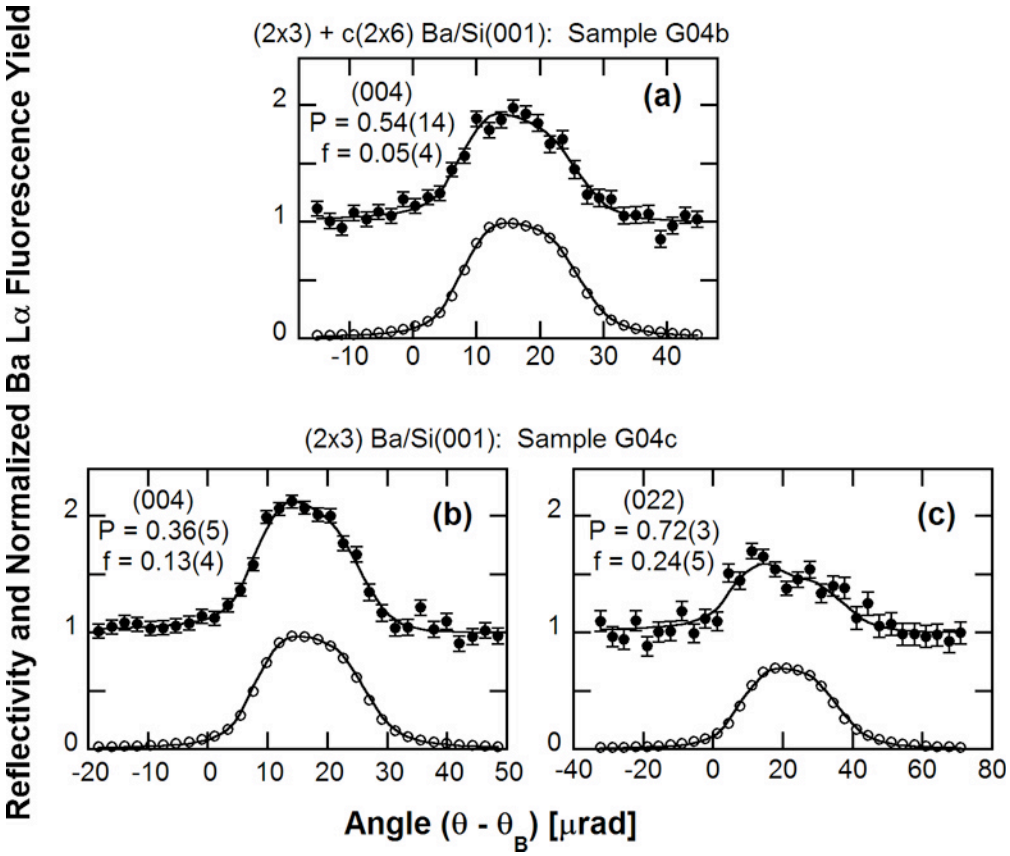

Fig. 6.7. Angular dependence of X-ray reflectivity (open circles) and normalized fluorescence yield (filled circles) data fit to dynamical diffraction theory for (a) Si(004) measurement of sample G04b; and (b) Si(004) and (c) Si(022) XSW measurements of sample G04c. Data collected at 12ID-D.

20 minutes at 947°C. Both of these data sets were collected more than 12 hours after the sample was annealed. The $P_{004} = 0.36 \pm 0.05$, $f_{004} = 0.16 \pm 0.04$, $P_{022} = 0.72 \pm 0.03$ and $f_{022} = 0.24 \pm 0.05$ values determined from these measurements are in reasonable agreement with the $P_{004} = 0.36 \pm 0.09$, $f_{004} = 0.08 \pm 0.06$, $P_{022} = 0.78 \pm 0.02$ and $f_{022} = 0.24 \pm 0.04$ measured on (2x1) Ba/Si(001) surfaces that had been sitting in the UHV chamber for > 10 hours after annealing. This finding suggests that the (2x3) surface underwent deterioration process(es) similar to those that occurred on the (2x1) Ba/Si(001) surfaces. Since only one reflection – the Si(004) – was used to measure the c(2x6) + (2x3) surface, and the f_H value of that measurement virtually is indistinguishable from zero, the only conclusion to be made about this sample is that it severely deteriorated. As the true f_H decreases, the uncertainties in the fitted values of both P_H and f_H increase.

6.3 Previous XSW study of Ba/Si(001)

Herrera-Gómez *et al.* [59] previously studied the (2x1) and (2x3) Ba/Si (001) surfaces with XSW using off-normal Si {111} reflections and also proposed that Ba occupies valley-bridge sites. Although P_H values from just one type of symmetrically non-equivalent reflection do not place as many restrictions on possible adsorption geometries as P_H values from multiple, non-equivalent reflections do, these {111} XSW measurements were consistent with Ba atoms occupying valley-bridge sites. Ba adatoms located at the bulk-primitive unit cell position indicated by our (004) and (022) XSW measurements would be expected to yield $P_{\{111\}} = 0.62$ (with the origin of the bulk fcc unit cell defined as shown in Fig. 2.1 and assuming equal population of both orientations of (2x1) surface domains).

Relative to the Si bulk unit cell shown in Fig. 2.1, Herrera-Gómez *et al.* measured $P_{\bar{1}\bar{1}1} = 0.58$, $f_{\bar{1}\bar{1}1} = 0.63$, $P_{1\bar{1}\bar{1}} = 0.63$ and $f_{1\bar{1}\bar{1}} = 0.52$ for a (2x1) Ba/Si(001) surface. The actual $P_{\{111\}}$ numbers reported in Ref. [59] were offset from these values by 1/8 because the unit cell origin used in this work was offset from that shown in Fig. 2.1 by [1/8, 1/8, 1/8]. The average value of these two $P_{\{111\}}$ measurements was used to conclude that adatoms in the (2x1) Ba/Si(001) phase occupy valley-bridge sites at a height 2.61 Å above the ideal bulk plane of second layer Si atoms (compared with the value of 2.69 Å upper and 2.48 Å lower limits cited in Section 6.2). The difference between the adatom heights that would be calculated if the two reported $P_{\{111\}}$ values were each considered individually (under the assumption of single surface site occupancy) is 0.27 Å. Interestingly, the $f_{\{111\}}$ value from the measurement that indicates the higher Ba position has a 17% lower than the $f_{\{111\}}$ value of the measurement corresponding to the lower Ba height. While it is possible that these differences are simply due to experimental error, it is also possible that they are due to some of the Ba on the surface with the lower $f_{\{111\}}$ occupying a higher position due to O contamination.

Herrera-Gómez *et al.* also made Si(111) XSW measurements on a (2x3) Ba/Si(001) surface. The average of the reported $P_{1\bar{1}\bar{1}} = 0.67$ and $P_{\bar{1}\bar{1}1} = 0.65$ values corresponds to Ba atoms in the (2x3) phase sitting 2.91 Å above the ideal bulk plane of second layer Si atoms. This value is 0.30 Å higher than the Ba height that Herrera-Gómez *et al.* cited for the (2x1) phase.

The XSW measurements of Sr/Si(001) surfaces presented in Chapter 5 did not detect any systematic difference between the heights of Sr atoms in the (2x3) and (2x1) phases. Although the P_H values measured on Sr/Si(001) surfaces did exhibit some sample to sample variations (a range of 0.2 in P_{004} and 0.1 in P_{022}), these variations were due to two different mechanisms (to be discussed in the next chapter) related to the presence of O on the surface. Any real difference that might exist between the Sr atom heights in the (2x3) and (2x1) phases appears to be negligible compared to these effects.

Ciani *et al.* [44] predicted that at 1/16 ML coverage, Ba atoms occupying valley-bridge sites would be located 2.77 Å above the ideal bulk plane of second layer Si atoms and that increasing the coverage to 1/4 ML would be accompanied by a change in this height to 2.53 Å. Further increases in coverage to 1/3 ML and 1/2 ML resulted in valley-bridge Ba adatom heights of 2.50 Å and 2.54 Å respectively. Ciani *et al.*'s calculated height for 1/2 ML is closer to the 2.61 Å indicated by Herrera-Gómez *et al.*'s results than it is to the 2.69 Å indicated by the Si(004) XSW data shown in Fig. 6.3(a). However, the DFT prediction that the Ba adatom height is nearly the same (within 0.05 Å) at 1/4 ML, 1/3 ML, and 1/2 ML does not agree with Herrera-Gomez *et al.*'s conclusion that Ba atoms in a 1/3 ML (2x3) phase sit 0.21 Å higher than those in a 1/2 ML (2x1) phase. While a noticeable 0.23 Å difference between the 1/16 ML and 1/4 ML heights was calculated, the Ba height was predicted to decrease with increasing coverage rather than the opposite trend reported by Herrera-Gómez *et al*. Although Ciani *et al*. did not report a Ba height for 1/6 ML coverage, their height calculations do seem to be in agreement with the finding (in this thesis work) that Sr atoms occupy nearly the same position in (2x3) and (2x1) surface phases.

6.4 Summary

XSW measurements have been made on (2x1), c(2x6) + (2x3) and pure (2x3) Ba/Si(001) surfaces. Data collected ~2 hours after the formation of a long-range ordered phase is consistent with Ba atoms occupying valley-bridge sites at a height 2.69 Å above the ideal bulk plane of second layer Si atoms. However due to changes occurring on the sample surface during the course of data collection, this height represents an upper limit on the actual Ba height. Possible mechanisms for sample deterioration as well as the magnitude of error this phenomenon introduces into the measurement of the Ba position are also discussed. Deterioration of the c(2x6) + (2x3) and pure (2x3) surfaces prior to the start of data collection was too significant to make any conclusions about the Ba position(s) in these ordered phases.

CHAPTER 7

Strontium and Oxygen on Silicon (001)

Various effects of O on Sr/Si(001) surfaces are described in this chapter. Results of an XPS study comparing the oxidation of (2x1) and (2x3) Sr/Si(001) surfaces are presented in Section 7.1. Section 7.2 presents evidence from XSW measurements indicating that the gradual accumulation of O (presumably from residual H_2O in the UHV chamber) appears to cause changes on Sr/Si(001) surfaces, similar to those reported for Ba/Si(001) surfaces in the previous chapter. It is noted that the induced changes appear to occur more slowly on Sr/Si(001) surfaces than they do on Ba/Si(001). Section 7.3 reports on another trend in the XSW and AES data indicating that the presence of O on the surface during anneals used to form long-range ordered Sr/Si(001) surface also affects the measured P_H values. However, this latter effect is different from the one that seems to be induced by gradual accumulation contaminants after formation of a long-range ordered phase.

7.1 XPS Investigation of Oxygen on (2x1) and (2x3) Sr/Si(001) Surfaces

As noted in previous chapters, the Sr/Si(001) surface phase most widely (and successfully) employed as a “template” layer for subsequent $SrTiO_3$ growth is the 1/2 ML

(2x1) surface phase. Experimental [27] and theoretical [24] evidence indicates that the (2x1) Sr/Si(001) surface is significantly more stable than the (2x3) Sr/Si(001) surface is against oxidation of underlying Si atoms. XPS studies were carried out in order to investigate the kinetics of oxidation of these two surface phases.

7.1.1 Experimental Procedure

The adsorption of O on (2x1) and (2x3) Sr/Si(001) surfaces held at elevated temperatures in O_2 partial pressures ranging from 1×10^{-9} Torr to 5×10^{-7} Torr was investigated with XPS in the MBE chamber described in Section 4.2.2. (2x1) and (2x3) Sr/Si(001) surfaces were prepared using the same methods described in Section 5.4.1. The particular (2x1) Sr/Si(001) samples studied by XPS were prepared by depositing ~5 ML Sr onto a clean (2x1) Si(001) surface held at room-temperature and then annealing for 25 minutes at 640 – 645°C. The (2x3) sample studied by XPS was prepared by depositing ~5M Sr onto a room-temperature (2x1) Si(001) substrate and then annealing for 25 minutes at 770°C. The surface periodicities were verified by LEED. AES indicated that the respective Sr coverages of (2x1) and (2x3) surfaces prepared under these conditions were always within 10% of 1/2 ML and 1/6 ML. At this point in the sample preparation process, the O content was below the detectable limit of AES.

While remaining in UHV, the samples were transferred to the XPS analysis stage, heated to 450°C and exposed to research purity (99.998%) O_2 for a specified amount of time. At the end of the desired exposure time, the O_2 supply was turned off (by closing the leak valve), and power to the sample heater was turned off within ~15 seconds after cutting off the O_2 supply. The O_2 partial pressure (P_{O_2}) values used for all of the data presented here were ≤ $1x10^{-8}$ Torr. When P_{O_2} values in this range were used, the chamber pressure recovered to < $2x10^{-10}$ Torr within 1 minute of closing the O_2 leak valve. Samples were then studied by XPS. The process of O_2 exposure (with the sample at 450°C) and XPS data collection with the sample temperature < 100°C was repeated up to 20 times on a given sample. These cycles consisted of O_2 exposures ranging from 0.1 Langmuir (L) to 475 L (1 Langmuir = $1x10^{-6}$ Torr·s).

XPS spectra were collected using the Mg Kα X-ray source and hemispherical electron energy analyzer described in Section 4.2.2. "Survey" scans from 0 – 600 eV binding energy were collected using a 117.40 eV analyzer pass-energy and a 1.00 eV step size. Finer scans around the O-1s, Si-2p and Sr-3d peaks were collected using an analyzer pass-energy of 23.5 eV and a 0.2 eV step size. Plots of electron counts per second vs. electron binding energy were analyzed using the software XPSPEAK version 4.1.

7.1.2 XPS Results and Discussion

Fig 7.1 shows the O-1s XPS peak collected after exposing a (2x3) Sr/Si(001) surface to 0.2 L O_2. This peak is centered near 531 eV and appears to consist of two different components. The inset of Fig. 7.1 shows this spectrum fit using two

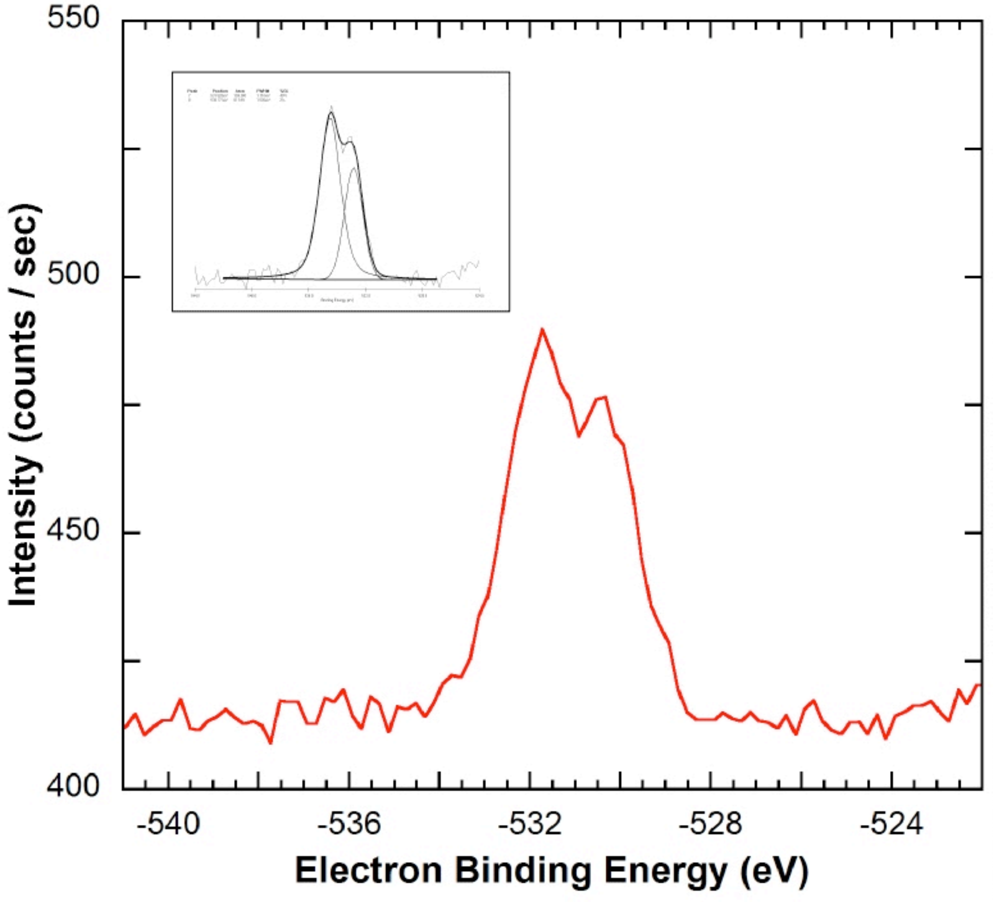

Fig. 7.1. XPS spectrum showing O-1s peak. Two components separated by ~1.6 eV used to fit this spectrum are shown in the inset. The peak at lower binding energy (shifted to the right) is attributed to O-Sr bonding, while that at higher binding energy (shifted to the left) is attributed to O-Si bonding. Data collected at Northwestern multi-purpose UHV surface science chamber.

components separated by 1.6 eV. Liang *et al.* [140] reported similar O-1s XPS spectra on Sr/Si(001) surfaces. The lower binding energy component was attributed to O-Sr bonding, while the higher energy component was proposed to be due to O-Si bonding.

The total area of the O-1s XPS peak as well as the relative intensities of the O-Sr and O-Si components changed with O_2 exposure on both (2x1) and (2x3) Sr/Si(001) surfaces. Fig. 7.2 shows plots of the coverage of O in the O-Sr and O-Si bonding environments, as well as the total O coverage, as functions of O_2 exposure on a (2x1) Sr/Si(001) surface. The coverage of O in the O-Sr bonding environment increases to ~0.5 ML within the first 0. L of O_2 exposure, but does not increase with further exposure. An enlarged version of the data between 0 and 50 L O_2 exposure is shown in Fig. 7.3(a).

Integrated areas of XPS spectra were converted to coverage values using the assumptions that the saturation coverage of O in the O-Sr bonding environment is equal to the coverage of Sr atoms on a given surface and that the Sr coverage on the (2x3) surface was 1/6 ML. Based on the relative intensities of the Sr-3d and O-1s XPS peaks and the atomic sensitivity factors for these signals in Ref. [141], the first of these two assumptions appears to be correct. The second assumption is supported by the plot in Fig. 5.14(b) showing that the Sr coverage of a surface exhibiting (2x3) periodicity is 1/6 ML and does not change with anneal temperatures in the 750 – 790°C range. Fig. 5.14(b) also shows that the Sr coverage of the (2x1) phase was sensitive too changes in anneal temperature through the entire range of anneal temperatures (600 - 670°C) over which it

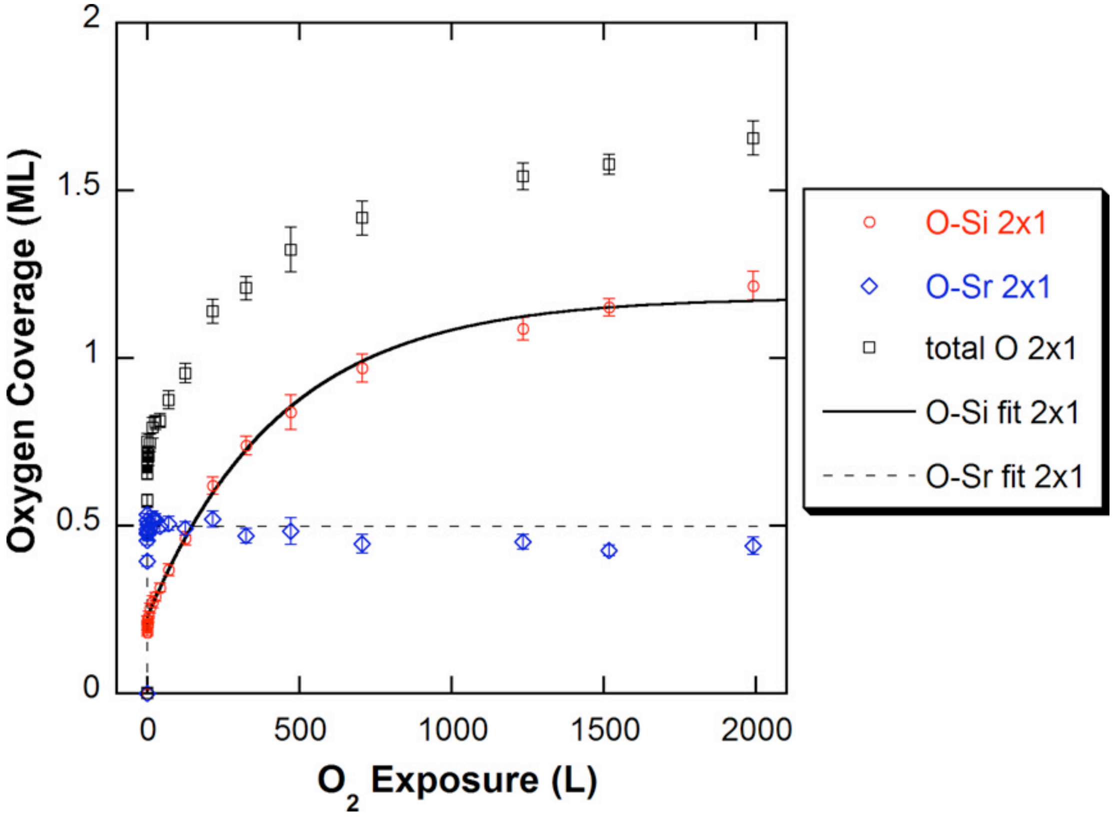

Fig. 7.2. Coverage of O bonded to Sr (diamonds), O bonded to Si as well as total O coverage for (2x1) Sr/Si(001) surface exposed to O_2 with the substrate held at 450°C. An O_2 partial pressure of $1x10^{-9}$ Torr was used during the first 2 L of O_2 exposure. Subsequent exposures were carried out at $1x10^{-8}$ Torr O_2. Data collected at Northwestern multi-purpose UHV surface science chamber.

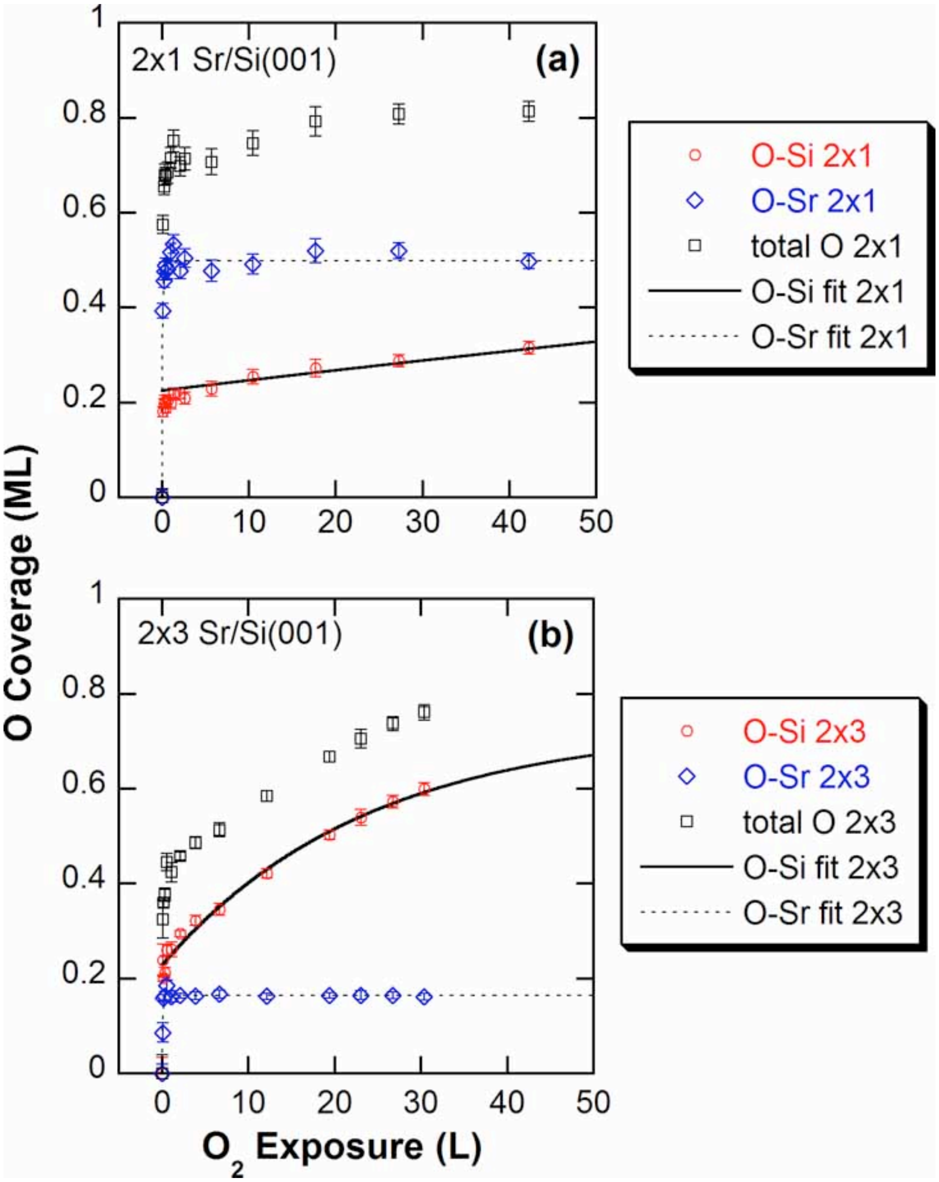

Fig. 7.3 (a) Coverage of O bonded to Sr (diamonds), O bonded to Si as well as total O coverage for (a) (2x1) and (b) (2x3) Sr/Si(001) surfaces exposed to O_2 with the substrate held at 450°C. For the data in (a), an O_2 partial pressure of 1×10^{-9} Torr was used during the first 2 L of O_2 exposure. The remainder of the exposures for the (2x1) surface and all exposures for the (2x3) surface were carried out at 1×10^{-8} Torr O_2. Data collected at Northwestern multi-purpose UHV surface science chamber.

was observed. The fact that the O in the O-Sr bonding coverage in Fig. 7.2 saturates near 0.5 ML indicates that the Sr coverage of the particular (2x1) Sr/Si(001) sample measured here was close to the proposed ideal coverage of 1/2 ML for the (2x1) phase.

Figs. 7.2 and 7.3(a) also show that the coverage of O in the O-Si bonding environment on this sample also increases sharply during the first ~0.5 L of O_2 exposure. Instead of remaining constant upon further exposure, as O in the O-Sr bonding environment does, the coverage of O bonded to Si continues to increase, although at a much slower rate than that observed during the initial stage of O_2 exposure. The oxidation of clean (2x1) Si(001) surfaces at temperatures up to ~640°C and P_{O_2} up to at least $1\text{x}10^{-6}$ Torr follow Langmuir-type reaction kinetics [142; 143] of the form:

$$\Theta(t) = \Theta_{sat}\left[1 - \exp(-k_t t)\right] \tag{7.1}$$

Where $\Theta(t)$ is the coverage at time, t; Θ_{sat} is the saturation coverage for the particular temperature and P_{O_2}; and the reaction rate constant, k_t is in units of *1/time* is equal to the initial rate of O accumulation – for clean Si surfaces, this O is initially bonded to partially oxidized Si in Si^{1+}, Si^{2+} and Si^{3+} oxidation states, but fully oxidized Si^{4+} becomes dominant after ~10 – 100 L O_2 exposure [144].

The data corresponding to O bonded to Si in Fig. 7.2 can be fit well to a Langmuir model if Eq. 7.1 is modified to:

$$\Theta(J) = \Theta_0 + \Theta_{sat}\left[1 - \exp(-k_L J)\right] \tag{7.2}$$

where Θ_0 accounts for the ~0.2 ML increase that occurs during the first ~0.5 L of exposure; J is the O_2 exposure in L; and k is the reaction constant in units of L^{-1}. The solid line in Fig. 7.2 shows a fit of the Si-bonded O coverage to Eq. 7.2 with $\Theta_0 = 0.21$, $\Theta_{sat} = 0.96$ ML, and $k_s = 2.41 \times 10^{-3}\ L^{-1}$. By comparison, the values of Θ_{sat} and k_s obtained from fitting the coverage of O bonded to Sr are 0.49 ML and 14.61 L^{-1}.

Fig. 7.3(a) shows an enlarged version of the 0 – 50 *L* range of the data plotted in Fig. 7.2., and the plot in Fig. 7.3(b) shows the coverage of O in O-Sr and O-Si bonding environments, as well as the total O coverage, measured over the course of 30 *L* O_2 exposure on a (2x3) Sr/Si(001) surface. It should be noted here that P_{O_2} for all exposures on the (2x3) surface was 1×10^{-9} Torr. This same pressure was used for the first 2 L of O_2 exposure on the (2x1) surface, but subsequent exposures were carried out at P_{O_2} of 1×10^{-8} Torr.

The coverage of O bonded to Sr on the (2x3) surface quickly saturates at 1/6 ML, with $k_s = 13.10$. This value is very similar to the reaction constant for O bonded to Sr on the (2x1) surface. However, fitting the coverage of O bonded to Si on the (2x3) surface yields $\Theta_0 = 0.23$, $\Theta_{sat} = 0.50$ ML, and $k_s = 4.23 \times 10^{-2}\ L^{-1}$. Previous studies [145] have shown that for P_{O_2} up to at least 3.0×10^{-7} Torr, the reaction rate constant k_t in Eq. 7.1 appears to change linearly with P_{O_2}, so it is improbable that the large difference between the k_s determined for the (2x3) and (2x1) surfaces is due to the different P_{O_2} levels employed. The fact that k_s for Si-bonded O on (2x3) surface is an order of magnitude larger than that on the (2x1) surface is consistent that – at least kinetically – the (2x1) surface is more stable against oxidation of Si than the (2x3) surface is. However, the use of different P_{O_2} values for exposures of the two surfaces makes a comparison of their thermodynamic stabilities more difficult. The fact that Θ_{sat} for the data collected on the (2x3) surface is roughly half that determined for the (2x1) surface is most likely due to the difference in P_{O_2} used in the two measurements since Θ_{sat} presumably represents a state of thermodynamic equilibrium. Further measurements, using the same P_{O_2} for both (2x3) and (2x1) surfaces are underway.

Preliminary results of data XPS data collected after exposing a 1/6 ML (2x3) Sr/Si(001) surface to 1x10^{-8} Torr O_2 is plotted in Fig. B.1 in Appendix B. Fitting the measured coverage of O bonded to Si to Eq. 7.2 yielded: $\Theta_0 = 0.20$, $\Theta_{sat} = 0.97$ ML, and $k_s = 1.50 \times 10^{-2}\, L^{-1}$. The saturation coverage, Θ_{sat}, of O bonded to Si for $P_{O_2} = 1\text{x}10^{-8}$ Torr appears to be the same (~1 ML) for both the (2x3) and (2x1) phases. However, this coverage is reached on a (2x3) surface at much lower O_2 exposures than it is on the (2x1) surface. The value of k_s obtained for the (2x3) surface exposed to 1x10^{-8} Torr O_2 is lower (by about a factor of 3) than that obtained for the (2x3) surface exposed to 1x10^{-9} Torr O_2. However, k_s for the (2x3) surface exposed to 1x10^{-8} Torr O_2 is still significantly larger (by about a factor of 6) than k_s of (2x1) surface exposed to 1x10^{-8} Torr O_2.

A common model [142] for the oxidation of the top two layers of Si atoms involves the insertion of an O atom into the "back bond" between a first and second layer Si atom. It is possible that the presence of Sr, along with the Sr atom bonded to it, can kinetically hinder the insertion of O into the back bond. In one sense, the stability of the (2x1) phase may simply be due to the presence of a greater number of Sr atoms.

7.2 Oxygen Accumulation on Room Temperature Sr/Si(001) Surfaces

As described in Chapter 6, significant changes were observed to occur in the measured P_H and f_H values of Ba/Si(001) over the course of ~1 – 2 hours, and it is likely that these changes were due to gradual accumulation of O (possibly in the form of –OH from residual H_2O in the 12ID-D UHV chamber). Similar effects were observed on some Sr/Si(001) samples. However, these effects – gradual upward shifts in measured P_{004} and P_{022} accompanied by decreases in f_{004} and f_{022} – did not occur as rapidly on Sr/Si(001) as they did on Ba/Si(001).

The rate of change of P_H and f_H values on Sr/Si(001) surfaces was never high enough during an actual XSW measurement to detect any change during the ~1 – 2 hours spent collecting a single data set. Figs. 7.4(a), (b) and (c) show the data from three different Si(004) XSW measurements made on sample E03b. The respective data sets in Fig. 7.4(a) and 7.4(b) were collected ~3 and ~6 hours after annealing the sample. The P_H and f_H values determined from each of these measurements are statistically equivalent. The changes observed on Ba/Si(001) surfaces were manifested as an increase in P_{004} (and P_{022}) and a decrease in f_{004} (and f_{022}) with time. The XSW data in Fig. 7.4(b) which was taken at a later time than the data in 7.4(a), actually exhibits the slightly higher f_{004} and lower P_{004} of the two measurements (but this difference is statistically insignificant). The

XSW data in Fig. 7.4(c) were collected ~24 hours after annealing the sample. The surface had changed significantly by the time this third measurement was made. The P_{004}

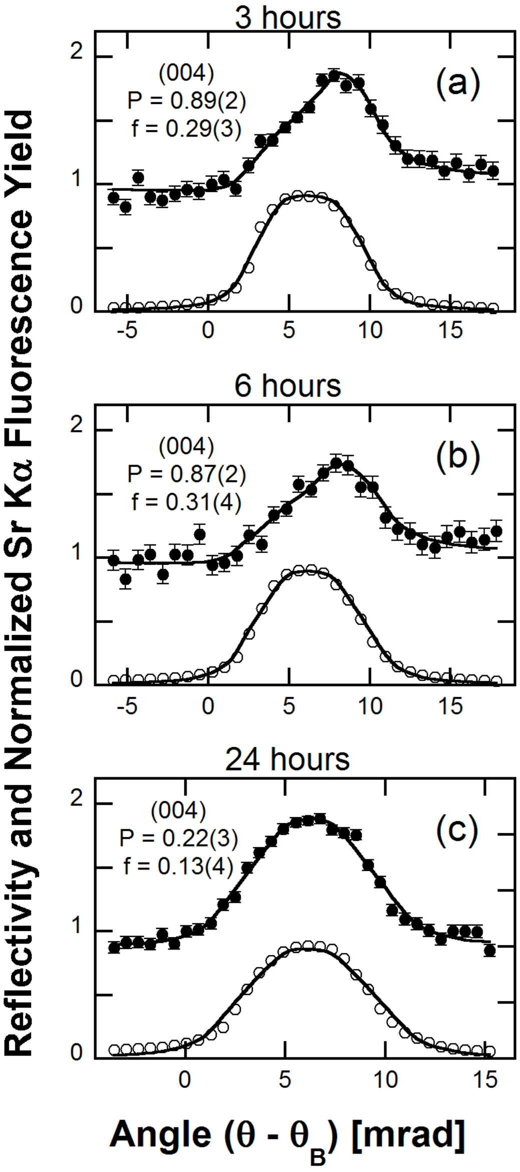

Fig. 7.4 Angular dependence of X-ray reflectivity (open circles) and normalized fluorescence yield (filled circles) data fit to dynamical diffraction theory for Si(004)

XSW measurements made (a) 3 hours, (b) 6 hours and (c) 24 hours after the 700°C anneal used to form sample E03b, a (2x1) Sr/Si(001) surface. Data collected at 12ID-D.

= 0.22 ± 0.04 (a.k.a. P_{004} = 1.22 ± 0.04) and f_{004} = 0.11 ± 0.04 are consistent with the increase in P_{004} and decrease in f_{004} observed with time on Ba/Si(001) surfaces.
If the physical processes responsible for the differences between the XSW data in Figs. 7.4(b) and 7.4(c) had been occurring at a reasonably constant rate, at least some difference would be expected between the data in Figs. 7.4(a) and 7.4(b). This apparently erratic behavior points to a contamination source that is not constant in time. It was observed on some occasions that moving the sample manipulator (used to align a sample onto a Bragg reflection) could cause the UHV chamber pressure to increase from its usual base pressure of ~1.5×10^{-10} Torr to ~1×10^{-9} Torr. These pressure spikes could provide a rather inconsistent contamination source.

A Si(022) XSW measurement made ~7 hours after the Si(004) data in Fig. 7.4(b) was collected yielded $P_{022} = 0.55 \pm 0.01$ and $f_{022} = 0.32 \pm 0.02$. The fact that this P_{022} value is somewhat higher than one-half of P_{004} [measured for most Sr/Si(001) surfaces] suggests that the surface had undergone some change by the time this measurement was made. Unfortunately, it is not known how much the "true" P_{022} and f_{022} values changed between collection of the Si(004) and Si(022) data. This uncertainty translates to the possibility of overestimating the ratio f_{022}/f_{004}. Recall that in Chapter 5, it was proposed that the systematic difference between the f_{022}/f_{004} ratios observed on (2x3) and (2x1) surfaces was used as evidence that the shape of the thermal distribution of Sr may differ between these two phases. Presumably, (2x3) and (2x1) surfaces were subject to this potential error in relatively equal amounts, and the difference in the f_{022}/f_{004} ratios of the two phases would have been detected even if f_{004} and f_{022} could be measured simultaneously.

The observation that Ba/Si(001) surfaces seem to change much more rapidly than Sr/Si(001) surfaces do could simply be due to coincidence. All XSW measurements of Ba/Si(001) surfaces presented in this thesis were performed during two beam times – one was just 10 days after the other. It is possible that an erratic contamination source could have been "worse" during these beam times than it was during measurements of Sr/Si(001) surfaces. However, Lettieri *et al.* [30] did find that the O partial pressure necessary to fully oxidize AEM atoms during MBE growth is lower for Ba than it is for Sr. Since Ba is the more electropositive of these two elements, it would be expected to be more reactive with O than Sr would be.

7.3 Effects of Oxygen Present During (2x1) and (2x3) Phase Formation

While the gradual accumulation of O on long-range ordered phases of Ba/Si(001) and Sr/Si(001) surfaces at room-temperature caused increases in P_H values and decreases in f_H values over time, the presence of O on the surface during anneals used to form long-range ordered phases seemed to have a different effect. Although high-temperature UHV anneals performed in the 12ID-D UHV chamber to remove the native-oxide of Si(001) substrates typically resulted in clean (2x1) Si(001) surfaces with O contamination levels less than 0.02 ML, some O contamination was always introduced during the Sr deposition process at 12ID-D (in contrast to the samples described in Sections 5.4 and 7.1).

Most Sr/Si(001) samples were characterized by AES within ~30 minutes after annealing to form a long-range ordered phase. The amount of O detected in these measurements varied significantly from sample to sample. Most of this variation is probably due to differences in the amount of O present on the surface before/during a high temperature anneal. The most heavily contaminated samples – with ~0.2 ML O – were prepared before the importance of extensively outgassing the Sr source was fully realized.

Fig. 7.5 shows data from Si(004) XSW measurements of four different Sr/Si(001) surfaces. The surface periodicity observed by LEED, and the O_{KLL}:Si_{LMM} AES ratio measured ~30 minutes after annealing are indicated along with the fitted P_{004} and f_{004} values for each data set. The shapes of the fluorescence yield curves vary substantially

among these data sets. The (2x1) Sr/Si(001) samples A09b and E03b corresponding to the respective data in Figs. 7.5(a) and (b) were both prepared by annealing as-deposited (3x1) Sr/Si(001) surfaces for 10 minutes at 700°C, but the O_{KLL}:Si_{LMM} AES ratio measured on sample A09b was higher than that on E03b by a factor of ~8. The P_{004} value measured on sample A09b – the surface with the higher oxygen content – is lower than that measured on sample E03b. This difference is reversed from the changes in P_H values that were observed to occur over time due to

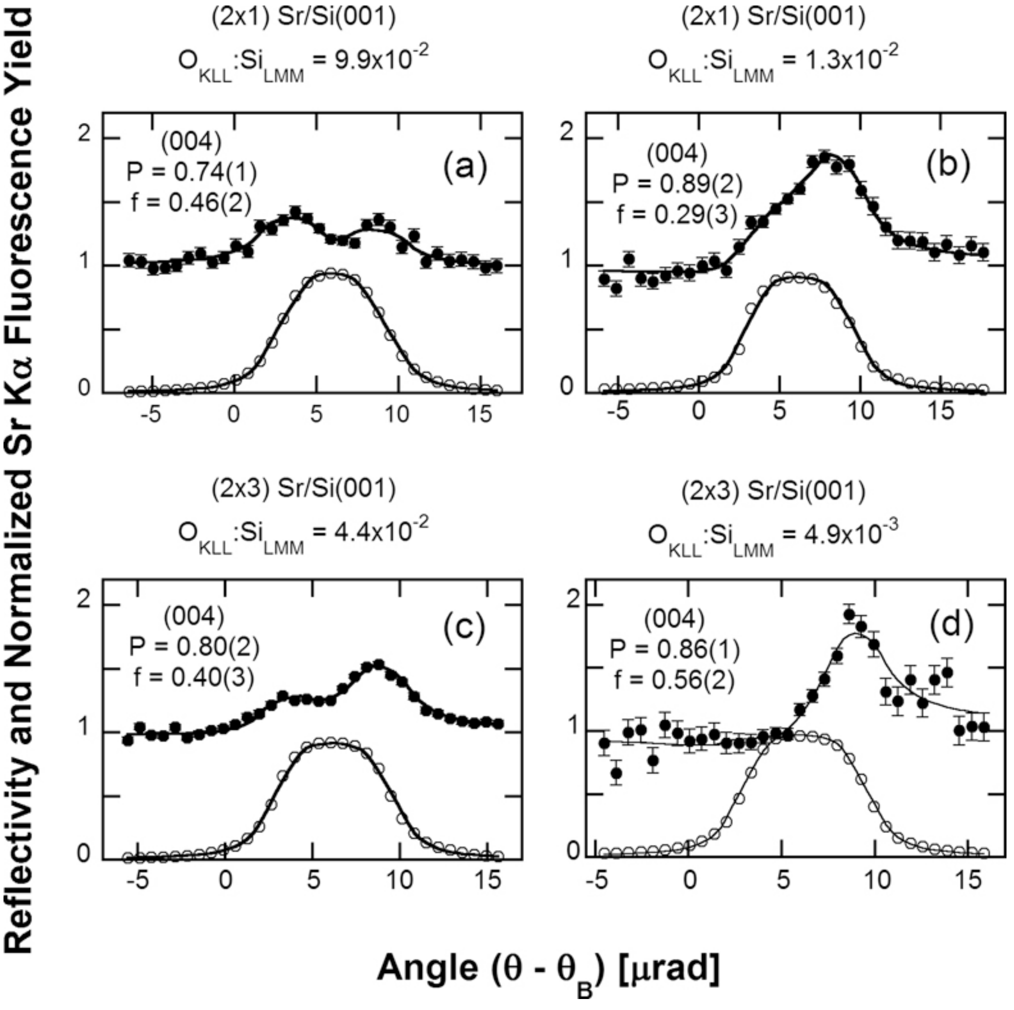

Fig. 7.5 Angular dependence of X-ray reflectivity (open circles) and normalized fluorescence yield (filled circles) data fit to dynamical diffraction theory for Si(004) XSW measurements made on Sr/Si(001) surfaces with varying amounts of O contamination as measured by AES after annealing to form (a) and (b) (2x1) or (c) and (d) (2x3) phases. Data collected at 12ID-D.

gradual, room-temperature accumulation of O on AEM/Si(001) surfaces. Figs. 7.5(c) and (d) show collected Si(004) data collected on two different (2x3) Sr/Si(001) surfaces – samples A11b and B02d. The O_{KLL}:Si_{LMM} AES ratio measured on sample A11b was ~9 times higher than that on B02d. Once again, the surface with the lower P_{004} is the one with the higher O content.

Apparently, the presence of oxygen on the surface during an anneal causes some of the Sr atoms to occupy position that is different from than that occupied by Sr in uncontaminated regions. However, the position of Sr in an oxygen bonding environment formed at high temperature is not in the same position suggested by changes in Ba and Sr P_H values due to O accumulation over time on a surface held at room-temperature. Figs. 7.6(a) and (b) show plots of P_{004} and P_{022} vs. the O_{KLL}:Si_{LMM} AES ratio measured after formation of (2x1) and (2x3) Sr/Si(001) surfaces via annealing at 700 – 800°C. Measurements made on the (2x1) Sr/Si(001) surface prepared by depositing Sr onto Si held at 615°C (see Section 5.2.2) are also included in this plot. All of the AES data reported in these plots were recorded within 45 minutes after heating the sample to form the ordered Sr/Si(001) phase. Both P_{004} and P_{022} decrease with increasing O content. These changes are consistent with the Sr atoms in the O bonding environment occupying a position that satisfies Eq. 3.36 and is lower [with respect to Si(004) diffraction planes] than ordered Sr in oxygen-free surface regions by as much as $d_{004}/2$.

It is important to remember that satisfying Eq. 3.36 does not place a restriction on n in Eq. 3.38. Since the atomic-scale structural changes responsible for the downward

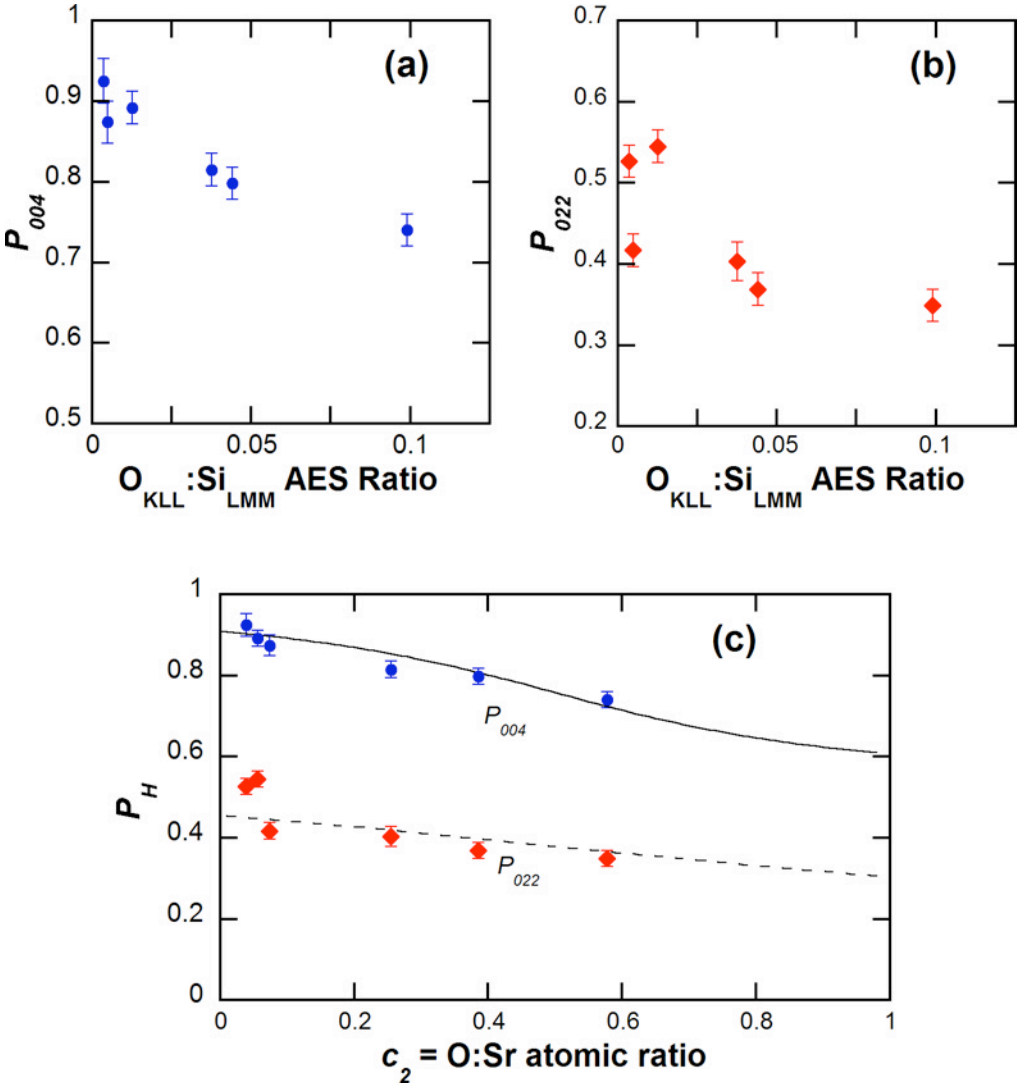

Fig. 7.6. P_{004} (circles) and P_{022} (diamonds) values plotted against (a) and (b) the ratio of the intensities of the O_{KLL} and Si_{LMM} AES signals and (c) the ratio of O atoms to Sr atoms on the surface. Fits of P_{004} (solid) and P_{022} (dashed) data to Eqs. 3.33 and 3.35 are also shown. Data collected at 12ID-D.

shift in the measured P_H take place at high temperatures that would allow for significant rearrangement of Si and Sr atoms on the surface, it is quite likely that Sr in the alternate position is not simply shifted downward from Sr atoms that are not in the oxygen bonding environment. The contamination levels measured on a particular substrate after annealing at 700°C and 750°C were usually within ~20% of the same value; but annealing at 800°C caused a significant drop in O content on the surface, suggesting that a thermal stability limit somewhere between 750°C and 800°C.

The same P_H values plotted in Fig.7.6(a) and (b) are shown again in Fig. 7.6(c), but the x-axis of the latter plot is in units of number of O atoms per Sr atoms. The O coverage was determined by comparing the O_{KLL}:Si_{LMM} AES ratios measured on samples in the 12ID-D chamber to the AES intensities measured on Sr/Si(001) samples exposed to O_2 in the MBE chamber at Northwestern University. These latter samples were also measured with XPS, and as described in Section 7.1, a conversion from O-1s XPS intensity to O coverage could be made based on the saturation intensity of O-1s electrons attributed to Sr-O bonding. There is undoubtedly a great deal of uncertainty in this series of unit conversions. In particular, there could be instrumental effects that need to be accounted for when comparing AES intensities measured with different sets of hardware and in different UHV chambers.

The curves in Fig. 7.6(c) are simultaneous fits of the measured P_{004} (solid line) and P_{022} (dashed line) to Eqs. 3.35 (using Eq. 3.33) assuming the ordered fraction consists of Sr occupying two sites which, if occupied exclusively, would each satisfy Eq. 3.36.

The fraction c_2 of ordered Sr in the oxygen bonding environment on each sample is assumed to be equal to the O:Sr atomic ratio.

The fitting parameters are the values $\boldsymbol{H}\cdot\boldsymbol{r}_j/(2\pi)$ of each site, where $\boldsymbol{H}$ is the Si(004) reciprocal lattice vector. $\boldsymbol{H}\cdot\boldsymbol{r}_j/(2\pi)$ is simply the P_H value that would be expected if the j^{th} site were occupied exclusively. The values given by this fit are $\boldsymbol{H}\cdot\boldsymbol{r}_1/(2\pi) = 0.91$ and $\boldsymbol{H}\cdot\boldsymbol{r}_2/(2\pi) = 0.61$. It is probable that some of the measured P_H values are also affected by some O accumulating on the sample at room-temperature (causing upward shifts in the measured P_H). This fact, as well as uncertainty in the conversion between O_{KLL}:Si_{LMM} AES ratios and O:Sr atomic ratios, and the possibility that the fraction of Sr in the alternate position may not be equal to the O:Sr ratio all need to be kept in mind when interpreting the plot and fit in Fig. 7.6(b). Additional fits were performed assuming different proportionality constants, k, between the O:Sr atomic ratio and the fraction of Sr in the second site. Decreasing the proportionality constant resulted in $\boldsymbol{H}\cdot\boldsymbol{r}_1/(2\pi)$ and $\boldsymbol{H}\cdot\boldsymbol{r}_2/(2\pi)$ both shifting downward and increasing it caused both values to shift upward. For the $k = 0.1$, lowest value tested, $\boldsymbol{H}\cdot\boldsymbol{r}_1/(2\pi) = 0.84$ and $\boldsymbol{H}\cdot\boldsymbol{r}_2/(2\pi) = 0.55$. For $k = 1.4$, the highest value tested, $\boldsymbol{H}\cdot\boldsymbol{r}_1/(2\pi) = 0.92$ and $\boldsymbol{H}\cdot\boldsymbol{r}_2/(2\pi) = 0.68$.

7.4 Summary

XPS measurements of Sr/Si(001) surfaces exposed to $1\text{x}10^{-9} - 1\text{x}10^{-8}$ Torr O_2 indicate that the coverage of O bonded to Sr saturates at an amount proportional to the Sr coverage within the first ~0.5 L of O_2 exposure. Beyond this exposure regime, the coverage of O bonded to Si follows Langmuir behavior. The reaction constant of Si oxidation appears to be about an order of magnitude higher for the (2x3) phase than it is for the (2x1) phase.

The presence of O contamination on Sr/Si(001) surfaces can affect the P_H values measured by XSW in two different ways. Gradual accumulation of contaminants over time causes increases in P_{022} and P_{004} as well as decreases in f_H values. Increased amounts of O on the surface during a high temperature anneal appear to cause decreases in P_{004} and P_{022}.

CHAPTER 8

SUMMARY AND OUTLOOK

8.1 Summary

This thesis work has employed a variety of surface-sensitive characterization tools to study sub-monolayer phases of Ba and Sr on Si(001). XSW measurements have been used to triangulate the position of AEM atoms (relative to the bulk primitive Si lattice) in (2x1) and (2x3) Sr/Si(001) phases as well as a (2x1) Ba/Si(001) phase. If it is assumed that the top layer Si atoms in these phases remain dimerized (as a variety of studies discussed in Chapter 2 have suggested) and that the AEM-Si bonding environment in these surface phases ought to be reasonably similar to that found in bulk AEM-Si compounds, then the XSW results strongly suggest that the adatoms occupy valley-bridge sites. This finding is in agreement with several theoretical calculations and one previous XSW study of Ba/Si(001), but differs from the conclusions reached by several other experimental investigations.

The coverage of AEM/Si(001) surface phase has, somewhat surprisingly, been a heavily debated topic in recent years. The XSW results presented in this work may provide an explanation for why there has been such disagreement over what should seemingly be simple pieces of information. On all of the samples studied in this work, a significant amount of AEM atoms were present as part of the “disordered fraction” – i.e.

they were part of the total coverage on the sample, but were not part the long-range ordered phase responsible for an observed diffraction pattern. The presence of a large disordered fraction could conceivably result in the overestimation of the coverage of a given phase. It is important to point out, however, that the AEM coverages of the (2x3) and (2x1) models proposed in Chapters 5 and 6 are actually the minimum values required geometrically for each of these surface periodicities.

Much of the discussion in Chapters 6 and 7 focused on issues related to surface contamination. The fact that the Sr/Si(001) samples discussed in Sections 5.4 and 7.1 exhibited contamination levels below the detectable limit of AES (and remained that way for several days) demonstrates that the contamination observed during experiments at 12ID-D could have been avoided under proper conditions. However, it is worth mentioning that during recent work using the 12ID-D chamber to study another metal/semiconductor surface system [Sn/Si(111)], the same standard UHV practices used during the Ba/Si(001) and Sr/Si(001) experiments were employed, and a sub-monolayer Sn/Si(111) surface with an ordered fraction of at least 90% was prepared [146]. The pressure inside the UHV chamber during this experiment was the same as that observed during AEM/Si(001) measurements, but the ordered fraction of Sn on this sample decreased by just 7% over the course of 42 hours. The contrast between this XSW experiment and those performed on AEM/Si(001) surfaces emphasizes that minimizing the levels of residual gases and other potential contaminants is even more important when studying the highly reactive Sr and Ba than it is during a “conventional” surface science experiment.

The extreme reactivity of AEM/Si(001) surfaces needs to be kept in mind during any future use of these surfaces as templates for epitaxial oxide growth. In order to optimize the effectiveness of the sub-monolayer template growth strategy, a number of processing parameters could be optimized to maximize the amount or AEM atoms that are actually coherent with the Si lattice. In addition to general minimization of contamination (from gaseous adsorption and surface diffusion) the temperature and duration of heat treatments used in the formation of AEM/Si(001) phases would also affect the relative amounts of ordered and disordered atoms.

8.2 Comparison with Previously Proposed Sr/Si(001) Phase Diagram

Perhaps the most detailed phase diagram presented for the Sr/Si(001) system is the one proposed by McKee et al. and shown in Fig. 2.5(c). The LEED and Sr coverage measurements presented in Chapter 5 are consistent with some portions of the McKee phase diagram, but also provide information indicating that certain revisions could be made to the phase diagram in Fig. 2.5(c). The surface periodicity and coverage data plotted in Fig. 5.14 is consistent with McKee et al.’s proposal that the (2x3) phase exists as a stioichiometric line compound at 1/6 ML. However, the c(2x6) periodicity that was found to accompany the (2x3) phase at coverages between 1/6 ML and 1/3 ML is absent from McKee et al.’s phase diagram. Work in this thesis indicates the presence of a two-phase region [(2x3) + c(2x6)] in the 1/6 – 1/3 ML coverage range. Although pure c(2x6) Sr/Si(001) periodicity was not observed, the local Sr coverage in this phase appears to be 1/3 ML.

The phase diagram in Fig. 2.5(c) shows a (2x1) phase with an ideal coverage of 1/4 ML and also indicates that the (2x1) phase is present as a single phase over coverages ranging from 1/4 ML to ~0.4 ML. The upper limit of this single phase region varies with temperature. However, as discussed in Chapter 2, based on simple geometric arguments, the local coverage of a (2x1) phase must be at least 1/2 ML. The plots in Fig. 5.14 indicate that (2x1) periodicity does occur, apparently as a single phase, over a range of coverages (as McKee et al. proposed), but this coverage range is ~0.3 – 0.6 ML rather than the 1/4 ML to 0.4 ML range indicated in the phase diagram in Fig. 2.5(c).

The McKee et al. phase diagram also contains a (3x1) phase at 5/8 ML. However, geometrical arguments similar to those used to explain why a (2x1) phase must have a local coverage of at least 1/2 ML can be used to show that a (3x1) phase could not have a local Sr coverage of 5/8 ML. Since the areal density of (3x1) unit cells on a Si(001) surface is 1/3 ML, the local ordered coverage of Sr in this phase would need to be an integer times 1/3 ML. 5/8 ML is close to the 2/3 ML coverage Ashman et al. [24] proposed for a (3x1) phase (based on DFT calculations). The as-deposited (3x1) surfaces observed in this thesis work also had global coverages near 2/3 ML. Although the coherent coverage on these (3x1) surfaces was significantly less than 2/3 ML, this value is the most likely local Sr coverage of the (3x1) phase.

The Sr/Si(001) phase diagram proposed by McKee et al. indicates that the Sr becomes incommensurate with the Si lattice at coverages above 5/8 ML. However, Ashman et al. predicted that a (5x1) phase would occur at 4/5 ML. The Sr coverages measured for surfaces exhibiting the (5x1) LEED patterns shown in Figs. 5.12(c) and (d) were in fact consistent with this prediction.

8.3 Outlook

Many aspects of AEM/Si(001) surfaces are worthy of further investigation. The idea, proposed in Section 5.3, that there is a significant difference between shapes of the thermal distributions of Sr atoms in the (2x3) and (2x1) phases requires much more testing before it can be accepted. XSW measurements using higher order harmonic Bragg reflections, such as Si(008) and Si(044) [in conjunction with Si(004) and Si(022) measurements] could directly probe the thermal vibration amplitudes. The mechanical stability requirements for scanning through the extremely narrow Si(008) rocking curve at an incident X-ray energy above the Sr K absorption edge could be very difficult to meet. However, "back-reflection" XSW measurements, performed using an incident energy that results in a Bragg angle near 90° and Darwin widths on the order 1° rather than a few μrad (Eq. 3.19 breaks down under these conditions) could be useful for measuring higher order harmonic reflections. EXAFS and/or surface x-ray diffraction (SXRD) would be useful for investigating whether or not the in-plane Si atom displacements [Fig. 5.11(a)] proposed to cause in-plane confinement of Sr in the (2x3) Sr/Si(001) phase actually occur.

In fact, the position and behavior of top layer Si atoms in AEM/Si(001) phases needs more investigation in general. While XPS and STM studies do support the assumption that top-layer Si atoms remain dimerized in the (2x3) and (2x1) phases, the conclusions of these investigations are not irrefutable. As described in Section 5.4, the formation of c(2x6) periodicity on a Si(001) surface requires a rearrangement of the dimer row pattern normally present on clean the (2x1) Si(001) surface. The sharp c(2x6) diffraction spots in the LEED patterns in Figs. 5.12(b) and (c) indicate that at least under certain conditions, the adsorption of Sr on Si(001) does induce dimer rearrangement.

In Chapter 5, the observation that the rate of c(2x6) Sr/Si(001) phase formation is slower than that of other Sr/Si(001) phases was proposed to be due to the rearrangement of top-layer Si atoms that c(2x6) periodicity would require. If top layer Si atoms in the 1/6 ML (2x3) Sr/Si(001) phase do remain dimerized, then a phase transition from the c(2x6) phase to the pure (2x3) phase might also be slower than transformations between other Sr/Si(001) phases [due to rearrangement of top layer Si atoms from whatever arrangement they exhibit in the c(2x6) phase into the rows of dimers in the (2x3) phase]. Further experiments monitoring the rate of Sr/Si(001) phase transitions would provide significant insight into these matters.

Further studies of the oxidation of AEM/Si(001) surfaces would provide another interesting avenue for research. Investigations in this area would be useful for understanding and improving the growth of epitaxial oxides on Sr/Si(001) template layers. An XSW experiment in which photoelectrons (rather than XRF) are monitored would be useful for obtaining information about the atomic distribution(s) of O atoms in different chemical states.

REFERENCES

[1] F. Sanchez, M. Varela, X. Queralt, M.V. Garciacuenca, J. Palau, R. Aguiar, J.L. Morenza, "Deposition of $YBa_2Cu_3O_x$ by Laser Ablation on Si(100) Using Different Buffer Layers," Applied Surface Science 69 (1993): 221-224.

[2] F. Sanchez, M. Varela, X. Queralt, R. Aguiar, J.L. Morenza, "Preparation of $SrTiO_3$ Thin-Films on Si(100) Substrates by Laser Ablation - Application as Buffer Layer for $YBa_2Cu_3O_7$ Films," Applied Physics Letters 61 (1992): 2228-2230.

[3] M. Lorenz, H. Borner, H. Hochmuth, K. Unger, "Depth profiling of Bi-Sr-Ca-Cu-O thin-films by secondary neutrals mass-spectrometry," Physica C 215 (1993): 445-457.

[4] H. Mori, I. Hiroshi, "Epitaxial Growth of $SrTiO_3$ Films on Si(100) Substrates Using a Focused Electron Beam Evaporation Method," Jpn. J. Appl. Phys. 30 (1991): L1415-L1417.

[5] T. Tambo, T. Arakawa, A. Shimizu, S. Hori, C. Tatsuyama, "Epitaxial growth of $Bi_2Sr_2CuO_x$ films onto Si(001) by molecular beam epitaxy," Applied Surface Science 159 (2000): 161-166.

[6] R.A. McKee, F.J. Walker, M.F. Chisholm, "Crystalline oxides on silicon: The first five monolayers," Phys. Rev. Lett. 81 (1998): 3014-3017.

[7] H. Yuan, R.S. Williams, "Solid-Phase Equilibria for Metal-Silicon-Oxygen Ternary Systems. 1. Mg, Ca, Sr, and Ba," Chem. Mater. 2 (1990): 695-700.

[8] R. Beyers, "Thermodynamic Considerations in Refractory Metal-Silicon-Oxygen Systems," Journal of Applied Physics 56 (1984): 147-152.

[9] R.E. Schlier, H.E. Farnsworth, "Structure and Adsorption Characteristics of Clean Surfaces of Germanium and Silicon," Journal of Chemical Physics 30 (1959): 917-926.

[10] E. Landemark, C.J. Karlsson, Y.C. Chao, R.I.G. Uhrberg, "Core-Level Spectroscopy of the Clean Si(001) Surface - Charge-Transfer within Asymmetric Dimers of the 2x1 and C(4x2) Reconstructions," Physical Review Letters 69 (1992): 1588-1591.

[11] R. Felici, I.K. Robinson, C. Ottaviani, P. Imperatori, P. Eng, P. Perfetti, "Room temperature Si(001)-(2x1) reconstruction solved by x-ray diffraction," Surface Science 375 (1997): 55-62.

[12] W. Monch, Semiconductor surfaces and interfaces, New York, Springer, 1995.

[13] C.B. Duke, "Semiconductor surface reconstruction: The structural chemistry of two-dimensional surface compounds," Chemical Reviews 96 (1996): 1237-1259.

[14] P.C. Weakliem, G.W. Smith, E.A. Carter, "Subpicosecond Interconversion of Buckled and Symmetric Dimers on Si(100)," Surface Science 232 (1990): L219-L223.

[15] T. Tabata, T. Aruga, Y. Murata, "Order-Disorder Transition on Si(001)-C(4x2)to(2x1)," Surface Science 179 (1987): L63-L70.

[16] R.A. Wolkow, "Direct Observation of an Increase in Buckled Dimers on Si(001) at Low-Temperature," Physical Review Letters 68 (1992): 2636-2639.

[17] D. Badt, H. Wengelnik, H. Neddermeyer, "Scanning-Tunneling-Microscopy at Low-Temperatures on the C(4x2)/(2x1) Phase-Transition of Si(100)," Journal of Vacuum Science & Technology B 12 (1994): 2015-2017.

[18] B.Z. Olshanetsky, A.A. Shklyaev, "Leed Studies of Vicinal Surfaces of Silicon," Surface Science 82 (1979): 445-452.

[19] R. Kaplan, "Leed Study of the Stepped Surface of Vicinal Si(100)," Surface Science 93 (1980): 145-158.

[20] A. Mesarwi, W.C. Fan, A. Ignatiev, "Oxidation of the Si(100) surface promoted by Sr overlayer: An x-ray photoemission study," Journal of Applied Physics 68 (1990): 3609-3613.

[21] A. Herrera-Gómez, F.S. Aguirre-Tostado, Y. Sun, P. Pianetta, Z. Yu, D. Marshall, R. Droopad, W.E. Spicer, "Photoemission from the Sr/Si(001) interface," Journal of Applied Physics 90 (2001): 6070-6072.

[22] R.Z. Bakhtizin, J. Kishimoto, T. Hashizume, T. Sakurai, "STM study of Sr adsorption on Si(100) surface," Appl. Surf. Sci. 94-5 (1996): 478-484.

[23] R.Z. Bakhtizin, J. Kishimoto, T. Hashizume, T. Sakurai, "Scanning tunneling microscopy of Sr adsorption on the Si(100)-2x1 surface," J. Vac. Sci.Technol. B 14 (1996): 1000-1004.

[24] C.R. Ashman, C.J. Forst, K. Schwarz, P.E. Blochl, "First-principles calculations of strontium on Si(001)," Physical Review B 69 (2004): 075309.

[25] W.C. Fan, N.J. Wu, A. Ignatiev, "Observation of Ordered Structures of Sr on the Si(100) Surface," Phys. Rev. B 42 (1990): 1254-1257.

[26] X. Hu, Z. Yu, J.A. Curless, R. Droopad, K. Eisenbeiser, J.L. Edwards Jr., W.J. Ooms, D. Sarid, "Comparative study of Sr and Ba adsorption on Si(100)," Appl. Surf. Sci. 181 (2001): 103-110.

[27] Y. Liang, S. Gan, M. Engelhard, "First step towards the growth of single-crystal oxides on Si: Formation of a two-dimensional crystalline silicate on Si(001)," Appl. Phys. Lett. 79 (2001): 3591-3593.

[28] Y. Wei, X.M. Hu, Y. Liang, D.C. Jordan, B. Craigo, R. Droopad, Z. Yu, A. Demkov, J.L. Edwards, W.J. Ooms, "Mechanism of cleaning Si(100) surface using Sr or SrO for the growth of crystalline $SrTiO_3$ films," Journal of Vacuum Science & Technology B 20 (2002): 1402-1405.

[29] D.P. Norton, C. Park, Y.E. Lee, J.D. Budai, "Strontium silicide termination and silicate epitaxy on (001) Si," Journal of Vacuum Science & Technology B 20 (2002): 257-262.

[30] J. Lettieri, J.H. Haeni, D.G. Schlom, "Critical issues in the heteroepitaxial growth of alkaline-earth oxides on silicon," J. Vac. Sci. Technol. A 20 (2002): 1332-1340.

[31] R.A. McKee, F.J. Walker, M.B. Nardelli, W.A. Shelton, G.M. Stocks, "The interface phase and the Schottky barrier for a crystalline dielectric on silicon," Science 300 (2003): 1726-1730.

[32] Z. Yu, J. Ramdani, J.A. Curless, C.D. Overgaard, J.M. Finder, R. Droopad, K.W. Eisenbeiser, J.A. Hallmark, W.J. Ooms, V.S. Kaushik, "Epitaxial oxide thin films on Si(001)," Journal of Vacuum Science & Technology B 18 (2000): 2139-2145.

[33] R. Droopad, Z.Y. Yu, H. Li, Y. Liang, C. Overgaard, A. Demkov, X.D. Zhang, K. Moore, K. Eisenbeiser, M. Hu, J. Curless, J. Finder, "Development of integrated hetero structures on silicon by MBE," Journal of Crystal Growth 251 (2003): 638-644.

[34] Y. Liang, Y. Wei, X.M. Hu, Z. Yu, R. Droopad, H. Li, K. Moore, "Heteroepitaxy of $SrTiO_3$ on vicinal Si(001): Growth and kinetic effects," Journal of Applied Physics 96 (2004): 3413-3416.

[35] Z. Yu, Y. Liang, C. Overgaard, X. Hu, J. Curless, H. Li, Y. Wei, B. Craigo, D. Jordan, R. Droopad, J. Finder, K. Eisenbeiser, D. Marshall, K. Moore, J. Kulik, P. Fejes, "Advances in heteroepitaxy of oxides on silicon," Thin Solid Films 462-63 (2004): 51-56.

[36] R. Droopad, Z. Yu, J. Ramdani, L. Hilt, J. Curless, C. Overgaard, J.L. Edwards, J. Finder, K. Eisenbeiser, J. Wang, V. Kaushik, B.-Y. Ngyuen, B. Ooms, "Epitaxial oxides on silicon grown by molecular beam epitaxy," J. Cryst. Growth 227-228 (2001): 936-943.

[37] W.C. Fan, A. Mesarwi, A. Ignatiev, "The effect of Sr and Bi on the Si(100) surface oxidation: Auger electron spectroscopy, low energy electron diffraction, and x-ray photoelectron spectroscopy study," J. Vac. Sci. Technol. A 8 (1990): 4017-4020.

[38] M.B. Nardelli, F.J. Walker, R.A. McKee, "Crystalline oxides on semiconductors: a future for the nanotransistor," Physica Status Solidi B-Basic Research 241 (2004): 2279-2286.

[39] J. Junquera, M. Zimmer, P. Ordejon, P. Ghosez, "First-principles calculation of the band offset at BaO/BaTiO$_3$ and SrO/SrTiO$_3$ interfaces," Physical Review B 67 (2003).

[40] R.A. McKee, F.J. Walker, M.F. Chisholm, "Physical structure and inversion charge at a semiconductor interface with a crystalline oxide," Science 293 (2001): 468-471.

[41] T. Urano, K. Tamiya, K. Ojima, S. Hongo, T. Kanaji, "Adsorption structure of Ba on an Si(001)-(2x1) surface," Surface Science 358 (1996): 459-463.

[42] A. Mesarwi, A. Ignatiev, "X-Ray Photoemission-Study of the Ba Si(100) Interface and the Oxidation of Si Promoted by Ba Overlayers," Journal of Vacuum Science & Technology a-Vacuum Surfaces and Films 9 (1991): 2264-2268.

[43] J. Wang, J.A. Hallmark, D.S. Marshall, W.J. Ooms, P. Ordejon, J. Junquera, D. Sanchez-Portal, E. Artacho, J.M. Soler, "Bonding and diffusion of Ba on a Si(001) reconstructed surface," Physical Review B 60 (1999): 4968-4971.

[44] A.J. Ciani, P. Sen, I.P. Batra, "Initial growth of Ba on Si(001)," Physical Review B 69 (2004): 245308.

[45] W.S. Cho, J.Y. Kim, S.S. Kim, D.S. Choi, K. Jeong, I.W. Lyo, C.N. Whang, K.H. Chae, "Atomic structure of Ba layer on Si(001)-(2 x 1) surface studied by low energy ion scattering," Surface Science 476 (2001): L259-L266.

[46] X. Yao, X.M. Hu, D. Sarid, Z. Yu, J. Wang, D.S. Marshall, R. Droopad, J.K. Abrokwah, J.A. Hallmark, W.J. Ooms, "Initial stages of Ba adsorption on the Si(100)-(2x1) surface at room temperature," Phys. Rev. B 59 (1999): 5115-5119.

[47] X. Hu, X. Yao, C.A. Peterson, D. Sarid, Z. Yu, J. Wang, D.S. Marshall, J.A. Curless, J. Ramdani, R. Droopad, J.A. Hallmark, W.J. Ooms, "Barium adsorption on Si(100)-(2 x 1) at room temperature: a bi- polar scanning tunneling microscopy study," Surface Science 457 (2000): L391-L396.

[48] R.W.J. Hollering, D. Dijkkamp, H.W.L. Lindelauf, P.A.M. Vanderheide, M. Krijn, "Optical 2nd-Harmonic Generation Study of Barium Deposition on Si(001)," Journal of Vacuum Science & Technology a-Vacuum Surfaces and Films 8 (1990): 3997-4000.

[49] C.P. Cheng, I.H. Hong, T.W. Pi, "Synchrotron-radiation photoemission study of Ba on a Si(001)2 x 1 surface," Physical Review B 58 (1998): 4066-4071.

[50] J.S. Kim, K.W. Ihm, C.C. Hwang, H.S. Kim, Y.K. Kim, C.G. Lee, C.Y. Park, "Adsorption of Ba on Si(001)2 x 1 surface," Japanese Journal of Applied Physics Part 1-Regular Papers Short Notes & Review Papers 38 (1999): 6479-6482.

[51] Y. Takeda, T. Ohtani, K. Ojima, T. Urano, S. Hongo, "UPS study of electronic states of Ba on Si(001) surface," Journal of Electron Spectroscopy and Related Phenomena 88 (1998): 619-624.

[52] W.C. Fan, A. Ignatiev, "Identification of Ordered Atomic Structures of Ba on the Si(100) Surface," Surface Science 253 (1991): 297-302.

[53] D. Vlachos, M. Kamaratos, C. Papageorgopoulos, "Ba Deposition on Si(100)2x1," Solid State Communications 90 (1994): 175-181.

[54] X.M. Hu, C.A. Peterson, D. Sarid, Z. Yu, J. Wang, D.S. Marshall, R. Droopad, J.A. Hallmark, W.J. Ooms, "Phases of Ba adsorption on Si(100)-(2 x 1) studied by LEED and AES," Surface Science 426 (1999): 69-74.

[55] Y. Takeda, T. Urano, T. Ohtani, K. Tamiya, S. Hongo, "Adsorption structure and silicide formation of Ba on the Si(001) surface," Surface Science 404 (1998): 692-696.

[56] X. Hu, C.A. Peterson, D. Sarid, Z. Yu, J. Wang, D.S. Marshall, R. Droopad, J.A. Hallmark, W.J. Ooms, "Phases of Ba adsorption on Si(100)-(2x1) studied by LEED and AES," Surf. Sci. 426 (1999): 69-74.

[57] K. Ojima, M. Yoshimura, K. Ueda, "STM observation of the 2 x 3 and c(2 x 6) structures on Ba/Si(100)," Surface Science 491 (2001): 169-174.

[58] R.A. McKee, F.J. Walker, J.R. Conner, R. Raj, "Basi$_2$ and Thin-Film Alkaline-Earth Silicides on Silicon," Applied Physics Letters 63 (1993): 2818-2820.

[59] A. Herrera-Gomez, P. Pianetta, D. Marshall, E. Nelson, W.E. Spicer, "Geometrical structure of the 1/2-ML (2X1) and 1/3-ML (2X3) Ba/Si(001) interfaces," Physical Review B 61 (2000): 12988-12991.

[60] X. Hu, X. Yao, C.A. Peterson, D. Sarid, Z. Yu, J. Wang, D.S. Marshall, R. Droopad, J.A. Hallmark, W.J. Ooms, "The (3 x 2) phase of Ba adsorption on Si(001)-2 x 1," Surface Science 445 (2000): 256-266.

[61] K. Ojima, M. Yoshimura, K. Ueda, "Observation of the Si(100)"1X2"-Ba surface by scanning tunneling microscopy," Physical Review B 65 (2002): 075408.

[62] R.L. Park, H.H. Madden, "Annealing Changes on (100) Surface of Palladium and Their Effect on Co Adsorption," Surface Science 11 (1968): 188-&.

[63] M.L. Green, E.P. Gusev, R. Degraeve, E.L. Garfunkel, "Ultrathin (< 4 nm) SiO$_2$ and Si-O-N gate dielectric layers for silicon microelectronics: Understanding the processing, structure, and physical and electrical limits," Journal of Applied Physics 90 (2001): 2057-2121.

[64] G.D. Wilk, R.M. Wallace, J.M. Anthony, "High-kappa gate dielectrics: Current status and materials properties considerations," Journal of Applied Physics 89 (2001): 5243-5275.

[65] C. Chaneliere, J.L. Autran, R.A.B. Devine, B. Balland, "Tantalum pentoxide (Ta$_2$O$_5$) thin films for advanced dielectric applications," Materials Science & Engineering R-Reports 22 (1998): 269-322.

[66] J. Robertson, "Interfaces and defects of high-K oxides on silicon," Solid-State Electronics 49 (2005): 283-293.

[67] S. Nakao, Z.C. Wang, P. Jin, Y. Miyagawa, S. Miyagawa, "Effect of high-energy Si+ ion irradiation on the crystallization behavior of amorphous strontium titanate films," Nuclear Instruments & Methods in Physics Research Section B-Beam Interactions with Materials and Atoms 191 (2002): 226-229.

[68] T. Hubert, U. Beck, H. Kleinke, "Amorphous and nanocrystalline SrTiO3 thin films," Journal of Non-Crystalline Solids 196 (1996): 150-154.

[69] K. Morii, T. Matsui, H. Tsuda, H. Mabuchi, "Meyer-Neldel rule in amorphous strontium titanate thin films," Applied Physics Letters 77 (2000): 2361-2363.

[70] R. Thomas, D.C. Dube, "Optical properties of sol-gel processed amorphous and crystalline $SrTiO_3$ thin films," Japanese Journal of Applied Physics Part 1-Regular Papers Short Notes & Review Papers 39 (2000): 1771-1775.

[71] Z.C. Wang, V. Kugler, U. Helmersson, E.K. Evangelou, N. Konofaos, S. Nakao, P. Jin, "Characteristics of $SrTiO_3$ thin films deposited on Si by rf magnetron sputtering at various substrate temperatures," Philosophical Magazine B-Physics of Condensed Matter Statistical Mechanics Electronic Optical and Magnetic Properties 82 (2002): 891-903.

[72] Z.C. Wang, V. Kugler, U. Helmersson, N. Konofaos, E.K. Evangelou, S. Nakao, P. Jin, "Electrical properties of $SrTiO_3$ thin films on Si deposited by magnetron sputtering at low temperature," Applied Physics Letters 79 (2001): 1513-1515.

[73] T. Matsumoto, A. Niino, S. Baba, K. Numata, S. Miyake, "Low temperature preparation of perovskite oxide films by ECR sputtering assisted with microwave treatment," Surface & Coatings Technology 174 (2003): 611-614.

[74] S. Miyake, S. Baba, A. Niino, K. Numata, "Preparation of high quality strontium titanate based thin films by ECR plasma sputtering," Surface & Coatings Technology 169 (2003): 27-31.

[75] P.C. Joshi, S.B. Krupanidhi, "Strontium-Titanate Thin-Films by Rapid Thermal-Processing," Applied Physics Letters 61 (1992): 1525-1527.

[76] P.C. Joshi, S.B. Krupanidhi, "Structural and Electrical Characteristics of $SrTiO_3$ Thin-Films for Dynamic Random-Access Memory Applications," Journal of Applied Physics 73 (1993): 7627-7634.

[77] R. Thomas, D.C. Dube, M.N. Kamalasanan, S. Chandra, A.S. Bhalla, "Structural, electrical, and low-temperature dielectric properties of sol-gel derived $SrTiO_3$ thin films," Journal of Applied Physics 82 (1997): 4484-4488.

[78] I. Kobayashi, Y. Wakao, K. Tominaga, M. Okada, "Preparation of $SrTiO_3$ Thin-Films by Metalorganic Chemical-Vapor-Deposition," Japanese Journal of Applied Physics Part 1-Regular Papers Short Notes & Review Papers 33 (1994): 4680-4683.

[79] B.K. Moon, H. Ishiwara, "Roles of Buffer Layers in Epitaxial Growth of $SrTiO_3$ Films on SIlicon Substrates," Jpn. J. Appl. Phys. 33 (1994): 1472-1477.

[80] T. Tambo, T. Nakamura, K. Maeda, H. Ueba, C. Tatsuyama, "Molecular beam epitaxy of $SrTiO_3$ films on Si(100)-2x1 with SrO buffer layer," Japanese Journal of Applied Physics Part 1-Regular Papers Short Notes & Review Papers 37 (1998): 4454-4459.

[81] T. Tambo, K. Maeda, A. Shimizu, C. Tatsuyama, "Improvement of electrical properties of epitaxial $SrTiO_3$ films on Si(001) - 2 x 1 by *in situ* annealing," Journal of Applied Physics 86 (1999): 3213-3217.

[82] J.Q. He, C.L. Jia, V. Vaithyanathan, D.G. Schlom, J. Schubert, A. Gerber, H.H. Kolhstedt, R.H. Wang, "Interfacial reaction in the growth of epitaxial $SrTiO_3$ thin films on (001) Si substrates," Journal of Applied Physics 97 (2005).

[83] R. McKee, F. Walker, M. Chisholm, "Crystalline oxides on silicon - alternative dielectrics for advanced transistor technologies," Mat. Res. Soc. Symp. Proc. 567 (1999): 415-425.

[84] R. Droopad, Z. Yu, J. Ramdani, L. Hilt, J. Curless, C. Overgaard, J.L. Edwards Jr., J. Finder, K. Eisenbeiser, W. Ooms, "Development of high dielectric constant epitaxial oxides on silicon by molecular beam epitaxy," Materials Science & Engineering, B: Solid-State Materials for Advanced Technology 87 (2001): 292-296.

[85] X.M. Hu, H. Li, Y. Liang, Y. Wei, Z. Yu, D. Marshall, J. Edwards, R. Droopad, X. Zhang, A.A. Demkov, K. Moore, J. Kulik, "The interface of epitaxial $SrTiO_3$ on silicon: in situ and ex situ studies," Applied Physics Letters 82 (2003): 203-205.

[86] H. Li, X. Hu, Y. Wei, Z. Yu, X. Zhang, R. Droopad, A.A. Demkov, J. Edwards, K. Moore, W. Ooms, J. Kulik, P. Fejes, "Two-dimensional growth of high-quality strontium titanate thin films on Si," Journal of Applied Physics 93 (2003): 4521-4525.

[87] G.Y. Yang, J.M. Finder, J. Wang, Z.L. Wang, Z. Yu, J. Ramdani, R. Droopad, K.W. Eisenbeiser, R. Ramesh, "Study of microstructure in $SrTiO_3$/Si by high-resolution transmission electron microscopy," Journal of Materials Research 17 (2002): 204-213.

[88] S.A. Chambers, Y. Liang, Z. Yu, R. Droopad, J. Ramdani, "Band offset and structure of $SrTiO_3$/Si(001) heterojunctions," Journal of Vacuum Science & Technology A 19 (2001): 934-939.

[89] F.S. Aguirre-Tostado, A. Herrera-Gomez, J.C. Woicik, R. Droopad, Z. Yu, D.G. Schlom, P. Zschack, E. Karapetrova, P. Pianetta, C.S. Hellberg, "Elastic anomaly for $SrTiO_3$ thin films grown on Si(001)," Physical Review B 70 (2004).

[90] F.S. Aguirre-Tostado, A. Herrera-Gomez, J.C. Woicik, R. Droopad, Z. Yu, D.G. Schlom, J. Karapetrova, P. Zschack, P. Pianetta, "Displacive phase transition in $SrTiO_3$ thin films grown on Si(001)," Journal of Vacuum Science & Technology A 22 (2004): 1356-1360.

[91] V. Shutthanandan, S. Thevuthasan, Y. Liang, E.M. Adams, Z. Yu, R. Droopad, "Direct observation of atomic disordering at the $SrTiO_3$/Si interface due to oxygen diffusion," Applied Physics Letters 80 (2002): 1803-1805.

[92] L.H. Tisinger, R. Liu, J. Kulik, X. Zhang, J. Ramdani, A.A. Demkov, "Ultraviolet-Raman studies of $SrTiO_3$ ultrathin films on Si," Journal of Vacuum Science & Technology B 21 (2003): 53-56.

[93] F. Amy, A. Wan, A. Kahn, F.J. Walker, R.A. McKee, "Surface and interface chemical composition of thin epitaxial $SrTiO_3$ and $BaTiO_3$ films: Photoemission investigation," Journal of Applied Physics 96 (2004): 1601-1606.

[94] F. Amy, A.S. Wan, A. Kahn, F.J. Walker, R.A. McKee, "Band offsets at heterojunctions between $SrTiO_3$ and $BaTiO_3$ and Si(100)," Journal of Applied Physics 96 (2004): 1635-1639.

[95] S.A. Chambers, T. Droubay, T.C. Kaspar, M. Gutowski, "Experimental determination of valence band maxima for $SrTiO_3$, TiO_2, and SrO and the associated valence band offsets with Si(001)," Journal of Vacuum Science & Technology B 22 (2004): 2205-2215.

[96] S.A. Chambers, Y. Liang, "Band discontinuities at epitaxial $SrTiO_3$/Si(001) heterojunctions," Applied Physics Letters 77 (2000): 1662-1664.

[97] A.C. Tuan, T.C. Kaspar, T. Droubay, J.W. Rogers, S.A. Chambers, "Band offsets for the epitaxial TiO_2/$SrTiO_3$/Si(001) system," Applied Physics Letters 83 (2003): 3734-3736.

[98] Z. Yu, J. Ramdani, J.A. Curless, J.M. Finder, C.D. Overgaard, R. Droopad, K.W. Eisenbeiser, J.A. Hallmark, W.J. Ooms, J.R. Conner, V.S. Kaushik, "Epitaxial perovskite thin films grown on silicon by molecular beam epitaxy," Journal of Vacuum Science & Technology B 18 (2000): 1653-1657.

[99] J. Ramdani, R. Droopad, Z. Yu, J.A. Curless, C.D. Overgaard, J. Finder, K. Eisenbeiser, J.A. Hallmark, W.J. Ooms, V. Kaushik, P. Alluri, S. Pietambaram, "Interface characterization of high-quality $SrTiO_3$ thin films on Si(100) substrates grown by molecular beam epitaxy," Appl. Surf. Sci. 159-160 (2000): 127-133.

[100] K. Eisenbeiser, J.M. Finder, Z. Yu, J. Ramdani, J.A. Curless, J.A. Hallmark, R. Droopad, W.J. Ooms, L. Salem, S. Bradshaw, C.D. Overgaard, "Field effect transistors with $SrTiO_3$ gate dielectric on Si," Applied Physics Letters 76 (2000): 1324-1326.

[101] D.M. Schaadt, E.T. Yu, V. Vaithyanathan, D.G. Schlom, "Nanoscale current transport in epitaxial $SrTiO_3$ on n(+)-Si investigated with conductive atomic force microscopy," Journal of Vacuum Science & Technology B 22 (2004): 2030-2034.

[102] J. Robertson, C.W. Chen, "Schottky barrier heights of tantalum oxide, barium strontium titanate, lead titanate, and strontium bismuth tantalate," Applied Physics Letters 74 (1999): 1168-1170.

[103] J. Robertson, "Band offsets of wide-band-gap oxides and implications for future electronic devices," Journal of Vacuum Science & Technology B 18 (2000): 1785-1791.

[104] C.J. Forst, C.R. Ashman, K. Schwarz, P.E. Blochl, "The interface between silicon and a high-k oxide," Nature 427 (2004): 53-56.

[105] X. Zhang, A.A. Demkov, H. Li, X. Hu, Y. Wei, J. Kulik, "Atomic and electronic structure of the Si/$SrTiO_3$ interface," Physical Review B 68 (2003): 125323.

[106] I.N. Yakovkin, M. Gutowski, "$SrTiO_3$/Si(001) epitaxial interface: A density functional theory study," Physical Review B 70 (2004).

[107] P.W. Peacock, J. Robertson, "Structure, bonding, and band offsets of (100)$SrTiO_3$-silicon interfaces," Applied Physics Letters 83 (2003): 5497-5499.

[108] T. Tambo, A. Shimizu, A. Matsuda, C. Tatsuyama, "Stability of two-step-growth $Bi_2Sr_2CuO_x$ films on Si(001) using SrO buffer layer," Japanese Journal of Applied Physics Part 1-Regular Papers Short Notes & Review Papers 41 (2002): 83-85.

[109] Y. Wang, C. Ganpule, B.T. Liu, H. Li, K. Mori, B. Hill, M. Wuttig, R. Ramesh, J. Finder, Z. Yu, R. Droopad, K. Eisenbeiser, "Epitaxial ferroelectric Pb(Zr, Ti)O_3 thin films on Si using $SrTiO_3$ template layers," Applied Physics Letters 80 (2002): 97-99.

[110] A. Lin, X. Hong, V. Wood, A.A. Verevkin, C.H. Ahn, R.A. McKee, F.J. Walker, E.D. Specht, "Epitaxial growth of $Pb(Zr_{0.2}Ti_{0.8})O_3$ on Si and its nanoscale piezoelectric properties," Applied Physics Letters 78 (2001): 2034-2036.

[111] K. Eisenbeiser, R. Droopad, Z. Yu, C. Overgaard, J. Kulik, J. Finder, S.M. Smith, S. Voight, D. Penunuri, "Crystalline oxide-based devices on silicon substrates," Journal of Electronic Materials 32 (2003): 868-871.

[112] B.T. Liu, K. Maki, Y. So, V. Nagarajan, R. Ramesh, J. Lettieri, J.H. Haeni, D.G. Schlom, W. Tian, X.Q. Pan, F.J. Walker, R.A. McKee, "Epitaxial La-doped $SrTiO_3$ on silicon: A conductive template for epitaxial ferroelectrics on silicon," Applied Physics Letters 80 (2002): 4801-4803.

[113] K. Eisenbeiser, R. Emrick, R. Droopad, Z. Yu, J. Finder, S. Rockwell, J. Holmes, C. Overgaard, W. Ooms, "GaAs MESFETs fabricated on Si substrates using a $SrTiO_3$ buffer layer," Ieee Electron Device Letters 23 (2002): 300-302.

[114] M.J. Bedzyk, G. Materlik, "2-Beam Dynamical Diffraction Solution of the Phase Problem - A Determination with X-Ray Standing-Wave Fields," Physical Review B 32 (1985): 6456-6463.

[115] N. Hertel, G. Materlik, J. Zegenhagen, "X-Ray Standing Wave Analysis of Bismuth Implanted in Si(110)," Zeitschrift Fur Physik B-Condensed Matter 58 (1985): 199-204.

[116] J. Zegenhagen, "Surface-Structure Determination with X-Ray Standing Waves," Surface Science Reports 18 (1993): 199-271.

[117] M.J. Bedzyk, L.W. Cheng, "X-ray standing wave studies of minerals and mineral surfaces: Principles and applications," Rev. Mineral. Geochem. 49 (2002): 221-266.

[118] R.G. Jones, I. Shuttleworth, C.J. Fisher, J.J. Lee, S.L. Bastow, R. Ithnin, J. Ludecke, M.P. Skegg, D.P. Woodruff, B.C.C. Cowie, "Surface structure determination using X-ray standing waves," Physics of Low-Dimensional Structures 11-2 (2001): 1-26.

[119] D.P. Woodruff, "Surface structure determination using X-ray standing waves," Reports on Progress in Physics 68 (2005): 743-798.

[120] B.W. Batterman, H. Cole, "Dynamical Diffraction of X Rays by Perfect Crystals," Reviews of Modern Physics 36 (1964): 681-717.

[121] A. Krolzig, G. Materlik, M. Swars, J. Zegenhagen, "A Feedback-Control System for Synchrotron Radiation Double Crystal Instruments," Nuclear Instruments & Methods in Physics Research Section a-Accelerators Spectrometers Detectors and Associated Equipment 219 (1984): 430-434.

[122] D.P. Woodruff, T.A. Delchar, Modern Techniques of Surface Science, Cambridge, Cambridge University Press, 1999.

[123] Y.W. Chung, Practical Guide to Surface Science and Spectroscopy, San Diego, Academic Press, 2001.

[124] Y. Qian, X-ray Standing Wave Investigation of Group III and V Elements Adsorbed on the Si(001) Surface: Structure, Dynamics and Kinetics, Evanston, Northwestern, 1995, 195.

[125] A. Ishizaka, Y. Shiraki, "Low-Temperature Surface Cleaning of Silicon and Its Application to Silicon MBE," Journal of the Electrochemical Society 133 (1986): 666-671.

[126] N. Roberts, R.J. Needs, "Total Energy Calculations of Dimer Reconstructions on the Silicon (001) Surface," Surface Science 236 (1990): 112-121.

[127] G. Rocktaschel, A. Weiss, "Zur Kenntnis Der Strontiumsilicide," Zeitschrift Fuer Anorganische Und Allgemeine Chemie 316 (1962): 231-236.

[128] K. Janzon, H. Schafer, A. Weiss, "Crystal Structure of Strontium Disilicide," Angewandte Chemie-International Edition 4 (1965): 245-247.

[129] G. Nagorsen, G. Rocktaschel, H. Schafer, A. Weiss, "Die Kristallstruktur Der Phase Sr_5Si_3," Zeitschrift Fur Naturforschung Part B-Chemie Biochemie Biophysik Biologie Und Verwandten Gebiete 22 (1967): 101-103.

[130] A. Widera, B. Eisenmann, H. Schafer, "Preparation and Crystal-Structure of Sr_2Si," Zeitschrift fuer Naturforschung, B: Chemical Sciences 31 (1976): 520-521.

[131] J. Evers, G. Oehlinger, A. Weiss, "Single-Crystal Data of the High-Pressure High-Temperature Phase of $SrSi_2$," Zeitschrift fuer Naturforschung, B: Chemical Sciences 38 (1983): 899-900.

[132] G.E. Pringle, "Structure of $SrSi_2$ - Crystal of Class O (432)," Acta Cryst. B 28 (1972): 2326-2329.

[133] J. Evers, G. Oehlinger, A. Weiss, "Effect of Pressure on Structures of Divalent Metal Disilicides MSi_2(M=Ca,Eu,Sr)," Journal of Solid State Chemistry 20 (1977): 173-181.

[134] G. Bruzzone, E. Franceschi, "Occurrence of M_2X Intermetallic Compounds (M = Ca, Sr, Ba-X = Si, Ge, Sn, Pb)," Journal of the Less-Common Metals 57 (1978): 201-208.

[135] H. Schafer, K.H. Janzon, A. Weib, "$BaSi_2$, a Phase with Discrete Si_4 Tetrahedra," Angewandte Chemie-International Edition 2 (1963): 393.

[136] K. Janzon, H. Schafer, A. Weiss, "Die Kristallstruktur Der Phase Ba_5Si_3," Zeitschrift Fur Naturforschung Part B-Chemie Biochemie Biophysik Biologie Und Verwandten Gebiete 21 (1966): 287-288.

[137] B. Eisenman, K.H. Janzon, H. Schafer, A. Weiss, "A Barium Silicide Ba_3Si_4," Zeitschrift Fur Naturforschung Part B-Chemie Biochemie Biophysik Biologie Und Verwandten Gebiete 24 (1969): 457-458.

[138] A. Widera, H. Schafer, "Preparation and Crystal-Structure of Ba_2Si," Zeitschrift fuer Naturforschung, B: Chemical Sciences 31 (1976): 1434-1435.

[139] F.A. Cotton, G. Wilkinson, C.A. Murillo, M. Bochman, Advanced Inorganic Chemistry, New York, John Wiley & Sons, 1999.

[140] Y. Liang, S.A. Chambers, S. Gan, D.R. Baer, "Interplay Between Interfacial Properties and Dielectric and Ferroelectric Behaviors of Barium Strontium Titanate Thin Films," (1999).

[141] J.F. Moulder, W.F. Stickle, P.E. Sobol, K.D. Bomben, Handbook of X-ray Photoelecron Spectroscopy, Eden Prairie, Minnesota, Perkin-Elmer Corporatioin, 1992.

[142] H. Watanabe, K. Kato, T. Uda, K. Fujita, M. Ichikawa, T. Kawamura, K. Terakura, "Kinetics of initial layer-by-layer oxidation of Si(001) surfaces," Physical Review Letters 80 (1998): 345-348.

[143] Y. Takakuwa, F. Ishida, T. Kawawa, "Phase transition from Langmuir-type adsorption to two-dimensional oxide island growth during oxidation on Si(001) surface," Applied Surface Science 216 (2003): 133-140.

[144] H.W. Yeom, H. Hamamatsu, T. Ohta, R.I.G. Uhrberg, "High-resolution core-level study of initial oxygen adsorption on Si(001): Surface stoichiometry and anomalous Si 2p core-level shifts," Physical Review B 59 (1999): R10413-R10416.

[145] Y. Enta, Y. Takegawa, M. Suemitsu, N. Miyamoto, "Growth kinetics of thermal oxidation process on Si(100) by real time ultraviolet photoelectron spectroscopy," Applied Surface Science 101 (1996): 449-453.

[146] A.A. Escuadro, D.M. Goodner, J.S. Okasinski, M.J. Bedzyk, "X-ray standing wave analysis of the Sn/Si(111)-root 3x root 3 surface," Physical Review B 70 (2004).

APPENDIX A

X-ray Scattering Studies of Perovskite-Semiconductor Heterostructures

A.1 XSW Studies of $SrTiO_3$/Si(001) Films Grown by Motorola

Three different samples of epitaxial $SrTiO_3$ grown on Si(001) provided by Dr. Z. Yu of Motorola Semiconductor Products Sector (Phoenix, Arizona) were studied using X-ray standing waves at beamline X-15A at the National Synchrotron Light Source (NSLS) at Brookhaven National Laboratory. The thicknesses of the MBE grown $SrTiO_3$ films were 2, 3 and 4 unit cells. All samples had 100Å epitaxial $BaTiO_3$ capping layers that prevented the STO film from being in direct contact with atmosphere. Using an incident photon energy of 18.5 keV, XSW measurements were made by monitoring the Sr-Kα fluorescence yield while scanning in energy through the Si(004) rocking curve.

Fig. A.1 shows the XSW data and corresponding fits for the sample with 2 unit cells $SrTiO_3$. Table A.1 shows the Sr f_{004} and P_{004} values determined for samples with STO films that were 2, 3 and 4 unit cells thick. Also shown are the f_{004} values expected for 2, 3 and 4 unit cells of STO grown coherently on Si(001). The measured f_{004} for all samples is significantly lower than the ideal value. Based on the facts that the fluorescence yield curves exhibit no asymmetry with respect to the rocking curves and that the fitted P_{004} values are near 0.75 on all three samples, the true f_{004} values for all three samples are indistinguishable from zero.

The fact that the measured f_H are lower than those expected for coherent STO-Si(001) interfaces could be due to a reaction that has produced an interfacial layer between the semiconductor and perovskite. $SrTiO_3$ films grown by the same method used to prepare samples for this study have been reported to be stable against the formation of interfacial amorphous layers when the STO thickness was ≤ 20 Å (~5 unit cells) [99]. When growth was continued beyond this critical thickness, amorphous SiO_2 or silicate layers were observed at the interface. It is possible that the 100 Å BTO capping layer used in the present work provided a driving force for an interfacial reaction similar to that produced when the thicker (> 5 unit cells) STO films were grown.

$SrTiO_3$ thickness (unit cells)	P_{004} (measured)	f_{004} (measured)	f_{004} (ideal)
2	0.75	0.10	0.77
3	0.73	0.18	0.76
4	0.74	0.13	0.73

Table A.1 $SrTiO_3$ film thickness, measured P_{004}, measured f_{004} and f_{004} value expected (for ideal $SrTiO_3$ film of particular thickness) for three different $BaTiO_3/SrTiO_3/Si(001)$ samples grown by Motorola. Data collected at National Synchrotron Light Source (NSLS) beamline X15A.

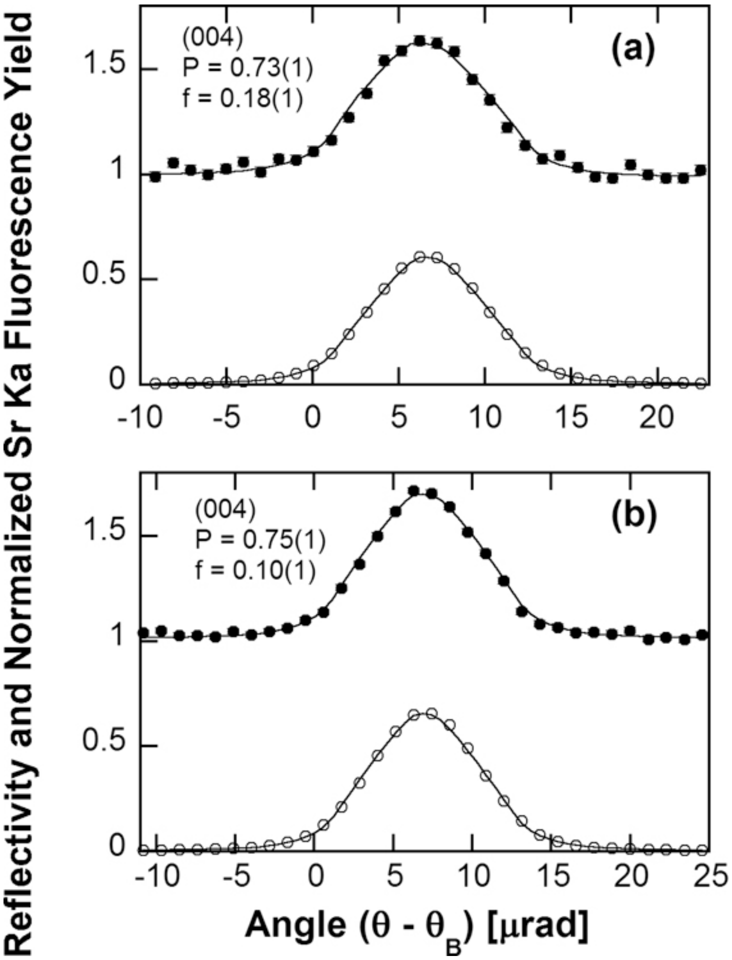

Fig. A.1. Angular dependence of X-ray reflectivity (open circles) and normalized Sr Kα fluorescence yield (filled circles) data fit to dynamical diffraction theory for Si(004) XSW measurement of $BaTiO_3/SrTiO_3/Si(001)$ samples with (a) 3 and (b) 2 unit cells of $SrTiO_3$. Data collected at X15A.

A.2 XSW and Crystal Truncation Rod Studies of Perovskite / Semiconductor Heterostructures Grown at Oak Ridge National Laboratory and Penn State University

XSW and crystal truncation rod (CTR) measurements were performed on $SrTiO_3$/Si(001) and $BaTiO_3$/Ge(001) thin films grown by molecular beam epitaxy (MBE) in the laboratories of R. A. McKee at Oak Ridge National Lab. CTR measurements were also made on $SrTiO_3$/Si(001) samples grown in the laboratory of D.G. Schlom at Penn State University.

Growth of the $SrTiO_3$/Si(001) samples was initiated with a sub-monolayer (2x1) phase of Sr on clean Si(001). Alternating layers of SrO and TiO_2 were then deposited to form the $SrTiO_3$ film. A 2.5 unit-cell sample was terminated with a SrO layer and was then capped with 20 Å of amorphous Ti. Other $SrTiO_3$/Si(001) samples (ranging in thickness from 4 to 30 $SrTiO_3$ unit cells) were terminated with a single TiO_2 layer. $BaTiO_3$/Ge(001) growth was carried out in a similar fashion, although the initiating layer was a sub-monolayer (2x1) phase of Ba on Ge(001). Alternating layers of BaO and TiO_2 were subsequently deposited to form the perovskites film. An additional sample, grown by depositing 3 unit cells of $Ba_{0.75}Sr_{0.25}O$ on Si(001) before depositing of 24 unit cells of $SrTiO_3$, was also studied. According to Vegard's law, the composition of the $Ba_{0.75}Sr_{0.25}$ layer is expected to result in perfect lattice matching (within ~0.01%) with the Si substrate.

XSW measurements were performed by scanning the single-crystal Ge(001) and Si(001) substrates in angle through the Ge(004) and Si(004) rocking curves while monitoring reflectivity with a scintillation detector and simultaneously collecting the fluorescence spectra with a Si(Li) solid state detector. The rocking curves along with the Ba, Sr and Ti fluorescence yields were fit to dynamical diffraction theory to determine f_{004} and P_{004} of metal atoms in the oxide films.

GIXD measurements were made using a five-circle "kappa" diffractometer and a six-circle "psi" diffractometer. In-plane h-k mesh scans as well as crystal truncation rod (CTR) measurements were made with the incidence angle (α) fixed at values between 0.2° and 0.5°.

Representative XSW and GIXD data are shown in Figs. A.2 – A.4. The XSW data in Fig. A.2 was collected from a sample consisting of 2 unit cells of $BaTiO_3$ on Ge(001). A fit of this data to dynamical diffraction theory was used to determine P_{004} = 0.57 ±0.03 and f_{004} = 0.15 ± 0.01 for Ba atoms in the film. These results were used to calculate an interface height of 2.42 Å between the $BaTiO_3$ film and Ge substrate. Fig. A.3 shows a segment of the (20L) CTR measured on the $SrTiO_3/Ba_{0.75}Sr_{0.25}O/Si(001)$ sample. A fit of this data suggests that the $Ba_{0.75}Sr_{0.25}O$ layer is no longer present, but instead, a mixed Ba-Sr silicide exists at the Si-$SrTiO_3$ interface. The (11L) CTR measured on a 5 unit cell $SrTiO_3$/Si(001) sample is plotted in Fig. A.4. The best fit (solid line) consists of one silicide layer above the Si(001) surface. The silicide layer was modeled as containing a weighted mix of Ba and Sr; its lateral position was found to be above the second-highest Si layer after comparing fits for each of the four high-symmetry sites. Specular reflectivity scans (not shown) clearly showed STO film peaks, but there was no sign of the BSO(002) peak, despite extensive searching.

Fitting and modeling of the CTR data was performed by Dr. Don Walko.

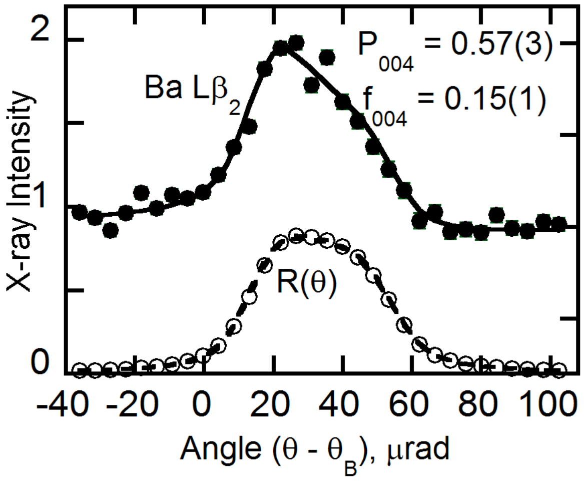

Fig. A.2. Angular dependence of x-ray reflectivity (open circles) and Ba Lβ_2 fluorescence yield (filled circles) data (fit to dynamical diffraction theory) for Ge(004) XSW measurement of 2 unit cells $BaTiO_3$ on Ge(001). Data collected at APS 5ID-C.

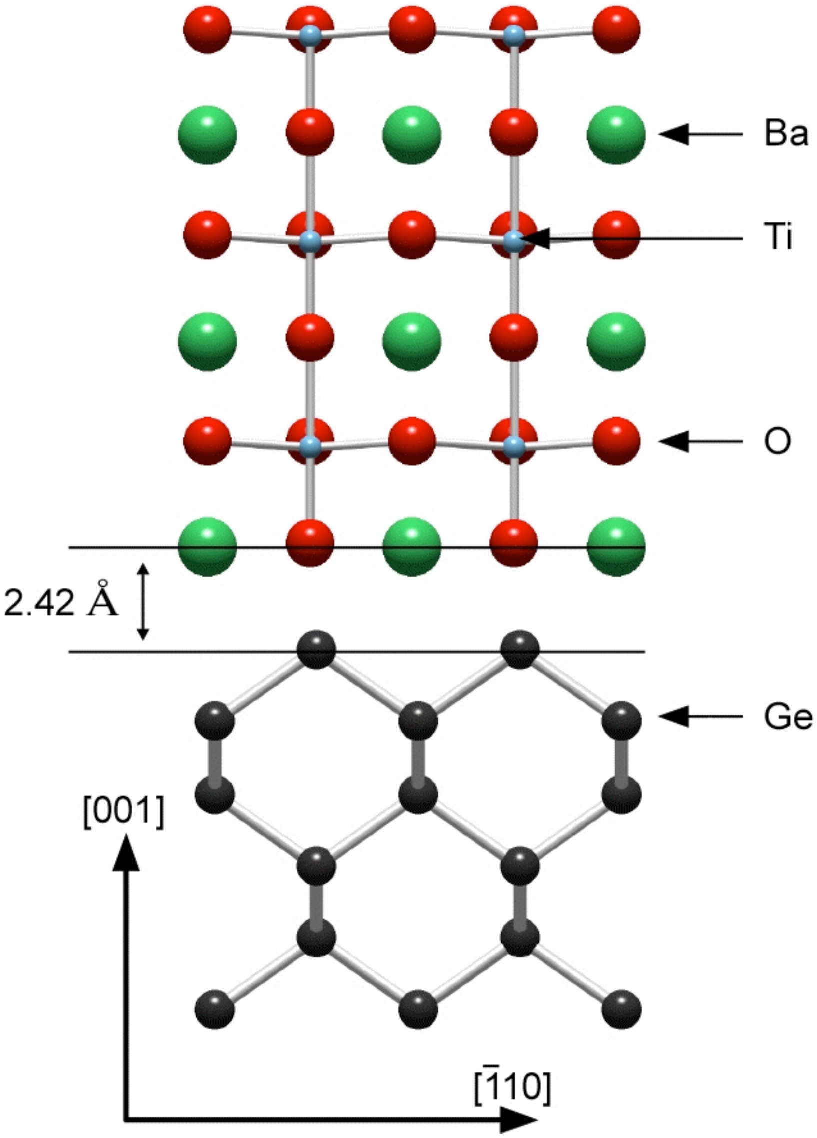

Fig. A.3. [110] projection of 2.5 $BaTiO_3$ unit cells on Ge(001) with an interface height of 2.42 Å.

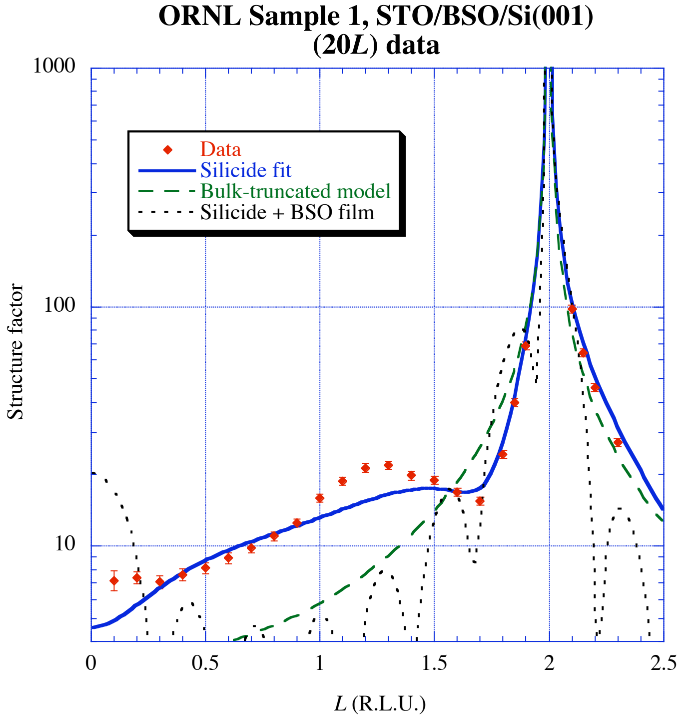

Fig. A.4. CTR data (diamonds) collected along (20L) rod of $SrTiO_3/Ba_{0.75}Sr_{0.25}O/SrTiO_3(001)$ heterostructure. A best fit (solid line) using a model that consists of a mixed Ba-Sr silicide rather than $Ba_{0.75}Sr_{0.25}O$ between the $SrTiO_3$ and Si(001). Data collected at 5ID-C.

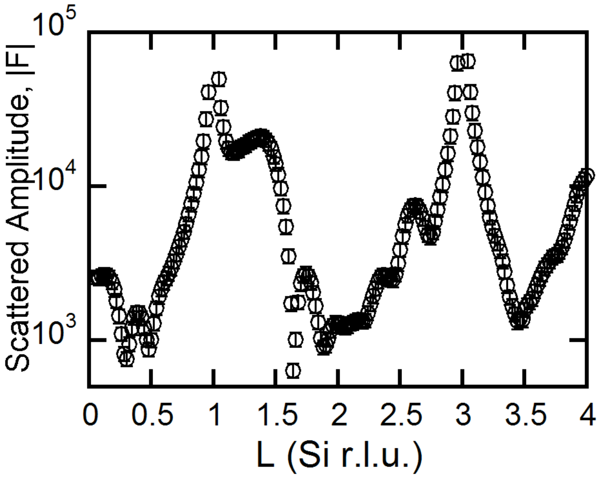

Fig. A.5. CTR data collected along (11L) rod from sample consisting of 5 unit cells $SrTiO_3$ on Si(001). Data collected at APS 7ID-C.

APPENDIX B

XPS Measurement of 1/6 ML (2x3) Surface Exposed to 1x10^{-8} Torr O_2

This appendix contains the results of XPS measurements made on a 1/6 ML (2x3) surface exposed to 1x10^{-8} Torr O_2. Fig. B.1 shows the coverage of O bonded to Sr, O bonded to Si and net O as a function of O_2 exposure in L. The experimental methods used in collecting this data are described in Section 7.1.1. Fitting the coverage of O bonded to Si to Eq. 7.2 yielded a rate constant $k_s = 1.5 \times 10^{-2} L^{-1}$. The value is more than 6 times higher than the value of k_s obtained for O bonded to Si on the (2x1) surface exposed to 1x10^{-8} Torr O_2 (see Fig. 7.2).

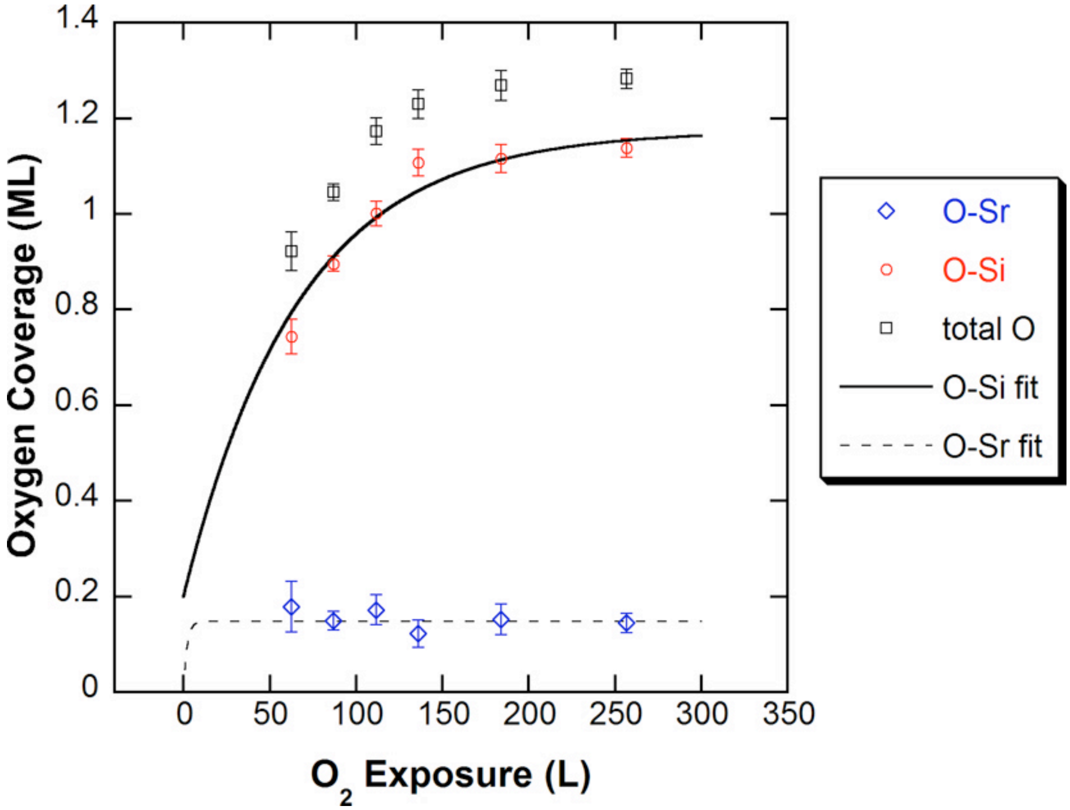

Fig. B.1. Coverage of O bonded to Sr (diamonds), O bonded to Si as well as total O coverage (squares) for (2x3) Sr/Si(001) surface exposed to O_2 with the substrate held at 450°C. An O_2 partial pressure of $1x10^{-8}$ Torr was used. Data collected at Northwestern multi-purpose UHV surface science chamber.